JET-IR(96)05
NOT FOR PUBLICATION

C F Maggi

Measurement and Interpretation of Spectral Emission from JET Divertor Plasmas

JET-IR(96)05

Measurement and Interpretation of Spectral Emission from JET Divertor Plasmas

C F Maggi.

JET Joint Undertaking, Abingdon, Oxfordshire, OX14 3EA, UK.

A Thesis submitted for the Degree of Doctor of Philosophy
in the University of Strathclyde

January 1997

Abstract

The thesis presents a spectroscopic investigation of the radiating properties and transport of impurity ions and neutral deuterium in high density, low temperature JET divertor plasmas. This is in the context of current studies aimed at the understanding of impurity dynamics in divertor tokamaks. The study combines atomic physics modelling of impurity and hydrogenic emission with the modelling of divertor plasma for the interpretation of VUV and visible spectral line emission and bolometer measurements. In particular, radiated power components were measured with a newly installed, double SPRED VUV spectrometer, which was absolutely calibrated *in situ* with branching ratio techniques. Different divertor plasma regimes were investigated, with emphasis on Ohmic and L-mode density limit discharges, detached and nitrogen seeded radiative divertor plasmas, both with carbon and beryllium targets. In these high density, low temperature divertor regimes charge exchange reactions with neutral deuterium are expected to influence the radiation distributions of impurity species. Low energy charge transfer between impurity ions and neutral deuterium donors has been included for the first time in divertor emission modelling. This has allowed a quantitative study of the effect of charge exchange on carbon impurity emission in realistic conditions of JET divertor discharges.

Acknowledgements

The work of this thesis was carried out at JET. During this time I have worked with a large number of people, some of whom have become very good friends. To all these people I am indebted for support, discussions and encouragement.

It is a pleasure to thank Hugh Summers, my supervisor, for continuous support and advice.

A special thank you is for Lorne Horton, who has supported and advised me (with great patience) from the very first day of this thesis and who was always there for discussions, encouragement and criticism.

I am indebted to Robert Wolf, Akko Maas and Bob Marshall for their hard work and dedication in the installation, commissioning and maintenance of the double SPRED diagnostic.

My friends (and office neighbours) Alberto Loarte and Ray Monk have contributed to make the last year of this thesis a very lively one. With them I have shared long discussions and many good laughs.

It is a pleasure to thank Peter Stangeby for his continuous interest in this work, for suggestions and discussion during his visits to JET and via e-mail while in Toronto.

I have enjoyed working with Woijchiech Fundamenski during his stay at JET and I hope I did not shock him too much when I told him that modelling and experiment never agree.

I am indebted to Berta Herrero for private communication of the C^{+3}/H state selective cross sections.

David Brooks and Gianluca Oppo have cheered me up during the two winter semesters spent in Glasgow and have helped me in several occasions to sort out the logistic problems connected with working at JET while being a PhD student of Strathclyde University.

Last, but not least, thank you to Ralph Dux for help and support in the final stage of this thesis.

Preface

The following publications and conference proceedings are associated with the work of this thesis and contain substantial contribution from the author of this thesis:

C.F. Maggi, L.D. Horton, R. König et al., 'Impurity line emission due to thermal charge exchange in JET edge plasmas', Control. Fusion and Plasma Physics (Proc. 21st EPS Conf., Montpellier, 1994) Vol 18B, II-826.

P. Breger, R. König, C.F. Maggi et al., 'High resolution spectroscopic measurements of impurity radiation distributions and neutral deuterium profiles in the JET scrape-off-layer', Control. Fusion and Plasma Physics (Proc. 22nd EPS Conf., Bournemouth, 1995) Vol 19C, III-377.

T. Lovegrove, L.D. Horton, R. König, J. Lingertat, A. Maas, C.F. Maggi et al., 'Investigation of opacity effects in the JET tokamak divertor region', Control. Fusion and Plasma Physics (Proc. 22nd EPS Conf., Bournemouth, 1995) Vol 19C, III-301.

C.F. Maggi, J.D. Elder, W. Fundamenski et al., 'Measurement and Analysis of radiated power components in the JET MkI divertor using VUV spectroscopy',

J. Nucl. Mater. (Proc. 12th PSI Conf., St-Raphael, 1996), in press.

S.J. Davies, P.D. Morgan, Y. Ul'Haq, C.F. Maggi et al., 'Parallel electron temperature and density gradients measured in the JET MkI divertor using thermal helium beams', J. Nucl. Mater. (Proc. 12th PSI Conf., St-Raphael, 1996), in press.

R. Guirlet, R.Giannella, L.D. Horton, A. Maas, C.F. Maggi, M. O'Mullane, 'Analysis of VUV Ne radiation in the JET divertor during Ne injections', Proc. 23rd EPS Conf., Kiev, 1996.

The author of this thesis is also one of the authors in the following JET papers:

D. Stork et al., 'Characterization of long pulse steady-state H-modes in the JET pumped divertor configuration', Control. Fusion and Plasma Physics (Proc. 22nd EPS Conf., Bournemouth, 1995) Vol 19C, II-125.

D.J. Campbell et al., 'Studies of reactor-relevant H-mode regimes in the JET pumped divertor', Plasma Phys. Control. Fusion **38** (1996) 1497.

R.D. Monk et al., 'Divertor Langmuir probe measurements in JET', Contrib. Plasma Phys. **36** (1996) S37.

C. Lowry et al., 'Divertor configuration studies on JET', J. Nucl. Mater. (Proc. 12th PSI Conf., St-Raphael, 1996), in press.

Contents

Chapter 1

Introduction

The problems of power exhaust with minimal erosion of the plasma facing components, the control of plasma purity and the ability to pump helium ash, produced by fusion reactions, while providing density control and high plasma energy confinement are central aspects for the demonstration of an experimental fusion reactor.

The divertor configuration appears at present to be the most favourable one to fulfill these requirements and has been adopted for the design of the International Thermonuclear Experimental Reactor (ITER). In this configuration, a poloidal magnetic field null is created close to the bottom of the vessel of the tokamak and the unconfined scrape-off-layer (SOL) plasma flows to the divertor target plates. Impurities, produced by sputtering at the plasma boundary surfaces, are confined by this plasma flow in a region far from the main plasma volume. Steep temperature and density gradients are established along the SOL, resulting in relatively high densities and low temperatures at the target plates, compared to their upstream values. The achievement of low temperature divertor plasmas is beneficial in reducing impurity production due to sputtering. Operation at high divertor plasma density improves gas compression in the divertor chamber, and thus leads to improved pumping. At the same time, reasonably high plasma edge temperatures are maintained, which appears to be a necessary condition for enhanced plasma energy confinement (H-mode).

Current divertor physics research indicates that the most promising concept for power and particle control in next step experiments relies on atomic processes to transfer the power and momentum from the edge plasma to the divertor chamber. The transfer of parallel momentum from the plasma to the recycling neutrals,

through charge exchange collisions, and subsequently to the target and vessel walls, is obtained in the so-called detached divertor regime. In this regime the plasma pressure at the divertor target is reduced with respect to the upstream value and low target temperatures are achieved. This reduces physical sputtering (although this is not expected to reduce chemical sputtering from carbon targets) and drives volume recombination processes in the divertor. Hydrogen recombination reduces the ion fluxes to the divertor target, as well as the energy fluxes, since most of the particles hitting the target surfaces are in the form of hydrogenic neutral species, which are not accelerated by the electrostatic sheath in front of the target. While hydrogen recycling alone cannot exhaust most of the power in the divertor, radiation from impurities, sputtered from the plasma boundary surfaces, appears to be more efficient. In addition, gases such as nitrogen, neon and argon are injected *ad hoc* in the plasma to enhance divertor cooling by radiation (the radiative divertor regime).

The Joint European Torus (JET) is carrying out a coordinated divertor physics programme in full support of the ITER divertor development. This programme is based on three different pumped divertor configurations, the MarkI, the MarkIIA and the ITER-specific Gas Box designs. Operation with the MkI pumped divertor configuration was carried out during the 1994/95 experimental campaign and data collected during this experimental period are presented in this thesis.

Diagnostic studies, together with analytical and numerical code modelling, are essential to the understanding of divertor plasma performance. One of the key aspects of divertor physics research is the study of impurity dynamics in divertor plasmas. The thesis presents a spectroscopic investigation of the radiating properties and transport of impurty ions and neutral deuterium in the divertor region of JET. The study combines atomic physics modelling of impurity and hydrogenic emission with the modelling of divertor plasma for the interpretation of line-of-sight integrated spectroscopic signals.

The thesis is structured as follows. The first part presents an overview of divertor physics experiments, carried out in JET with the MkI pumped divertor, and of atomic processes necessary for the modelling of spectral line emission from hydrogenic and impurity species in divertor plasmas. The second part of the thesis is devoted to the instrumentation side of the work. The final part focuses on the measurement, modelling and interpretation of spectral line emission from the divertor region, the study of divertor impurity transport and the investigation of thermal

charge exchange between carbon impurity ions and neutral deuterium.

An overview of the divertor physics experiments carried out at JET with the MkI divertor geometry is presented in Chapter 2. The divertor concept is first introduced and the main reasons why present day tokamak fusion research concentrates on operation with diverted plasmas are addressed. The bulk of the Chapter is devoted to the discussion of the various areas of the experimental programme for divertor studies that were carried out during this period and to which I participated as team core member of the Divertor Physics Task Force. Emphasis is given to those areas in which the spectroscopic measurements and analysis of data presented in this thesis have been carried out, namely Ohmic and L-mode density limit discharges, detached and radiative divertor plasma regimes.

In Chapter 3 the atomic processes relevant to divertor plasma studies are reviewed. The discussion therefore emphasizes collision processes at low temperatures (1-100 eV) and moderate to high densities ($10^{18} - 10^{21} m^{-3}$). Initially, collisions involving neutral hydrogen and hydrogenic species are addressed. Subsequently, the discussion is extended to collisions involving impurities and to collisions between impurity ions and neutral hydrogen, namely charge exchange at thermal energies. A review of low energy charge transfer cross sections for collisions between carbon ions and neutral hydrogen is presented. This constitutes the basis of a study of the effect of charge exchange with neutral deuterium on divertor impurity emission, which is the subject of Chapter 8. The theory of the collisional radiative population model used in this thesis is then briefly reviewd. This allows calculation of the radiated power loss and photon emissivity coefficients that are necessary for prediction and interpretation of spectral emission and radiation distributions from divertor plasmas. Validation of the carbon data against absolutely calibrated spectroscopic measurements in the VUV wavelength range, as part of the work of this thesis, has stimulated a revision of the entire carbon data set, and the production of a new set of internally consistent rate coefficients. This includes also a complete set of stage to stage and state selective charge exchange recombination rate coefficients for carbon, that were calculated as part of the work of this thesis (see Chapter 8).

The second part of the thesis is devoted to the instrumentation side of the work. A new double SPRED spectrometer was installed and commissioned during the MkI divertor experimental campaign, for the observation of VUV emission from the divertor region. This multichannel spectrometer allows measurement of hydrogenic

and impurity spectra with moderate spectral and time resolution, but spanning a wide wavelength range, between 150 to 1450 Å. Therefore, it represented an essential tool for the study of the ionic composition and radiation losses of intrinsic as well as injected impurities from MkI divertor plasmas. The characteristics and performance of the divertor double SPRED spectrometer are described in Chapter 4. In Chapter 5 the method used to achieve an absolute intensity calibration for the double SPRED is discussed. This was obtained *in situ* using branching ratio techniques, and cross calibrating with other divertor diagnostics, namely visible spectroscopy (D_α and visible bremsstrahlung emission). Subsequently, the consistency of the SPRED sensitivity calibration with divertor bolometer measurements was verified successfully. The absolute intensity calibration of the SPRED spectrometer constitutes the fundamental basis for the analysis of the measured VUV emission presented in this thesis. Without it, all interpretative work in this thesis that involves modelling of transport and radiation characteristics of impurity and hydrogenic species in the divertor would not have been possible.

The third part of the thesis focuses on the measurement, modelling and interpretation of spectral line emission from the divertor region. Chapter 6 outlines the fundamental concepts of hydrogen plasma and impurity transport in the divertor and edge region. Starting from a full 2D approach, the solutions of the transport equations for the hydrogen plasma are then derived in the Onion Skin Model, which is the approach used in the thesis. It is shown how solving for the SOL plasma requires iteration with a model for the hydrogen neutrals, which contribute to the source and loss terms in the continuity equations. The model used to describe the impurity production and transport is discussed in the second part of the Chapter.

One of the key questions for the understanding of impurity dynamics in divertor plasmas (and especially in detached and radiative divertor regimes) is what species are the main contributors to the total radiation, measured by the bolometers. This aspect can only be studied spectroscopically and is part of the analysis of Chapter 7. VUV spectroscopic measurements of radiated power components from MkI divertor plasmas are presented. These measurements were performed both with carbon and beryllium divertor targets and the radiation characteristics of plasmas diverted on the two different target materials are discussed. Spectroscopic observations and measurement of impurity radiation during controlled Be target melting experiments are also reported. The effect of plasma-wall clearance on the relative importance of

deuterium and carbon impurity radiation is studied spectroscopically for Ohmic discharges in which the electron density was increased to the density limit. Extensive measurements were also performed during nitrogen impurity gas puffing for radiative divertor studies. Spectroscopic measurements of divertor emission, in the VUV and visible wavelength range, and bolometer mesurements are then compared with interpretative code modelling of plasma and impurity transport in low density and plasma detachment regimes. It is shown that simultaneous VUV and visible spectroscopic measurements of divertor plasma emission provide essential information in this area of study.

In Chapter 8 the effect of charge exchange with neutral deuterium on carbon impurity emission in the divertor region is studied. Charge exchange recombination with neutral deuterium modifies the equilibrium ionization balance of carbon, even at low neutral deuterium densities. For this reason, high density, low temperature divertor plasmas, rich in recycling neutral deuterium, are expected to be influential on carbon impurity radiation through charge transfer reactions. The main question related to this study is whether charge exchange can alter substantially the carbon impurity radiated power distributions in the divertor region. This aspect is of particular interest in detached and radiative divertor regimes, where the aim is to maximize radiative cooling of the plasma in the divertor volume, without increasing the impurity content of the core plasma. The effect of low energy charge exchange on carbon impurity emission is studied quantitatively in the model of JET MkI divertor discharges. To achieve this, the impurity transport code was modified to include charge transfer reactions between neutral deuterium donors and impurity ion receivers and a complete set of charge exchange rate coefficients for carbon were calculated.

Finally, Chapter 9 contains the conclusions.

Chapter 2

Overview of Divertor Experiments in JET during the MkI Campaign

2.1 Introduction

This Chapter presents an overview of the divertor physics experiments carried out in JET with the MkI geometry (1994/95), during which the data presented and analysed in this thesis have been collected. I will first discuss the main reasons why present day tokamak fusion research concentrates on operation with diverted plasmas; I will then give a brief description of the JET MkI pumped divertor and finally I will discuss the various areas of the experimental programme for divertor studies that were carried out during the MkI campaign.

The first two sections are devoted to a brief introductory description of the tokamak configuration and of the JET tokamak.

2.2 The Tokamak

The tokamak is a toroidal confinement system where the plasma is compressed and confined by magnetic fields. The principal magnetic field is the toroidal magnetic field B_ϕ, but this alone cannot confine the plasma. In fact the toroidal field is not uniform and its magnitude varies roughly as $1/R$, with R the distance from the axis of symmetry, Z (see Fig. 2.1). This means that the plasma particles are subject to a vertical drift motion (the sum of the ∇B drift and of the curvature drift), which drives the particles perpendicularly to the magnetic field. This motion

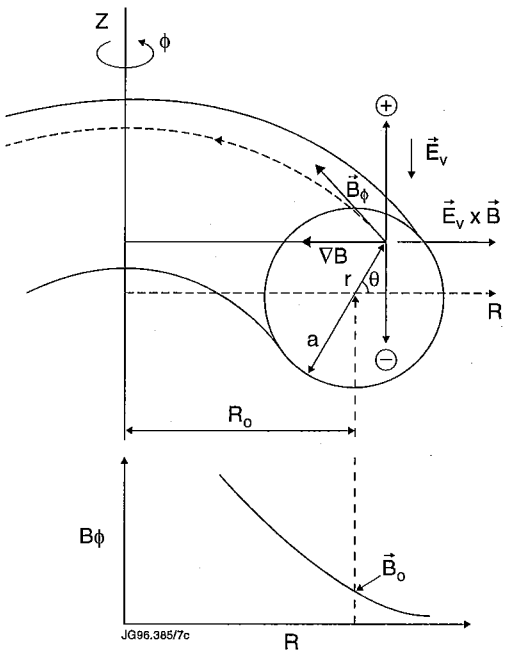

Figure 2.1: Particle drift motions in a purely toroidal magnetic field configuration. a and R_0 are the minor and major radius of the torus, $\vec{B}_\phi$ is the toroidal magnetic field, with value B_0 on the axis of the plasma column, $\vec{E}_V$ is the vertical electric field.

depends on the charge of the particles and is thus in opposite direction for electrons and ions, producing a vertical electric field $\vec{E}_V$ (see Fig. 2.1). This results in a $\vec{E} \times \vec{B}$ drift, which is the same for electrons and ions and causes a global horizontal displacement of the plasma in the outward direction, destroying the configuration [1]. This is avoided by adding a poloidal magnetic field, $\vec{B}_\theta$, to the toroidal field. In this way the magnetic field lines become helical and lie on closed and nested magnetic surfaces, thus providing a connection between top and bottom half of the toroidal plasma along the field lines, which short circuits the electric field $\vec{E}_V$. In the tokamak the toroidal field is produced by external coils and the poloidal field by inducing a toroidal current in the plasma by transformer action, where the plasma acts as the secondary winding of the transformer (see Fig. 2.2). Since the transformer operation requires a time-varying current in the primary winding, the tokamak can only operate in pulses and the flux swing of the transformer sets the limit of the pulse duration. Steady state operation is only possible with non-inductive current drive methods, e.g. lower hybrid current drive. The plasma shape and position are controlled by additional coils and together with the plasma current they are controlled by feedback systems. Tokamak plasmas are initially heated ohmically by

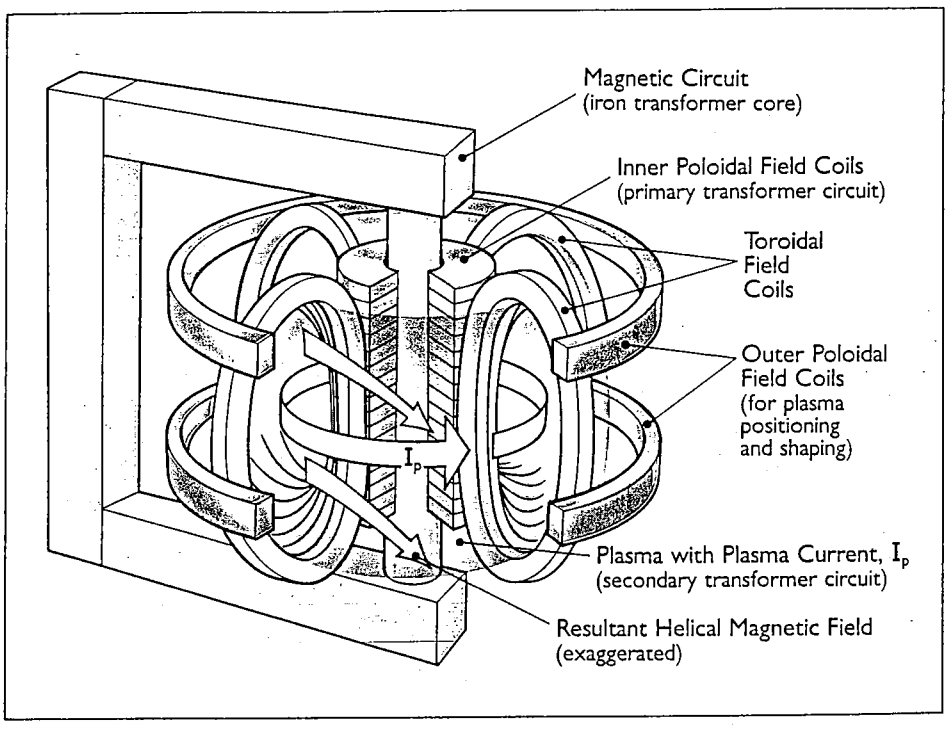

Figure 2.2: Schematic representation of the magnetic configuration of the tokamak.

the plasma current because the plasma is resistive. However, the plasma resistivity decreases with increasing temperature as $T_e^{-3/2}$ and additional heating mechanisms are needed to reach ignition, e.g. injecting energetic beams of neutral atoms (H, D) and/or launching RF waves that are resonantly absorbed by the plasma ions. An important parameter to evaluate the economic efficiency of a tokamak reactor is the efficiency with which the external magnetic field compresses the plasma. This is expressed by the ratio of the plasma kinetic pressure, $p = nT$, and the magnetic pressure, $B^2/2\mu_0$:

$$\beta = \frac{p}{B^2/2\mu_0}. \tag{2.1}$$

Since the fusion power for a D-T reaction at $\sim$ 10 keV is proportional to p^2, high values of β are desirable to maximize fusion power production. However, high values of β make the plasma MHD unstable and there appears to be a limiting value for β:

$$\beta_{max}(\%) = \frac{2.8\ I_P\ [MA]}{B_\phi\ [T]\ a[m]}. \tag{2.2}$$

The confinement of the plasma is not perfect and some interaction of the plasma with the vessel walls inevitably takes place. The particles that escape from the plasma carry an appreciable part of the energy exhausted from the plasma and

transfer it to the walls, which are therefore subject to heat and particle loads during the plasma discharge. Plasma-wall interactions must be kept to a minimum in order to avoid radiative cooling and contamination of the main plasma due to erosion of the material constituting the inner wall of the vessel. A measure of the overall impurity level in the plasma is given by the effective charge of the plasma, Z_{eff}, defined as:

$$Z_{eff} = \sum_{H,Z} Z^2 n_Z / \sum_{H,Z} Z n_Z = 1 + \sum_{Z} Z(Z-1)\frac{n_Z}{n_e} \tag{2.3}$$

where quasineutrality of the plasma ($\sum Z n_Z = n_e$) has been used to yield the second equality. One approach to minimize these plasma-wall interactions is to limit the plasma radius with a material limiter plate, which defines the last closed flux surface. The most promising approach instead makes use of a magnetic limiter, or separatrix, whereby the plasma outside the last closed flux surface is diverted to a remote chamber and strikes on target plates, the divertor configuration (see following sections). As the total heating power into the plasma, P_{in}, is increased the plasma energy confinement degrades, approximately as $1/\sqrt{P_{in}}$, leading to a low confinement mode of operation (L-mode). With divertor configuration a transition can occur above a certain threshold power to a regime (H-mode) in which the energy confinement time is enhanced by a factor of 2 or more with respect to L-mode. JET is a divertor tokamak and so is the design of ITER, the first prototype of a thermonuclear reactor. The following section describes briefly the main characteristics of the JET tokamak.

2.3 The JET Tokamak

With a plasma major radius $R_0 = 2.96$m and a total plasma volume of about $80m^3$ JET (Joint European Torus) is the largest tokamak in the world. JET is the largest project of the nuclear fusion research programme of the European Atomic Energy Community and was designed to obtain and study plasmas in conditions and with dimensions approaching those needed in a fusion reactor. Since the installation of a pumped divertor in 1994 (see later on in this Chapter) a significant fraction of JET's experiments are in full support of ITER.

The overall dimensions of the JET tokamak are about 15m in diameter and 12m in height. The toroidal vacuum vessel, with D-shaped cross section (plasma

minor radius (horizontal) $a = 1.25$m and (vertical) $b = 2.10$m), constitutes the heart of the machine. The toroidal component of the magnetic field is generated by 32 D-shaped coils equally spaced around the torus and enclosing the vacuum vessel. The primary winding of the transformer are the inner poloidal field coils, situated at the center of the machine, which are used to induce the toroidal plasma current I_P (the secondary winding) that generates the poloidal component of the magnetic field. A massive 8-limbed transformer core provides the coupling between the primary winding and the toroidal plasma current. A set of six outer poloidal field coils surround the machine toroidally (but inside the transformer core), providing positioning, shaping and stabilization of the plasma inside the vessel. The production of the plasma current by transformer action implies that JET operates in a pulsed mode. The maximum pulse rate is one every 15 min (constrained by the time required to cool down the vessel structures and the magnetic components in between pulses) and the maximum duration is of 20-30 s (limited by the maximum current that can flow in the primary winding of the transformer) with the plasma current sustainable at peak values for several seconds. The plasma current can also be driven non inductively using the Lower Hybrid Current Drive system. The wave accelerates the electrons in the plasma at the lower hybrid frequency and so drives a current, which can in principle extend the duration of the discharge to 60 s. The maximum toroidal field at the plasma center is $B_0 = 3.45$T and the maximum plasma current is $I_P = 6$MA with divertor configuration. Since 1994 JET operates primarily in the divertor configuration, provided by 4 in-vessel divertor coils, which allow a large variety of different divertor configurations to be established. This is complemented by a toroidally continuous divertor cryopump for the control of the plasma density and of particle recycling. Two additional heating systems are used in JET, neutral beam injection (NBI) and radio frequency (RF) heating, with a total maximum power available of order 40MW. JET is also equipped with over 60 different diagnostic systems for the monitoring and study of plasma parameters. These include diagnostics for the measurement of density and temperature, magnetic signals, boundary plasma parameters, neutron fluxes and an ample set of spectroscopic diagnostics ranging from the X-ray to the visible and IR part of the spectrum. A set of over twenty diagnostics are specifically devoted to divertor physics studies [2].

An overview of the divertor physics experiments carried out in JET with the MkI divertor (1994/95) is the subject of the remaining part of this Chapter.

2.4 The Divertor Concept

Magnetically confined fusion plasmas interact with the surfaces of the confining vessel. These interactions produce impurities, which contaminate the plasma. Also, the erosion of the first wall of the vessel associated with the incident ion fluxes may limit seriously the lifetime of a burning reactor. For several reasons impurity contamination of the main plasma works against the achievement of ignition in a reactor and is thus one of the crucial aspects of research in the field of thermonuclear fusion. Impurities that reach the core plasma (especially medium-high Z impurities) produce strong line and bremsstrahlung radiation. These radiative energy losses reduce the central temperature and, thus, the fusion power. High impurity densities in the core are also detrimental because they increase the total plasma pressure, thus diluting the fuel and pushing the plasma to exceed the MHD pressure limit (eq. 2.2). Also, fuel dilution reduces the heating power available from $D-T$ reactions. Thus, although impurity production cannot be prevented, it is imperative to try and confine these events to regions as far as possible from the main plasma, to screen the main plasma from those impurities that are inevitably produced and to minimize erosion of the vessel walls. In the poloidal divertor configuration (which is the most common one and the only discussed here), a magnetic separatrix defines the last closed flux surface (LFCS). One or more divertor coils produce a current I_d, parallel to the plasma current I_p, thus diverting the poloidal magnetic field and creating a magnetic null (the X-point), as shown in Fig. 2.3. In this way, the consequent open flux surfaces outside the LCFS can be diverted from the main plasma - usually to a separate chamber - where the plasma-surface interactions take place at the divertor target plates (see Fig. 2.4).

This configuration offers two fundamental advantages with respect to limiter plasmas: a) because the location of the main plasma-surface interaction is far away from the main plasma, the plasma purity is increased; b) the neutralization of the plasma at the target plates can result in a build-up of the neutral pressure, improving the pumping efficiency [3]. A third, unexpected advantage of the divertor configuration was the achievement of enhanced confinement with additional heating, the so called H-mode [4], which is characterized by steep density and temperature gradients just inside the separatrix. Experiments carried out with diverted plasmas showed from the beginning that in this configuration temperature and density gradi-

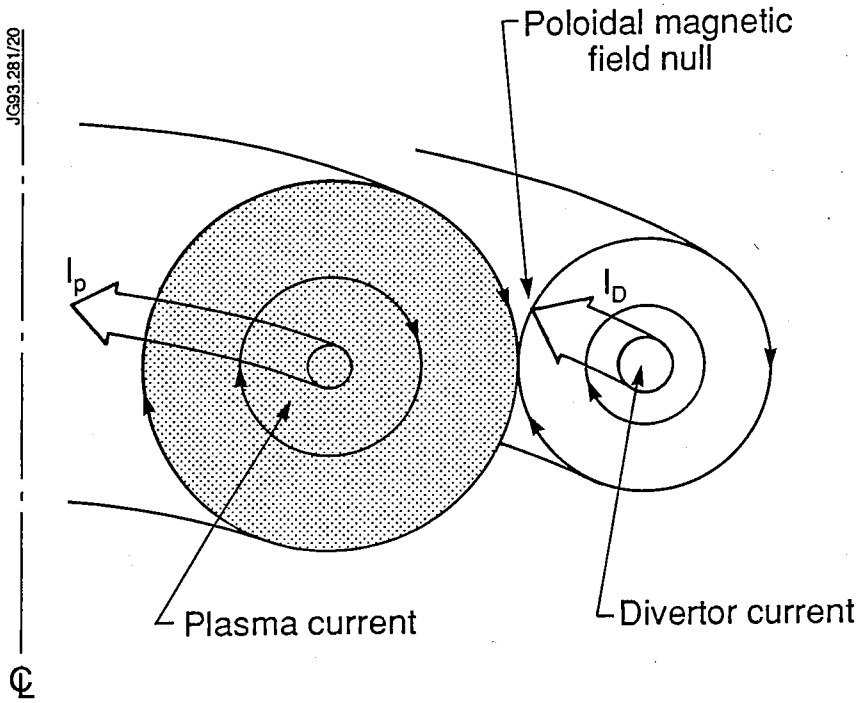

Figure 2.3: Scheme of the poloidal divertor configuration, showing how a divertor current I_d, parallel to the plasma current I_p, produces a null of the poloidal magnetic field (from ref. [3]).

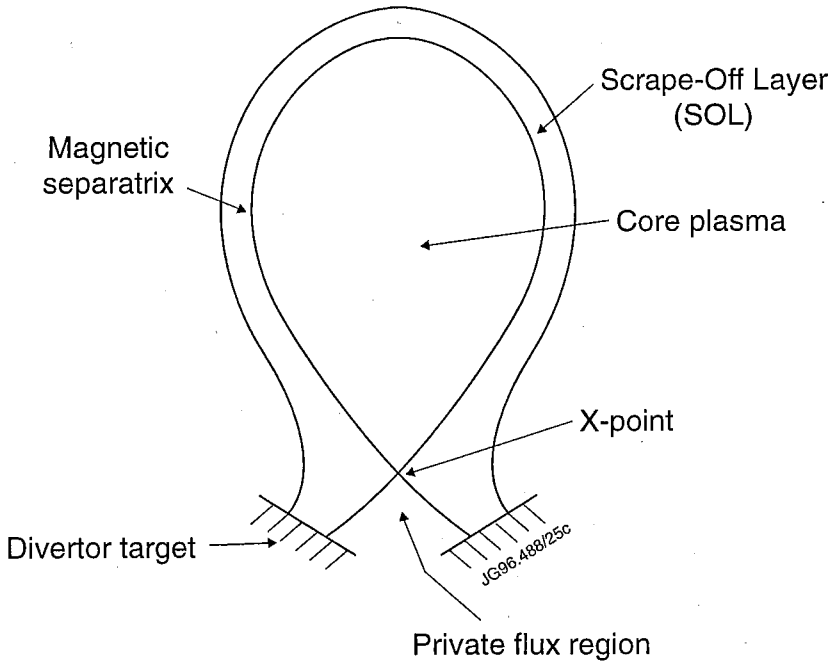

Figure 2.4: Scheme of the divertor configuration (poloidal cross section of the torus), introducing some terminology.

ents arise along the SOL, resulting in relatively high densities and low temperatures at the target plates, with respect to their upstream values [3],[5].

The establishment of low temperature and high density in the divertor are beneficial features: low temperature at the target reduces impurity sputtering (see Chapter 6), while maintaining the edge plasma temperature relatively high (which appears to be a necessary condition for maintaining the H-mode). High plasma density in the divertor should reduce the escape probability of neutrals into the main plasma, with the concomitant benefits of improved shielding: improved gas compression (good for pumping); reduction of impurity contamination of the main plasma; reduction of wall sputtering by charge exchange neutrals; reduction of edge cooling by recycling hydrogen and impurities.

At present the divertor configuration appears the most favourable one for the achievement of ignition in a reactor and has been adopted for the design of the ITER reactor [6]. JET has operated with diverted plasmas since 1989. More recently, with the installation of in-vessel divertor coils and a cryopump, the divertor configuration has become the standard one for JET. The remaining part of this Chapter is devoted to an overview of the extensive divertor physics experiments carried out in JET during 1994/95 with the MkI pumped divertor.

2.5 The JET MkI Divertor

2.5.1 Structure and Characteristics

The main characteristics of the MkI pumped divertor are shown in Fig. 2.5. Four internal divertor coils have allowed the establishment of a large variety of magnetic configurations at plasma currents up to 6 MA. In addition, the relatively open geometry has allowed sweeping of the strike points across the target at frequencies of 4Hz and amplitudes up to 10cm, thus increasing the effective target 'wetted' area for heat deposition. The divertor target structure consisted of narrow, water-cooled inconel beams on which carbon fibre composite (CFC) tiles and Be tiles, close to the end of the MkI experiments, were mounted in pairs. The tiles had been carefully designed, machined and aligned so as to avoid tile edge exposure to the incident magnetic field lines. This resulted in improved power handling of the target, compared to the old JET divertor (see later, Section 2.6). A toroidally continuous cryopump, located be-

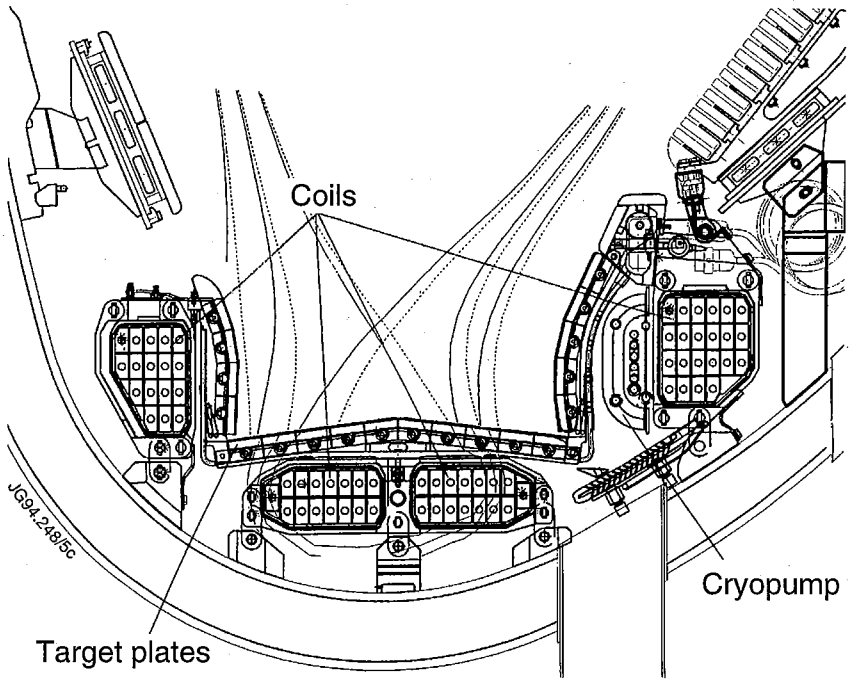

Figure 2.5: Poloidal cross section of the MkI divertor, showing its main components. This geometry is relatively open, requires sweeping of the strike points across the divertor targets and can accommodate a large variety of of magnetic configurations.

low the divertor target plates on the outer side of the divertor, see Fig. 2.5, provided active particle control during plasma discharges (see Section 2.8). A large set of diagnostics, specifically aimed at divertor plasma diagnosis, played an important role throughout the experimental campaign, providing a staggering amount of data that only in part have been, and are being, analyzed. These diagnostics included several bolometer arrays and VUV spectroscopy for the measurement of deuterium and impurity radiation; divertor and SOL Langmuir probes, providing target and main SOL plasma parameters; IR and CCD cameras for the observation of tile heating and impurity influx profiles; visible spectroscopy for influxes and impurity measurements; ionization gauges situated below the divertor tiles and at the entrance of the cryopump, providing measurements of the neutral fluxes in the divertor chamber. These diagnostics are not described here, but will be described in the course of the thesis, as their measurements are used or referred to. In particular, Chapters 4 and 5 are entirely devoted to the description of the characterization and absolute calibration of the divertor double SPRED spectrometer (an entirely new diagnostic for the MkI divertor), as part of the work for this thesis. The data collected with this VUV spectrometer constitute the bulk of the measurements, and related analysis,

presented in Chapters 7 and 8.

2.5.2 Aims of the MkI Divertor

With the pumped divertor JET has carried out an experimental campaign in which the central problems of the ITER divertor concept have been addressed: efficient dissipation of heat exhaust with minimal erosion of the divertor target; particle control, including helium; impurity screening. The experimental programme of divertor studies has included several areas, namely [7]:

- the study of power handling of the divertor target;

  the study of fuelling and pumping effects and their role in impurity retention and particle control;

- the characterization of ELMy H-mode discharges;

- the study of helium transport and exhaust;

- the study of the physics of divertor detachment;

- the study of radiative divertor plasmas;

- the study of the influence of divertor configuration on plasma performance;

- the comparison of CFC and Be divertor targets.

The experiments carried out in these areas of the programme are overviewed in the following sections, giving emphasis to those areas in which the measurements and analysis of data of this thesis work have been carried out (i.e radiative and detached divertor plasmas and comparison of plasmas on CFC and Be targets from a spectroscopic point of view).

2.5.3 Future Developments in the Area of Divertor Studies in JET

The divertor experiments with the MkI geometry were only the first part of a long term divertor programme that JET is carrying out in support of ITER. Two additional divertor geometries are part of this strategy, the MkIIA and the ITER-specific, MkIIGB (Gas Box), which are compared in Fig. 2.6. At the time of writing this,

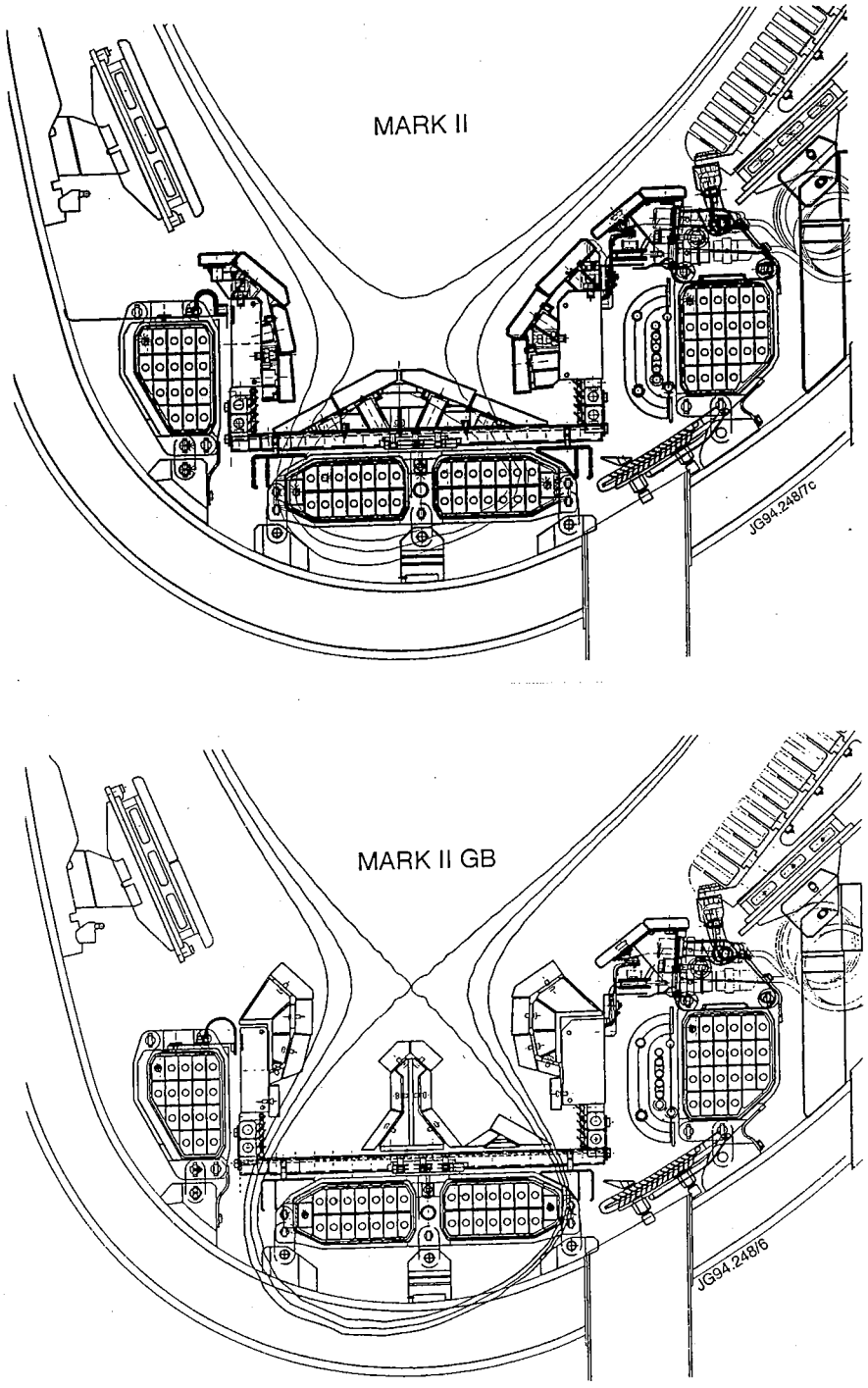

Figure 2.6: Comparison of the two additional JET pumped divertor geometries for ITER-relevant divertor studies: a) the MarkIIA, more closed, should lead to improved pumping. b) the ITER-specific Gas Box: domed, deep divertor with high X-point.

the installation of the MkIIA divertor structure has beeen completed and, after two months of plasma restart operation, JET is now in full operation with the MkIIA divertor [8]. The installation of the MkIIGB divertor is planned for mid-1997, after an extensive experimental phase of D-T operation commencing at the end of 1996.

2.6 Power Handling of the Divertor Target

One of the critical problems with divertor configurations is that of high peak heat loads on the target plates. In fact in a divertor tokamak the power conducted to the SOL is unfortunately concentrated onto a relatively small 'wetted' area. One of the possible methods to reduce the target power load is to spread the power over a larger surface. Therefore, considerable care must be taken in the divertor design, for instance by precisesly inclining the plates so that the angle between plates and field lines is very small, thus increasing the 'wetted' area.

One of the important aspects of the MkI experimental campaign was the study of divertor plasmas under steady-state conditions at high power. Particular care had been taken in the design and installation of the MkI divertor target, so as to optimize its power handling, in particular by avoiding exposure of tile edges to the plasma flow. In previous JET divertor configurations (91/92) this frequently limited the range of heating power due to the occurrence of carbon blooms [9]. In addition, the strike points were swept across the target plates at 4 Hz with an amplitude of up to 10cm in order to increase the effective 'wetted' area of the target. The performance of the target was investigated in a wide range of plasma conditions, at input powers of up to 32MW and in steady-state H-modes lasting up to 20 s. The result of this was that the MkI divertor showed an excellent power handling capability and the power handling did not limit the performance in JET (both with CFC and Be target tiles) [10]. Frequent ELMs (see Section 2.7) turned out to be very effective in alleviating the heat load on the strike zones, by spreading the power over a large surface area of the divertor target. The drawback of ELMs is that in this way the power deposition cannot be controlled and the power may end up in zones that have a poor power handling capability. This has a severe implication on the design of a reactor, where significant fractions of heat load may be deposited by giant ELMs on areas of the first wall that are not designed for this. Therefore, the investigation of means of dissipating the effects of giant ELMs or of avoiding them

is still an open problem.

2.7 Characterization of ELMy H-modes

H-mode plasma operation in JET with the MkI divertor was inevitably characterized by the presence of frequent, regular ELMs (Edge Localized Modes), the so-called ELMy H-mode. ELMs are associated with short, separated bursts of energy and particles released from the main plasma to the edge and divertor and are thought to be due to MHD instabilities driven by the steep gradients of edge temperature and density in H-mode plasmas [11]. Although the role of ELMs in spreading the power to the divertor target in a fashion that cannot yet be controlled represents an open problem, the ELMs are beneficial in reducing the density and the impurity accumulation in the core plasma, which is a characteristic of H-mode discharges. As a consequence of this, it is found that in general only the ELMy H-mode can achieve steady state conditions. For these reasons, the ELMy H-mode is presently the candidate regime for extrapolation to a reactor, such as ITER, whose design is based on the requirement for ignition in a regime with confinement enhancement factor above L-mode between 1.6 and 2.0 [6]. Such extrapolations are inferred using scaling laws that compare the energy confinement achieved in current tokamak experiments. For instance, the ITER89-P scaling [12] (developed for L-modes) is a commonly used one and is used here:

$$\tau_E^{89P} = 0.048\ m^{0.5} I_p^{0.85} R^{1.2} a^{0.3} \kappa^{0.5} \bar{n_e}^{0.1} B^{0.2} P^{-0.5} \tag{2.4}$$

where m [amu] is the mass of plasma ions, I_p [MA] is the plasma current, R [m] is the major radius, a [m] is the minor radius, κ is the elongation, $\bar{n_e}$ ($\times 10^{19} m^{-3}$) is the line averaged density, B [T] is the magnetic field on axis, P [MW] is the total heating power. Hence $H_{89P} = \tau_E / \tau_E^{89P}$ defines the enhancement of energy confinement over L-mode, according to this scaling, and is used as a figure of merit when studying H-mode discharges. In JET, due to the excellent power handling of the MkI target, together with the use of the cryopump and the sweeping of the strike points, long pulse steady state ELMy H-modes were established, lasting up to 20 s, with $H_{89P} \sim 2$. An example of one such discharge is shown in Fig. 2.7.

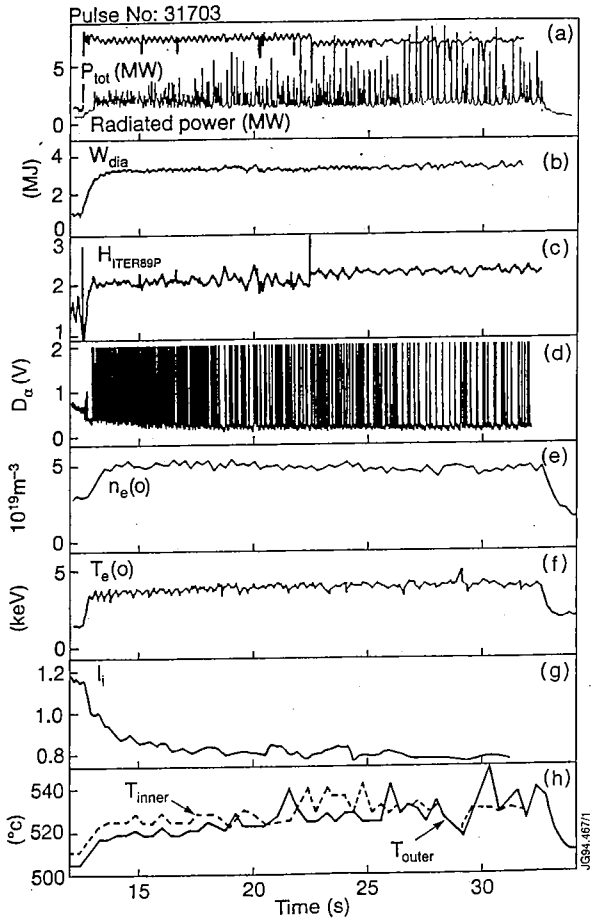

Figure 2.7: A 20 s steady state ELMy H-mode discharge in JET with the MkI divertor (from ref. [13]).

2.8 Fuelling and Pumping

Active particle control and helium exhaust is required for steady state operation in a reactor. This can be achieved with fuelling and active pumping of the plasma. In JET the plasma can be fuelled by neutral beam injection (NBI), pellets (but this method was not available with the MkI divertor) and by injecting cold gas. The cold (room temperature) gas was injected in the torus by means of a gas introduction system, consisting of 10 toroidally and poloidally distributed gas introduction modules that can be operated individually. This system was also used to inject gaseous impurities in the plasma for specific experiments (e.g. radiative divertor studies, see Section 2.11).

There are two main reasons for fuelling a discharge: a) to replenish the D-T fuel; b) to increase the density which is needed to achieve high fusion power and to obtain a high density, low temperature divertor plasma. Thus, in order to maintain steady state conditions, there has to be a method to remove particles from the plasma. With the MkI pumped divertor, active particle removal during plasma discharges was provided by the divertor cryopump. The cryopump was operated at 4.8K, allowing all gases, but He and H_2, to be pumped away by cryosorption. The pump was also equipped with an Ar spray, to spray and condense an Ar layer on the liquid helium cooled surfaces, to allow pumping of He and H_2 by cryotrapping (Ar frosting). Particle removal with the cryopump was achieved at all separatrix positions on both horizontal and vertical plates, with a maximum variation of the pumping speed of only a factor of 2, and with optimum pumping when the outer strike point was located in the outer corner of the target (the location closest to the pumping duct, see Fig. 2.5) [14]. The particle removal rate is directly proportional to the neutral pressure in front of the pump duct, which exhibited broad profiles, consistent with strong neutral recirculation in the sub-divertor region (see Section 2.12). This is thought to explain the weak dependence of pumping rate on strike point position with the MkI divertor. Density control in steady state was achieved in ELMy H-modes both for NBI only and gas fuelled discharges. The combination of fuelling and active pumping allowed the steady state density to be varied by a factor of about 1.5, as shown in Fig. 2.8.

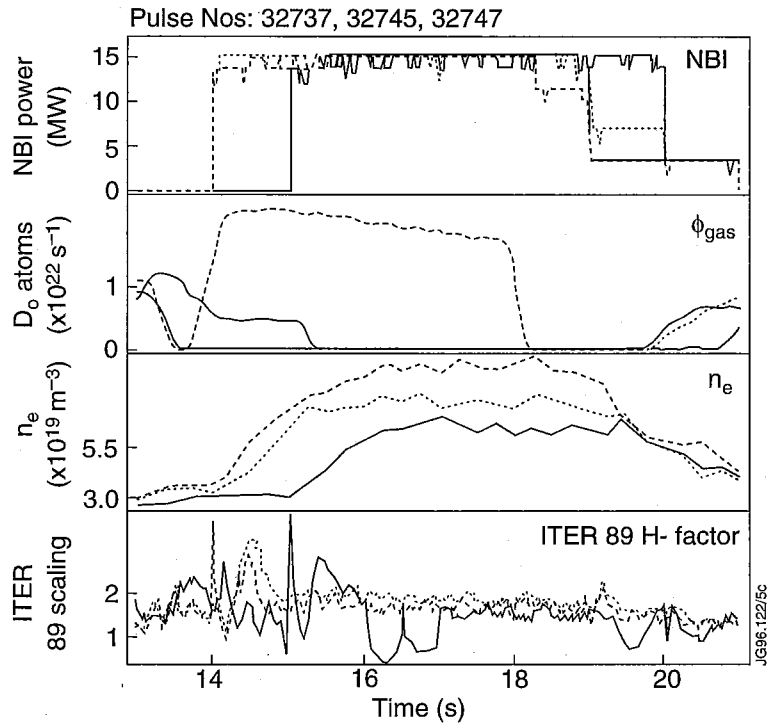

Figure 2.8: Illustration of the use of pumping and fuelling to vary the density in steady state ELMy H-modes, while high confinement is maintained (from ref. [14]).

2.9 He Transport and Exhaust

Helium is a special impurity in a fusion reactor: it is not produced primarily by plasma-wall interaction, but in the plasma core as a product of D-T fusion reactions. It is crucial for the performance of a burning reactor to be able to control the concentration of this impurity and to be able to remove He ash from the plasma core so as to prevent fuel dilution. In present day tokamaks these aspects cannot be studied in the realistic conditions of a burning plasma, but they are simulated by He puffing experiments. In these experiments, therefore, the He source, instead of originating at the plasma centre, is in the SOL, where the He is puffed. From the puffing location He particles are allowed to diffuse to the plasma centre and then the pumping is optimized and the exhaust capability of the system is studied.

When investigating the He exhaust capabilities the figure of merit is τ^*_{He}/τ_E, with τ^*_{He} the global residence time of the He ash in the plasma chamber and τ_E the plasma energy confinement time. Analytical studies have shown that for an ignited and stationary burning D-T plasma the He ash needs to be removed from the plasma within 7-15 energy confinement times, the exact value depending on the

impurity content of the plasma [15]. This puts a severe constraint on the He exhaust efficiency and prompts for regimes where the global He confinement time does not depart too much from the energy confinement time.

The He exhaust efficiency can be defined as $\epsilon_{He} = Q_{Exh}/(\Gamma_{He}\ A_{pl})$, with Q_{Exh} the exhaust rate for helium and $\Gamma_{He}\ A_{pl}$ the helium efflux from the core [16]. It expresses the probability of a helium particle being pumped away from the plasma. The exhaust efficiency depends on several parameters, such as the exhaust efficiency of the pumping facility, the recycling coefficient at the plasma-wall surfaces and the efficiency with which He is refuelled in the plasma. Thus, the exhaust efficiency depends strongly on the mechanisms which govern the flow of helium within the SOL and divertor regions. The pumped divertor configuration has the potential for a high He exhaust efficiency, since it is predicted that, as in the case of the other impurities, strong deuterium fluxes to the divertor plates will induce a frictional drag on the helium producing helium enrichment in the divertor chamber (higher helium concentrations in the divertor than in the core plasma). This facilitates He pumping [5]. In addition, interest has recently moved towards He exhaust studies in H-mode, this regime being currently the favourite candidate for ITER operation [6]. While experiments on TEXTOR (a pumped limiter tokamak) have not produced favourable results in H-mode, encouraging results have been obtained in DIII-D in diverted, ELMy H-mode plasmas with active pumping [16]. JET also carried out a series of helium exhaust experiments during the MkI phase in L-mode and ELMy H-mode plasmas, although with poorer results. It appears that this was mainly caused by the helium pumping capability being limited by technical problems.

In order to be able to pump helium in JET, an argon frost layer has to be condensed on the cryopump surface between plasma discharges to allow helium pumping by cryotrapping (Ar frosting). This technique did not work well in JET because the argon quickly contaminated the plasma leading to a disruption. Because of this, several pulses were required to clean the vessel walls, by which time a high enough D_2 load had accumulated on the pump (since D_2 is also pumped by the the argon frost) to substantially decrease the helium pumping speed [14]. Therefore, unfortunately, the data from these experiments were somewhat inconclusive. A ratio $\tau^*_{He}/\tau_E > 10$ was found for L-mode discharges and in excess of 20 for ELMy H-modes, but it is not clear what fraction of this result was due to a transport limit or to the pump degradation. Further experiments are therefore required to

clarify this finding. However, no evidence was found of helium accumulation in the plasma core and hence helium core transport does not appear to be a limiting factor in these experiments [17]. In JET the time evolution and radial profile of the plasma core helium concentration is measured using charge exchange recombination spectroscopy. From measurements of the intensity of the He II $n = 4 - 3$ transition (at 4685.7 Å), induced by charge exchange with energetic deuterium neutrals injected with NBI ($He^{+2} + D \longrightarrow He^{+}(n = 4) + D^{+}$; $He^{+}(n = 4) \longrightarrow He^{+}(n = 3) + h\nu$), the core helium density is deduced [17].

2.10 Physics of Divertor Detachment

The exhaust of particles, momentum and energy from a burning plasma is such that the divertor target plates will not survive unless a significant fraction of the power is exhausted by volume losses. In ITER it is predicted [6] that, with 300MW of α particle heating power and 100MW of additional heating, less about 100 MW of bremsstrahlung radiation, up to 20 MW/m^2 will fall onto the divertor target. Since an upper limit of 5 MW/m^2 is generally accepted as compatible with active cooling of the divertor components, a significant heat flux reduction will have to be obtained in the divertor through enhanced radiation. However, the additional requirement for $Z_{eff} \leq 1.2$ (excluding the contribution from He ash) reduces significantly the allowable density of an impurity radiator. The only condition in which appreciable power levels can be radiated and impurity sputtering reduced is that of divertor plasma detachment (detached radiative divertor), that is, with simultaneous loss of momentum along the SOL field lines [18]. Extensive experiments were carried out in JET to investigate plasma detachment in a variety of regimes (Ohmic, L-mode and H-mode). Detachment has been achieved in JET in Ohmic and L-mode discharges with D_2 fuelling only, but the relevant regime for ITER is that of enhanced confinement (H-mode). To achieve detachment in H-mode discharges extensive experiments were carried out with impurity seeding in the divertor (see Section 2.11).

The MkI divertor operated at higher densities and lower temperatures for a given upstream SOL density than the previous divertor geometry of 91/92. At these high divertor densities, the ion saturation current to the divertor target, J_{sat}, measured by Langmuir probes imbedded in the target plates, was seen first to increase and then to decrease as the core plasma density was increased [19]. This is the operational

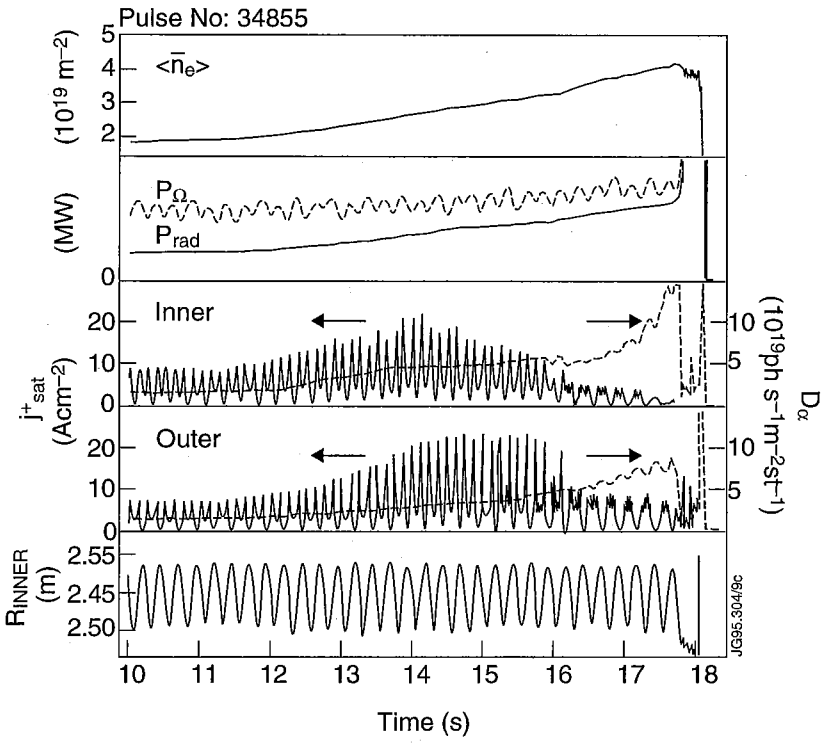

Figure 2.9: Evolution of some global plasma parameters for an Ohmic discharge illustrating the transition to divertor plasma detachment. a) Line integrated plasma density; b) total input and radiated power; c) inner and d) outer D_α emission and ion saturation current to the target; e) strike point sweeping (from ref. [20]).

definition of a detached plasma in JET (and in other divertor tokamaks). This decrease of J_{sat} with increasing plasma density was also used to operate stable detached plasmas using feedback control on J_{sat} and to control gas fuelling of the discharge. In Ohmic and L-mode plasmas a clear sequence of events was observed as the core plasma density was increased by means of D_2 puffing towards the density limit [20] (see Fig. 2.9):

- the ion saturation current, the D_α emission and the neutral pressure (measured by the pressure gauges) increased more than linearly with core plasma density (the 'high recycling regime', [5]).
- at $n_e \sim 3 \times 10^{19} m^{-3}$, J_{sat} reached a peak and then began to fall gradually with increasing core plasma density.
- D_α emission and neutral pressure continued to increase while J_{sat} decreased to very low values, which is the signature of detachment; there was an increase

in radiation from the X-point region and only a small portion of the divertor radiation came from the region below the X-point.

- if the plasma density was further increased, a MARFE formed in the inner wall, entered the main plasma and usually a density limit disruption occurred.

During the high recycling phase of the discharge, the electron temperature at the strike points fell from about 20 eV to about 10 eV and visible line emission from C II (or Be II) decreased, indicating a reduction in impurity sputtering. As the plasma detached, initially in the inner divertor and, if the density was further increased, also in the outer divertor, the J_{sat} near the separatrix dropped by an order of magnitude and T_e fell to about 2-5 eV at the divertor targets. It has to be noted, however, that at these low temperatures the standard interpretation of Langmuir probe I-V characterisics becomes questionable [21], with the result that the value of the electron temperature at the target is overestimated (especially in the inner divertor; see also Chapter 6 and 7). During the detached phase of the discharge the drop in ion saturation current is associated with a decrease of the static electron pressure, $p_e = n_e \times T_e$, in the divertor (measured by the fixed Langmuir probes). At the same time the pressure remains constant in the SOL (where it is measured by a reciprocating Langmuir probe at the top of the tokamak) where a broadening of the density profile is observed [20].

It was also observed that the use of the cryopump lowered the divertor neutral pressure [14] and required a higher plasma density to achieve the same degree of detachment as an unpumped discharge.

In high density H-mode discharges, when D_2 puffing was increased into ELMy H-modes, it was observed that the ELM frequency increased and τ_E strongly degraded, with finally a transition back to L-mode. This determined the H-mode density limit. Therefore, with intrinsic impurities (i.e. carbon) and D_2 fuelling, detached plasmas could not be obtained in H-mode. Plasma detachment was only achieved with impurity seeding, as described in Section 2.11.

2.11 Radiative Divertor Plasmas

As I have already discussed, one of the key issues for next generation tokamaks, such as ITER, is the exhaust of most of the power conducted to the SOL before it reaches

the divertor target plates. During the MkI phase various experiments were carried out in JET aimed at reducing the heat loads to the target plates using different methods. Sweeping of the strike points across the target resulted in a very effective method for increasing the total target 'wetted' area [10] (Section 2.6). However, sweeping requires a relatively open divertor structure, which is not beneficial in terms of neutral leakage from the divertor volume. The MkII design, being more closed, will not allow such extensive sweeping as the MkI. Another method that was investigated was increasing the flux expansion in the divertor (i.e. widening of the SOL footprint at the target). However, divertor plasmas operated with high flux expansion led to increased interaction of the plasma with the walls (due to the reduced wall clearance), and thus to increased wall sputtering, which strongly affected the density limit (see Chapter 7). Numerous experiments were thus carried out aimed at reducing the target heat load by increasing the radiation in the divertor volume. This was achieved using D_2 puffing as well as impurity seeding (N_2, Ne and, for a small number of discharges, Ar were used). Whereas with intrinsic impurities (and D_2 puffing) radiative detachment could only be achieved in Ohmic and L-mode discharges, the injection of extrinsic impurities was essential for obtaining high radiated power fractions and detachment at high input power levels and improved confinement. In these experiments the additional heating ranged from 8-16 MW of NBI and up to 32 MW of combined NBI and RF heating.

In a typical ELMy H-mode in JET, without gas fuelling, the intrinsic total radiated power fraction is low ($\sim$ 20%). Note that smaller machines, such as ASDEX-U and DIII-D, have intrinsic total radiated power fractions of $\sim$ 50% already and that the radiation is carbon dominated (carbon being the plasma-facing material). With the MkI divertor JET was characterized by a lower level of intrinsic impurity radiation, due to high plasma purity ($Z_{eff} \sim 1$) and so, in proportion, more extrinsic impurity radiation was required to obtain the high radiated power fractions needed for detachment. In this respect JET is a more ITER-relevant tokamak.

Radiation losses did rise in JET H-mode plasmas with very strong D_2 gas fuelling and up to 50% of the total input power could be radiated. However, it was found that strong D_2 puffing caused the confinement to degrade [22], [8] and a transition back to L-mode occurred (see Fig. 2.10).

Following the success of ASDEX-U in achieving detached radiative divertor plasmas with Ne seeding [23], a series of experiments with impurity seeding in high power

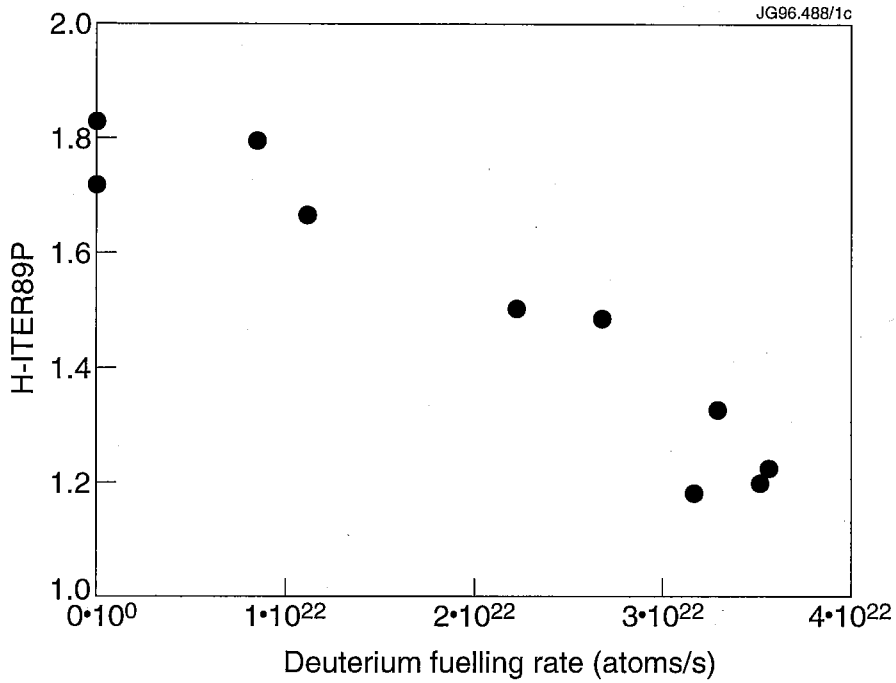

Figure 2.10: Degradation of the energy confinement with increasing D_2 fuelling rate in a series of ELMy H-mode discharges, from ref. [8].

divertor discharges were carried out in JET, achieving radiation losses of up to 80% and simultaneously reducing the power conducted to the target, P_t:

$$P_t = P_{heat} - P_{rad} - P_{CX} - \dot{W} \tag{2.5}$$

where P_{heat} is the total input power, P_{rad} is the total radiated power, P_{CX} is the power loss to the walls due to neutral charge exchange and W is the plasma stored energy. Numerical studies for JET and ITER have shown that P_{CX} does not exceed 20-30% of the total input power [24], while bolometer measurements during high power H-mode radiative discharges show that P_{CX} ~1MW at detachment in the divertor [25]. It is crucial to investigate how the radiated power, P_{rad}, is distributed between bulk and divertor radiation, with:

$$P_{rad} = P_{rad}^{bulk} + P_{rad}^{div}. \tag{2.6}$$

Impurity seeding does indeed increase P_{rad} and decrease the power to the target (as expected), but has a detrimental effect on the plasma purity and dilution, since not all of the seeded impurities are confined in the divertor and some fraction of the power is radiated in the bulk. For all injected impurity species, both divertor and bulk radiation were observed to increase with increasing total radiated power

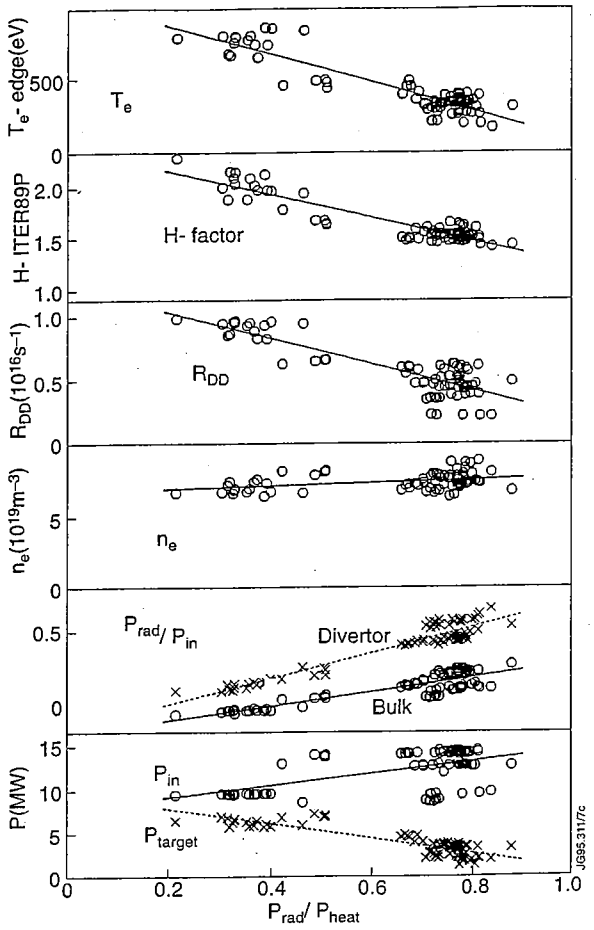

Figure 2.11: Degradation of plasma performance with increasing radiated power fraction in N_2 seeded and D_2 fuelled ELMy H-mode radiative divertor discharges (from ref. [7]). P_{heat} denotes the total input power.

fraction, although at different rates for different impurities [22]. Ne was the least favourable impurity in JET. The highest Z_{eff} was measured with Ne while only about 65% of the total input power could be radiated. This is to be compared against 80% radiated with N_2 or Ar. With Ar, $Z_{eff} < 2$ was achieved, but P_{rad}^{bulk} was high, whereas with N_2 P_{rad}^{bulk} grew moderately, although Z_{eff} was higher ($Z_{eff} \leq 3$). Fig. 2.11 shows the effect of increasing radiated power fraction P_{rad}/P_{heat} on plasma performance in the case of N_2 seeded radiative divertor discharges. In particular, the edge electron temperature, the energy confinement (with respect to the ITER89-P scaling), and the neutron yield drop with increasing radiated power fraction.

The radiation shells from carbon and nitrogen have a sharp maximum near the separatrix, while the neon radiation shell extends inside the LCFS. The fact that Ne radiates more efficiently at electron temperatures inside the separatrix is consistent

with the equilibrium power loss functions (see Fig. 3.17). The radiating behaviour of nitrogen appeared more favourable for low temperature divertor regimes and so N_2 seeded radiative discharges were extensively studied in JET. This is in contrast with the success of Ne as an extrinsic radiator in TEXTOR [26] and ASDEX-U [23]. Another operational point against neon seeding in JET was that controlling the radiated power fraction with Ne was very difficult. Even with active cryopumping, the Ne content in the plasma took several seconds to decay [27]. Also, Ne retention was not improved by changing the D_2 fuelling location from divertor to main chamber [28]. On the other hand, with Ne a smaller particle input was needed to achieve the same input power fraction, due to the different recycling behaviour of neon and nitrogen. While neon is completely recycling, nitrogen appears to be strongly pumped by the vessel walls, since the radiation level decays by about 50% within the first second after the nitrogen source is turned off [27]. In addition, substantial levels of nitrogen radiation were observed by VUV spectroscopy for several discharges after the last pulse in a given series of nitrogen radiative divertor discharges. Fig. 2.12 shows an example of nitrogen radiative divertor detachment (pulse 33204, on the horizontal CFC target), with 15 MW of NBI heating and combined $D_2 + N_2$ injection. Fig. 2.13 shows the radiated power components, measured by the divertor double SPRED (see Chapters 4, 7) for the same pulse, indicating that nitrogen accounts for about 80% of the total radiated power at detachment. In all these discharges, as the impurity gas is injected, the radiation rises initially especially in the divertor, with the radiation maximum well below the X-point. With the build-up of nitrogen and the rise of Z_{eff} the radiation maximum moves towards the X-point and when the total radiated power fraction has reached about 70% the radiation has detached from the target and is concentrated around the X-point [29]. This transition from predominantly divertor radiation to X-point can be maintained stable for several seconds and can be ended without disruption. When the plasma is fully detached the radiating region has its centre above the X-point, as shown in Fig. 2.14 by the tomographic reconstruction of the bolometer measurements for pulse 33204. The radiated power fractions of $\sim 80\%$ obtained with radiative divertor plasmas in JET are thought to be sufficient to prevent target damage, overheating and erosion in ITER. The achieved H-factor ~ 1.5 in these discharges would be sufficient for ignition in ITER, but the Z_{eff} is too high!

One of the key questions for the understanding of detached plasmas is what

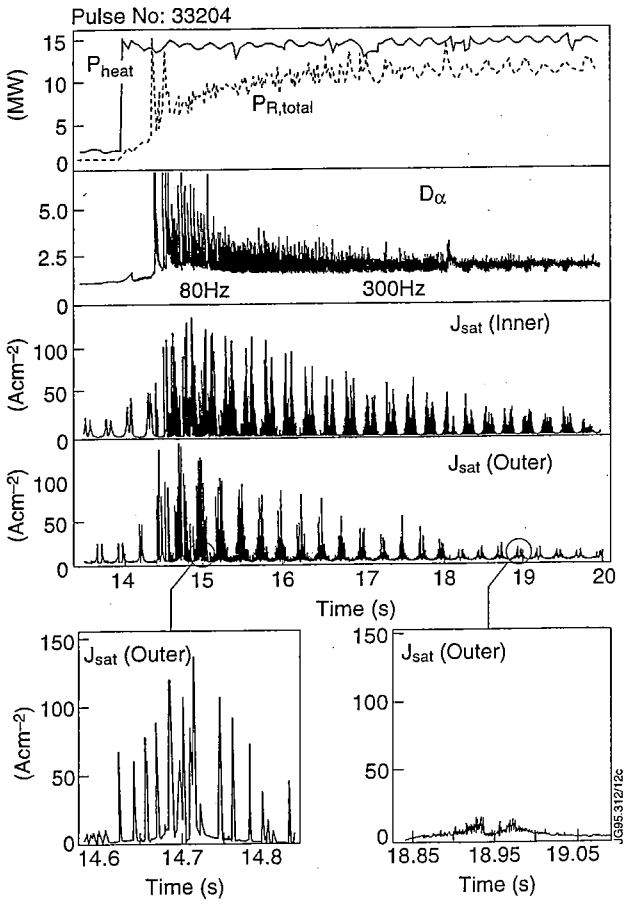

Figure 2.12: Main plasma parameters for a nitrogen radiative divertor discharge (pulse 33204), from ref. [27].

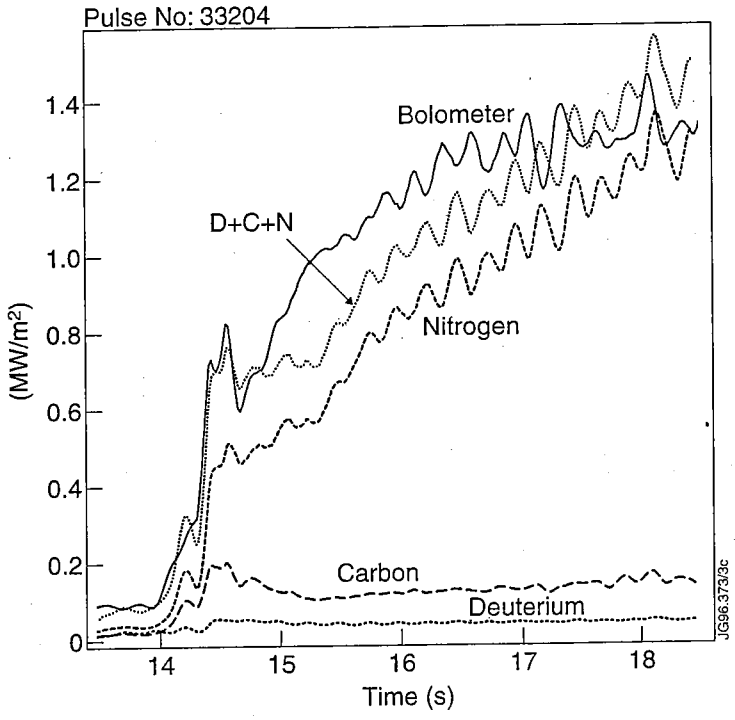

Figure 2.13: Radiated power components for pulse 33204 measured with the divertor double SPRED spectrometer (see Chapters 4,7).

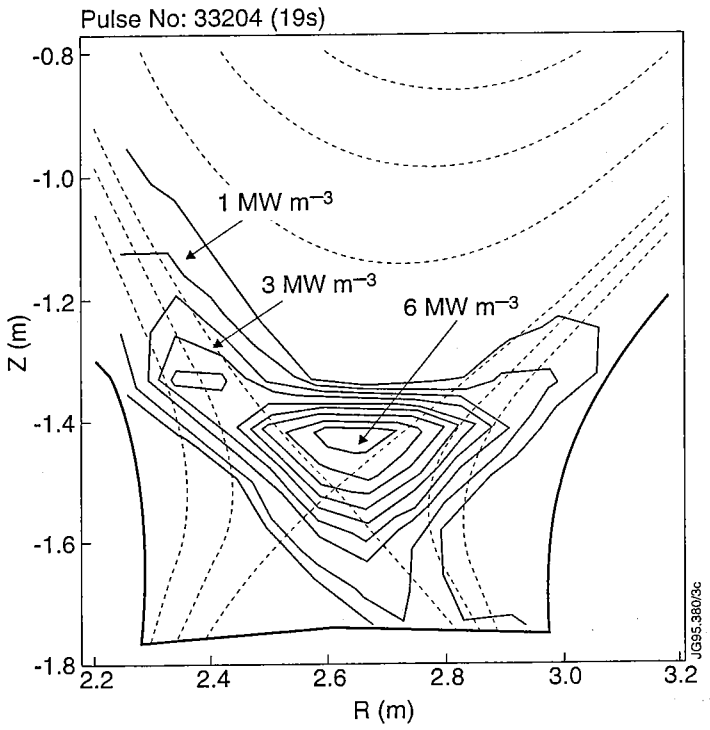

Figure 2.14: Bolometer tomographic reconstruction showing the distribution of radiated power for the detached phase (19 s) of pulse 33204, from ref. [27].

species are the main contributors to the measured radiation and in which regions the radiation is predominantly taking place. The latter aspect has been studied with bolometer measurements, as reported above. The former point, that is concerning the contributors to the total radiation, can only be addressed spectroscopically and is part of the analysis of this thesis (see Chapter 7).

2.12 Influence of Divertor Configuration on Plasma Performance

The geometry of the MkI divertor has allowed the study of plasmas diverted onto either the horizontal or vertical target plates (see Fig. 2.15). In addition, by varying the current in the divertor coils, it was possible to obtain a range of different magnetic configurations. 2D fluid code modelling had predicted that plasma operation on the vertical target plates would reduce the escape probability of the neutrals from the divertor, thus leading to more peaked density profiles at the target and in the SOL, further reducing T_e and providing access to plasma detachment at lower main plasma densities [30]. Contrary to expectations, the characteristics of plasmas diverted on horizontal and vertical targets appeared to be very similar [31].

These findings are of great importance in light of the preference for the ITER divertor design of the vertical plate cofiguration, based on the favourable predictions by the models for this design. The current explanation of the discrepancies between code results and experiment is that the MkI divertor geometry, with slots between pairs of tiles, was effectively very transparent to neutrals, facilitating recirculation of the neutrals in the private flux region (this point, and its implications on divertor plasma modelling, will be discussed further in Chapter 7). When these effects are included in the model, the simulations tend to agree better with the experiment [32]. However, this area, being of great consequence for ITER, needs further investigation and will be one of the aims of plasma operation with the MkII divertor.

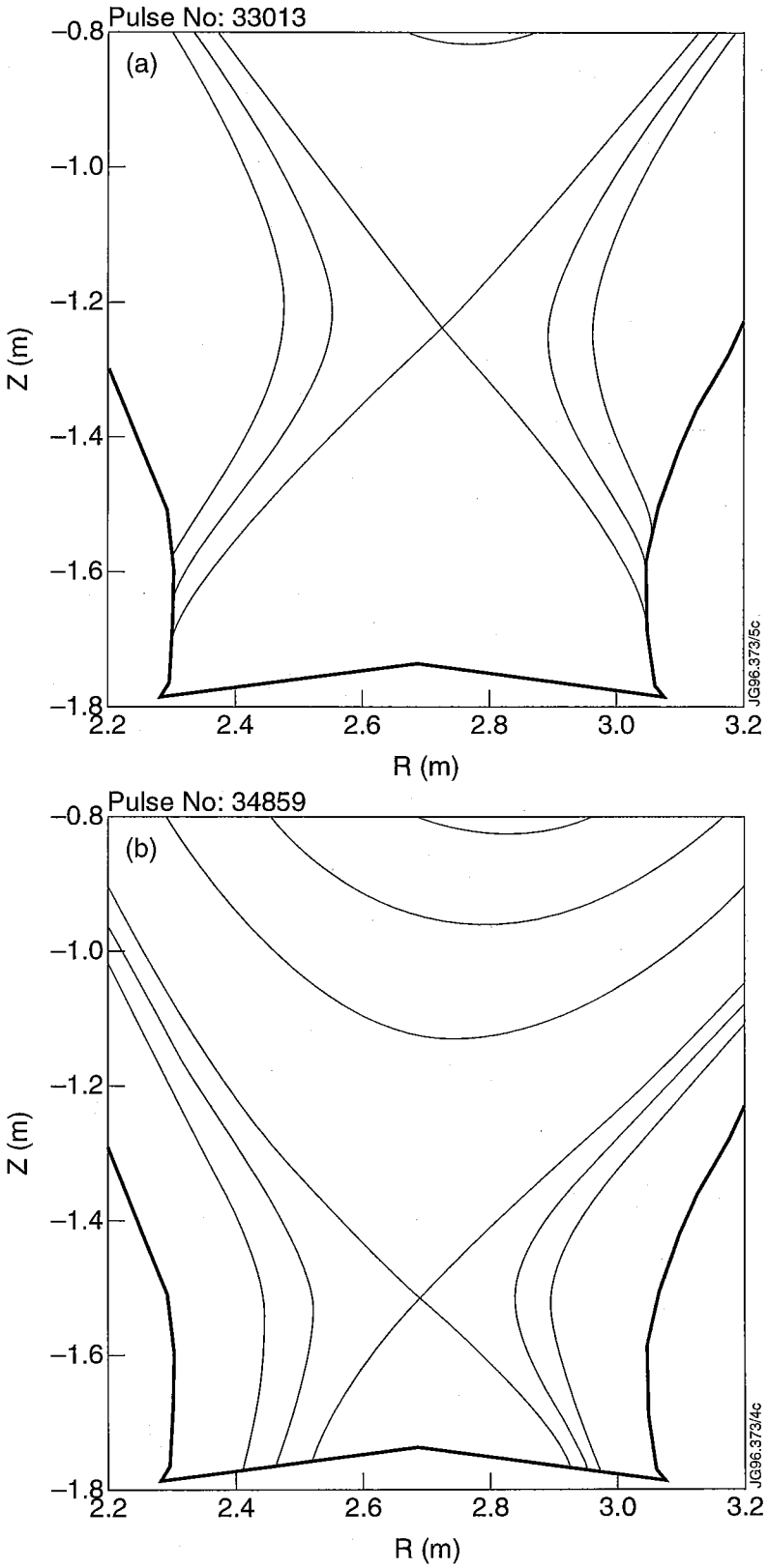

Figure 2.15: Magnetic equilibria for two representative discharges, one on the vertical (a) and one on the horizontal (b) target plates (divertor expanded view).

2.13 Comparison of CFC and Be Divertor Targets and Be Melt Experiment

In the last two months of the MkI experimental campaign JET operated with beryllium tiles of similar geometry to the CFC tiles and a full experimental programme was carried out to compare CFC and Be as target plasma facing materials. The campaign was then concluded with experiments devoted to controlled melting of the Be tiles, with the aim of studying the behaviour of plasmas on molten and damaged beryllium. Note that JET is the only tokamak in the world to be able to carry out such experiments since no other fusion project has developed and committed part of its technical expertise to safe operation with Be components. In addition, coating of the vessel plasma facing surfaces with Be evaporation is routinely employed in JET as a successful vessel conditioning technique. In fact, as a result of this, oxygen levels are extremely low in JET, due to the strong gettering action of beryllium on oxygen.

Due to the careful tile design of the MkI divertor, no melting on tile edges was observed during the Be phase of operation. However, several surface melting events occurred, i.e. during initial, unswept, power handling investigations and as a result of giant ELMs during high performance operation. However, the damage to the tiles was of little depth and a full experimental programme could be carried out with sweeping of the strike points across the target. The general characteristics of plasmas diverted on CFC and Be targets were very similar, with no difference observed in the radiation levels, detachment characteristics, value of the density limit or H-mode plasma behaviour [33]. An important aspect of this experiment was that even during Be target operation the plasma intrinsic impurity content was carbon dominated (note that, excluding the divertor surfaces, the plasma limiting surfaces in JET are carbon and inconel). It is thought that that carbon sputtered from the main chamber walls, flowed along the SOL and redeposited on the divertor surfaces, had a dominant role in the impurity dynamics. It will be shown in Chapter 7 of this thesis that Be radiation was definitely marginal during these experiments and that the principal impurity radiator was carbon, regardless of the divertor target material.

In the final phase of the MkI experimental campaign a series of discharges were carried out with the aim of producing controlled melting of the Be tiles [34]. The

objectives of these experiments were threefold: to study plasma operation on molten Be, to study operation on a melt-damaged Be surface and to test the concept of Be vapour shield formation put forward by ITER [6]. According to this concept, at abnormal heat loads to the divertor target, as the temperature for Be melting is reached ($1270°C$), a Be vapour layer is formed, which radiates half of the power to the tiles, thus self-protecting the divertor target. Initial melting was achieved in JET at the end of a series of partially unswept discharges with D_2 gas puffing. Subsequently, substantial melting occurred in unswept discharges without D_2 gas puffing, where up to 75MJ were deposited on the targets and the radiated power fraction rose to 70% for several seconds (see also Chapter 7). No evidence of Be target self-protection was observed in these experiments, thus not verifying the ITER vapour shield concept.

Plasma operation was recovered after the target melting, showing that the damage to the tiles had only minor implications for continued operation in medium/high density plasma regimes and that Be is not yet excluded from being a candidate as divertor target material for ITER.

Chapter 3

Atomic Processes in Divertor Plasmas

3.1 Introduction

Atomic processes play a fundamental role in divertor plasmas. The plasma particle balance in the divertor region is determined by the recycling of plasma ions at the divertor plates. When striking the divertor target, such ions recombine into neutral hydrogen atoms and molecules, which then reenter the plasma where they ionize, dissociate or charge exchange. The ionization and recombination collisions determine the contributions to the source/loss terms in the particle balance equation. Especially in high recycling and detachment regimes, the plasma momentum balance is strongly influenced by friction with the neutrals through charge exchange and elastic collisions (see Chapters 2, 7). The energy balance in the divertor volume can be altered substantially through impurity and hydrogen radiation and ionization, charge exchange and, at very high densities, radiation transport [35].

Present day divertor research indicates that the most promising concepts for power and particle control in next step experiments, such as ITER, rely on atomic processes to transfer the power and momentum from the edge plasma to the divertor chamber [36]. Thus considerable emphasis is placed on hydrogen and impurity (especially low Z) atomic physics at low temperatures (0.5-100 eV) and moderate to high densities (10^{19}-$10^{21} m^{-3}$). In fact, the challenge is to develop a divertor design where atomic physics processes are strong enough to reduce the energy flux on the divertor plates by a factor of 5 to 10 or more (to the ITER requirement value

of $5MW/m^2$, considered prudent for actively cooled components [6]). Hydrogen recycling alone is not sufficient to exhaust most of the power in the divertor. On the other hand, radiation from impurities, which are present in the plasma due to sputtering at the boundary surfaces, appears to be more efficient. In addition, gases such as nitrogen, neon and argon are injected on purpose in the plasma to enhance divertor cooling by radiation (see Chapter 2). The radiating ability of the impurities increases strongly with increasing Z, increasing electron density and increasing impurity concentration. However, while trying to maximize impurity radiation in the divertor region, the impurity concentration in the core plasma must be kept below the fraction above which ignition becomes impossible due to dilution and radiation losses from the core plasma (e.g. below 6.7% for carbon, 2.4% for neon, 0.25% for iron). Thus, the atomic physics important for divertor plasmas encompasses the physics of hydrogenic species (atoms, ions, molecules) and the physics of heavier atoms and ions (impurity species).

In this Chapter, atomic processes are considered on the basis of their particular relevance to the plasma edge and divertor region. The discussion therefore emphasizes collisions at low temperature and moderate to high density. Only a brief review of the fundamental atomic processes and of the collisional radiative theory is presented here, since extensive treatment can be found in [37], [38], [39] and references therein.

3.2 Relevant Atomic Processes

In this Section the atomic processes relevant to divertor plasma studies are reviewed. In this perspective, initially collisions involving neutral hydrogen and hydrogenic species are addressed. Subsequently the discussion is extended to collisions involving impurity species and to collisions between impurity ions and neutral hydrogen, namely charge exchange at thermal energies.

The rate coefficient in atomic collisions between plasma species, such as electrons and ions, is generally expressed as $< \sigma v > (cm^3 s^{-1})$, where $\sigma(v)$ is the reaction cross section, v the collision velocity and the average is over the velocity distribution functions of the reacting species. The free electron and proton velocity distributions

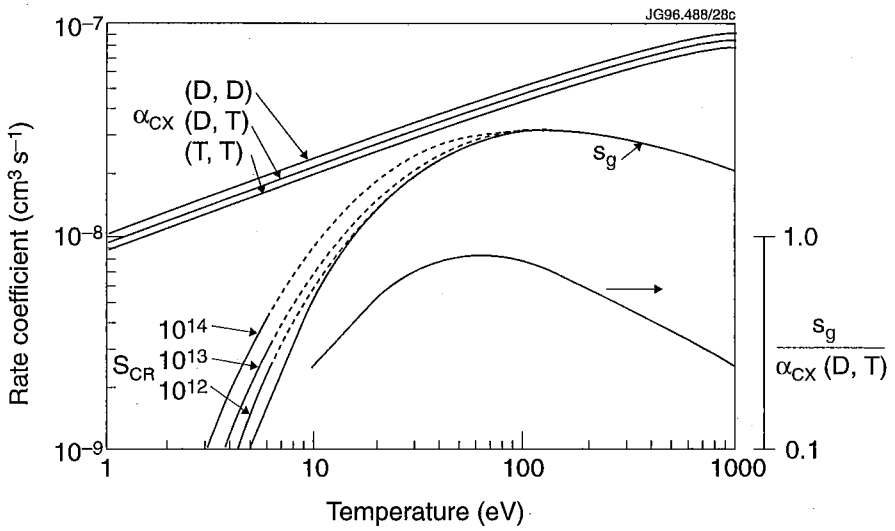

Figure 3.1: Charge exchange and ionization rate coefficients for Hydrogen, from ref. [40].

are assumed Maxwellian:

$$f(\vec{v})\ d^3\vec{v} = (\frac{m}{2\pi kT})^{3/2} e^{-\frac{mv^2}{2kT}} d^3\vec{v} \tag{3.1}$$

with m the mass of the particle, $\vec{v}$ its velocity, k the Boltzmann's constant and T the particle kinetic temperature. This is the usual assumption in fusion plasmas, where the energy equilibration times for electrons and protons are short (see discussion in Chapter 6) compared to the plasma confinement time ($\sim$ 1s in JET). Collisions with plasma electrons are usually dominant because in conditions of approximate equipartition of kinetic energy between electrons and protons the electrons have much greater velocities. However, in some cases the reaction cross sections for ion-atom interactions are so large to overcome the disadvantage of low velocity. An important case for divertor plasmas is charge exchange of hydrogen neutrals, as will be discussed in the following Section.

3.2.1 Collisions involving Hydrogenic Species

The most likely reaction an hydrogen atom undergoes near the divertor target plates is a charge exchange collision with a proton, especially for temperature values $<$ 10 eV (see Fig. 3.1):

$$H + H^+ \longrightarrow H^+ + H. \tag{3.2}$$

In this Chapter 'hydrogen' denotes, for convenience, any of the hydrogen isotopes, since there is no distinction between them, except in their speed. In laboratory

fusion plasmas hydrogen can be present in all of its isotopic forms, but generally deuterium is the working gas. The rate coefficient for the species-symmetric and energy resonant reaction of eq. 3.2 is so large that this process strongly influences the behaviour of hydrogen recycling in the divertor and boundary plasma. The charge exchange process does not influence the particle balance in the plasma, but influences the momentum and energy balance of the plasma ions (see Chapter 6). For charge exchange to be important, the neutrals have to be able to penetrate into the plasma, undergo a charge exchange collision and the fast charge exchange neutral leave the plasma transferring the momentum - and some energy - to the walls many times before an ionization event. This takes place at $T_e \leq 5$ eV, when the mean free path for charge exchange atoms is much larger than the ionization mean free path.

Electron impact ionization occurs when a free plasma electron has energy that exceeds the hydrogen ionization potential, I_H, so that in a collision it can remove the bound electron:

$$H(1s) + e^- \longrightarrow H^+ + e^- + e^-. \tag{3.3}$$

The reaction rate coefficient is S_g. Ionization from $H(1s)$ constitutes a substantial sink for the plasma electron energy, with a loss of 13.6 eV per ionization event. At finite electron densities, ionization can occur both by direct collisional ionization from the ground state but also via multistep excitation and deexcitation/radiative decay followed finally by an ionizing collision. The collisional radiative ionization coefficient S_{CR} describes the enhanced effective rate coefficient with respect to S_g (see Fig. 3.1) and it increases with n_e. In the limit of $n_e \longrightarrow 0$, $S_{CR} \longrightarrow S_g$, thus S_g is also called the 'zero-density' ionization coefficient. The reaction rate per unit volume for electron impact ionization is given by $n_e n(H) S_{CR}$.

The inverse process of electron impact ionization is three-body recombination:

$$H^+ + e^- + e^- \longrightarrow H(i) + e^-. \tag{3.4}$$

Due to the small cross sections for three-body interactions to low excited levels i, the rate coefficient for this process is very small. However, it has to be noted that the reaction rate per unit volume, $n_e^2 n(H^+)\alpha^T$, is proportional to the square of the electron density. This process can become the dominant recombination mechanism in very high density divertor plasmas.

Electron and proton collisions induce bound-bound excitation and deexcitation

transitions:

$$H(i) + e^- \rightleftharpoons H(j) + e^- \tag{3.5}$$

$$H(i) + p \rightleftharpoons H(j) + p \tag{3.6}$$

where i and j are two quantum shells. Collisions with plasma electrons are usually dominant because in conditions of equipartition of kinetic energy between electrons and protons the electrons have much greater velocities. Also, the reaction cross sections are at maximum at collision speeds when the electron energy is of order 10 times the transition energy. Thus proton collisions are only important when the transition energies involved are very small. This is the case of transitions that redistribute populations between degenerate l-subshells for hydrogen and H-like ions. Otherwise, for low levels of impurity ions and atoms, where the states are well separated in energy, electron collisions are the dominant collisional excitation/deexcitation mechanism.

Collisional excitation causes the electron to lose an amount of kinetic energy equal to the energy difference $\Delta E(i,j)$ between the levels i and j. This energy is transferred to the atom in the form of internal energy. The excited state j generally has a very short lifetime ($\tau_{es} \sim A^{-1} \sim 10^{-8}$ s, with A the transition probability for spontaneous emission) and thus decays radiatively very fast to a lower level k, with k not necessarily the same level as i, and a photon is emitted with energy $h\nu = \Delta E(j,k)$:

$$H(j) \longrightarrow H(k) + h\nu. \tag{3.7}$$

In optically thin plasmas, which is the approximation adopted in this thesis (see also Chapter 7) the photon escapes from the plasma, so its energy is lost to the walls of the vessel where it is absorbed. Provided the excitation energy of the transition is fairly small compared to the incident electron energy, electric dipole excitation rates are generally the largest. The deexcitation rate coefficient is obtained according to the principle of detailed balance:

$$q_{i\to j} = \frac{\omega(j)}{\omega(i)} e^{-\frac{\Delta E(i,j)}{kT_e}} q_{j\to i} \tag{3.8}$$

with $\omega(i)$, $\omega(j)$ the statistical weights of states i, j.

Protons can also recombine by radiative recombination:

$$H^+ + e^- \longrightarrow H(j) + h\nu \tag{3.9}$$

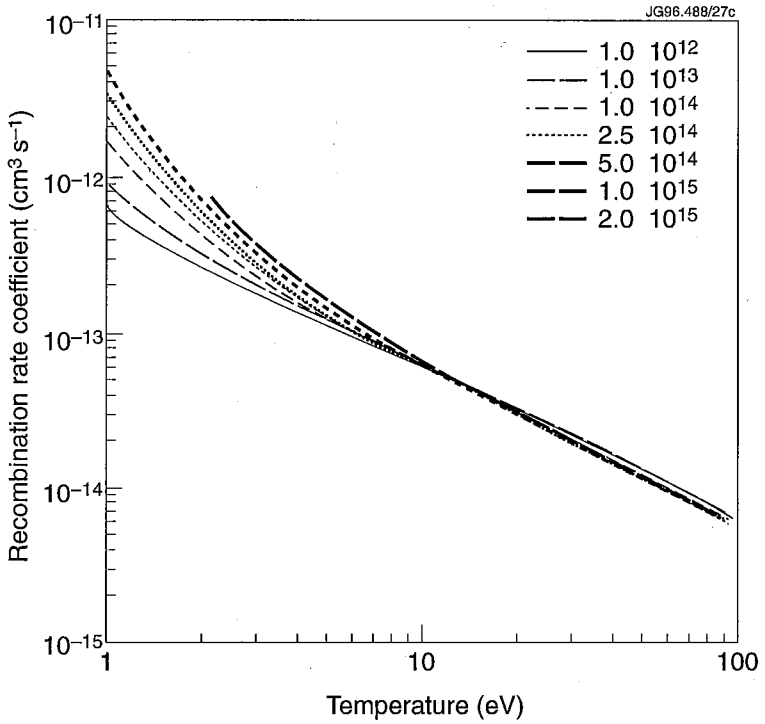

Figure 3.2: Collisional radiative recombination rate coefficient for hydrogen as a function of temperature for various electron densities (from ADAS).

where a free electron is captured into a bound state of the hydrogen atom, with the photon carrying away the excess energy of the interaction. The reaction rate per unit volume is $n_e n(H^+)\alpha^R$.

The total collisional radiative recombination rate coefficient for hydrogen, which contains radiative and three body recombination, is shown in Fig. 3.2. This coefficient is small, except at very low electron temperatures ($T_e \leq 1$ eV) and high electron densities. This is relevant to detached plasma regimes, as explained in Chapter 7.

3.2.2 Collisions involving Impurity Species

Impurity radiation in divertor plasmas is mainly due to radiative decay of excited states of impurity ions in the plasma. The distribution of these ions is determined by transport, ionization and recombination processes. Impurities emerge from the boundary surfaces predominantly as neutrals and radiate as they are ionized and finally return to the walls where they are neutralized.

Collision processes similar to those described for the hydrogen atoms occur for impurity elements, but in this case the situation is more complex due to the greater

number of bound electrons. This increases the possible configurations for the ions and thus the number of possible collision processes. Also, not only the outer shell electrons but also the inner shell (or core) electrons may participate in the reactions. In particular, an additional and usually dominant recombination process for non-hydrogenic impurity ions is enabled by the presence of additional bound electrons. This is the case of dielectronic recombination. The process occurs in two stages, resonant capture followed by radiative stabilization:

$$A^{+(z+1)}(\gamma) + e^- \rightleftharpoons A^{+z}(\gamma', j) \tag{3.10}$$

$$A^{+z}(\gamma', j) \longrightarrow A^{+z}(\gamma'', j) + h\nu \tag{3.11}$$

where γ, γ', γ'' denote the parent configuration and core levels. First a free electron excites a core electron in the parent ion and simultaneously loses enough energy to enter a bound level j (resonant capture). This condition is transient. The doubly excited state lies above the ionization threshold for the initial parent configuration and can either break up by autoionization (left pointing arrow in the first reaction) or stabilize by radiatively decaying to a lower configuration (eq. 3.11), where γ and γ'' are not necessarily the same configuration. The reaction rate per unit volume is $n_e n(A^{+z+1})\alpha^D$.

The effective collisional radiative ionization rate coefficient for non H-like impurity ions is also modified with respect to what described in the previous section, since direct inner shell ionization and inner shell excitation autoionization also contribute to the ionization process.

3.2.3 Collisions between Hydrogen Atoms and Impurity Ions: Thermal Charge Exchange

Cross sections for these processes are typically large ($\geq 10^{-15} cm^{-2}$), hence charge exchange can be the dominant inelastic process in environments containing both charged ions and significant concentrations of hydrogen neutrals, such as the divertor and edge plasma regions.

Consider e.g. the net reactions:

$$C^{+6} + H \longrightarrow C^{+5} + H^+ \tag{3.12}$$

$$C^{+5} + H^+ \longrightarrow C^{+6} + H. \tag{3.13}$$

The first reaction has a large cross section, since contributions to the total capture occur from high n-states of the recombining ion with the hydrogen ground state donor. The cross section for the second reaction is small, due to repulsion between the two positive ions and the non resonant ground state C^{+5} donor. For divertor conditions the reactions of the first type are important and studied here.

Consider the more general electron capture reaction:

$$A^{+z} + H \longrightarrow A^{+(z-1)} + H^{+} \tag{3.14}$$

where a multiply charged impurity ion A^{+z} colliding with a neutral hydrogen atom captures the electron, thus recombining into the lower ionization stage $A^{+(z-1)}$. The basic parameters influencing the electron capture process are the relative collision velocity, v, the ionic charge of the recombining ion and the number of electrons participating in the collision system. In general, the collision velocity is compared to the orbital velocity of the bound H-electron, v_0, and determines the adiabaticity of the collision process. Three dynamical regions are identified: a low velocity region ($v \ll v_0$), an intermediate velocity region ($v \sim v_0$) and a high velocity region ($v \gg v_0$) [41]. The ionic charge, z, connects the strength of the different potential and dynamic interactions of the system. The number of electrons in the ion-atom system increases the number of possible reaction pathways and also affects the symmetry properties of the collision. In this section the main focus will be on low energy collisions, which are relevant to divertor plasmas.

The common feature of the electron capture process - at all energies - is that the highest probability for electron transfer occurs when the energies of the initial and final state in the transition are close to each other. In the low velocity collision regime this condition of energy quasi-resonance induces certain final electronic states of the recombined ion to be preferentially populated with respect to others.

The most probably populated n-level in the recombined ion scales approximately as $n \sim n_0\ z^{3/4}$, with z the charge of the recombining ion and n_0 the principal quantum number of the hydrogen donor in the initial state [41].

Besides the n- (energy) selectivity, which has been discussed above, the electron capture process is also selective with respect to the l and m quantum numbers. The angular momentum selectivity depends on the specific transition mechanism and is mainly affected by the collision velocity, the ionic charge of the projectile and by the rotation of the internuclear axis.

Experimentally, state selective charge transfer cross sections are generally measured with translational energy spectroscopy (TES) or with photon emission spectroscopy (PES) [41]. With TES the change in the kinetic energy of the charge exchange projectile ions is measured. Population of states with different binding energy in the recombined ions leads to projectiles with different kinetic energies and from the translational energy spectra state selective cross sections are measured. Since these spectra show only the relative importance of the various reaction channels, state selective cross sections can only be derived by comparison with absolute total charge exchange cross sections. With PES the radiation emitted from the excited levels populated by electron capture is measured. Thus, with absolutely calibrated spectrometers PES allows the direct measurement of absolute state selective cross sections. However, the main difficulties of this method are due to the need for absolutely calibrated photon detectors (often with the necessity to cover wide wavelength ranges) and to the requirement of precise atomic data on energy levels and transition probabilities for the final excited states of the projectile ions. Experimental measurements of state selective electron capture cross sections at low collision energies are still scarce, because of the difficulty to produce sufficiently intense, low energy ion beams. Therefore, at low collision energies most of the available electron capture cross section data are from theoretical calculations.

At low collision energies, where the electron involved in the capture process is strongly delocalized, charge exchange processes are described by a quasi-molecular picture. The electronic states are represented in terms of the molecular orbitals (MO's) of the temporary molecule formed by the target and the projectile during the collision. With increasing collision velocity ($v \sim v_0$) the electron is bound either to the target atom or to the ion A^{+z} and the quasi-molecular picture becomes inadequate. In this regime, atomic and ionic states give a good representation of the electronic motion (AO's). Most of the theories on electron capture are based on a semi-classical approximation, in which the motion of the heavy nuclei is described by a classical trajectory, $\vec{R} = \vec{R}(t)$, and the electronic motion quantum mechanically. Due to the large masses of the ions involved in the reaction, this approximation is justified down to very low collision velocities.

Consider a collision between a fully stripped ion A^{+Z} (Z is the nuclear charge) and an H atom. The motion of the electron is described by the time-dependent

Schrödinger equation, at fixed $\vec{R}$:

$$i\frac{\partial}{\partial t}\Psi(\vec{r},t) = H^{el}\Psi(\vec{r},t) \tag{3.15}$$

with initial conditions:

$$\Psi \longrightarrow \varphi^{H}(1s) \qquad for \;\; t \longrightarrow -\infty \tag{3.16}$$

where $\varphi^{H}(1s)$ describes the ground state orbital of the hydrogen atom. H^{el} is the electronic Hamiltonian:

$$H^{el} = -\frac{1}{2}\nabla^2_{\vec{r}} - \frac{Z}{r_1} - \frac{1}{r_2} \tag{3.17}$$

where $\vec{r}$ denotes the set of electronic coordinates in an inertial frame of reference, $\vec{r}_1$ and $\vec{r}_2$ are the position vectors of the electron relative to the ion A^{+Z} and to the H atom. The probability for the active electron to end in a specific final state j of the system is given by:

$$P_j(b) = |< \varphi_j|\Psi >_{t\to+\infty}|^2 \tag{3.18}$$

with b the collision impact parameter. Identifying j with the set of electronic states $j \equiv (nlm)$, the cross section for capture into an (nlm) final state is:

$$\sigma_{nlm} = 2\pi \int_0^{+\infty} P_{nlm}(b)\, b\, db. \tag{3.19}$$

Summing σ_{nlm} over m, or over l and m for a given n, gives the state selective cross sections for capture into specific l-subshells or into specific n-shells:

$$\sigma_{nl} = \sum_m \sigma_{nlm} \tag{3.20}$$

and

$$\sigma_n = \sum_l \sigma_{nl}, \tag{3.21}$$

while the total charge exchange cross section is:

$$\sigma_{tot} = \sum_n \sigma_n. \tag{3.22}$$

Denoting with $\{\chi_n\}$ the orthonormal complete basis set such that:

$$\Psi = \sum_n c_n(t)\, \chi_n \tag{3.23}$$

eq. 3.17 is then expanded in the set of the coupled equations for the expansion coefficients c_n. In the case of interest $\{\chi_n\}$ is the set of adiabatic molecular eigenfunctions defined by [42]:

$$H^{el}\chi_n(\vec{r},\vec{R}) = E_n(R)\chi_n(\vec{r},\vec{R}). \tag{3.24}$$

The eigenvalues $E_n(R)$ and the eigenfunctions $\chi_n(\vec{r},\vec{R})$ for each electronic state n depend parametrically on the internuclear distance R, which is held fixed during the calculation. To account for the rotation of the internuclear axis a transformation is taken to a rotating frame with the same origin as the inertial frame.

A plot of the eigenenergies $E_n(R)$ of the system versus the internuclear distance R (the so called 'adiabatic correlation diagram') connects the electronic energies of the system at finite values of R with those in the 'united atom limit' ($R \to 0$) and those in the 'separated atom limit' ($R \to \infty$). If the system $A^{+Z} - H$ is at rest, the energy curves of adiabatic states with the same symmetry (e.g Σ, Π etc.) cannot cross, as it is stated by the von Neumann-Wigner theorem [42]. However, due to the relative motion of the nuclei during the collision, this rule is violated and transitions take place at the pseudocrossing of the energy curves. With decreasing R, the rotational coupling becomes more important since the angular velocity scales as bv/R^2 and is responsible for the population of the l-subshells. It couples states with different symmetry , according to the selection rule $\Delta\Lambda = \pm 1$.

This method of solving the coupled equations is the so-called Perturbed Stationary State Method (PSS) and is widely used in numerical calculations of charge exchange cross sections. However, it presents the disadvantage that the motion of the active electron is imperfectly included. This deficiency directly affects the calculations of the cross sections for the charge exchange process. In order to account for the translational motion of the active electron one has to multiply the wave function χ_n by a phase factor $F_n = exp\,(i\alpha_n)$, where α_n depends, in general, on $\vec{v}$, $\vec{r}$ and $\vec{R}$. However, these phase factors are not uniquely defined, and the choice of the optimal ETF's is still a subject of controversy.

Consider now a collision between a partly stripped ion A^{+z} and an hydrogen atom at low impact energies. Since capture takes place at large internuclear separations, it is generally assumed that the electron core of the incident ion does not participate in the dynamics of the collision and is therefore regarded as static in its ground state configuration throughout the collision. Outside the core, at large R, the screening of the excess nuclear charge is approximately complete and the projec-

tile potential is well represented by the Coulomb force: $V_p = -z/r_p$, where r_p is the distance of the active electron from the projectile. The core electrons contribute to the charge exchange process by interacting electrostatically with the active electron. Due to this interaction, additional crossings become available in the range of internuclear separations relevant for the capture process. This interaction is stronger at lower velocities, since the interaction time is longer.

3.2.4 Review of Charge Exchange Cross Section Data for Carbon

C^{+1}/H:

For the reaction:

$$C^{+1} + H \longrightarrow C^{+0} + H^{+} \tag{3.25}$$

total charge transfer cross sections have been assembled from experimental and theoretical data in the recommended cross section data tables by Janev et al. [43] (see references therein) in the energy range 0.05 - 33 keV/amu. Fig. 3.3 shows the low energy subset of these data used in this thesis. No recent work on this reaction has been found since this review, also quoted in the more recent review by Phaneuf [44]. No state selective cross sections have been found in the literature for this reaction.

C^{+2}/H:

For the reaction:

$$C^{+2}(1s^2 2s^2\ ^1S) + H \longrightarrow C^{+1}(1s^2 nln'l') + H^{+} \tag{3.26}$$

state selective cross section calculations from Heil et al. [45] were used (see Fig. 3.4). These are the only data referred to also in the compilations of Tawara [46] and Janev [43]. The data suggest that electron capture into the ground state $C^{+}(2s^2 2p\ ^2P)$ is only important at low energies, although the cross section is small and decreases with increasing energy. A second channel, $C^{+}(2s2p^2\ ^2D)$, becomes accessible and dominant at higher energies. In general, cross sections for this reaction are quite small and large uncertainties exist in the calculated data. Capture from metastable state ions $C^{+2}(1s^2 2s2p\ ^3P)$ might affect the total cross section, as shown qualitatively by the experiments of McCullough et al. [47] in the keV/amu energy range.

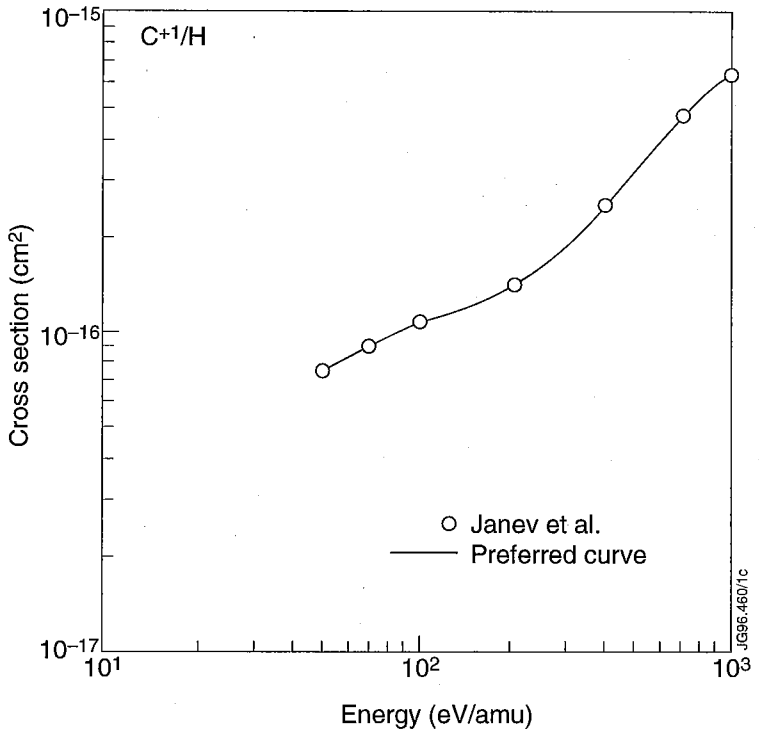

Figure 3.3: Total charge transfer cross sections for C^{+1}/H collisions, from Janev et al. [43].

The total charge transfer cross section for this reaction is shown in Fig. 3.5, together with the recommended total cross section of Janev [43] (see references therein). Due to the lack of state selective cross section data in the energy range $E > 10$ eV/amu, in the calculation of the charge exchange rate coefficients (see Chapter 8) it is assumed that all electron capture occurs into the $2s2p^2$ (^2D) level, while capture into $2s^22p$ (^2P) goes to zero.

C^{+3}/H:

For the reaction:

$$C^{+3}(1s^22s) + H \longrightarrow C^{+2}(1s^2nln'l') + H^+ \tag{3.27}$$

theoretical and experimental cross section data from the existing literature have been assembled and compared. Theoretical calculations based on the molecular orbital curve crossing model have been carried out by Blint et al. [48], Watson and Christensen [49], Heil et al. [50] in the thermal energy range. These calculations were driven by astrophysical interest, since the cross section for this reaction becomes very large in the few eV range. These calculations were later extended by Bienstock et al. [51] to energies up to 5000 eV/amu. Opradolce et al. [52] performed

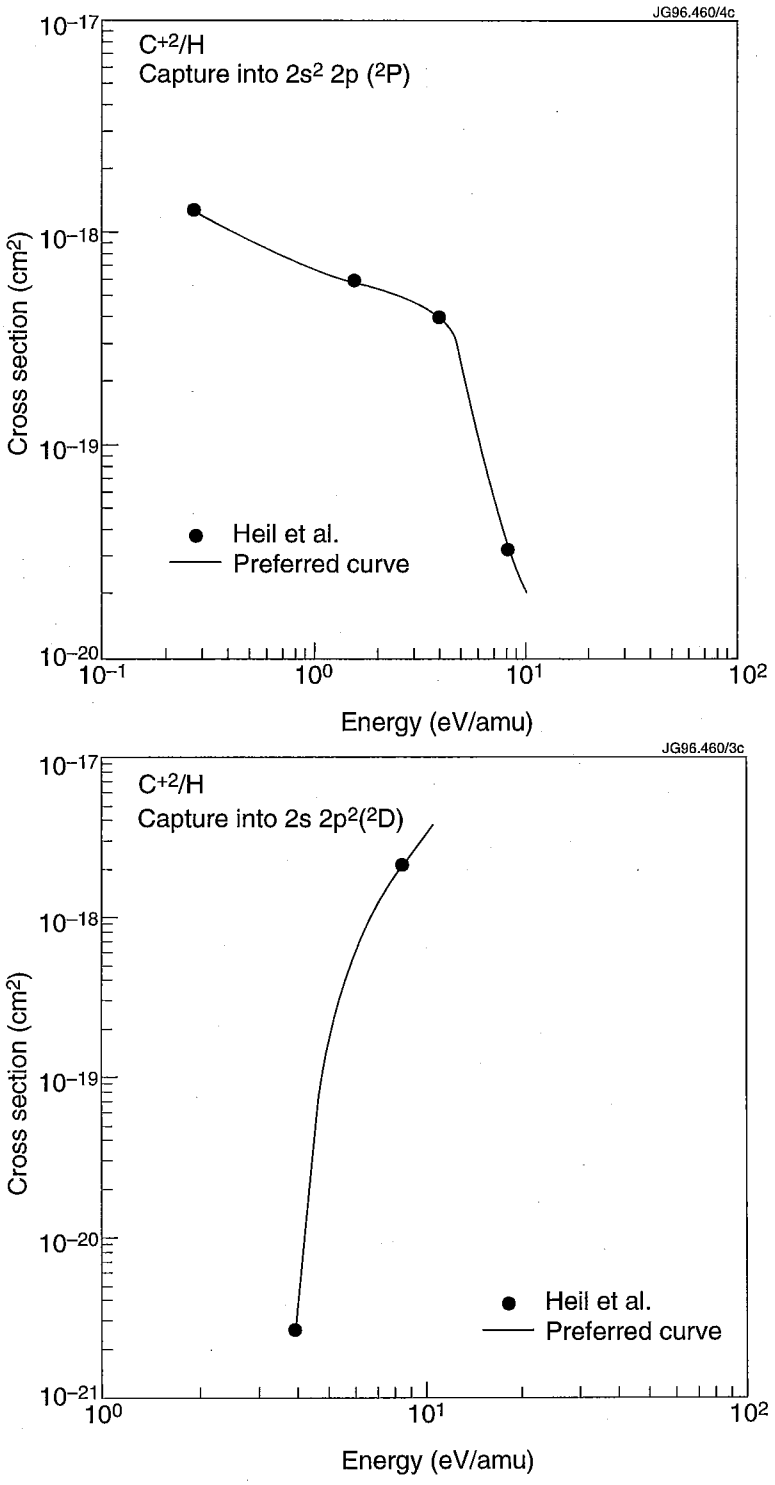

Figure 3.4: State selective electron capture cross sections for C^{+2}/H collisions, from Heil et al. [45].

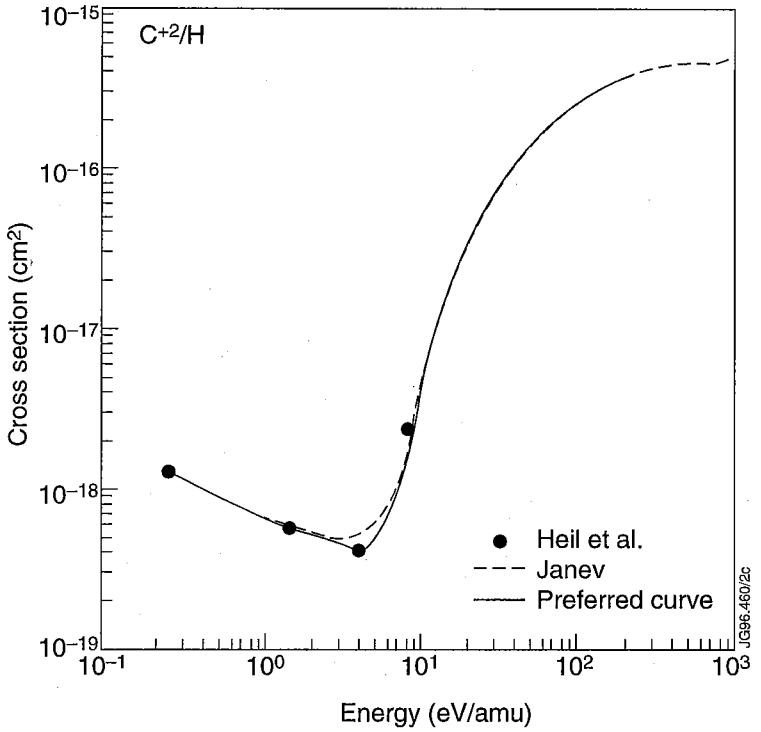

Figure 3.5: Total electron capture cross section for C^{+2}/H collisions, from Heil et al. [45] and comparison with the recommended cross section data of Janev [43].

molecular orbital calculations including translation factors in the energy range 10 - 5000 eV/amu, with both radial and rotational coupling. The work covered capture into triplet states only. Translation effects were found to be important, except at energies of few eV. Errea et al. [53] have calculated total and state selective cross sections for collision energies between 0.04 and 9 keV/amu. The calculations were performed using a 22-states molecular orbital calculation with a common translation factor. These calculations are performed assuming the initial channel to be a singlet (triplet) and then obtaining the total cross section from summation of the singlet and triplet results multiplied by the appropriate statistical weights (1/4 for singlets and 3/4 for triplets):

$$\sigma_{tot} = \frac{1}{4}\sigma_{singlet} + \frac{3}{4}\sigma_{triplet}. \tag{3.28}$$

In the triplet manifold the dominant channel is capture into $C^{+2}(3s\ ^3S)$. In the singlet manifold, capture into $C^{+2}(2p^2\ ^1S)$ is the dominant channel at intermediate energies. The total cross section is dominated by the triplet component. Herrero et al. [54] have extended the work of Errea et al. to lower energies, providing theoretical cross sections in the collision energy range 0.004 -90 eV/amu. For this low

energy range the authors adopted a quantal treatment of the molecular dynamics. The authors also performed calculations of cross sections for charge exchange with deuterium, in light of the recent experiments carried out by Havener et al. [55] for this reaction. At low energies such cross sections are found to be significantly smaller than those for H, owing to the dynamical effect of the reduced mass. At the lowest energies considered (0.003 eV/amu), the difference in the cross sections for H can reach 50% of that of D; at energies $E \geq 0.1$ eV/amu the D cross sections are practically identical to those for H. The state selective cross sections used in this thesis are from B. Herrero (private communication, 1996).

Total charge transfer cross sections have been measured by Phaneuf et al. [56] in the 10 -160 eV/amu energy range and at 2 -5 keV/amu by Gardner et al. [57], Phaneuf et al. [58] and Crandall et al. [59]. State selective electron capture has been investigated by Ciric et al. [60] in the 0.7 - 4.6 keV/amu energy range using photon emission spectroscopy and by McCullough et al. [47] in the 0.6 - 18 keV/amu range and by Wilkie et al. [61] from 50 to 1500 eV/amu using translational energy spectroscopy. Recently, Havener et al. [55] have measured total cross sections using merged beams in the energy range 0.3 - 3000 eV/amu, with the low-energy measurements ($\leq$ 560 eV/amu) performed with D instead of H. In ref. [55], a comparison of the measured and calculated total C^{+3}/H charge transfer cross sections is presented up to very high energies. Fig. 3.6 shows a comparison of low energy total cross sections, relevant to the work of this thesis, including the more recent data from Herrero et al. The preferred curve is drawn through the data by Herrero et al. and Errea et al. for higher energies. Figs. 3.7, 3.8 and 3.9, 3.10 show examples of the largest state selective cross sections from the triplet and singlet manifolds, respectively.

C^{+4}/H:

For the reaction:

$$C^{+4}(1s^2) + H \longrightarrow C^{+3}(1s^2nl) + H^+ \tag{3.29}$$

all the theories predict that the dominant electron capture occurs in the $n = 3$ levels of C^{+3} and that the contribution from other levels is small, which is confirmed experimentally. For instance, at very high energies (1 - 7 keV/amu), Dijkkamp et al. [62] have shown that the measured electron capture cross sections into $4l$ states

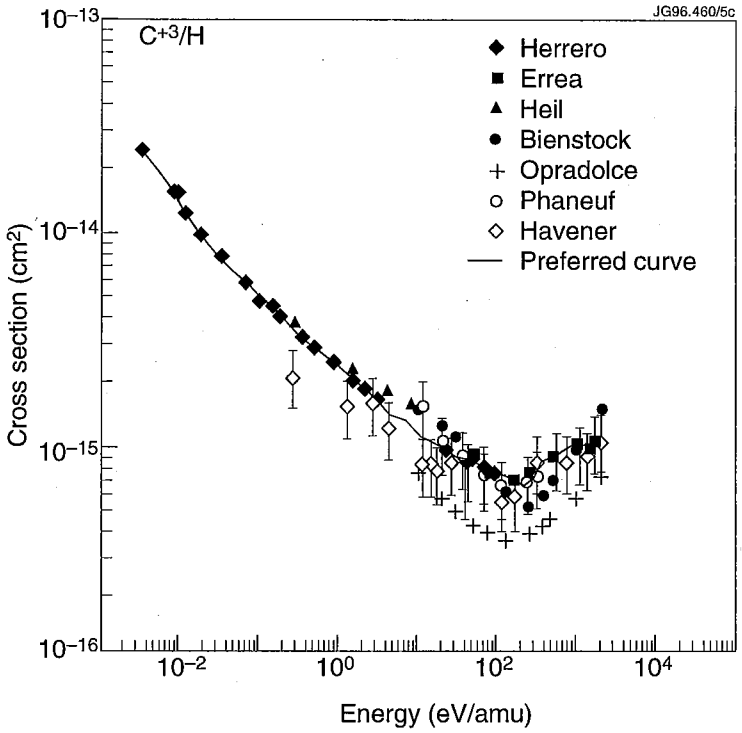

Figure 3.6: Total electron capture cross sections for C^{+3}/H collisions at low energies, with preferred curve through the data of Herrero et al. [54] and Errea et al. [53].

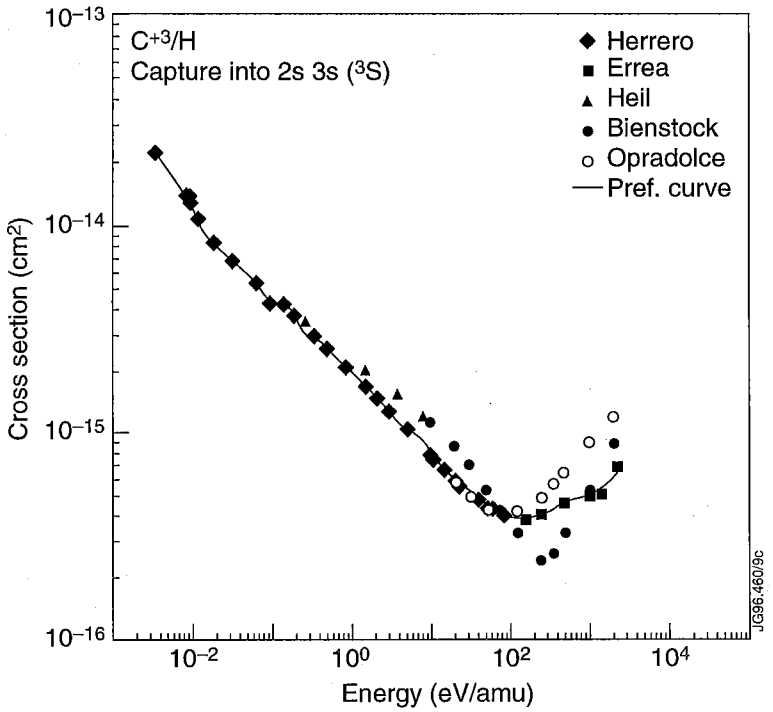

Figure 3.7: State selective charge exchange cross sections for C^{+3}/H collisions at low energies for capture into $2s\ 3s\ ^3S$. The preferred curve is through the data of Errea et al. [53] and Herrero et al. (private communication).

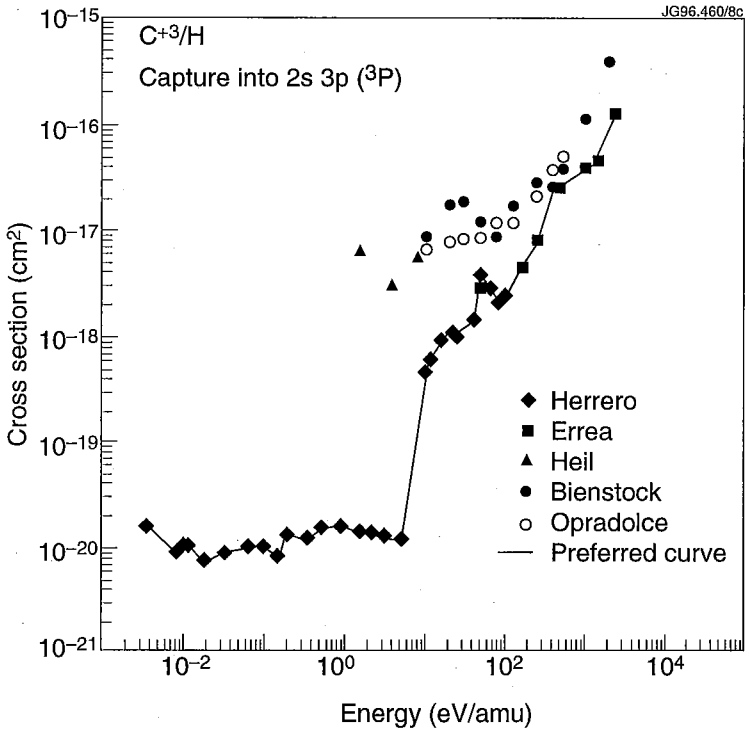

Figure 3.8: State selective charge exchange cross sections for C^{+3}/H collisions at low energies for capture into $2s\ 3p\ ^3P$. The preferred curve is through the data of Errea et al. [53] and Herrero et al. (private communication).

are more than one order of magnitude smaller than the $3l$ capture cross sections and that they decrease with decreasing energy (also predicted by the calculations of Fritsch and Lin [63]). The main reference used in this thesis is the work by Hoekstra [64], where the first measurements of state selective charge exchange cross sections in the energy range 50 -1330 eV/amu are reported and compared to existing theoretical and experimental data. Hoekstra measured state selective cross sections for the reactions:

$$C^{+4}(1s^2) + H \longrightarrow C^{+3}(1s^2 3l) + H^+ \tag{3.30}$$

by means of photon emission spectroscopy. The results were compared with theory and it emerges that, especially for energies below 200 eV/amu, there are considerable discrepancies between experiment and theory. Experimental results in the low energy region are still scarce, mainly due to difficulties in producing both intense slow highly charged ion beams and dense atomic hydrogen targets.

Theoretical works that include both total and state selective cross sections are reported here. The calculations by Gargaud et al. [65] (MO7) and Gargaud and McCarroll [66] (MO4) use molecular orbitals as basis set and are essentially the

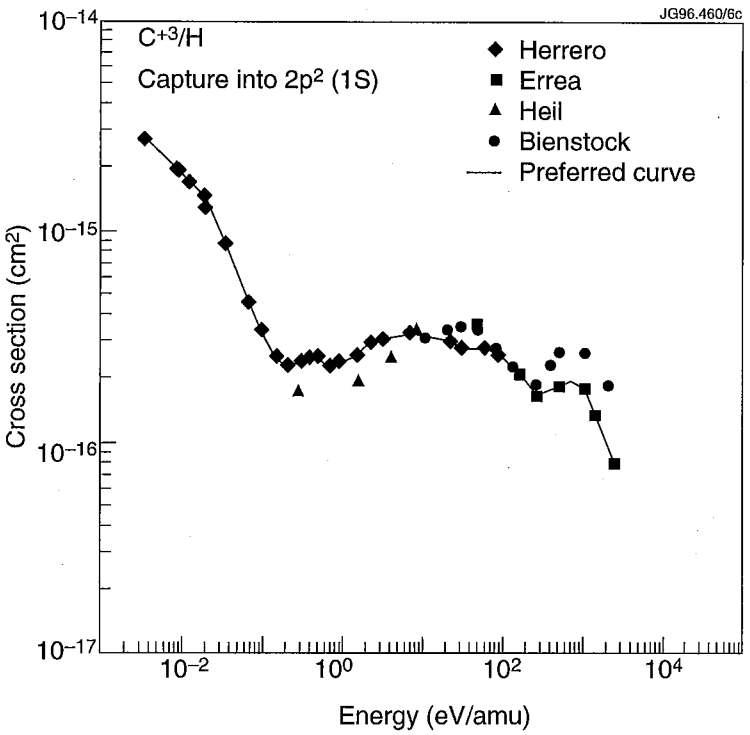

Figure 3.9: State selective charge exchange cross sections for C^{+3}/H collisions at low energies for capture into $2p^2\ ^1S$. The preferred curve is through the data of Errea et al. [53] and Herrero et al. (private communication).

same, but for the number of molecular states included. The more recent calculations (MO7) include both radial and rotational coupling, whereas MO4 included only radial coupling. Fritsch and Lin [63] use atomic orbitals (AO). In the energy range 100-300 eV/amu, the calculations based on molecular state expansion (MO) (Olson et al. [67], Hanssen et al. [68], Gargaud et al. [65]) are in good agreement with each other, but they overestimate the experimental total electron capture cross section by almost a factor of two. The AO calculations of Fritsch and Lin are in better agreement with the experiments.

The experimental results by Hoekstra are an extension to lower energies of the state selective charge exchange cross sections measurements by Dijkkamp et al. [62] and are in good agreement with the measurements of total electron capture cross sections of Phaneuf et al. [56]. The measured state selective $\sigma(3l)$ electron capture cross sections are compared in Figs. 3.11-3.13 with the results of theoretical calculations. Also shown is the preferred curve through the data. Shown in Fig. 3.14 are the total cross sections for capture into $n = 3$, together with the total cross sections measured by Phaneuf et al. [56] and Panov et al. (in ref. [69]). Fair agreement is

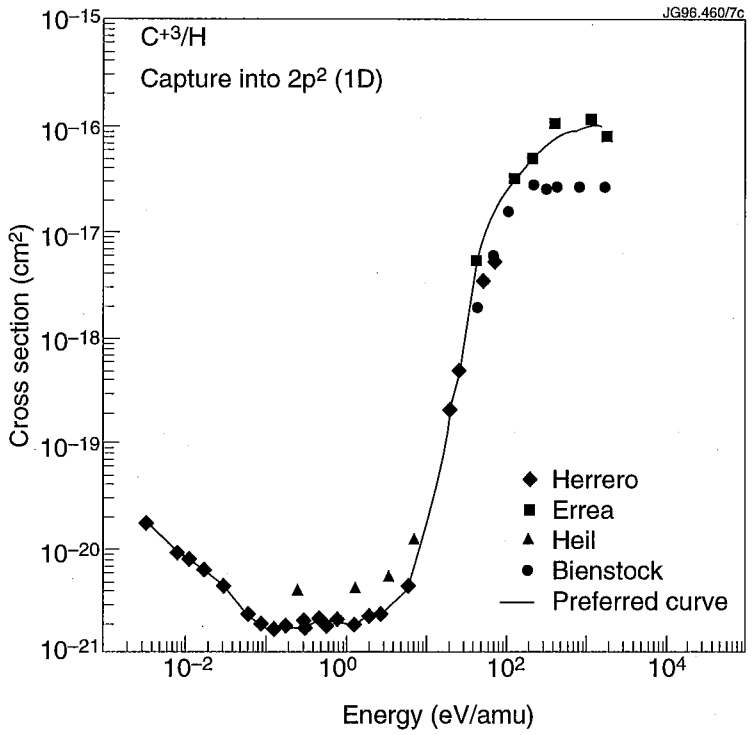

Figure 3.10: State selective charge exchange cross sections for C^{+3}/H collisions at low energies for capture into $2p^2\ ^1D$. The preferred curve is through the data of Errea et al. [53] and Herrero et al. (private communication).

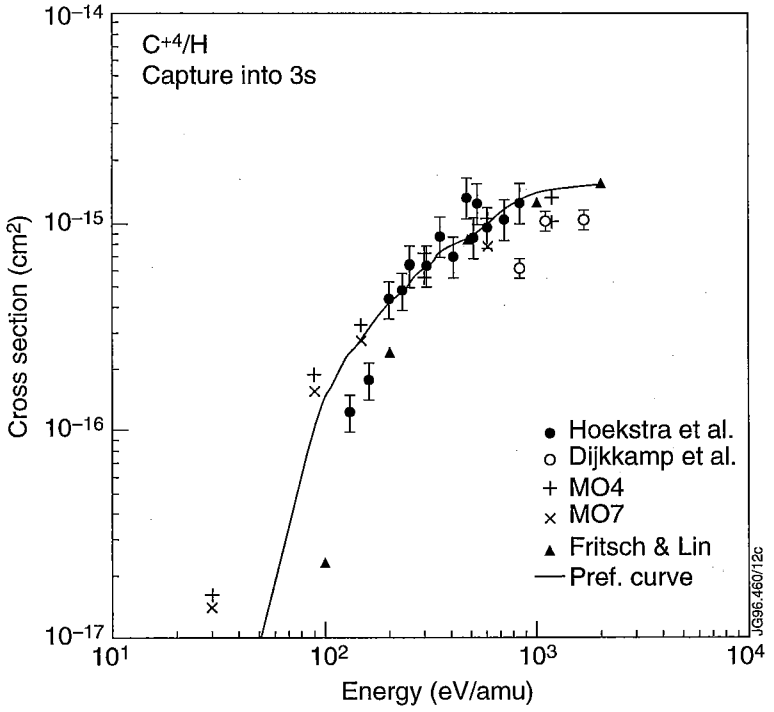

Figure 3.11: C^{+4}/H state selective charge exchange cross sections for capture into $3s$ and preferred curve through the data.

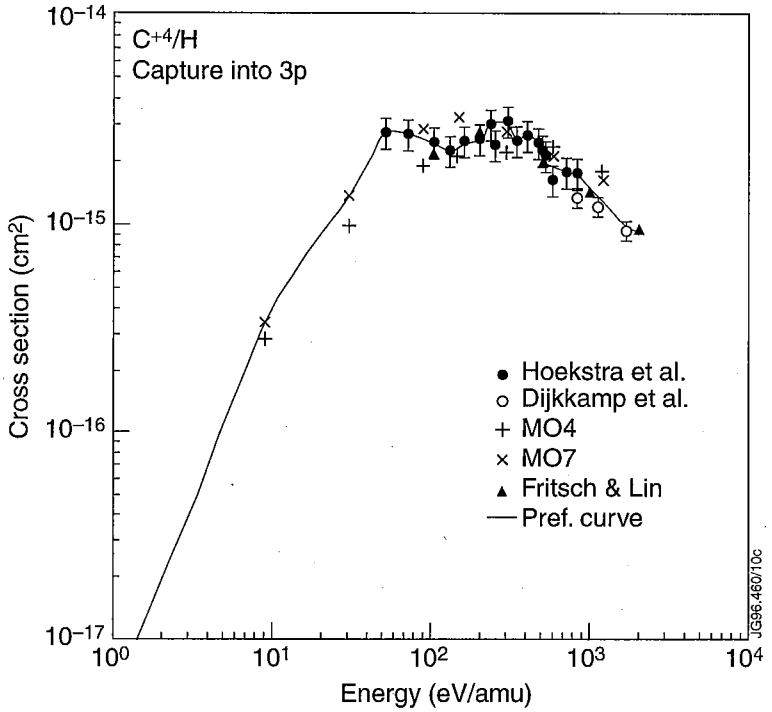

Figure 3.12: C^{+4}/H state selective charge exchange cross sections for capture into $3p$ and preferred curve through the data.

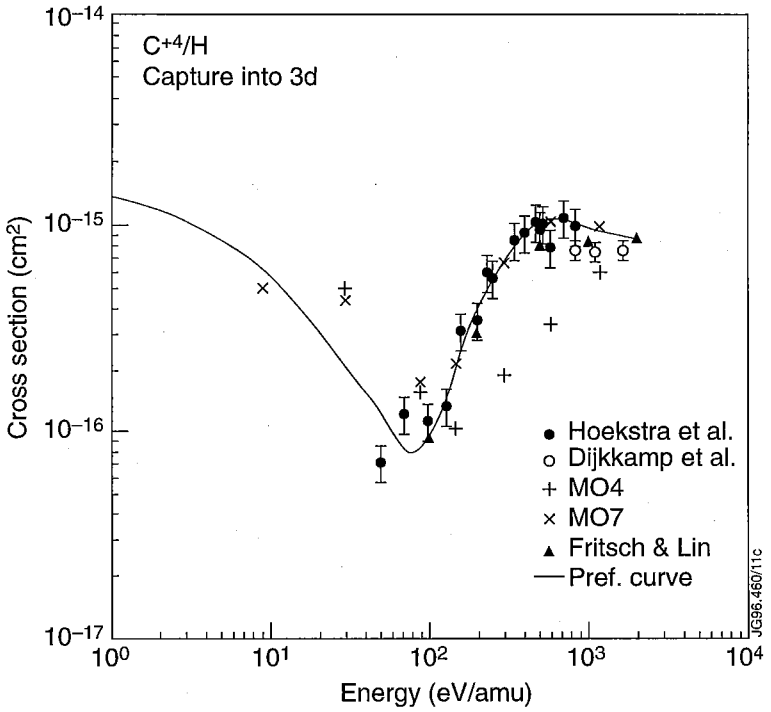

Figure 3.13: C^{+4}/H state selective charge exchange cross sections for capture into $3d$ and preferred curve through the data.

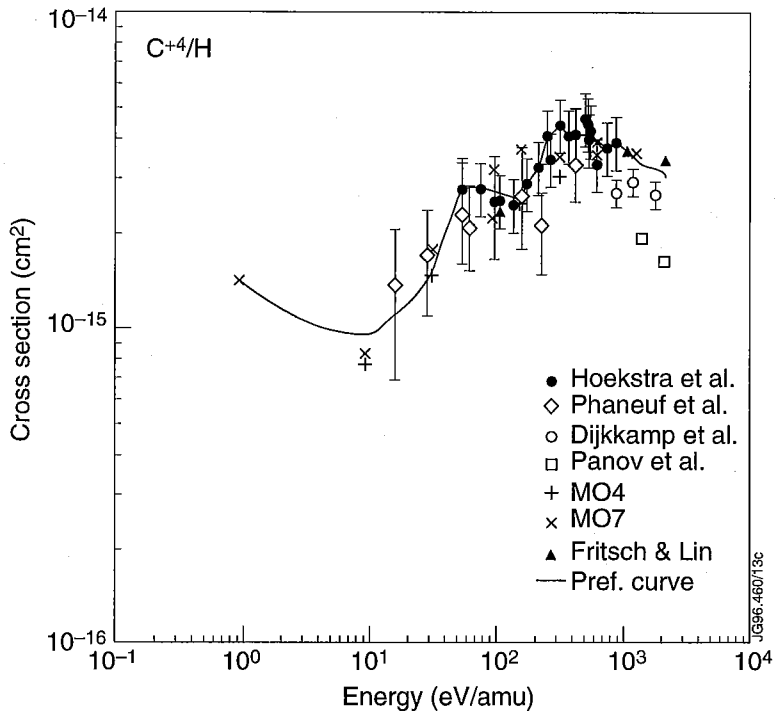

Figure 3.14: Total electron capture cross sections for C^{+4}/H collisions and preferred curve through the data.

found between measurements and theory for the total cross sections, while some discrepancies appear in the case of the state selective cross sections. Hoekstra's measurements confirm the discrepancy between experiment and MO7 in the energy range 80 - 200 eV/amu. From the comparison of the calculated and measured state selective cross sections Hoekstra concludes that:

a) below 200 eV/amu $\sigma(3s)$ decreases more rapidly with energy than the MO results.

b) below 400 eV/amu $3p$ is the most dominantly populated state with a more or less constant cross section. Therefore the difference between experiment and MO7 for $\sigma(3p)$ is the reason for the difference observed in comparing the total charge transfer cross sections.

c) The increase in $\sigma(3d)$ at the lowest energies, predicted by MO7 and MO4, is not seen in the experiment.

Hoekstra then concludes that the agreement between the measured σ_{tot} and the MO4 caculations is somehow fortuitous, given the discrepancies for $\sigma(3s)$ and $\sigma(3p)$. On the contrary, the AO results are in good agreement with the experiments in the range 0.1 -10 keV/amu. More experiments are needed to benchmark these calculations, especially in the low energy range.

C^{+5}/H:

For the reaction:

$$C^{+5}(1s) + H \longrightarrow C^{+4}(1s\ nl) + H^{+} \tag{3.31}$$

the main reference used in this thesis is the work by Shimakura et al. [70]. Previous theoretical works include only two studies: Shipsey et al. [71] and Bottcher and Heil [72]. Shipsey et al. used a semiclassical molecular-orbital method with a small basis set at intermediate collision energies (only five channels were used, therefore omitting some of the important reaction channels) and completly neglecting the ETF's. Only total cross sections were reported. The work by Bottcher et Heil is a five-channel quantum mechanical calculation within the MO approach at low collision energies (1 - 300 eV/amu). Also in this case the ETF's were neglected. In addition, benchmark measurements of total cross sections for this reaction were carried out by Phaneuf et al. [56] and Crandall et al. [59].

Shimakura et al. used quantum mechanical close-coupling methods for collision energies below 15 eV/amu and semiclassical close coupling methods for energies above 15 eV/amu. ETF's were included. In the semiclassical calculations 16 states were included. The dominant capture occurs into $n = 4$ states of C^{+4} ions at lower energies; at higher energies capture into $n = 3$ states also becomes important. For the triplet manifold, $C^{+4}(1s4s)$ is the dominant channel for electron capture below 500 eVamu. Above this energy, the state selective cross section for this channel rapidly decreases and the $C^{+4}(1s4d)$, $C^{+4}(1s4p)$ and $C^{+4}(1s3p)$ channels become more important. For the singlet manifold, below 500 eV/amu the $C^{+4}(1s4s)$ and $C^{+4}(1s4f)$ channels mainly contribute to the total cross section. The $C^{+4}(1s4f)$ channel has the second highest cross section due to the fact that the energy level of this state is closest to that of the $C^{+4}(1s4s)$ state. At higher collision energies the $C^{+4}(1s4d)$, $C^{+4}(1s3p)$ and $C^{+4}(1s3d)$ channels become increasingly important. The total cross section is obtained from the weighted average of the singlet and triplet cross sections, as already mentioned for the case of the C^{+3}/H system. The total cross sections are in excellent agreement with the measurements, as shown in Fig. 3.15. The measurements by Crandall et al. were performed only at one (very high) energy point for this reaction and are not shown. A comparison with the total recommended cross sections compiled by Janev et al. [43] is also shown in Fig. 3.15. The state selective electron capture cross sections from Shimakura et al. [70] were

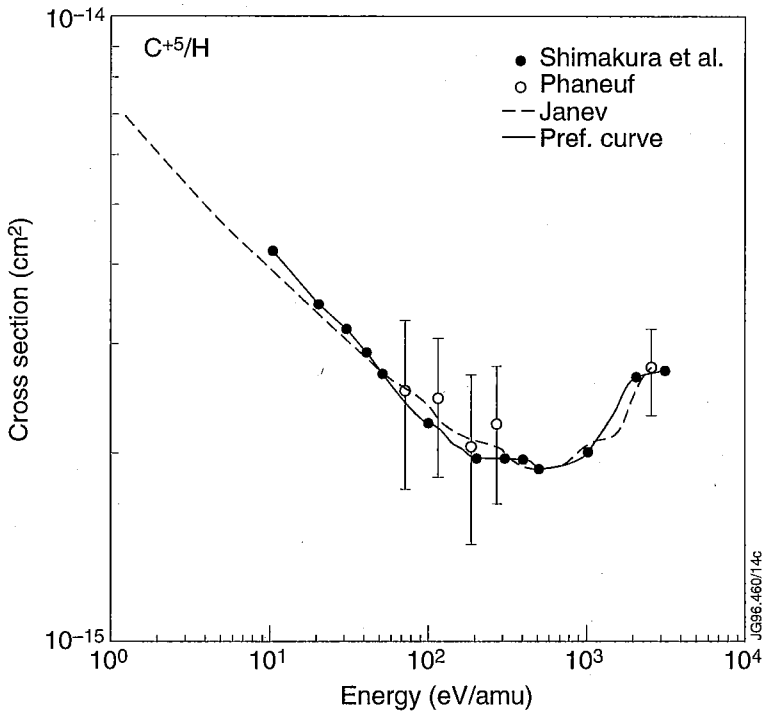

Figure 3.15: Total electron capture cross sections for C^{+5}/H collisions and preferred curve through the data.

used for the calculation of the charge exchange rate coefficients (see Chapter 8) for this reaction.

C^{+6}/H:

For the reaction:

$$C^{+6} + H \longrightarrow C^{+5}(1s\ nl) + H^{+} \tag{3.32}$$

total charge transfer cross sections have been assembled from experimental and theoretical data in the compilation by Janev [73]. For this reaction the total cross section data were taken from the critical assessment by Phaneuf et al. [74] (and references therein).

State selective electron capture cross sections into nl-subshells of C^{+5} were also assembled, from the calculations of Green et al. [75], Fritsch and Lin [76] and Kimura and Lin [77]. The dominant process is electron capture into $n = 4$ states of C^{+5} ions. Green et al. used MO calculations to calculate nl state selective cross sections for capture into $n = 3, 4, 5$ in the energy range 13 eV-27 keV/amu. Since data for capture into $n = 3$ are obtained for $E \geq 1.3$ keV/amu, they are not of interest for this work and were not used here. Fritsch and Lin calculated electron

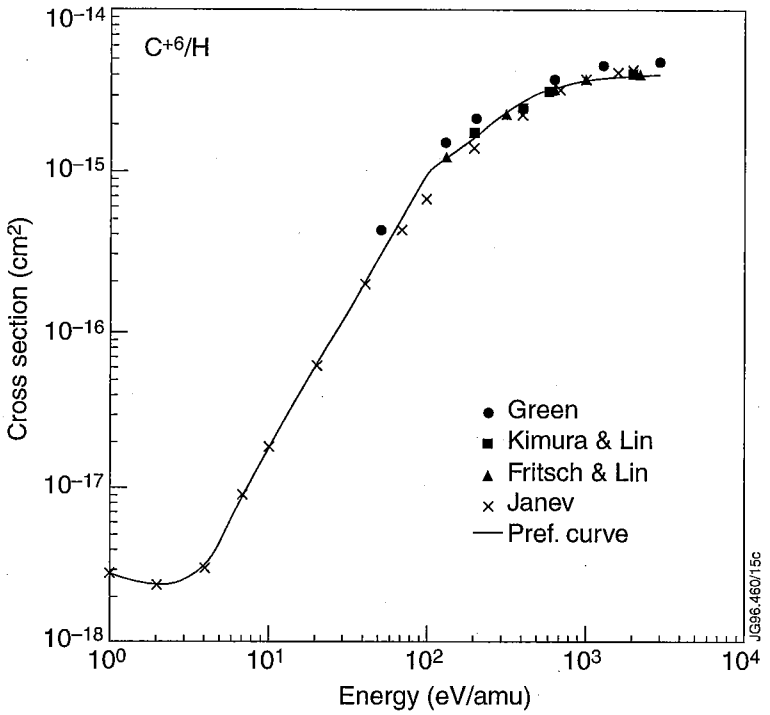

Figure 3.16: Total electron capture cross sections for C^{+6}/H collisions and preferred curve through the data.

capture cross sections into $n = 4, 5$ l-subshells in the energy range 0.1-30 kev/amu using AO. Kimura and Lin used a unified treatment calculation, which combines the features of the AO and MO expansion, using the most suitable basis sets in each portion of the configuration space during the collision. Cross sections were calculated in the energy range 0.2-4 keV/amu. The calculated total cross sections from different methods are in good agreement, as shown in Fig. 3.16 and agree with the experimental data (not shown in the plot, but contained in the recommended data by Janev). However, the MO calculations of Green et al. predict more capture into $n = 5$ states than the AO and unified treatment calculations. This difference is maximum in the 100-200 eV/amu energy range and is of the order of a factor 6 to 10.

For the work of this thesis, state selective cross sections for capture into $n = 4, 5$, $\sigma_n = \sum_l \sigma_{nl}$, were used to calculate effective charge exchange emissivity coefficients for C^{+5} ions with bundle-n collisional radiative calculations. The preferred curve through the cross section data for capture into $n = 5$ was chosen to lie between the MO and AO/unified treatment calculations. Instead, the calculated cross sections for capture into $C^{+5}(n = 4)$ from the various sources are in good agreement.

3.3 Radiated Power Loss

In this Section the theory for the calculation of the total power radiated by fusion plasmas is briefly reviewed. In general, radiation appears in the form of line radiation, recombination continuum and bremsstrahlung. In divertor/SOL plasmas radiation is emitted predominantly in the form of line radiation.

3.3.1 Radiated Power Loss Coefficients

The power radiated per unit volume by ions of type A^{+z} can be written as:

$$Total\ radiated\ power\ = n_e n(A^{+z}) P(A^{+z}) \qquad [Wm^{-3}] \tag{3.33}$$

with $P(A^{+z})$ the power loss coefficient $[Wm^3]$, which sums over the entire spectrum of emitted frequencies [78]. In optically thin plasmas the radiation is emitted in three forms, line radiation, recombination continuum and bremsstrahlung, arising from bound-bound, free-bound and free-free electron transitions in the fields of positive ions. Since for each of the three forms radiation is emitted following a collision between an electron and the ion (with the exception of charge exchange of impurities with neutral hydrogen), the total radiated power density from ion A^{+z} can be written as:

$$n_e n(A^{+z}) P(A^{+z}) = n_e n(A^{+z})[P_{LT}(A^{+z}) + P_{RB}(A^{+z}) + \frac{n_H}{n_e} P_{RC}(A^{+z})] \tag{3.34}$$

where P_{LT} is the total line power coefficient from excitation mostly within low-level states, P_{RB} is a composite coefficient which sums cascade, recombination radiation, dielectronic stabilization and bremsstrahlung contributions and P_{RC} is the charge exchange recombination power coefficient for charge exchange with neutral hydrogen.

The line power loss is the sum over all possible lines arising from ion A^{+z} due to excitation. This is expressed as:

$$P_{LT}(A^{+z}, \sigma) = \sum_{i,j} (n_i A_{i \to j}) \frac{hc}{\lambda_{i,j}} \tag{3.35}$$

where n_i is the upper level in the transition $i \to j$ and $hc/\lambda_{i,j}$ is the energy difference between levels i, j.

In the collisional radiative calculation the total line power coefficients are calculated in the metastable resolved picture (see Section 3.4) by multiplying the effective

excitation emission coefficient by the transition energy and by summing over all radiative transitions:

$$P_{LT}(A^{+z},\sigma) = \sum_{i,j} \frac{hc}{\lambda_{i,j}} q_{eff}^{exc}(\lambda_{i,j},\sigma) \tag{3.36}$$

where $q_{eff}^{exc}(\lambda_{i,j},\sigma)$ is the effective emission coefficient due to excitation to level i of metastable σ (see Section 3.4.2). Since excitation rates decrease rapidly to higher quantum shells ($\sim 1/n^3$), only excitations to the first few quantum shells contribute significantly to the total line power, with most of the power being radiated out of the resonance lines of a given ion. The calculation used to produce the total line power coefficients is the projection/expansion calculation and is extensively described in [37]. It involves the projection of bundle-n S matrices for the high level populations on the low level set of LS coupling states. The level set for this calculation includes LS resolved terms up to a maximum quantum shell, typically n_{max} = 3,4 or 5 and bundle-n S quantum shells from $n_{max}+1$ up to $n = 500$.

Unresolved line power coefficients are also produced, because only in this form are the total line power coefficients compatible with the transport code calculations, which do not include the capability of following independently the metastable states and ground states of the various ionic species (see Chapter 6). The unresolved coefficients are obtained by bundling the metastable resolved line power coefficients, assuming quasi-static equilibrium between metastable and ground state populations:

$$P_{LT}(A^{+z}) = \sum_{\sigma} P_{LT}(A^{+z},\sigma) \left(\frac{n^{(z)}(\sigma)}{n_{TOT}^{(z)}} \right)^{eq} \tag{3.37}$$

with:

$$n_{TOT}^{(z)} = n(1)[1 + \sum_{\sigma \neq 1} \left(\frac{n(\sigma)}{n(1)} \right)] \tag{3.38}$$

where $(n^{(z)}(\sigma)/n^{(z)}(1))$ is the σ-metastable/ground population fraction of ion A^{+z}, $(n_{TOT}^{(z)})^{eq}$ is the total equilibrium population of ion A^{+z}, $P_{LT}(A^{+z},\sigma)$ are the metastable resolved collisional radiative line power coefficients and $P_{LT}(A^{+z})$ is the collisional radiative equilibrium total line power coefficient, which assumes the metastable populations in quasi-static equilibrium with the ground state population.

The composite recombination-bremsstrahlung power coefficient is expressed as:

$$P_{RB} = P_B(\gamma,z) + \sum_{\rho} [P_{RR}(\gamma \rightarrow \rho, z) + P_{RS}(\gamma \rightarrow \rho, z) + P_{RC}(\gamma \rightarrow \rho, z)] \tag{3.39}$$

with P_B, P_{RR}, P_{RS} and P_{RC} the bremsstrahlung, radiative recombination, dielectronic stabilization and recombination cascade radiated power loss coefficients [37].

3.3.2 Radiated Power Loss Functions

Having identified the mechanisms that lead to radiated power loss by ions of type A^{+z}, it is possible to define, following [39], [78], the radiated power loss function for element A as:

$$P(A) = \sum_{z=0}^{Z_0} \frac{n(A^{+z})}{n(A)} P(A^{+z}) \tag{3.40}$$

with:

$$n(A) = \sum_{z=0}^{Z_0} n(A^{+z}) \tag{3.41}$$

$$n(A^{+z}) = \sum_{\sigma} n(A^{+z}, \sigma) \tag{3.42}$$

$$P(A^{+z}) = \sum_{\sigma} P(A^{+z}, \sigma) \frac{n(A^{+z}, \sigma)}{n(A^{+z})}. \tag{3.43}$$

The calculation of $P(A^{+z})$ was described in the previous section. In order to obtain the power loss function, the fractional stage abundances $n(A^{+z})/n(A)$ of element A are required. These depend on the time history of the plasma, that is are a function of time, temperature and density. For illustration, let's consider the simplest situation, that of ionization balance:

$$\frac{n(A^{+z+1})}{n(A^{+z})} = \frac{S_{CR}^{z}}{\alpha_{CR}^{z+1}} \tag{3.44}$$

obtained from the solution of the time dependent ionization balance equations for each impurity charge state:

$$\frac{dn(A^{+z})}{dt} = n_e n(A^{+(z-1)}) S_{CR}^{z-1} - n_e n(A^{+z})(S_{CR}^{z} + \alpha_{CR}^{z}) + n_e n(A^{+(z+1)}) \alpha_{CR}^{z+1}. \tag{3.45}$$

The fractional abundances are obtained from the collisional dielectronic ionization and recombination coefficients S_{CR} and α_{CR}, which are described in the following Section. The equilibrium solution applies to those situations in which the plasma parameters change on longer time scales than those required for the ions to reach their steady state of ionization equilibrium. Then, the distribution of the population fractions depends mostly on temperature and very slightly on density. This situation does not apply to the more complex dynamics characteristic of divertor plasmas, where impurity ions, in traversing the divertor plasma volume, experience rapidly varying plasma conditions (strong T_e and n_e gradients) and therefore do not have sufficient time to reach equilibrium. However, this example is used here to

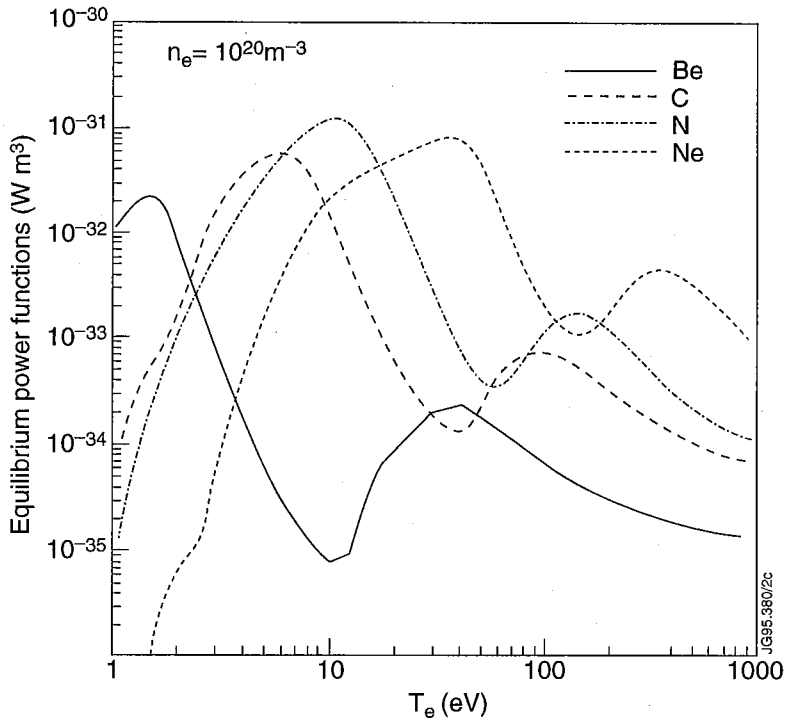

Figure 3.17: Equilibrium radiated power loss functions for Be, C, N and Ne (from ADAS).

outline some characteristic features of the power loss function. Fig. 3.17 shows the equilibrium power loss functions for various impurity elements that are of particular interest for impurity transport studies in the JET divertor. The 2-peak shape of the power loss function reflects the atomic shell structure and the dominant line power. The peak at lower temperature is due to the contribution of the $n = 2$ shell ions (mostly Be-like and Li-like), while the higher temperature peak is due to radiation from He-like and H-like ions. The minimum between the two peaks corresponds to the large energy difference existing between the single electron shell ($2s$ for Li-like ions) and the closed shell state ($1s^2$ for He-like).

3.4 The Collisional Radiative Model

It is clear from the discussion in the previous sections of this Chapter that the heaviest task for atomic physics calculations rests on the evaluation of the excited state populations of the atomic and ionic species in the plasma. The impurity fractional abundances, $n(A^{+z})/n(A)$, or, more specifically, the densities $n(A^{+z})$ for $z = 0, ...Z_0$, are the solutions of the time dependent ionization balance equations

(eq. 3.45). These require a full model encompassing both the atomic physics and the plasma transport. The models aimed at calculating these distributions are discussed in Chapter 6 of this thesis.

This Section presents an overview of the collisional-radiative population calculations that have been carried out or used - within ADAS [38], [37] - for this thesis work. Essentially, these calculations produce all the atomic coefficients necessary for spectral emission and radiation studies, as well as for studies of impurity and plasma transport.

3.4.1 The Statistical Balance Equations

Let's consider an ion A^{+z} in its i-th excited state, with population density n_i. The rate of change of n_i is given by:

$$\begin{aligned}\frac{dn_i}{dt} = & - \left(\sum_{i>j} A_{ij} + \sum_{j\neq i} n_e q^e_{ij} + \sum_{j\neq i} n_p q^p_{ij} + \sum_{\gamma} n_e S_{i\gamma} + \sum_{\gamma} A^a_{i\gamma} \right) n_i + \\ & \left(\sum_{j>i} A_{ji} + \sum_{j\neq i} n_e q^e_{ji} + \sum_{j\neq i} n_p q^p_{ji} \right) n_j + \\ & \sum_{\gamma} \left(\alpha^D_{i\gamma} + \alpha^R_{i\gamma} + n_e \alpha^T_{i\gamma} + \frac{n_H}{n_e} \alpha^{CX}_{i\gamma} \right) n_e n^{z+1}_{\gamma} \end{aligned} \tag{3.46}$$

with the various coefficients as defined in the previous sections. Collisional-radiative matrix elements are introduced [38] as:

$$C_{ij} = -(A_{ij} + n_e q^e_{ji} + n_p q^p_{ji}) \qquad for \;\; j \neq i \tag{3.47}$$

with C_{ii} the total losses from level n_i:

$$C_{ii} = \left(\sum_{i>j} A_{ij} + \sum_{j\neq i} n_e q^e_{ij} + \sum_{j\neq i} n_p q^p_{ij} + \sum_{\gamma} n_e S_{i\gamma} + \sum_{\gamma} A^a_{i\gamma} \right) \tag{3.48}$$

and define a composite recombination coefficient, written as:

$$r_{i\gamma} = \alpha^D_{i\gamma} + \alpha^R_{i\gamma} + n_e \alpha^T_{i\gamma} + \frac{n_H}{n_e} \alpha^{CX}_{i\gamma}. \tag{3.49}$$

Then eq. 3.46 can be rewritten in matrix form:

$$\frac{dn_i}{dt} = -\sum_j C_{ij} n_j + \sum_{\gamma} r_{i\gamma} n_e n^{+(z+1)}_{\gamma}. \tag{3.50}$$

In order to solve this set of equations some simplifications are introduced. The first simplification concerns the time required by the various level populations of the ion to reach a steady state [39], [78]. These relaxation times can vary significantly from level to level and consequently allow for a classification of the levels of the ions into two groups, namely metastable states (ground and metastable levels) and excited states. For the excited states the time constant associated with relaxation to the ground/metastable state is of the order of the radiative lifetime: $\tau_{es} \leq A^{-1}$ and has a typical value of $\tau_{es} \sim 10^{-8}$ s. The ground level of an ion is stable against radiative decay, thus its lifetime is governed by collisional processes with the other species present in the plasma (mainly electrons), hence $\tau_g \sim (n_e \sum_{coll} q_{coll})^{-1}$, where the sum is taken over all the collisional processes considered and q_{coll} is the rate coefficient for the specific process. τ_g is of the order of the plasma transport time scales. Metastable levels can be grouped with ground levels. In fact, radiative decay of metastable states may occur only via slow forbidden transitions and this implies that their lifetimes are much longer than those of the ordinary excited levels. However, the electron density plays a fundamental role in this case, influencing the balance between radiative decay and collisional decay of the metastables. For conditions typical of divertor plasmas ($n_e \sim 10^{18} - 10^{21} m^{-3}$), metastable levels have lifetimes comparable to those of the ground levels. Hence: $\tau_{es} \ll \tau_m \leq \tau_g$. These considerations allow to assume the excited states in statistical equilibrium with the instantaneous ground and metastable state populations. This is called a *quasi-static approximation.* Thus:

$$\frac{dn_i}{dt} = 0 \qquad for \;\; i > m \tag{3.51}$$

$$\frac{dn_\sigma}{dt} \neq 0 \qquad for \;\; 1 \leq \sigma \leq m \tag{3.52}$$

where σ is the metastable state index and m is the number of metastables in ion A^{+z}. Thus, the population densities of the excited levels can be evaluated locally, relative to the population density of the ground state and of the metastable states separately. Only local conditions of plasma electron and ion densities and temperatures are required in this calculation. Ground and metastable levels, by contrast, require the solution of time dependent transport equations, which depend on global parameters and specific plasma boundary conditions (see Chapter 6). That is, a separation of the equations of statistical balance is introduced into (i) those establishing the stage of ionization and (ii) those describing excitation leading to the emission of radiation.

The infinite set of differential equations describing the level populations reduces to an infinite set of ordinary equations plus a small number of differential equations. Further assumptions are required to solve this system. At densities relevant to divertor plasma operation (up to $n_e \sim 10^{21} m^{-3}$), where radiative processes dominate over collisions, excited levels are considerably depopulated with respect to ground and metastable levels. The latter give the main contribution to the total population of the ion. Very highly excited states can then be excluded from the statistical balance equations. For spectroscopic applications, the remaining excited levels can be conveniently grouped in two different sets [78], [37]: the set of low excited levels, which include the upper states of most relevant spectrum lines and therefore require careful calculation; the set of highly excited levels, generally introducing corrections to account for cascading, redistributive collisions, stepwise ionization losses and recombination processes.

a) Excited Level Populations

By partitioning eq. 3.50 so that the subset of equations related to the metastable levels are excluded, and combining with eq. 3.51, the equilibrium populations of the excited states are obtained:

$$\sum_j C_{ij} n_j = -\sum_\sigma C_{i\sigma} n_\sigma + \sum_\gamma r_{i\gamma} n_\gamma^{+(z+1)} n_e \tag{3.53}$$

where the subscripts i, j denote just the normal excited states $i, j > \sigma$, and multiplying by the inverse matrix C_{ji}^{-1}:

$$n_j = -\sum_\sigma \left(\sum_i C_{ji}^{-1} C_{i\sigma} / n_e \right) n_\sigma n_e + \sum_\gamma \left(\sum_i C_{ji}^{-1} r_{i\gamma} \right) n_\gamma^{+(z+1)} n_e \tag{3.54}$$

where the first and second term on the righthandside express the contributions to the population of level j from excitation from metastables σ's and recombination from parents γ's, respectively.

b) Metastable Populations

If it is assumed that the metastable populations have reached steady state equilibrium with the ground state populations, then by setting the time derivatives to zero, $dn_\sigma/dt = 0$, their populations can be derived in a way equivalent to that described for the ordinary excited states. In equilibrium, the total ion population is then described by equation 3.38.

The validity of this assumption in the context of impurity transport studies in divertor plasmas is discussed in Chapter 7. Comparisons of theoretical estimates with spectroscopic measurements are given and the issue of the need of following metastable and ground state populations independently in the transport codes is addressed.

3.4.2 Spectral Line Intensities and Photon Emissivity Coefficients

From a spectroscopic point of view, the intensity of a spectral line, I_λ, of wavelength λ, emitted in the transition from upper level i to lower level j of an ion A^{+z} is given by:

$$I_\lambda = \frac{1}{4\pi}\int_{LOS} \epsilon_{i\to j}(\lambda)dl \qquad [ph/cm^2 sr\ s] \tag{3.55}$$

where the integral is over the spectroscopic line of sight, LOS, through the plasma, of a given spectrometer, and $\epsilon_{i\to j}(\lambda)$ is the emission due to spontaneous radiative decay between the bound atomic states i, j of energy difference $hc/\lambda = \Delta E_{ij}$:

$$\epsilon_{i\to j} = n_i A_{ij}. \tag{3.56}$$

From the expressions of the excited state populations derived in the previous Section, it is possible to express the spectral emissivities (and intensities) in terms of effective emissivity coefficients:

$$\begin{aligned}\epsilon_{i\to j}(\lambda) = \quad & \sum_\sigma n_e n_\sigma q^{exc}_{eff}(i\to j,\sigma) + n_e n^{z+1} q^{rec}_{eff}(i\to j,\sigma) + \\ & n_H n^{z+1} q^{CX}_{eff}(i\to j,\sigma)\end{aligned} \tag{3.57}$$

where q^{exc}_{eff}, q^{rec}_{eff} and q^{CX}_{eff} are the effective emissivity coefficients for electron impact excitation, recombination and charge exchange with neutral hydrogen. This formulation is particularly suited for transport studies, since it allows the expression of spectral intensities in terms of the product of the densities of the colliding species (described by the transport equations) and of atomic coefficients dependent only on local plasma parameters. Moreover, in this way the separate contributions from excitation, recombination and charge exchange to the spectral emission are immediately recognized.

3.4.3 The Effective Collisional Radiative Coefficients

The collisional radiative ionization and recombination rate coefficients, already introduced in previous sections, are derived from the solution of the statistical balance equations. Consider for simplicity an ion with single ground (σ) and parent (γ) levels. The rate of change of the ground state population of A^{+z} is given by:

$$\frac{dn_\sigma}{dt} = -\sum_j C_{\sigma j} n_j - C_{\sigma\sigma} n_\sigma + r_{\sigma\gamma} n_e n_\gamma^{z+1}. \tag{3.58}$$

Substituting for n_j, using eq. 3.54 for the excited states:

$$\begin{aligned}\frac{dn_\sigma}{dt} = & - \left(C_{\sigma\sigma}/n_e + \sum_j C_{\sigma j} \left(\sum_i C_{ji}^{-1} C_{i\sigma} \right) /n_e \right) n_e n_\sigma + \\ & \left(r_{\sigma\gamma} - \sum_j C_{j\sigma} \left(\sum_i C_{ji}^{-1} r_{i\gamma} \right) \right) n_e n_\gamma^{z+1}\end{aligned} \tag{3.59}$$

from which the effective ionization and recombination coefficients are deduced:

$$S_{\sigma\gamma}^{eff} = \left(C_{\sigma\sigma} + \sum_j C_{\sigma j} \left(\sum_i C_{ji}^{-1} C_{i\sigma} \right) \right) /n_e \tag{3.60}$$

$$\alpha_{\gamma\sigma}^{eff} = r_{\sigma\gamma} - \sum_j C_{\sigma j} \left(\sum_i C_{ji}^{-1} r_{i\gamma} \right). \tag{3.61}$$

The effective (or collisional radiative) ionization rate coefficient $S_{\sigma\gamma}^{eff}$ describes the growth of ion A^{+z} due to ionization from metastable σ of ion A^{+z} and due to ionization via multistep excitation through the excited states of ion A^{+z}. The effective recombination rate $\alpha_{\gamma\sigma}^{eff}$ describes the rate at which electrons are captured from ion $A^{+(z+1)}$, but only including those electrons that cascade to state σ of A^{+z}. The calculation is then generalized to the case of multiple parents in ion $A^{+(z+1)}$ and multiple metastables of A^{+z}, but it is not reported here so as to avoid unnecessary formulation (see however [37] for the explicit formulation).

Chapter 4

Description and Characterization of the JET Divertor Double SPRED Spectrometer

4.1 Introduction

The SPRED spectrometer has been widely used as a routine impurity monitor in tokamak plasmas in the past 10-15 years [79]. This multichannel spectrometer allows the observation of impurity spectra with moderate spectral and time resolution, but over a wide VUV wavelength range, which, depending on the grating used, spans from 100 to 1700 Å. It therefore provides an essential tool for the study of the ionic composition and radiation losses of intrinsic as well as injected impurities in thermonuclear plasmas. A characteristic feature of this instrument is the use of a toroidal holographically recorded, aberration corrected diffraction grating (Jobin Yvon Optical Systems), operating at an angle of incidence of about 71°. The holographically recorded grooves are curved to place the desired spectrum on a flat focal field, without loss of resolution, to accommodate the use of multichannel detectors. The curvature of the grooves and the toroidal substrate dimensions are adjusted to correct aberrations. At JET a SPRED spectrometer, with a near horizontal line of sight close to the vessel midplane, has been used for several years to monitor VUV emission from the bulk plasma. In this Chapter the characteristics and performance are described of a new double SPRED spectrometer, installed and commissioned during the MkI campaign, for the observation of VUV radiation from the diver-

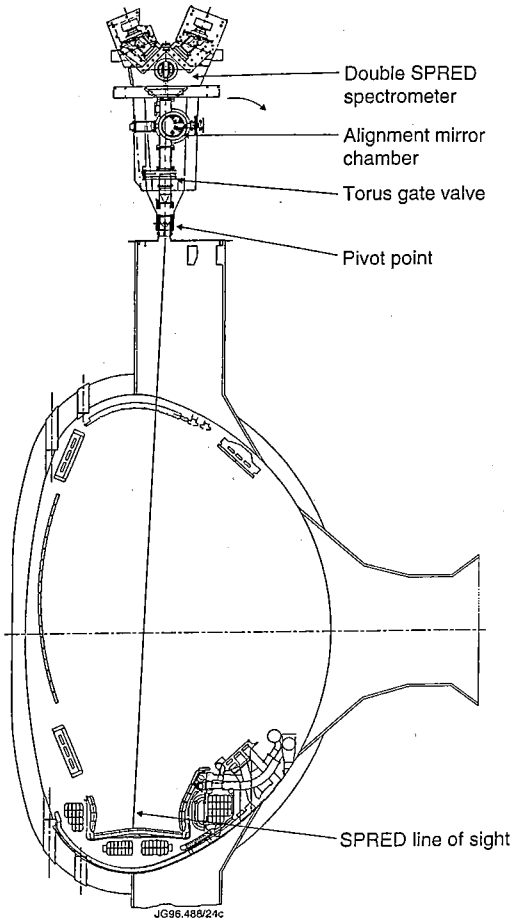

Figure 4.1: Setup of the divertor double SPRED spectrometer on octant 6 of the JET tokamak. The solid line represents the fixed line of sight to the inner MkI divertor target used during the 1995 operation period.

tor region. The absolute calibration of the double SPRED system is presented in Chapter 5.

4.2 Experimental Setup

Fig. 4.1 shows the position of the double SPRED spectrometer on the JET tokamak and its viewing line through the main plasma to the divertor region. A fixed line-of-sight to the inner divertor, also shown in Fig. 4.1, was maintained throughout the 1995 experimental campaign. The spectrometer is mounted on a frame and its components, shown in Fig. 4.2, are situated within a 350 kg forged stainless steel block, whose function is to shield the detectors from neutrons and γ-rays produced during high performance pulses.

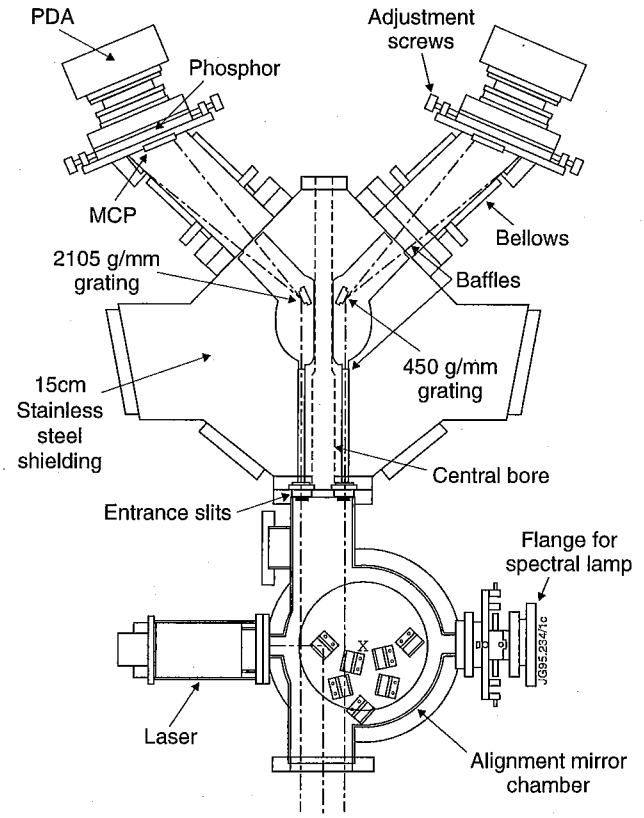

Figure 4.2: Cross section of the double SPRED system, showing its various components.

A central bore through the SPRED chamber provides an additional viewing line for another light collection system. In the later phase of the experimental campaign this was used by an optical fibre connected to a visible spectrometer to obtain an *in situ* absolute intensity calibration of the VUV spectrometers using branching ratio techniques (see Chapter 5). The system is also equipped with a chamber containing several mirrors on a rotary table for the alignment of the spectrometer assembly (see Fig. 4.2). Unfortunately, the design of such chamber was not complete at the time of operation, so that the alignment system could not be used during the 1995 experimental campaign.

4.3 Optical Arrangement

The divertor double SPRED spectrometer (McPherson, model 251 M2) consists of two independent SPRED spectrometers with fixed gratings, mounted in the same vacuum chamber (see Fig. 4.2). The lines-of-sight of the spectrometers are inclined at

0.6° to one another and meet at the divertor target plates. The two toroidal gratings (Jobin-Yvon Optical Systems, type IV) [80] have groove densities of 450 g/mm and 2105 g/mm, covering the spectral range 180-1450 Å and 140-440 Å respectively. The gratings are platinum coated, in contrast to similar gratings used in other fusion experiments [79], [81], [82] which are gold coated. Platinum was chosen, in the original design of the spectrometer, as a acoating material due to its higher reflectance than gold in the 400-1400 Å wavelength region [83], [84]. The dimensions of the two SPRED spectrometers are identical, except for the angles of incidence at the grating. The 2105 g/mm grating, in fact, operates at an angle of incidence 1.3° larger than that used for the 450 g/mm grating, 70.6°, in order to measure spectra down to about 150 Å. The entrance slits of the spectrometers are 25 μm wide (radial direction) and 2.5 mm high (toroidal direction) and a mask between the entrance slit and the grating defines the illuminated ruled area of the grating to 3 mm $\times$ 18 mm. An additional mask between the grating and the detector provides a screen against possible wall reflections. The spatial resolution of the two spectrometers in the poloidal and toroidal direction of the tokamak at the divertor plates is determined by the effective grating dimension, the distance of the grating to the entrance slit and the distance between the entrance slit and the divertor tiles. This results in a spatial resolution of 13.7 cm (450-SPRED) and 12.8 cm (2105-SPRED) poloidally and of 12.9 cm toroidally. In order to obtain improved resolution in the poloidal direction, a set of masks with different widths, to be positioned between the entrance slit and the grating, were manufactured. Due to the tight time scales of the experiments, these masks could not be installed and the data collected during the 1995 experimental campaign are characterized by the resolutions reported above.

4.4 Detectors

Each SPRED spectrometer is equipped with a multichannel detector system (MDS) consisting of a microchannel plate (MCP) image intensifier [85] and of a phosphor screen coupled to a 2048-pixel linear self-scanning Si photodiode array (PDA) by a fiber-optic image conduit. A schematic of the detector is shown in Fig. 4.3.

An incident UV photon is converted into a photoelectron and amplified by the MCP. When leaving the MCP the electrons are accelerated and focused onto the phosphor screen, where they are converted into visible photons. The phosphor screen

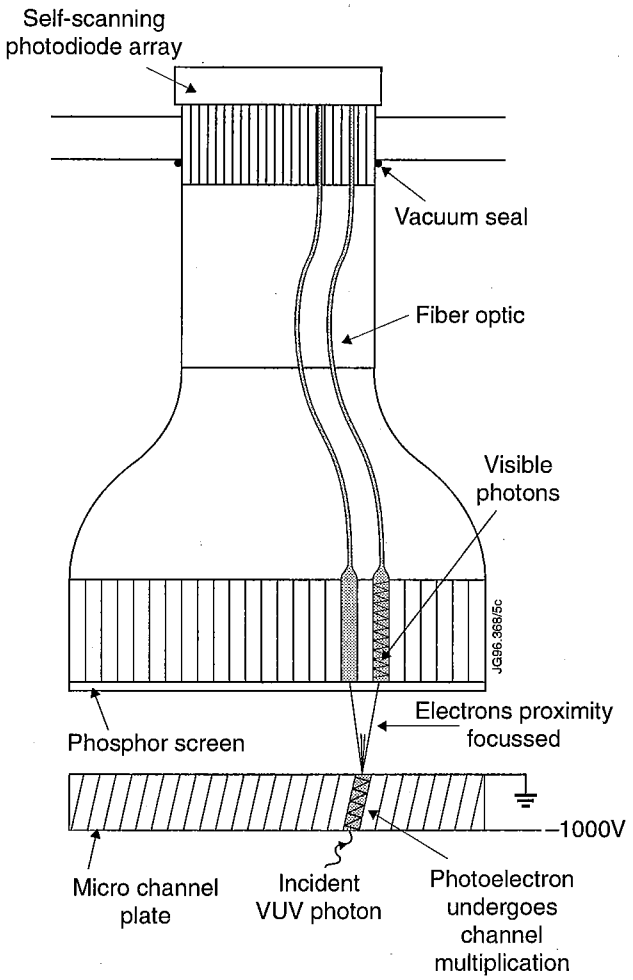

Figure 4.3: Schematic of the multichannel detector system for the JET divertor double SPRED spectrometer. VUV photons hitting the input face of the microchannel plate (MCP) produce photoelectrons that are amplified within the MCP channels. On exit, the electrons are accelerated and proximity focused onto the phosphor screen, where they are converted into visible photons. The phosphor screen is coupled to a 2048-pixel photodiode array (PDA) by a fiber optic image conduit.

is deposited on the face of a fiber optic image conduit, which allows the PDA to be located entirely outside the vacuum.

The MCPs are of the HOT, Galileo Electro Optics Corporation type, designed to produce a high output current [86]. The single channels have a diameter of 10 μm with center to center spacing of 12 μm and are biased by 8° to the input face in order to suppress ion feedback at the output of the channels. In fact, as the MCP gain increases, so does the probability of producing positive ions in the high charge density region at the output of the MCP channel [85]. Such ions are produced by electron collisions with residual gas molecules desorbed from the channel walls under

electron bombardment and can produce additional secondary electrons resulting in a degradation of the MCP performance. Biasing the channels with respect to the MCP input face suppresses the ion feedback and allows operation of the single channels at higher gain. The maximum MCP operation voltage is 1 kV, at which level the gain is about 10^4 electrons/photon. The front surface of the MCP is coated with CuI to enhance its sensitivity especially at long wavelength. The MCP - phosphor system can be operated in two modes. In the first, the MCP output is grounded and up to -1 kV is applied to the input, while the phosphor has a positive potential, typically 4 kV. In this case the MCP is sensitive to photons and positive ions. This mode can have the disadvantage that if, for instance, ion gauges are used to monitor the spectrometer vacuum, occasional intensity spikes occur due to the detection of ions from the gauges. This problem can be avoided by operating the detector in the electron and photon detection mode, that is by grounding the input of the MCP and applying up to +1 kV to the output. The positive phosphor potential then has to be increased by the output MCP voltage. As expected, the two modes exhibit the same sensitivity to VUV photons. Since ion gauges were not used on the spectrometer, the positive ion mode was chosen. This is the safer option, since it avoids any possibility of the voltage between the MCP and phosphor being raised to 5 kV, as would happen if the MCP alone were to trip in the electron mode with the present electronic circuits. No evidence of spikes due to positive ions coming from the plasma has been found during the experimental period.

The self scanning PDAs consist of two 1024-diode arrays (Reticon RL2048S), each diode being 25 μm wide and 2.5 mm high. Thus the full array has twice the width of the diode arrays previously used in the SPRED instruments, with the result of increasing the number of pixels in a spectral feature by about a factor 1.6 [86]. This has been achieved without any loss of information that would result from a 'dead space' between the two diode arrays. In combination with an MCP with an active area of 52 mm diameter and a straight fiber-optic conduit, the increased width of the PDA allows a 51.2 mm wide area of the dispersion plane to be imaged onto the detector, instead of the 40 mm flat focal field used in earlier SPRED designs. Consequently, the spectral coverage is increased by more than 300 Å for the 450-SPRED and by over 50 Å for the 2105-SPRED, with respect to the standard SPRED design. In addition, two bellows provide the adjustment of the detector head assembly, which can be moved 10 mm in either direction along the SPRED focal

plane, to modify the observed spectral range. The adjustment translates to about 250 Å and 50 Å in either direction for the 450-and 2105-SPREDs, respectively. During the 1995 experimental campaign the 2105-SPRED detector was set in the direction of the longer wavelengths, thus covering the region 140-440 Å. Only a slight degradation of the spectral resolution above 350 Å was noticed (see Section 4.6). The 450-SPRED detector was also set towards the longer wavelengths, to cover the range 180-1450 Å. This arrangement is suited for measurements of spectral emission from carbon impurities (although the C IV resonance transition falls outside the wavelength range), therefore missing the Be III resonance line at 100 Å, which is usually measured by SPRED systems with 450 g/mm grating.

The PDA transforms the visible photons into electrical signals, which are integrated and counted. It is controlled and read by an optical multichannel analyser that allows flexible control over the PDA operation. The analogue signals are digitized by a single 16 bit analogue to digital converter with a readout speed of 5 μs/pixel, thus resulting in a minimum readout time of about 11 ms per spectrum.

The gain characteristics of the MCPs and phosphor screens were first measured in the laboratory using a hollow cathode light source (McPherson, model 629) [87]. This source produces high intensity lines in the UV range in a stable discharge. It has to be noted, however, that the source was not absolutely calibrated and therefore no absolute intensity calibration of the two SPREDs could be performed in the laboratory. The SPRED housing was pumped down to 10^{-7} mbar and the plasma source aligned. Helium was used for the discharge and the He II 304 Å line was used to determine the dependance of the detectors sensitivity on MCP and phosphor voltage. The plasma source is of asymmetric design, with the gas inlet on one side and the anode on the other. The operational regime was of I = 100-300 mA, V = 500-1100 V and gas pressure p = 0.4 mbar. The source was aligned to the entrance slit of the spectrometer using a HeNe laser. The source was then attached to a special flange on the SPRED housing, such that the laser beam went through its He inlet along the axis of the cathode onto the apex of the grating. The lamp operated reliably and produced a continuous discharge throughout the tests.

The operational regime of the detectors was reached slowly to prevent damaging of the components. Fig. 4.4 shows the normalized MCP gain characteristics. They show the expected exponential behaviour with the voltage applied to the MCP. The reproducibility of independent measurements for each spectrometer was better than

5% for voltages above 800 V. Measurements from different regions of the MCP gave similar results. It is noted that the absolute gains of the two MCPs were found to be different. The MCP gain of the 450-SPRED was measured to be 18 times that of the 2105-SPRED during the tests performed in the laboratory, using the hollow cathode source run with identical parameters. Cross calibrations performed during plasma operations indicated that this factor had fallen to about 4 for the He II 304 Å line. These comparisons include the effect of the gratings and other detector components. The observed change in time may indicate that the MCPs were being progressively conditioned.

The MCPs gain characteristics can be described by the following power laws [86]:

$$450 - SPRED : G_{MCP} = 4.812 \times 10^{-46} U_{MCP}^{15.144} \quad (4.1)$$

$$2105 - SPRED : G_{MCP} = 2.177 \times 10^{-37} U_{MCP}^{12.216} \quad (4.2)$$

where the MCP voltage, U_{MCP}, is in volts. The MCP gain characteristic of the JET single SPRED, with a horizontal viewing line, is similar [88] and is also shown in Fig. 4.4. The gain characteristics of the phosphor screens were measured by the same technique and are shown in Fig. 4.5. Only a small variation was found between the two SPRED detectors. The phosphor gain depends weakly on the applied voltage and is approximated by a second order polynomial:

$$450 - SPRED : G_{Ph} = 9.93 \times 10^{-4} - 5.81 \times 10^{-5} U_{Ph} + 7.73 \times 10^{-8} U_{Ph}^2 \quad (4.3)$$

$$2105 - SPRED : G_{Ph} = 9.68 \times 10^{-2} - 1.74 \times 10^{-4} U_{Ph} + 1.00 \times 10^{-7} U_{Ph}^2. \quad (4.4)$$

In order to optimize the overall detector gain it is therefore necessary to operate the MCPs at the highest possible voltage. So as to avoid risking electrical breakdown, voltage limits for the double SPRED were set to 1 kV for the MCPs and 4 kV for the phosphor screens. The limit on the phosphor voltage is also determined by the separation of the MCPs and phosphor surfaces (see Section 4.6).

4.5 Wavelength Calibration and Linear Dispersion

The wavelength calibration was determined empirically, by a least square fit of the pixel position of the peak of a set of spectral lines, for which the wavelength had been

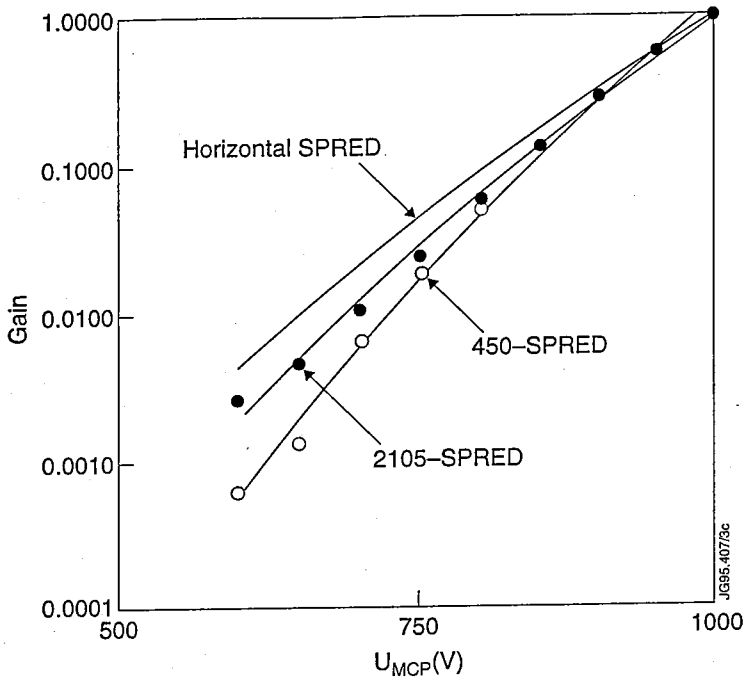

Figure 4.4: Normalized MCP gain characteristics as a function of applied MCP voltage for the 450- and 2105-SPRED. The gain is normalized to that at 1000 V. The measured data (circles) are compared with the fit to a power law (solid lines), see eq. 4.1, 4.2. Also shown, for comparison, is the MCP gain characteristic of the JET single SPRED with a horizontal viewing line [88].

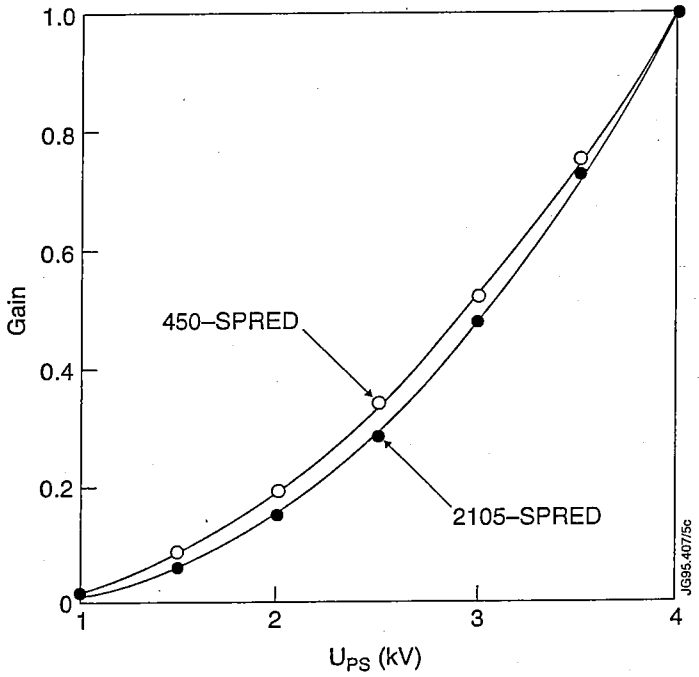

Figure 4.5: Normalized phosphor gain characteristcs as a function of applied phosphor voltage for the 450- and 2105-SPRED. The gain is normalized to that at 4000 V. The measured data (circles) are compared with the fit to a second order polynomial (solid lines), see eq. 4.3, 4.4.

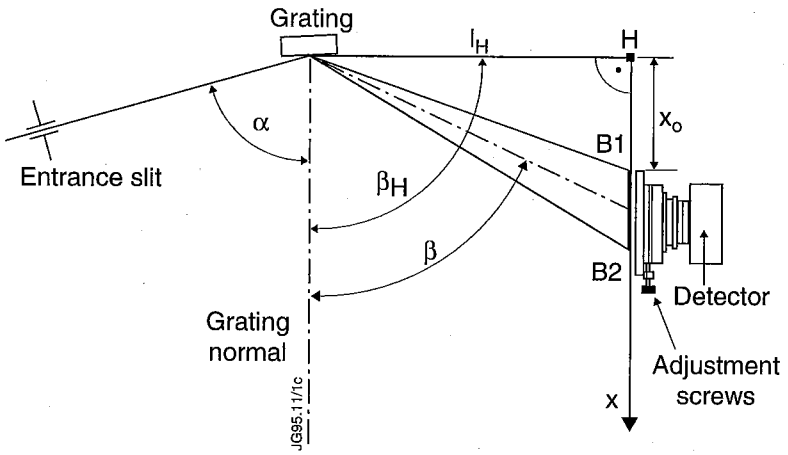

Figure 4.6: Optical arrangement of grating and detector for each SPRED spectrometer. α and β are the angles of incidence and reflection with respect to the grating normal and x_0 marks the position of the first pixel of the detector on the flat focal field.

identified, to the analytical function derived by combining the grating equation, for a reflection grating, with the geometry of the optical arrangement of the spectrometer. The latter is shown in Fig. 4.6. The theoretical wavelength is given by the grating equation as a function of the angles of incidence and diffraction:

$$k\lambda = \frac{1}{N}(\sin\alpha - \sin\beta) \tag{4.5}$$

where k is the diffraction order, N the groove density, α and β the angles between grating normal and incident and reflected light. The angle of incidence to the center of the grating is fixed and β can be deduced by the geometry of the system. Considering a projection of the PDA onto the plane of the flat focal field, the position of a pixel p onto the PDA is projected at a distance x from the origin of the focal field:

$$x = x_0 + p\Delta x \tag{4.6}$$

where x_0 is the position of the first pixel of the detector onto the focal field and Δx is the width of the pixel projected onto the flat focal field ($\Delta x = 0.025$ mm). The flat focal field lies between B1 and B2. Eq. 4.6 can be rewritten in terms of the diffraction angle β:

$$x = l_H \tan(\beta_H - \beta) \tag{4.7}$$

where l_H is the distance from the grating apex to the plane of the focal field and β_H is the angle between l_H and the grating normal. By substituting into equation 4.5:

$$\lambda(p) = \frac{1}{kN}[\sin\alpha - \sin(\beta_H - \arctan(\frac{x_0 + p\Delta x}{l_H}))]. \tag{4.8}$$

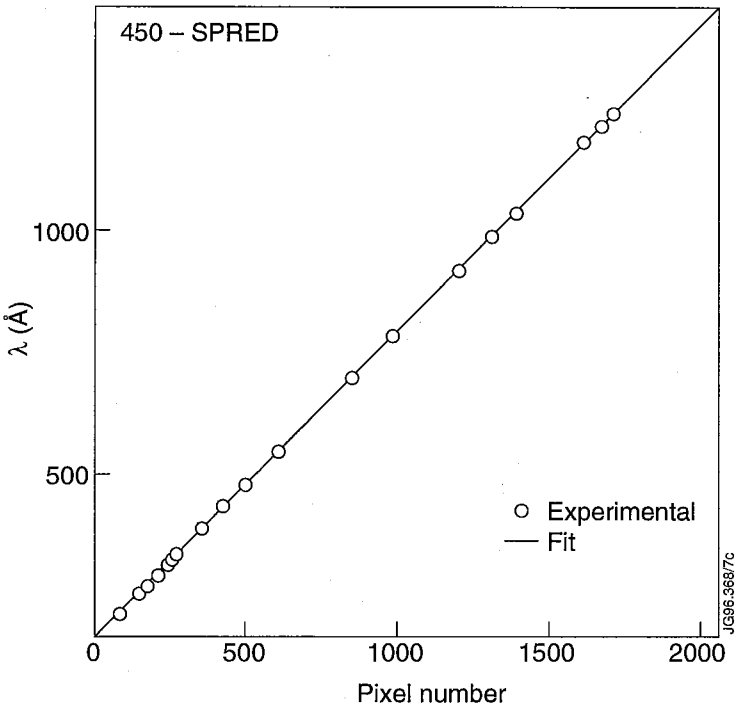

Figure 4.7: Wavelength calibration for the 450-SPRED spectrometer. The solid line represents the fit of the theoretical curve to the experimental data (open circles).

This analytical relation, fitted to the experimental values of $\lambda(p)$, can be used to confirm some of the geometrical measurements of the spectrometer. Since the detector can be moved along the x-axis, x_0 is a free parameter. Figures 4.7 and 4.8 show the fitted functions for the 450- and 2105-SPRED, respectively, using x_0, α and β_H as free parameters.

The theoretical linear dispersion is given by the derivative of equation 4.8:

$$\frac{d\lambda}{dp} = \frac{1}{kN}\frac{l_H \Delta x}{l_H^2 + (x_0 + p\Delta x)^2}\cos(\beta_H - \arctan(\frac{x_0 + p\Delta x}{l_H})). \tag{4.9}$$

It is evaluated using the parameters obtained from the fit to equation 4.8 and is plotted in Fig. 4.9. Also plotted in Fig. 4.9 is the experimental dispersion, obtained by dividing the wavelength difference of neighbouring lines by their pixel difference, which results in some scatter around the theoretical curve.

4.6 Spectral Resolution

The most important contribution to the spectral line shape in spectra recorded with the SPRED spectrometers is the instrument function [89]. This depends critically

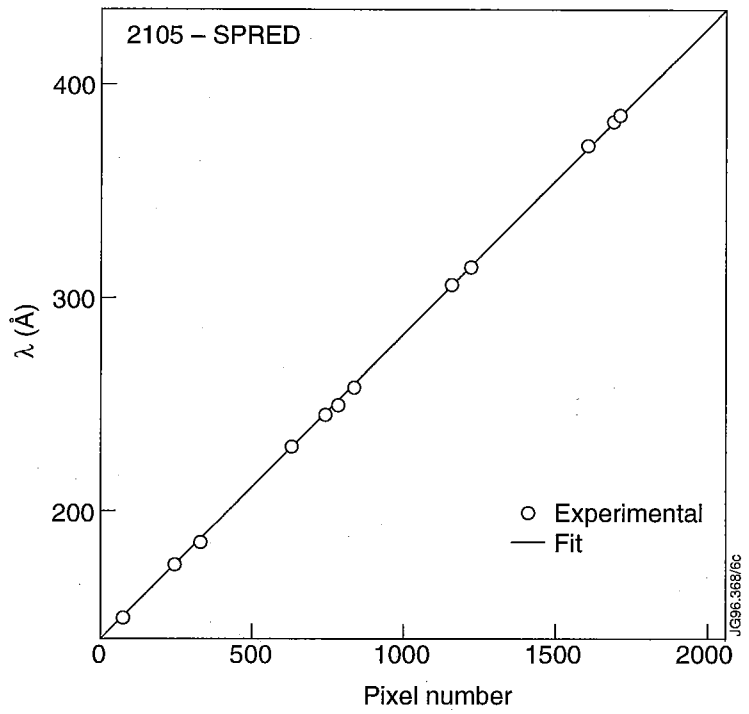

Figure 4.8: Wavelength calibration for the 2105-SPRED spectrometer. The solid line represents the fit of the theoretical curve to the experimental data (open circles).

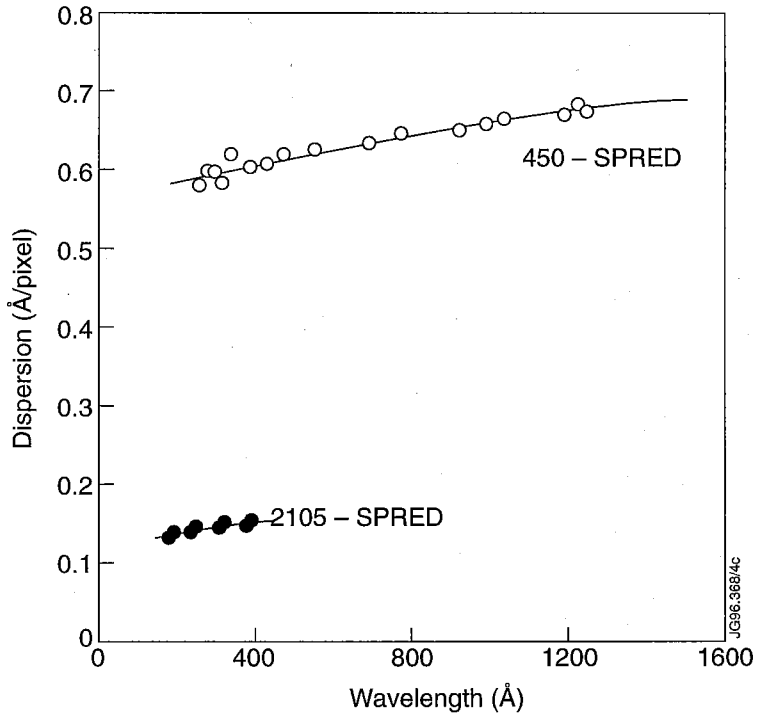

Figure 4.9: Linear dispersion for the 450- and 2105-SPRED spectrometers: experimental data (circles) and theoretical curve (solid line), evaluated using the parameters from the fits of Fig. 4.7 and Fig. 4.8. The experimental dispersion is obtained by dividing the wavelength difference of adjacent lines by their pixel difference.

on the illumination of the grating. The hollow cathode source used for testing the spectrometers in the laboratory does not fill the acceptance angle of the spectrometer. This results in a narrower line profile than when an extended source, such as the JET plasma, is used. For this reason, spectra obtained during JET plasma pulses have been used to determine the spectral resolution and its dependence on wavelength. The spectral lines used have been selected so as to avoid line blending which would result in spuriously broad lines. The chosen lines are fitted using a function that can represent a Gaussian, a Lorentzian or a mixture of the two [90], depending on a profile parameter, γ:

$$F(p) = \frac{1}{(1 + (2^{\gamma^2} - 1)(2\frac{p-p_0}{\Delta p_{1/2}})^2)^{\frac{1}{\gamma^2}}} \tag{4.10}$$

where $\Delta p_{1/2}$ is the FWHM in pixels. As γ is varied, the line shape $F(p)$ changes continuously from a Gaussian ($\gamma \to 0$) to a Lorentzian ($\gamma = 1$). For both SPRED systems the line profile was found to be closer to a Gaussian, in the case of the 2105-SPRED almost reaching a pure Gaussian shape at the shorter wavelengths, where the line width is narrowest. The spectral resolution is defined according to the Rayleigh criterion [91], that states that two spectral lines of equal intensity are resolved in nth order if the nth order maximum of the first line occurs at the first zero just beyond the nth maximum of the second line. The spectral resolution is plotted in Fig. 4.10 and is comparable to the values found for other SPRED instruments [92]. The measured spectral resolution for the 450-SPRED shows no clear dependence on wavelength and no loss of resolution due to the extended focal field used can be observed. In contrast, there is evidence of some deterioration in the resolution above 350 Å for the 2105-SPRED. The spectral resolution for the 2105-SPRED is about a factor of 4 better than that of the 450-SPRED.

The spectral resolution also depends on the voltages applied to the detectors. The most significant component to the instrument function is due to the charge spreading in the gap between the phosphor and the MCP. The diameter of such charge cloud scales by $s/\sqrt{V_{ph}}$, where s is the MCP-phosphor gap and V_{ph} the MCP-phosphor potential difference. A broadening of the line width from the hollow cathode light source of up to 40% was observed in the laboratory when the phosphor voltage was reduced from 4 to 0.5 kV. Given that a high phosphor voltage is required to maximize the gain factor, the operating parameters have to balance

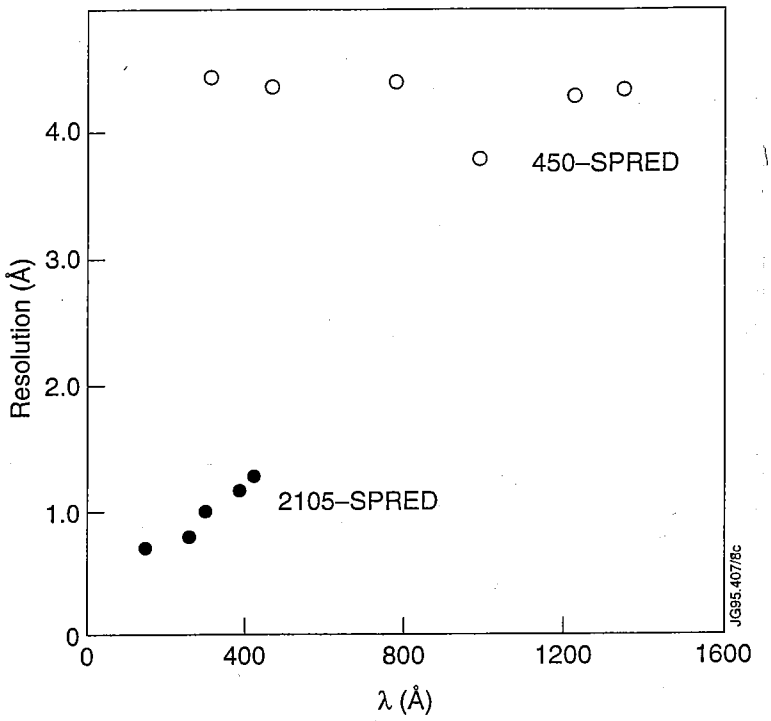

Figure 4.10: Spectral resolution for the 450-SPRED (open circles) and for the 2105-SPRED (full circles). There is evidence of some deterioration in the resolution above 350 Å for the 2105-SPRED, while the 450-SPRED shows no loss of resolution due to the extended flat focal field.

the requirement of high resolution and high gain factor without risking electrical breakdown. Consequently, the detectors were operated at a voltage of 4 kV, with a fixed MCP-phosphor gap of 0.75 mm. Reducing the MCP voltage from 1000 to 650 V results in a small improvement in the resolution of about 5%.

Chapter 5

Absolute Intensity Calibration of the JET Divertor Double SPRED

5.1 Introduction

The absolute intensity calibration of the double SPRED spectrometer constitutes the fundamental basis for the analysis of the measured VUV emission and, consequently, for all interpretative work in this thesis that involves modelling of transport and radiation characteristics of the impurities and hydrogenic species.

The double SPRED was absolutely calibrated *in situ* using branching ratio techniques. A measurement of the brightness of two spectrum lines that originate from the same upper level establishes the relative sensitivity of the spectrometer at the two wavelengths. If the sensitivity is known absolutely at one of the wavelengths, such measurements are used to calibrate the instrument at the other wavelength, where absolute calibration may otherwise be difficult, e.g. in the vacuum UV [93]. This method has the advantage that all the *in situ* optics and restrictions in the viewline of the system to be calibrated are included in the calibration. However, the number of suitable line pairs is limited, necessitating interpolations over considerable wavelength intervals, leading to unavoidable uncertainties in the calibration curve. It will be clear from the following discussion that this was indeed one of the main problems encountered during the calibration of the JET divertor double SPRED. This practical difficulty originates from the fact that although in principle many line pairs are available for a branching ratio calibration, the choice is limited, either because of accidental overlap with other lines or because one or the other of

Ion	λ_{VUV} (Å)	VUV Transition	λ_{Vis} (Å)	Visible Transition
He II	243.0	4 - 1	4685.7	4 - 3
C IV	312.4	$3p\ ^2P - 2s\ ^2S$	5801.5	$3p\ ^2P - 3s\ ^2S$
D I	1025.44	3 -1	6561.0	3 -2

Table 5.1: Pure branching ratios used for the sensitivity calibration of the JET divertor double SPRED spectrometer.

the pair components is too weak to measure.

5.2 Branching Ratios

As described in Chapter 4, the double SPRED system allowed for an additional line of sight, parallel to those of the two VUV spectrometers, through the central bore of the SPRED housing. A 30 mm diameter lens telescope was mounted on top of the double SPRED and connected via optical fibre to a high resolution Czerny Turner spectrometer in the JET diagnostic hall. The combined set of grating, detector, fibre optic and telescopic system was calibrated against a standard tungsten lamp, ignoring possible vignetting and without the window which provides the vacuum interface between the VUV spectrometer and the telescope. The vacuum window was assumed to transmit 100 % of the light (which is accurate to few percent) and therefore to introduce no modification to the calibration.

The calibration curve for the JET divertor SPRED spectrometers was constructed using two sets of branching ratios. The first set includes line pairs from pure branches, with one line measured in the visible region and the other, to be calibrated, in the vacuum UV. Table. 5.1 contains a list of such line pairs. Within this category, the very limited number of usable line pairs is noted. The most important reason was the complexity of the spectra emitted from a cold and dense divertor plasma (by contrast to emission e.g. from the inner wall) where the brightest lines emerge from a substrate of many weaker lines. These weak lines, especially for the 450 g/mm grating, cannot be resolved due to the low spectral resolution. This implied that several line pairs had to be excluded because the VUV component could not be isolated. An example of this situation is the C III line pair 574.3 Å ($2s2p\ ^1P - 2s3d\ ^1D$)/5696.0 Å ($2s3p\ ^1P - 2s3d\ ^1D$). These characteristics of the spectra also prevented the use of branching ratios where both lines are emitted in the vacuum UV. Examples of

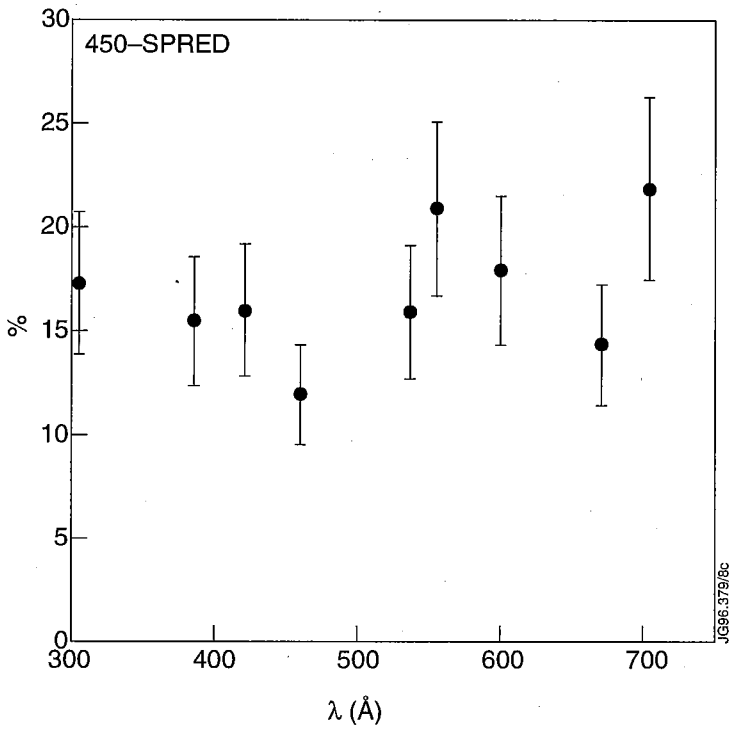

Figure 5.1: Intensity of second order spectrum lines (counts/s) relative to the first order as a function of wavelength in first order for the 450 g/mm SPRED.

this situation are the C IV 244.9 Å ($2s\ ^2S - 4p\ ^2P$)/1198.6 Å ($3d\ ^2D - 4p\ ^2P$) and 296.9 Å ($2p\ ^2P - 4s\ ^2S$)/1230.5 Å ($3p\ ^2P - 4s\ ^2S$) line pairs, where in both cases the lines at longer wavelength could not be measured, even with a longer integration time.

For the 450 g/mm SPRED a further complication emerged from the fact that this grating does not suppress the second diffraction order to acceptable levels. Therefore additional blending occurs. Fig. 5.1 shows the intensity (in counts/s) of lines in second order relative to the same lines in first order as a function of wavelength in first order. As a consequence of this, e.g. the long wavelength component in the C IV line pair 289.2 Å ($2p\ ^2P - 4d\ ^2D$)/1108.0 Å ($3p\ ^2P - 4d\ ^2D$) could not be resolved from the O IV 554.4 Å ($2s^2 2p\ ^2P - 2s 2p^2\ ^2P$) line in second order and this branching ratio had to be abandoned. In other cases it was rather the poor spectral resolution that limited the choice of possible line pairs, e.g. in the case of the N IV 247.2 Å ($2s^2\ ^1S - 2s3p\ ^1P$)/6383 Å ($2s3s\ ^1S - 2s3p\ ^1P$) branch (where the UV line is blended with the much stronger N V line at 247.66 Å ($2p\ ^2P - 3d\ ^3D$)) or in that of the N V 162.6 Å ($2s\ ^2S - 4p\ ^2P$) /764.8 Å ($3d\ ^2D - 4p\ ^2P$) branch (where the 3d-4p line cannot be resolved from the much stronger N IV resonance line at

Ion	λ_1 (Å)	Transition 1	λ_2 (Å)	Transition 2
C IV	312.4	$3p\ ^2P - 2s\ ^2S$	384.1	$3d\ ^2D - 2p\ ^2P$
C IV	312.4	$3p\ ^2P - 2s\ ^2S$	419.6	$3s\ ^2S - 2p\ ^2P$

Table 5.2: Modelled line ratios used for the sensitivity calibration of the JET divertor double SPRED spectrometer.

765.1 Å ($2s^2\ ^1S - 2s2p\ ^1P$)). Finally, all oxygen line pairs had to be excluded since, in contrast to other fusion machines, oxygen levels have been considerably reduced in JET since the introduction of Be evaporation. Thus O line intensitites were too weak to measure in the visible range.

Given the scarcity of usable branching ratios with visible lines, it was necessary to supplement the findings with a second set of line ratios with different upper levels that are measured by the double SPRED. For such ratios modelling of the different upper level population in the transition must be invoked. Let I_1 and I_2 be the intensities of two such lines, measured by one SPRED spectrometer, then:

$$\frac{I_1}{I_2} = \frac{c(\lambda_1)\int_{LOS} S(\lambda_1)dl}{c(\lambda_2)\int_{LOS} S(\lambda_2)dl} = \frac{c(\lambda_1)S(\lambda_1)}{c(\lambda_2)S(\lambda_2)} = \frac{n_k}{n_{k'}}\frac{A_{k\to l}}{A_{k'\to l'}} \tag{5.1}$$

where $c(\lambda_1)$ and $c(\lambda_2)$ are the calibration factors at the measured wavelengths λ_1 and λ_2 in the transitions $k \to l$ and $k' \to l'$, with upper level densities n_k and $n_{k'}$, and spontaneous emission coefficients $A_{k\to l}$ and $A_{k'\to l'}$ respectively. $S(\lambda_1)$ and $S(\lambda_2)$ are the signal strengths (counts/s) recorded by the PDA. If the ratio $n_k/n_{k'}$ is insensitive to electron density and temperature variations in regimes typical of divertor plasma operation, then the ratio of the signal strengths at the two wavelengths is a measure of the relative sensitivity $c(\lambda_1)/c(\lambda_2)$. Table 5.2 contains a list of such line ratios.

A study of the C IV $n(3p)/n(3d)$ and $n(3p)/n(3s)$ excited level density ratios is shown in Fig. 5.2 and 5.3 for a range of electron temperatures and densities relevant to the MkI divertor operation. These results were obtained using the collisional radiative population model described in Chapter 3. It can be seen that in both cases the strongest variation occurs with electron temperature, but even this is well within the error bar of the absolute calibration points.

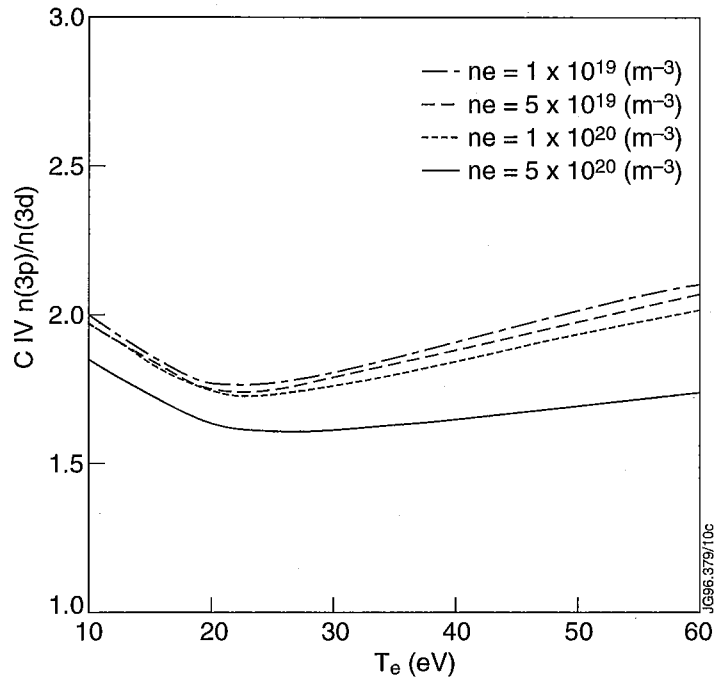

Figure 5.2: C IV $n(3p)/n(3d)$ ratio as a function of electron temperature in the divertor, for different electron densities.

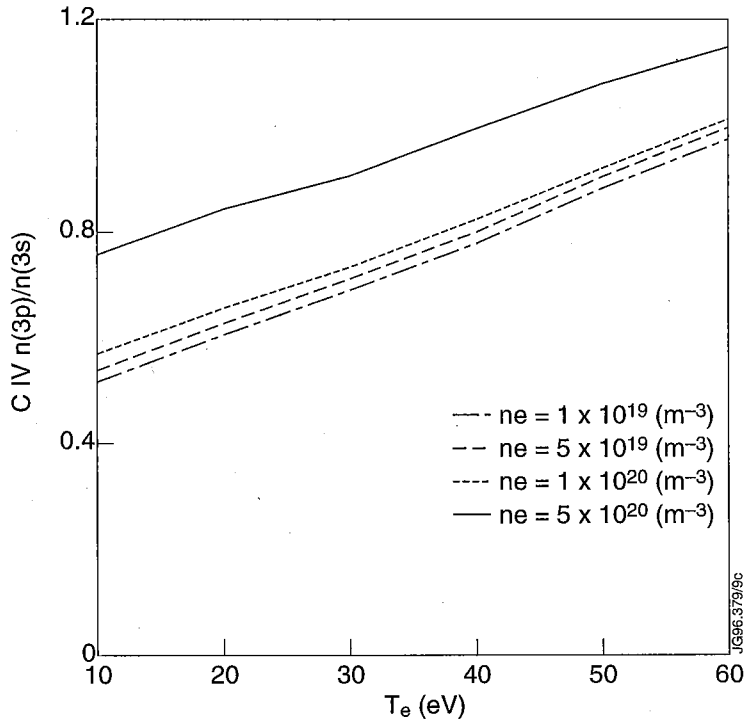

Figure 5.3: C IV $n(3p)/n(3s)$ ratio as a function of electron temperature in the divertor, for different electron densities.

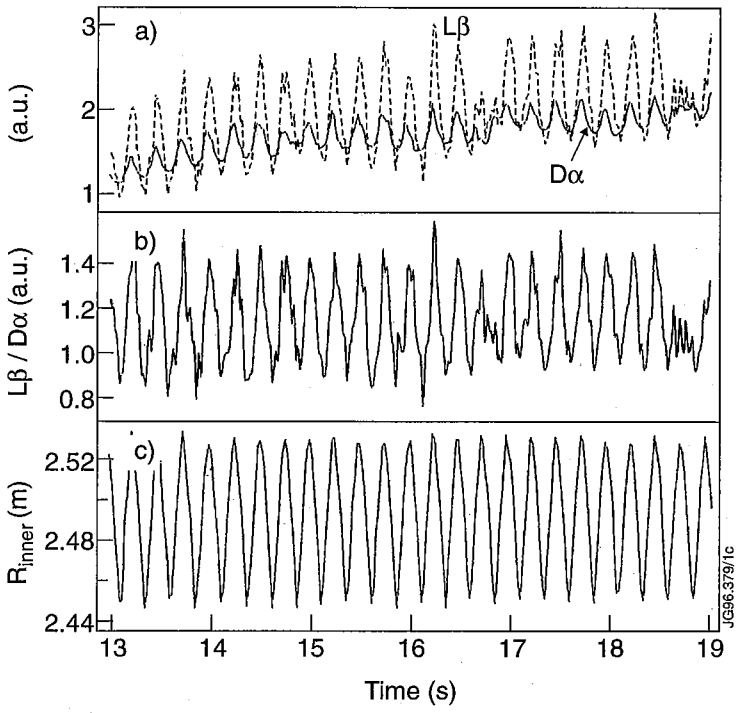

Figure 5.4: Deuterium L_β and D_α line intensities measured by the 450-SPRED and along the SPRED visible line of sight, respectively, for pulse 34765 (a); (b) ratio of L_β to D_α, showing the effect of the strike point sweeping (c) during the pulse.

5.3 Consistency of Calibration with other Divertor Diagnostics

Due to difficulties in the installation of the telescope, the acceptance cone of the visible system was larger than that of the VUV spectrometers. The consequence of such difference is exemplified in Fig. 5.4, where the ratio of L_β to D_α emission is plotted versus time for an Ohmic discharge with divertor configuration on the horizontal target. The effect of the sweeping of the (inner) strike point on the line ratio clearly shows that the VUV and visible systems are viewing different regions of the DI emission volume. This constitutes an important source of error in establishing the absolute sensitivity of the VUV spectrometers. For this reason, and in order to quantify a sudden loss in sensitivity in the visible system during operations, the reason of which could not be identified, the visible signals measured along the double SPRED line of sight were cross calibrated against those of other divertor visible spectroscopic diagnostics. These included a CCD camera viewing almost the whole of the horizontal divertor floor from the top of the vessel and a

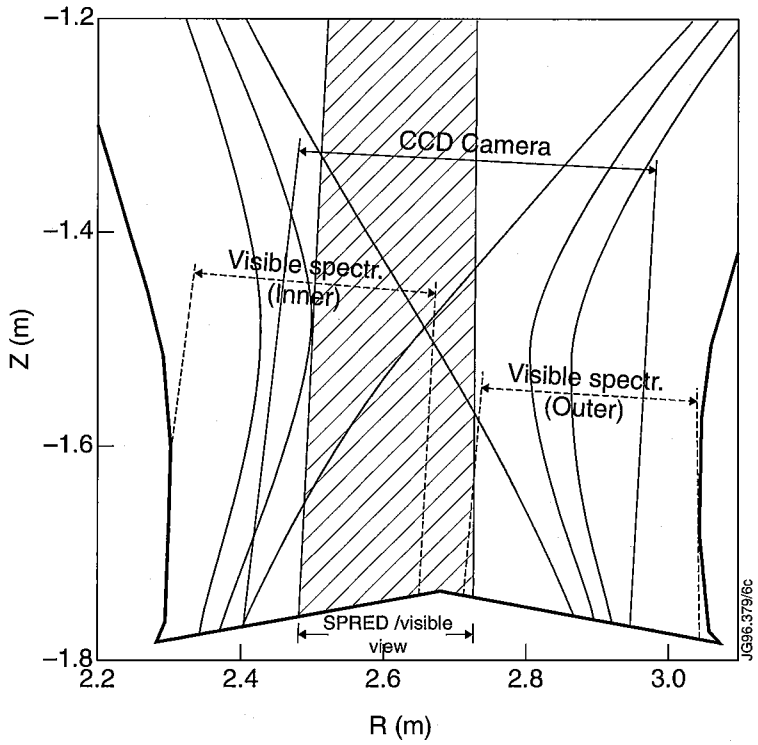

Figure 5.5: Cross section of the MkI divertor target with views of the CCD camera for D_α measurements and of the wide angle visible spectrometer. The SPRED/visible view is marked with dashed lines.

wide angle visible light collection system, equipped with narrow band interference filters and photomultiplier tubes, viewing the whole of the inner and outer divertor regions from two vertical lines of sight. Fig. 5.5 shows the view of such diagnostics in the divertor region.

The CCD camera provides emission profiles across the divertor target with high sampling rate (about 1ms) and 2.5mm spatial resolution at the target plates, so that an average of this profile over the viewing area of the other two diagnostics provides an effective method for cross calibration. This minimizes the uncertainties related to differences in the acceptance cones. Moreover, in this way the movement of the observed radiation layer, e.g. due to sweeping of the strike zones, and any change to the emission profile induced by transport is followed. To illustrate this, in Fig. 5.6 the D_α line intensity measured along the SPRED/visible line of sight is compared to its reconstruction from the average of the CCD camera emission profile for the Ohmic pulse 34859. A smoothing in time was performed, to account for the difference in time resolution between the two systems. It can be seen from Fig. 5.6 that the experimental D_α intensity from the SPRED/visible LOS is well reproduced. The

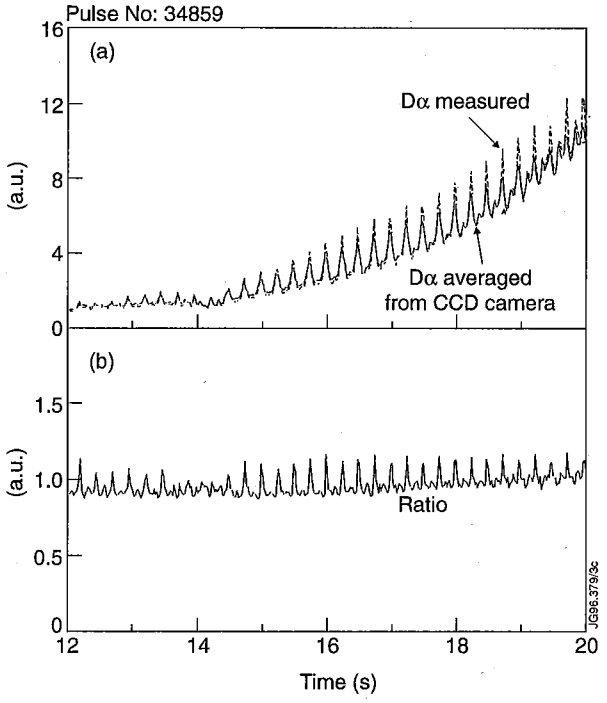

Figure 5.6: (a) Deuterium D_α line intensity measured along the visible line of sight of the double SPRED for pulse 34859 and CCD camera D_α emission profile averaged over the SPRED/visible acceptance cone; (b) ratio of the two signals.

oscillations in the ratio of the two signals are caused by the fact that the geometry of the SPRED/visible view, with respect to the CCD camera, cannot be perfectly reproduced. This introduces an uncertainty of 20% in the averaged signal. Fig. 5.7 shows two profiles measured by the CCD camera, for the same pulse, at the times corresponding to the limits of amplitude of the strike point sweeping, respectively.

Initially the D_α emission from the CCD camera and from the inner divertor view of the visible spectrometer were compared. This comparison has an intrinsic uncertainty, since the CCD camera's view is slightly narrower than that of the visible system (see Fig. 5.5). This difference is in fact sufficient to cause part or, for certain sweeping amplitudes or strike zone positions, the whole of the inner emissivity peak to disappear from the CCD camera's view (see Fig. 5.7). In addition, the calibrated D_α signal measured by the CCD camera was systematically a factor of three to four more intense than that measured by the visible spectrometer. This discrepancy has been identified as due to a calibration error of the CCD camera for D_α and recalibration of the system has recently been performed.

For these reasons, it was necessary to support the comparison by considering

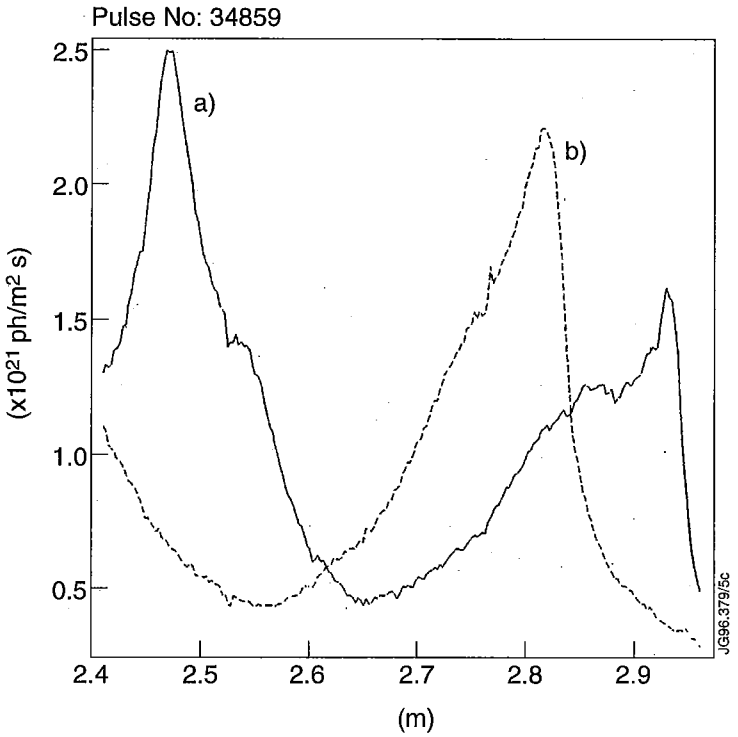

Figure 5.7: Deuterium D_α profiles measured by the CCD camera for the same pulse of Fig. 5.6 at the times corresponding to maximum (a) and minimum (b) amplitude of the strike point sweeping.

additional D_α measurements in the divertor. These were provided by the same visible light collection system described above, but along a discrete set of high spatial resolution vertical chords (with spot size of about 33 mm diameter at the divertor target), spaced across the divertor target as shown in Fig. 5.8. An average of the CCD camera D_α profile over each chord falling within the camera's view was then performed. By averaging this way, the problems with out-of-sight light are greatly diminished.

When comparing D_α emission from these divertor diagnostics, signals measured at different toroidal locations of the tokamak (the CCD camera, the visible spectrometer and the SPRED spectrometers are situated each in a different octant of the torus) were found to vary in different ways when neutral beam heating was applied. The reason for this is not yet clear. By contrast, during Ohmic discharges the temporal evolution of the D_α emission was exactly the same for all three diagnostics and therefore Ohmic discharges were chosen for the cross calibration.

The wide angle and the high resolution views of the visible spectrometer are internally consistent and their calibration disagrees with that of the CCD camera. The

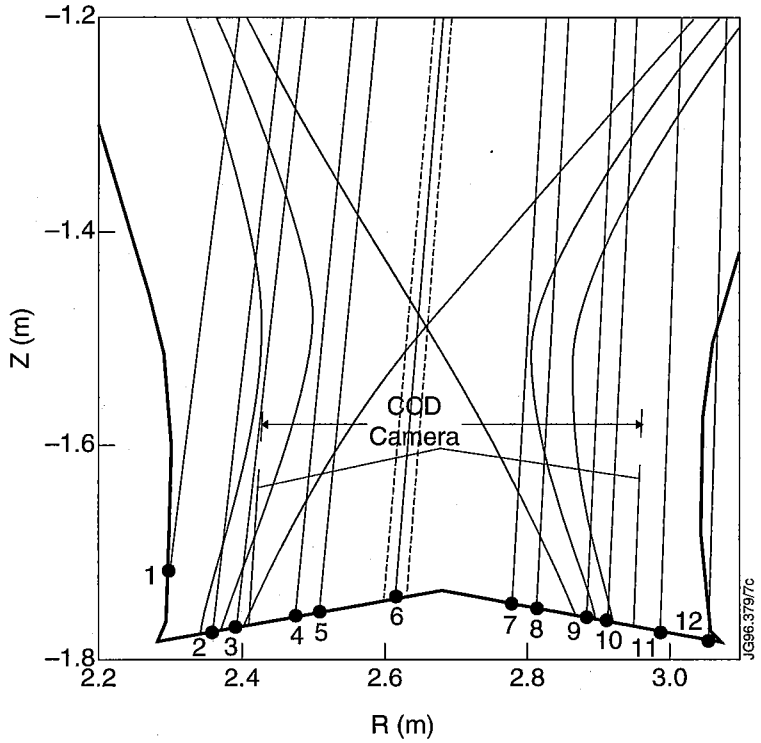

Figure 5.8: Divertor view of the twelve high spatial resolution vertical visible chords. The dashed lines, only shown for view no. 6, show the spatial resolution of the visible chords.

calibration from the visible spectrometer has been adopted and the CCD camera D_α intensity renormalized accordingly. An additional consistency check with Langmuir probe measurements supports the calibration of the visible spectrometer. That is, the ion flux to the divertor target plates measured by the Langmuir probes tends to agree with the flux derived from D_α measured with the visible spectrometer, but is significantly lower than that derived from the CCD camera measurements. The plasma ion influx Γ_{D+} is estimated from the D_α line intensity as:

$$\Gamma_{D+} = I_{D_\alpha} \cdot S/XB \tag{5.2}$$

where S/XB denotes the theoretical ionizations per photon for D_α emission and I_{D_α} is the measured D_α line intensity. This relation, valid in an ionizing plasma, no longer holds when the divertor plasma is strongly cooled and the density is increased. Thus, during detachment, a measurement of D_α intensity no longer constitutes an influx measurement.

The recalibrated CCD camera D_α profiles were then averaged over the acceptance cone of the 450-SPRED to obtain the calibration point at 1025.4 Å. In this way the uncertainty due to the different acceptance cones of the VUV and visible

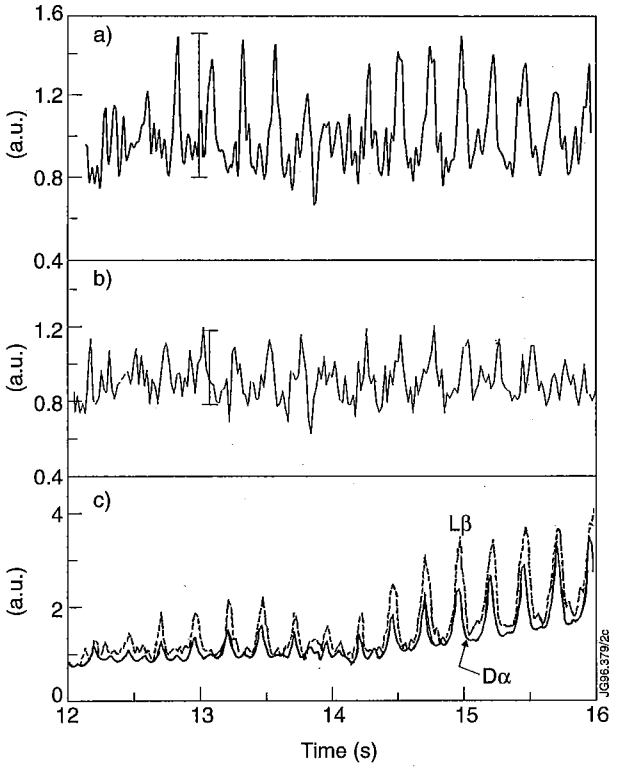

Figure 5.9: (a) Ratio of L_β intensity to D_α intensity measured along the SPRED/visible LOS and (b) ratio of L_β intensity to D_α profile averaged over the 450-SPRED acceptance cone for pulse 34859; (c) L_β intensity measured with the 450-SPRED and average of D_α emission profile measured with the CCD camera over 450-SPRED acceptance cone.

lines of sight is somewhat reduced. This is shown in Fig. 5.9 where the ratio of L_β intensity to D_α intensity measured along the SPRED/visible LOS (a) and the ratio of L_β intensity to D_α profile averaged over the 450-SPRED LOS (b) are compared for pulse 34859. The deviation from the mean value of the ratio is improved from about 30% to 20% when averaging the D_α profile. Since the error in the calibration of the visible spectrometer is 15% and the error in the cross calibration of the CCD camera is 20%, this results in an error in the VUV calibration point at 1025.4 Å of 35%.

Cross calibration at other wavelengths than D_α was obtained by comparison of visible bremsstrahlung emission. For this it is assumed that the baseline level measured by the SPRED/visible spectrometer at these wavelengths is dominated by continuum emission. The photon emissivity due to visible bremsstrahlung is expressed as:

$$\epsilon(\lambda)d\lambda = \frac{32\pi e^6}{3hc^3(4\pi\epsilon_0)^3}\frac{n_e^2 Z_{eff}}{T_e^{1/2}}\left(\frac{2\pi}{3m_e^3 e}\right)^{1/2}\lambda^{-1}e^{-\frac{hc}{\lambda e T_e}}g_{eff} \tag{5.3}$$

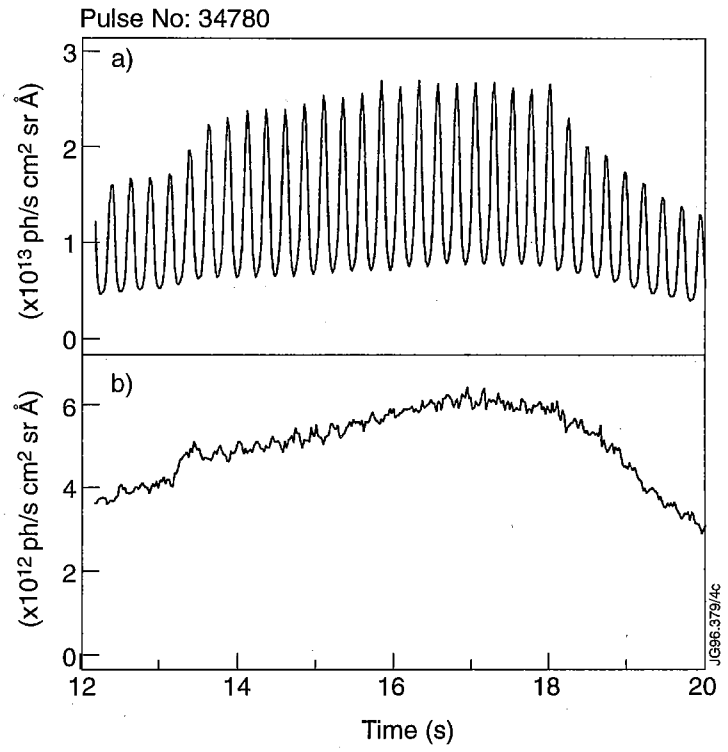

Figure 5.10: Visible bremsstrahlung emission for pulse 34780 measured by a vertical chord traversing the outer divertor region (a) and a chord which does not view the divertor (b). Emission from chord (a) shows strong sensitivity to the divertor density.

where e is the elementary charge, c the speed of light, h the Planck constant, m_e the electron mass, n_e the electron density, Z_{eff} the plasma effective charge, T_e the electron temperature, g_{ff} the free-free Gaunt factor [94]. At JET the continuum emission is measured in the line free region around $\lambda = 5235$ Å. The visible bremsstrahlung emission was scaled from 5235 Å according to eq. 5.3, to the wavelength of interest (see Table 1). For lines of sight crossing the divertor region, the visible bremsstrahlung emission is influenced by emission from the divertor volume at moderate to high electron densities, due to the n_e^2 dependence. This is shown in Fig. 5.10 for pulse 34780, where the continuum emission from a vertical chord traversing the outer divertor region (a) shows strong sensitivity to the strike point sweeping, while chord (b), which does not view the divertor, is immune to this effect. As long as lines of sight with the same geometry are considered, a cross calibration can be performed reliably using continuum emission from different divertor spectroscopic diagnostics.

The CCD camera view for bremsstrahlung is narrower than that for D_α and there are fewer high resolution visible chords allocated to bremsstrahlung measure-

ments than there are for D_α. Therefore cross calibration between the two systems was only possible for one view in the outer divertor. Contrary to the case of D_α, comparisons between the CCD camera and the visible system continuum measurements showed consistency of the two calibrations at this wavelength. The sensitivity of the SPRED/visible spectrometer at the wavelengths listed in Table 5.1 was thus renormalized to that of the CCD camera's continuum emission. Since the error in the calibration of the CCD camera is 15%, the error in the averaging of the bremsstrahlung signal onto the SPRED/visible acceptance cone is 20% and the error in the line ratio of VUV and visible/SPRED lines of sight is 30%, this results in an error of 40% in the calibration points at 243 Å and 312.4 Å.

The final consistency check of the SPRED spectrometers calibration was performed against radiated power measurements from a bolometer with a line of sight similar to that of the double SPRED. The good agreement between total radiated power, measured by the bolometer, and assembled total radiation from individual components from different radiators confirms the reliability of this VUV calibration. The spectroscopic study of radiation distributions in the MkI divertor is the subject of Chapter 7.

5.4 Comparison with Calibrations from other SPRED Systems

A comparison of the JET divertor double SPRED sensitivity curves with those of other similar systems is presented. Since the absolute ordinates of the sensitivity curves depend on specific conditions that are characteristic of the mode of operation of each single instrument (e.g. MCP and Ph voltages), the calibration curves from other SPRED instruments have been normalized to those of the JET double SPRED.

Fig. 5.11 shows the inverse sensitivity of the TFTR 450 g/mm SPRED, reported by Stratton et al. [81], normalized to that of the JET 450 g/mm SPRED at 312.4 Å. The TFTR SPRED was calibrated against a syncrotron radiation source and an error of 30% in the calibration is reported. The maximum of the JET-SPRED sensitivity curve is found at longer wavelengths than the TFTR-SPRED. This difference does not seem to be due to the different coatings used for the two gratings, platinum for the JET-SPRED and gold for the TFTR-SPRED. In fact, the Pt/Au reflectance

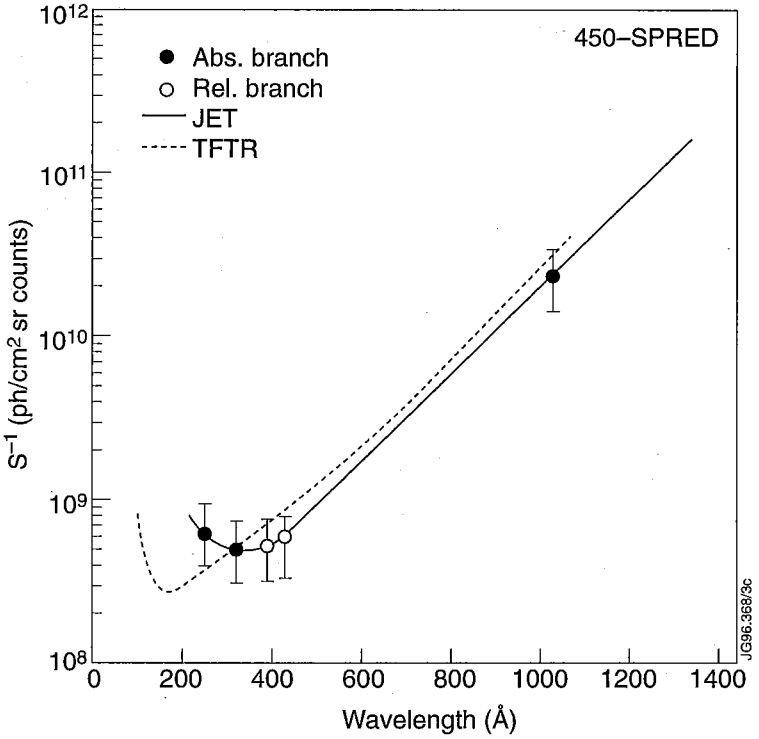

Figure 5.11: Comparison between TFTR [81] and JET divertor 450 g/mm-SPRED inverse sensitivity curves. The TFTR-SPRED curve was normalized to the JET curve at 312.4 Å.

curves ratio is maximum at 400 Å (ratio = 1.6) at normal incidence, but it reduces to 1.2 at 75° [83]. This difference is not large enough to explain the discrepancy in the two calibration curves, which, however, falls within the error bars of the branching ratio measurements.

Zastrow et al. [82] reported a comparison of the sensitivity curve for the Extrap-T1 450 g/mm SPRED with the TFTR SPRED and JET SPRED reported in [95], which is shown in Fig. 5.12. Their sensitivity curve also showed differences from that of the TFTR-SPRED, although no explanation for this difference was reported.

The inverse sensitivity curve for the 2105 g/mm SPRED is compared in Fig. 5.13 with that of the PBX SPRED reported by Stratton et al. [81], obtained using charge exchange recombination spectroscopy [96]. The PBX curve has been normalized to the JET curve at 312.4 Å , which is a measured calibration point for both systems. The two calibrations are in good agreement, within the experimental error bar, in the wavelength range where the two instruments overlap.

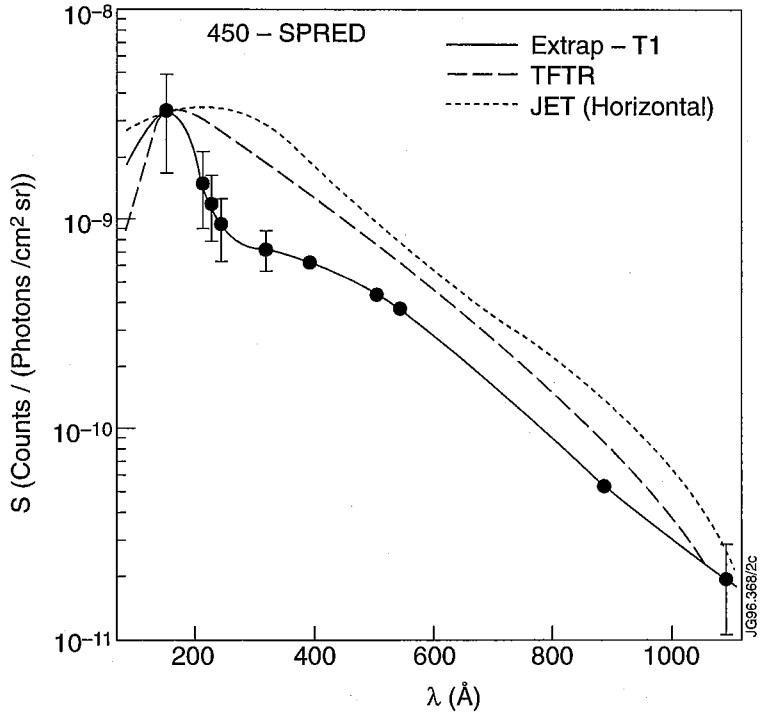

Figure 5.12: Comparison of inverse sensitivity curves for Extrap-T1, TFTR [81] and JET [95] 450 g/mm-SPRED systems, reported in [82].

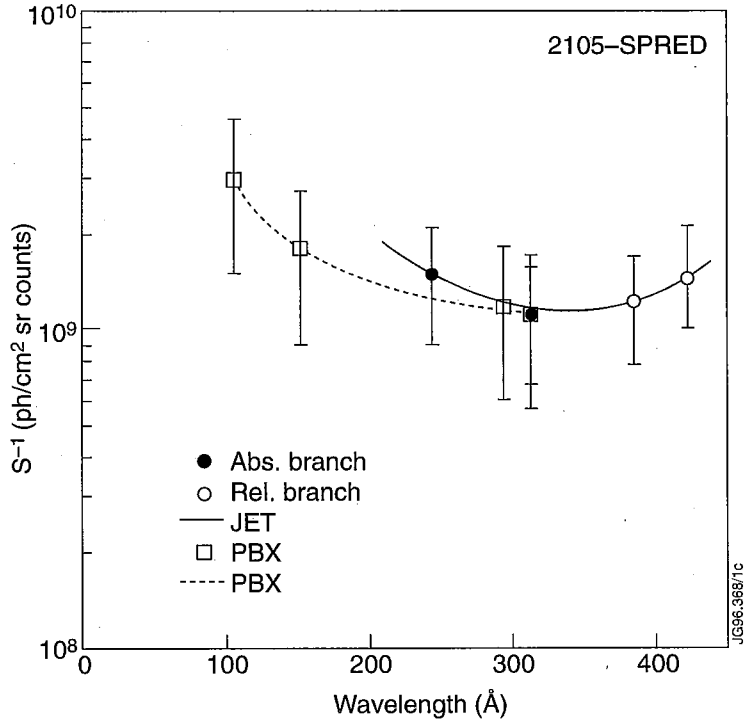

Figure 5.13: Comparison between PBX [81] and JET divertor 2105 g/mm-SPRED inverse sensitivity curves. The PBX curve was normalized to the JET curve at 312.4 Å.

Chapter 6

Description of Divertor and Edge Plasma Modelling

6.1 Introduction

This Chapter outlines the fundamental concepts of hydrogen plasma and impurity transport modelling in the divertor and edge region. Starting from a full 2D approach, the solutions of the transport equations for the hydrogen plasma are then derived in the Onion Skin Model (OSM). This model is then adopted in Chapters 7 and 8. The main limitations of the model are identified, although they are discussed in more detail in Chapters 7 and 8. It is shown how solving for the SOL plasma parameters description requires iteration with a model for the hydrogenic neutrals, since the latter contribute to the source and loss terms in the continuity equations. The model used to describe impurity production and transport is presented in the last three sections. This model does not provide at present a self-consistent treatment of the impurity and hydrogenic plasma transport. For this, iteration between the impurity and the plasma solutions to account properly for impurity - plasma ion collisions would be required. The transport codes used in this thesis are the Monte Carlo codes DIVIMP (Onion Skin Model for the hydrogenic plasma and Impurity Transport) [97] and NIMBUS (2D Neutral Hydrogen Transport) [98].

6.2 Modelling of the Hydrogen Plasma

The hydrogenic plasma is described in the fluid approximation by a set of transport equations for the electrons and the ions. They are obtained by taking the first three velocity moments of the collisional Vlasov equation and are written in the form of conservation equations for particles, momentum and energy. For each plasma species (electrons and ions), in steady state:

$$\nabla \cdot (n\vec{v}) = S_P - R_P \tag{6.1}$$

describes the conservation of particles, where n is the density and $\vec{v}$ the velocity of the particles. S_P represents the particle source, due to ionization of the neutrals:

$$S_P = n_0 n_e S \tag{6.2}$$

where n_0 is the neutral density and S is the ionization rate coefficient for hydrogen. R_P is a particle sink term for ions and electrons, due to recombination:

$$R_P = n_e n_i \ \alpha_{rec} \tag{6.3}$$

where n_i is the ion density and α_{rec} the recombination rate coefficient.

The momentum balance equation is expressed as:

$$\nabla \cdot (nm\vec{v}\vec{v}) + \nabla p + \nabla \cdot \underline{\Pi} - en(\vec{E} + \frac{1}{c}\vec{v} \times \vec{B}) = \vec{R} - \vec{S}_M \tag{6.4}$$

where m is the mass, p the pressure, $\underline{\Pi}$ the stress tensor (accounting for viscosity), $\vec{E}$ and $\vec{B}$ are the macroscopic electric and magnetic fields, e is the electronic charge, c the speed of light and $\vec{R}$ denotes the transfer of momentum due to friction between electrons and ions. $\vec{R}$ is made up of two parts:

$$\vec{R} \equiv \vec{R}^e = -\vec{R}^i = \vec{R}_U + \vec{R}_T \tag{6.5}$$

where $\vec{R}_U$ is the force of friction, due to the existence of a relative velocity, $\vec{u} = \vec{v}_e - \vec{v}_i$, between the electrons and the ions, and $\vec{R}_T$ is the thermal force, due to a gradient in the electron temperature [99]. S_M is the ion momentum loss due to neutral atom - ion charge exchange collisions, whereby a fast ion loses momentum colliding with a slow neutral (although this could also be a source term for the ions in case they charge exchange with a fast neutral), and can be expressed as:

$$\vec{S}_M = m(\vec{v} - \vec{v}_0) \ n_0 n_i \ \alpha_{CX} \tag{6.6}$$

with α_{CX} the charge exchange rate coefficient for hydrogen and v_0 the neutral velocity. This term becomes important in the description of detached plasmas, as discussed in Chapter 7.

The energy balance equation is written as:

$$\nabla \cdot (\vec{q} + \frac{5}{2} nkT\vec{v} + \frac{1}{2} nmv^2\vec{v}) + \nabla \cdot (\underline{\Pi} \cdot \vec{v}) - en\vec{E} \cdot \vec{v} = Q - S_E \qquad (6.7)$$

where $\vec{q}$ is the heat flux carried by particles due to conduction, $(5/2kT + 1/2mv^2)n\vec{v}$ is the convected heat flux, Q is the heat generated in a gas of particles of a given species as a consequence of collisions with particles of other species and S_E is the energy loss term, due to radiation and ionization potential losses (mainly for the electrons).

The system of equations 6.1, 6.4 and 6.7 is closed by expressing the moments of higher order $\underline{\Pi}$, $\vec{q}$, $\vec{R}$ and Q as a function of the moments of lower order n, $\vec{v}$ and T. The link between moments of higher and lower order is given by the transport coefficients. They are obtained for the condition in which the local distribution function is close to a Maxwellian, that is under the assumption that collisions are sufficient to maintain 'nearly' Maxwellian ion and electron distribution functions. This linearization of the problem generally applies to the situation of a fully ionized gas of electrons and ions due to the small ratio of the masses. For this reason, in fact, the electrons and the ions equilibrate separately in a time much shorter than that required for the two species to reach equilibrium with each other. It is therefore possible to consider solutions of local equilibrium with different average velocities and temperatures for electrons and ions.

In a short time scale τ_{ee} the electron population reaches energy equilibration due to e-e collisions, since large momentum and energy transfers occur. In a time scale τ_e (the electron-ion scattering time) the electron velocity becomes isotropic due to electron-ion collisions, which are characterized by large electron momentum transfer and small electron energy transfer. Since the relative velocity in electron-ion collisions is of the same order of that for e-e collisions, the two processes have approximately the same probability. Therefore in a time scale $\tau_e \approx \tau_{ee}$ a local equilibrium for the electron population is established. Thus the electron distribution function becomes locally a Maxwellian. Following Braginskii [99] τ_e is expressed as:

$$\tau_e = \frac{3\sqrt{m_e} T_e^{3/2}}{4\sqrt{2\pi}\Lambda e^4 n_i} \qquad (6.8)$$

where Λ is the Coulomb logarithm. Large momentum and energy transfers occur in ion-ion collisions, so that the ion distribution function becomes isotropic and Maxwellian in a time scale τ_i (the ion-ion scattering time). This can be written as:

$$\tau_i = \frac{3\sqrt{m_i}T_i^{3/2}}{4\sqrt{\pi}\Lambda e^4 n_i}. \tag{6.9}$$

Therefore, if the electron and ion temperatures are of the same order, the electron to ion equilibration times scale as the square root of the ratio of the masses, $\tau_e/\tau_i \approx (m_e/m_i)^{1/2}$. The electron-ion energy equilibration takes place on a longer timescale, τ_{ei}^{ϵ}. Since the energy transfer between ions and electrons is of order m_e/m_i times the energy of the electron, the characteristic time for e-i energy transfer is of order $\tau_{ei}^{\epsilon} \approx (m_i/m_e)\tau_e$. In presence of a magnetic field, the transport coefficients depend on the dimensionless quantity $\omega\tau$, with ω the cyclotron frequency, $\omega_{e,i} = |e|B/(m_{e,i}\, c)$. The expressions for the transport coefficients used here are those derived by Braginskii [99] and apply to the case $\omega_{e,i}\tau_{e,i} >> 1$ (strong magnetic field).

The transport equations should be supplemented by Poisson's equation:

$$\nabla^2\phi = n_e - n_i \tag{6.10}$$

but a good approximation in pure hydrogen collisional plasmas is to assume quasineutrality [100]:

$$n_e \simeq n_i \equiv n. \tag{6.11}$$

By expressing the electric field E as:

$$E = -\nabla\phi \tag{6.12}$$

and neglecting the transverse terms, which are considered anomalous, the transport equations become tractable.

Assuming symmetry in the toroidal direction, the transport equations can be reduced to a set of 2-D equations describing the transport along ($\|$) and across ($\perp$) the magnetic field lines. Parallel transport is assumed to be classical, while cross field transport is assumed to be diffusive, with anomalous transport coefficients. The continuity equation becomes:

$$\frac{\partial(nv_{\|})}{\partial x_{\|}} + \frac{\partial(nv_{\perp})}{\partial x_{\perp}} = S_P - R_P. \tag{6.13}$$

The flux of particles perpendicular to the magnetic field, $\Gamma_\perp = nv_\perp$, is expressed as due to diffusion across the magnetic flux tubes:

$$\Gamma_\perp = -D_\perp \frac{\partial n}{\partial x_\perp} \tag{6.14}$$

with $D_\perp$ the cross-field diffusion coefficient [99].

The momentum balance equation becomes:

$$\frac{\partial}{\partial x_\parallel}(p + nmv_\parallel^2) + \frac{\partial}{\partial x_\perp}(mv_\parallel nv_\perp) - en\vec{E} = \vec{R} + S_M \tag{6.15}$$

where the viscosity term has been neglected (it is not negligible for the ions and it might be important), the transverse term $\vec{v} \times \vec{B}$ has been neglected and only the parallel terms in the $\vec{v}\vec{v}$ tensor have been retained. $\vec{R}_U$ and $\vec{R}_T$ are expressed as [99]:

$$\vec{R}_U = -\frac{m_e n_e}{\tau_e}(0.51u_\parallel + u_\perp) \tag{6.16}$$

$$\vec{R}_T = -0.71 n_e \frac{\partial T_e}{\partial x_\parallel}. \tag{6.17}$$

The energy balance equation for the ions becomes (neglecting the viscosity term):

$$\begin{aligned} \frac{\partial}{\partial x_\parallel}[(\frac{5}{2}kT_i + \frac{1}{2}mv^2)nv_\parallel + q_\parallel^i] \quad + \quad & \frac{\partial}{\partial x_\perp}[(\frac{5}{2}kT_i + \frac{1}{2}mv^2)nv_\perp + q_\perp^i] + \\ & -en\vec{E}\cdot\vec{v} = Q_\Delta + S_E^i \end{aligned} \tag{6.18}$$

with $(\frac{5}{2}kT_i + \frac{1}{2}mv^2)\Gamma_\parallel$ the ion parallel heat convection term and $q_\parallel^i$ the ion parallel heat conduction term, where:

$$q_\parallel^i = -\chi_\parallel^i \frac{\partial T_i}{\partial x_\parallel} \tag{6.19}$$

with $\chi_\parallel^i$ the parallel ion thermal conductivity [99] and the corresponding set of terms describing the convected and conducted heat fluxes across the field lines, $q_\perp^i$, $\chi_\perp^i$ (transverse heat fluxes are neglected). Q_Δ is the ion-electron equipartition term, expressing the heat acquired by ions in collisions with the electrons:

$$Q_\Delta = 3\frac{m_e n_e}{m_i \tau_e}(T_e - T_i). \tag{6.20}$$

S_E^i is the ion energy source/loss term due to charge exchange collisions with the neutrals. In fact such collisions can lead to either cooling or heating of the ion depending on whether the ion collides with a cold or a hot neutral.

The energy balance equation for the electrons becomes:

$$\frac{\partial}{\partial x_{||}}[\frac{5}{2}kT_e n v_{||} + q^e_{||}] + \frac{\partial}{\partial x_{\perp}}[\frac{5}{2}kT_e n v_{\perp} + q^e_{\perp}] + en\vec{E}\cdot\vec{v}_e = -Q_{\Delta} - \vec{R}\cdot\vec{u} - S^e_E \quad (6.21)$$

where the viscosity term is neglected (it is not very important for electrons due to the small mass) and the kinetic term in the expression of the convected heat flux is neglected due to the small electron mass. The heat flux $\vec{q}_e$ due to conduction for the electrons is composed of a thermal part, in which the transverse electron heat flux is neglected:

$$\vec{q}^e_T = -\chi^e_{||}\frac{\partial T_e}{\partial x_{||}} - \chi^e_{\perp}\frac{\partial T_e}{\partial x_{\perp}} \quad (6.22)$$

and a friction part:

$$\vec{q}^e_U = 0.71 n_e T_e u_{||} \quad (6.23)$$

due to the relative velocity of electrons and ions, with $\chi^e_{||}$ and $\chi^e_{\perp}$ the electron thermal conductivities. The transverse component of $\vec{q}^e_U$ is not included. The heat generated in the electrons due to electron - ion collisions is $-Q_{\Delta} - \vec{R}\cdot\vec{u}$. Heat is transferred from the ions to the electrons if $T_i > T_e$ (hence the negative sign $-Q_{\Delta}$). Also, heat is generated in the electrons equal to the work from the force of friction exerted on the electrons by the ions, $-\vec{R}\cdot\vec{u}$. S^e_E represents the energy lost by the electrons in inelastic collisions with the recycling neutral hydrogen atoms. Energy (13.6 eV) is lost by the electrons in every collision that causes ionization of a hydrogen neutral and in every collision that causes excitation/deexcitation of a hydrogen neutral there is an energy/loss gain. Similarly, energy is lost in the electron channel due to impurity radiation and ionization. Thus, a solution for the hydrogen background plasma requires a simultaneous solution for the impurity transport. This aspect is further discussed in Section 6.4. Another point to be noted is that solution of the transport equations for the hydrogen plasma relies on the ability to quantify the source/sink terms present in these equations. This requires coupling with a model for the hydrogen neutrals which is discussed in the following section.

6.3 Solution of the Hydrogen Plasma Transport Equations: the Onion Skin Model Approach

Rather than solving the full 2D transport equations described in the previous Chapter, a simpler approach is the so-called Onion Skin Model. This is the approach

adopted in this thesis, by using the DIVIMP code. Since parallel transport for ions and electrons occurs on a much faster time scale than perpendicular transport, it is possible to describe the motion parallel to the field lines neglecting perpendicular transport. This means that each flux tube in the SOL can be modelled individually, starting from appropriate plasma boundary conditions for each flux tube. The perpendicular profiles are defined at one poloidal location and then mapped along the SOL using classical transport.

The most reliable experimental profiles available are almost always at the target plates, so that DIVIMP uses initial conditions there. At JET, T_e and n_e profiles are measured by an array of Langmuir probes imbedded in the JET divertor tiles. This has always been thought to offer the advantage of providing a more realistic solution of the background plasma in the region where most of the impurities are produced. However, as the divertor plasma becomes colder and denser (and eventually detaches) the interpretation of Langmuir probe I-V characteristics becomes unreliable. At JET, there is ample evidence that probe measurements during the MkI campaign greatly overestimated the electron temperature at the target as the electron density increased [21]. This puts large error bars on the input boundary conditions and weakens the arguments reported above, mostly at high density.

For each flux tube the transport equations are solved starting from the target plates at $s = 0$, where s denotes the distance along the field from the target, and moving upstream along the field line. The boundary conditions at the target, $s = 0$, are $n(0)$, $T_e(0)$ measured by the Langmuir probes. The ion temperature, $T_i(0)$, is not measured directly and is thus effectively a free parameter. Generally it is assumed $T_i(0) = T_e(0)$. For the velocity it is assumed $v(0) = c_s(0)$, with c_s the ion sound speed:

$$c_s = \left(\frac{kT_e + kT_i}{m_i} \right)^{1/2}. \tag{6.24}$$

Thus, the particle conservation equation specifies the particle flux $\Gamma(s)$:

$$\Gamma(s) = n(s)v(s) = n(0)c_s(0) + \int_0^s S_P(s')ds'. \tag{6.25}$$

The recombination sink term is not included in the model at present. This term becomes important for target temperatures of order 1 eV, when the divertor plasma ceases to be fully ionizing. This seems to be the regime that characterizes detached plasmas and is discussed in Chapter 7.

By solving the momentum balance equation for electrons and ions simultaneously, the friction and electric field force terms cancel, giving:

$$n(s)(kT_e(s) + kT_i(s) + mv^2(s)) = n(0)(kT_e(0) + kT_i(0) + mc_s^2(0)) + - \int_0^s S_M(s')ds'. \quad (6.26)$$

By integrating the energy balance equation for the electrons it is possible to solve for the variation of T_e along the field lines:

$$\frac{dT_e}{ds} = \frac{1}{\chi_{0e}T_e^{5/2}}\left(P_{\|}^e(0) + \frac{5}{2}kT_e(s)\Gamma(s) - \int_0^s(-Q_\Delta(s') - S_E^e(s'))ds'\right). \quad (6.27)$$

$P_{\|}^e(0)$ is the electron heat flux at the electrically floating target:

$$P_{\|}^e(0) = \gamma_e\, kT_e\, \Gamma(0) \quad (6.28)$$

where γ_e is the electron sheath energy transmission factor [100], [3]:

$$\gamma_e = \frac{2}{1-\delta_e} - \frac{e\phi_f}{kT_e} \quad (6.29)$$

with δ_e the secondary electron emission coefficient and $e\phi_f$ the sheath voltage drop. $\gamma_e = 5$ in this model, which is close to the value for $\delta_e = 0$ [101].

In a similar way, the energy balance equation for the ions yields:

$$\frac{dT_i}{ds} = \frac{1}{\chi_{0i}T_i^{5/2}}\left(P_{\|}^i(0) + \left(\frac{5}{2}kT_i(s) + \frac{1}{2}mv^2(s)\right)\Gamma(s)\right) - \int_0^s(Q_\Delta(s') + S_E^i(s'))ds' \quad (6.30)$$

with boundary condition $P_{\|}^i(0)$, the ion heat flux to the target, expressed as [100], [102]:

$$P_{\|}^i(0) = \left(\frac{5}{2}kT_i(0) + \frac{1}{2}M_0^2\,(kT_e(0) + kT_i(0))\right)\Gamma(0) \quad (6.31)$$

where:

$$M_0 = \frac{v(0)}{c_s(0)} \quad (6.32)$$

is the Mach number at the target.

The parallel transport is thus described by four equations for $n(s)$, $v(s)$, $T_e(s)$ and $T_i(s)$. Numerically it is necessary to solve for $n(s)$, $v(s)$ and $T(s)$ simultaneously, due to the presence of the convection and energy equipartition terms in the energy balance equation.

Using the parallel momentum balance equation for the electrons it is possible to calculate the ambipolar electric field experienced by the impurity ions (see Section 6.5). From equation 6.15, neglecting contributions from momentum sources, viscosity and friction, one obtains:

$$E = -\frac{1}{en}\frac{d(nkT_e)}{ds} - \frac{0.71}{e}\frac{dT_e}{ds}. \tag{6.33}$$

The major problem when mapping the plasma solution around the SOL is posed by the source/loss terms in the transport equations. Initially, the analytic sources/losses are put in and a first approximation (the starter plasma) is calculated by the Onion Skin Model. This approximate background plasma is then fed into the 2D Monte Carlo code for the neutrals, NIMBUS [98], which returns a better estimate of the source/loss terms, as well as a 2D distribution of the hydrogen neutrals. By iterating between the plasma model and the neutrals code a converged solution is obtained. The converged NIMBUS solution provides the ionization source distribution, the momentum loss distribution and the hydrogen radiation/ionization losses. It is to be noted that the impurity radiation losses remain as an analytic expression, as a function of the distance along the field lines. It is feasible to iterate on the impurity solutions, as discussed in Section 6.4, but this is not implemented at present in the model.

6.4 Modelling the Impurities

In order to model the impurity behaviour it is necessary to describe the mechanisms that produce the impurities and determine their transport in the plasma. It is certainly the case that impurity production occurs predominantly by sputtering. At present, the most complete model for the transport of the impurities is obtained by solving a system of fluid equations, one for each impurity charge state, similar to that described in Section 6.2 for the hydrogenic plasma. Even at small impurity levels, a feedback interaction occurs between the background plasma and the impurities. Thus, as more impurities are released into the SOL, more power is radiated. This changes the plasma energy, which in turn reduces the sputtering yield. Therefore, in principle, one should solve for the hydrogenic plasma and the impurities (all charge states) simultaneously.

Such complex 2D multifluid, multispecies calculations are indeed addressed using codes such as EDGE2D/NIMBUS [103] at JET, with equivalent codes for other machines. In these codes the 2D transport equations for the hydrogenic plasma are solved simultaneously with the 2D conservation equations for particles and momentum for all charged states of the impurity. The energy equation for the impurities is replaced by assuming instant thermalization of the impurities with the background plasma ions, but the effect of impurity radiation on the plasma energy is included in the energy balance equation for the hydrogenic plasma. These codes take several tens of hours of CPU time to converge on high power workstations.

However, none of the transport codes available at present includes a proper treatment of the impurity ion metastable states. This would involve solving a set of transport equations for each metastable state of a specific ion, rather than considering the metastable states as ordinary excited levels (see Chapter 3), which is the present working assumption. Although it is believed that this simplification can introduce some error, especially when modelling ionization stages that have a strong metastable population (e.g. C III), this complexity has so far been ignored because of the current difficulties encountered in impurity transport models as they stand. In Chapter 7 this issue is discussed comparing atomic modelling with spectroscopic measurements of C III divertor line emission .

A simpler approach is to consider the impurities as a test fluid [104] which interacts with the hydrogen background plasma via collisions and the ambipolar electric field, but neglecting collisions of impurities with themselves and feedback from impurities on the hydrogen background. This approach requires the impurity density to be quite low, that is:

$$\sum_Z Z^2 n_Z << n_e \approx n_i. \tag{6.34}$$

where n_Z is the density of impurities of charge Z. In this situation, a Monte Carlo code, such as DIVIMP, instead of dealing with a test fluid, follows the impurity particles individually, from their point of formation (as neutrals or ions) until they escape the plasma or hit some boundary surface. It is therefore implicit to this approach that the impurities do not interact with themselves. That the impurity-background ion collisions do not influence the hydrogenic plasma depends on the level of sophistication desired for the background plasma itself. It is of course possible to calculate these terms for a given (starting) hydrogenic plasma and then iterate between the

impurity model and the plasma model until convergence is reached. The present version of DIVIMP does not include this option. These simplifications are suited for interpretative work, since they allow reasonable control on the various parameters involved in the model. The computations are also fast, requiring only a few minutes of CPU time to reach a solution. However, it does not provide a consistent treatment of the impurity and hydrogenic plasma transport. The implications of this aspect will be examined in the next chapters.

6.5 Impurity Transport in the Trace Impurity Approach

As for the hydrogenic plasma, the perpendicular transport for the impurities is anomalous. In DIVIMP it is treated by specifying a constant cross-field diffusion coefficient $D_\perp$ (the same for all impurity ionization stages) and by incrementing the cross-field distance of the ion by a step equal to $\pm(2D_\perp \Delta t)^{1/2}$ every Monte Carlo time step Δt. Usually $D_\perp = 1m^2/s$ is assumed, since nothing is known experimentally on this transport coefficient. In principle some information could be extracted from impurity ion profiles upstream from the target, but these unfortunately are not available.

The parallel transport for the impurities is considered to be classical. For a given charge state Z, in steady state, the continuity equation can be written as:

$$\begin{aligned}\frac{d(n_Z v_Z)}{ds} &= n_{Z-1} n_e S_{Z-1} + n_{Z+1}(n_e \alpha_{rec,Z+1} + n_H \alpha_{CX,Z+1}) + \\ &\quad - n_Z(n_e S_Z + n_e \alpha_{rec,Z} + n_H \alpha_{CX,Z}).\end{aligned} \tag{6.35}$$

Since the impurity particles are followed individually, the modification of their charge state is considered by defining a time for change of charge state, τ_{ch}:

$$\frac{1}{\tau_{ch}} = \frac{1}{\tau_{iz}} + \frac{1}{\tau_{rec}} + \frac{1}{\tau_{cx}} \tag{6.36}$$

where τ_{iz} is the characteristic time for ionization:

$$\tau_{iz} = \frac{1}{n_e S}, \tag{6.37}$$

τ_{rec} is the characteristic time for recombination:

$$\tau_{rec} = \frac{1}{n_e \alpha_{rec}}, \tag{6.38}$$

and τ_{cx} is the characteristic time for charge exchange recombination:

$$\tau_{cx} = \frac{1}{n_H \alpha_{CX}}. \tag{6.39}$$

The ionization and recombination rates are drawn from ADAS [38], (see Chapter 3). The proper inclusion of charge exchange in this model is one of the central aspects of this thesis (see Chapter 8).

At each Monte Carlo time step Δt the rates of ionization, recombination and charge exchange are calculated as a function of the local value of the electron temperature and density. Then a random number ξ_1, uniform in [0,1], is drawn. If $0 < \xi_1 < \Delta t/\tau_{ch}$ then a change of charge state occurs. A second random number ξ_2 is drawn to establish if the ion has recombined to the stage below (electron recombination or charge exchange) or ionized to the stage above.

In the momentum balance equation the total force on the impurity ion is [105], [106]:

$$F = m_I v_I \frac{dv_I}{ds} = F_P + F_E + F_F + F_T + F_\eta \tag{6.40}$$

where m_I and v_I are the mass and the velocity of the impurity ion. F_P is the impurity pressure force:

$$F_P = -\frac{1}{n_I}\frac{dp_I}{ds}. \tag{6.41}$$

F_E is the electrostatic force on the impurities due to the ambipolar electric field E, which provides the quasi neutrality of the plasma (for zero net current):

$$F_E = eZ_I E \tag{6.42}$$

with eZ_I the impurity charge and E is obtained from the electron momentum balance equation (eq. 6.33). F_F is the friction force between the impurity ion and the hydrogenic plasma flow:

$$F_F = \frac{m_I(v_B - v_I)}{\tau_S} \tag{6.43}$$

with v_B the velocity of the background plasma flow and τ_S the Spitzer slowing down time [107]:

$$\tau_S = \frac{3(kT_i)^{3/2} m_I^2}{4\sqrt{2\pi} e^4 n_i Z_I^2 Z_i^2 \Lambda \sqrt{m_i}(m_i + m_I)} \tag{6.44}$$

where Λ is the Coulomb logarithm. τ_S represents the rate at which the mean velocity of the impurity particles is decreased by Coulomb collisions with the background plasma. The impurities are slowed down mostly by the hydrogenic ions and the

electron contribution is negligible. The expression for τ_S given in eq. 6.44 is obtained assuming a Maxwellian velocity distribution for the hydrogenic ions and in the limit $v_I << (2kT_i/m_i)^{1/2}$ [107], that is for impurity velocities smaller than the thermal velocity of the hydrogenic ions (which may involve some error). F_T is the thermal diffusion force, which arises due to the presence of electron and ion temperature gradients in the plasma flow:

$$F_T = \alpha \frac{dT_e}{ds} + \beta \frac{dT_i}{ds} \tag{6.45}$$

with coefficients α and β from Neuhauser et al. [104]:

$$\alpha = 0.71 Z_I^2 \tag{6.46}$$

$$\beta = -3 \frac{1 - \mu - 5\sqrt{2} Z_I^2 (1.1\mu^{5/2} - 0.35\mu^{3/2})}{2.6 - 2\mu + 5.4\mu^2} \tag{6.47}$$

with $\mu = m_I/(m_I + m_i)$. F_η, the viscous force, is neglected in this model. The impurity pressure gradient force is treated in DIVIMP as parallel diffusion in velocity space by introducing a characteristic time $\tau_{||}$, which is defined following Spitzer [107] as:

$$< (\Delta v)^2 > \tau_{||} = v_{Th,I}^2 \tag{6.48}$$

with $v_{Th,I} = (2kT_I/m_I)^{1/2}$ the impurity ion thermal velocity and $< (\Delta v)^2 >$ the rate of increase of velocity dispersion, in velocity space, in the direction of the initial motion (i.e. along the field lines). $\tau_{||}$ is given by:

$$\tau_{||} = \frac{3 m_I k T_I \sqrt{\frac{kT_i}{m_i}}}{4\sqrt{2\pi} e^4 n_i Z_I^2 Z_i^2 \Lambda} \tag{6.49}$$

for a Maxwellian velocity distribution of the hydrogenic background ions. At each Monte Carlo time step Δt, a random number of gaussian distribution ξ_G is drawn and the increment Δv of the impurity ion velocity is calculated:

$$\begin{aligned} \Delta v \;=\; & \left(< (\Delta v_{||})^2 > \Delta t \right)^{1/2} \xi_G + \frac{(v_B - v_I)}{\tau_S} \Delta t + \frac{Z_I e E}{m_I} \Delta t + \frac{\alpha}{m_I} \left(\frac{dT_e}{ds} \right) \Delta t + \\ & + \frac{\beta}{m_I} \left(\frac{dT_i}{ds} \right) \Delta t \end{aligned} \tag{6.50}$$

with:

$$\left(< (\Delta v_{||})^2 > \Delta t \right)^{1/2} = \left(\frac{2kT_I}{m_I} \frac{\Delta t}{\tau_{||}} \right)^{1/2}. \tag{6.51}$$

The energy balance equation is replaced by thermalization of the impurity ions with the background ions, occurring in a timescale τ_T, the Spitzer energy transfer collision time [107], for Maxwellian distributions of the hydrogenic ion and impurity ion velocities:

$$\tau_T = \frac{3m_I m_i}{8\sqrt{2\pi}e^4 n_i Z_I^2 Z_i^2 \Lambda}\left(\frac{kT_i}{m_i} + \frac{kT_I}{m_I}\right)^{3/2} \tag{6.52}$$

so that the impurity ion temperature T_I is calculated at each Monte Carlo time step as:

$$\Delta T_I = \frac{(T_i - T_I)}{\tau_T}\Delta t. \tag{6.53}$$

6.6 Impurity Production: Physical and Chemical Sputtering

One of the complications encountered when modelling the impurity behaviour in the plasma edge is modelling of the impurity source. In general, impurity influx into the plasma is caused by (plasma and impurity) ion and charge exchange neutral bombardment of the surface of the plasma facing materials. For most materials this leads to physical sputtering, that is ejection of surface atoms, which receive sufficient kinetic energy through collisions with the incident particles to overcome the surface binding energy of the solid [108].

Sputtering is measured by the number of emitted target atoms per incident particle, the sputtering yield, Y. Hence, in order to model the impurity source, a model is required for the sputtering yield. For a given target-projectile combination, the sputtering yield depends on the energy and angle of incidence of the bombarding particle and the sputtered atoms exhibit characteristic angular and energy distributions. For graphite, and in general carbon composite wall materials, an additional mechanism has been found responsible for impurity production, particularly at low plasma edge temperatures. This is chemical sputtering, in which molecules are formed on the wall surface due to a chemical reaction between the incident particles (both energetic hydrogenic ions and thermal hydrogen atoms) and the carbon atoms of the solid. The binding energies of the molecules to the surface is low enough to allow desorption at the temperature of the solid [109] (e.g. $\sim 300°$ C for the divertor target tiles at JET).

For carbon plasma facing materials, it is possible to say that in general both chemical and physical sputtering occur, but that the effect of chemical sputtering is only observable at particle energies close to or below the threshold energy for physical sputtering (about 30 eV for carbon). This is indeed the case in JET, where the vessel walls are covered in carbon fibre composite (CFC) as well as the divertor target tiles of the first phase of the MkI experimental campaign. The other relevant plasma facing material is beryllium, both as a surface coating, periodically evaporated on the CFC surfaces for oxygen gettering and as solid tiles, replacing the CFC divertor tiles during the second phase of the MkI campaign. Be reacts effectively with oxygen and oxide layers are formed on the surface of the metal, thus considerably reducing the oxygen level in the plasma. Oxidised metal surfaces have been observed to have sputtering yields up to a factor of five lower than those of clean metal surfaces [109]. This is thought to be due to the dilution of the metal atoms in the oxide and to a higher binding energy. DIVIMP simulations of Be II visible emission from the JET divertor observed with a flux camera and a visible spectrometer (described in Chapter 5) seem to confirm this (see Chapter 7). The interpretation of the dynamics of Be emission in JET, however, is complicated by the presence of carbon layers redeposited on the Be tiles. In fact carbon proves to be the dominant intrinsic impurity, regardless of the material of the divertor. This aspect is also discussed in Chapter 7. The reduction of the sputtering yield for oxidised Be, with respect to the pure metal, has been observed to change at elevated temperatures. For Be the oxide layer dissolves at 600 °C and at this temperature the sputtering yield for D^+ bombardment is expected to correspond to that of the pure metal [110]. This has indeed been observed at JET during experiments aimed at melting of the Be divertor target tiles and, again, is discussed in Chapter 7.

There are some further complexities that have not yet been mentioned. Firstly, the sputtering yield data measured in the laboratory refer to clean and polished targets and in this case are in reasonable agreement with results from code simulations. However, the surfaces of the tokamak vessel, which are exposed to plasma particle bombardment, exhibit increasing roughness, so that the actual yield has quite a different behaviour. Moreover, redeposited layers (not necessarily in the region of erosion) may have different (and unknown) sputtering behaviour [111]. These factors put large error bars on the available experimental and calculated sputtering data used in the impurity transport models. It must also be mentioned that the

simultaneous impact of energetic ions, charge exchange neutrals, electrons etc. on the plasma facing surfaces is thought to lead to a non linear superposition of the effects caused by the impacting species acting separately (synergistic effects) [109], [110], thus introducing another source of uncertainty in the yields.

It follows that *ab initio* modelling of the impurity source is an almost impossible task when modelling the impurity transport. Practically, the source usually has to be adjusted to match the impurity level as measured by spectroscopy. In the model used in this thesis, a total sputtering yield, Y_{tot}, due to the hydrogenic flux is calculated by NIMBUS or, alternatively, by DIVIMP itself as:

$$Y_{tot} = Y_{phys} + Y_{chem} \tag{6.54}$$

with Y_{phys} and Y_{chem} the physicsl and chemical sputtering yields. In addition, the selfsputtering yield, Y_{self}, due to impurity ions hitting the walls, is calculated in DIVIMP. Y_{phys} is taken from the review of sputtering data by Eckstein et al. [112], which are fitted with the Bohdansky formula for normal incidence of the projectile ($\alpha = 0°$) on the target surface:

$$Y_{phys}(E_0, \alpha = 0°) = Q S_n \left(1 - \left(\frac{E_{th}}{E_0}\right)^{2/3}\right)\left(1 - \frac{E_{th}}{E_0}\right)^2 \tag{6.55}$$

where E_0 is the energy of the incident particle, E_{th} the threshold energy for physical sputtering, S_n the nuclear stopping cross section:

$$S_n = \frac{3.44\sqrt{\frac{E_0}{E_{TF}}} ln\left(\frac{E_0}{E_{TF}} + 2.72\right)}{1 + 6.36\sqrt{\frac{E_0}{E_{TF}}} + \frac{E_0}{E_{TF}}\left(6.88\sqrt{\frac{E_0}{E_{TF}}} - 1.71\right)} \tag{6.56}$$

with E_{TF} the Thomas-Fermi energy [108]. Q and E_{th} are fitting parameters. Fig. 6.1 shows the sputtering yield for carbon bombarded by H, D and T at normal incidence as a function of energy, from ref. [112].

The energy and angular distributions of the sputtered impurity atoms also constitute necessary information when modelling impurity transport and are expressed by the differential sputtering yield [108]. It can be shown that for plasma surface interactions in fusion devices a good assumption for the angular distribution of the sputtered atoms is a cosine distribution [113], so that in cylindrical coordinates:

$$\frac{d^3 Y_{phys}}{dE d\vartheta d\varphi} = Y_{phys}(E_0, \alpha = 0°) g(\vartheta, \varphi) f(E) = Y_{phys}(E_0, \alpha = 0°) \frac{2\cos\vartheta}{2\pi} f(E) \tag{6.57}$$

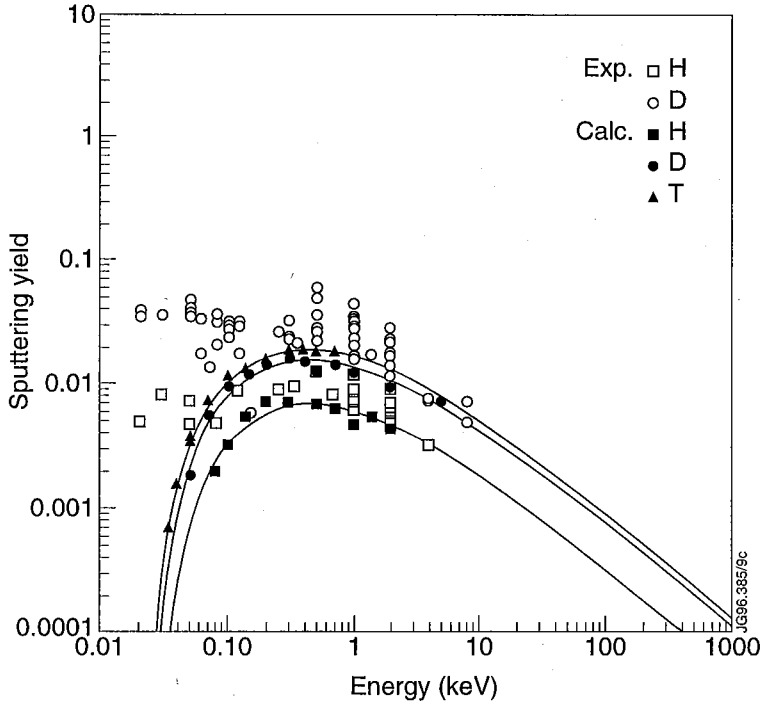

Figure 6.1: Sputtering yield of carbon for H, D and T (measurements and calculations). Figure adapted from ref. [112].

with $f(E)$ representing the normalized energy distribution function of the physically sputtered target atoms. The energy distribution of the sputtered neutrals is assumed to follow the Thompson distribution [114], so that:

$$f(E) = 2E_B \frac{(E_{max} + E_B)^2}{E_{max}^2} \frac{E}{(E + E_B)^3}, \qquad E \leq E_{max} \tag{6.58}$$

with E_B the binding energy of the solid. The energy distribution has a cut off at the maximum energy that can be transferred to the sputtered particle, which is assumed to be:

$$E_{max} = \frac{E_B}{E_{th}} E_0 - E_B. \tag{6.59}$$

The energy E of the sputtered atom is selected in a Monte Carlo way, by picking a random number ξ_E, uniform in [0,1], and setting:

$$\xi_E = \int_0^E f(E')dE' \tag{6.60}$$

and thus calculating $E = E(\xi_E)$. The angle of emission of the sputtered impurity neutral is obtained by picking two random numbers, ξ_ϑ and ξ_φ, uniform in [0,1], so that $\vartheta(\xi_\vartheta)$ and $\varphi(\xi_\varphi)$ are calculated, and then projecting these polar angles into an angle in the poloidal plane with respect to the normal to the emitting surface.

For chemical sputtering the situation is more complicated. Although several models have been put forward [115], [116], [117], at present there are still large discrepancies between them and the available experimental data. Such experimental data are scarce and often for conditions far from those relevant to fusion experiments. However, it is clear that in the case of carbon impurities physical sputtering alone is far from providing a correct description of the impurity source. The transport model described here allows testing of the different chemical sputtering models available in the literature and chemical sputtering is modelled by releasing thermal carbon atoms at fixed energy (usually 0.1 eV). In this context, however, it has to be noted that the calculation of the hydrogenic fluxes to the divertor target relies strongly on Langmuir probe measurements, which are characterized by large uncertainties as the divertor plasma progresses towards detachment, that is when modelling of the chemical sputtering is most important. This aspect of impurity source modelling is discussed further in Chapters 7 and 8 in connection with the interpretation of the spectroscopic emission from the JET divertor.

Chapter 7

Spectroscopic Analysis and Modelling of Radiated Power Components from the JET MkI Divertor

7.1 Introduction

In the model of hydrogenic and impurity emission from the divertor region, the understanding of the transport mechanisms that determine the specific radiation profiles, both in terms of spatial distributions and of ionization balance, is only preliminary, especially in high density and plasma detachment regimes. A further complication is due to the large uncertainties associated with modelling of the impurity source, as exemplified by carbon in this study. Simultaneous spectroscopic observations of divertor plasma emission, both in the VUV and visible region, provide essential information in this area of study. In this Chapter spectroscopic measurements from the JET divertor and their comparison with interpretative code modelling are presented.

The VUV line emission, which forms the basis for analysis in this Chapter, was measured by the divertor double SPRED (see Chapters 4 and 5). The integral radiated power assembled from VUV spectroscopy measurements in different impurity scenarios and plasma regimes is consistent with that measured with a bolometer

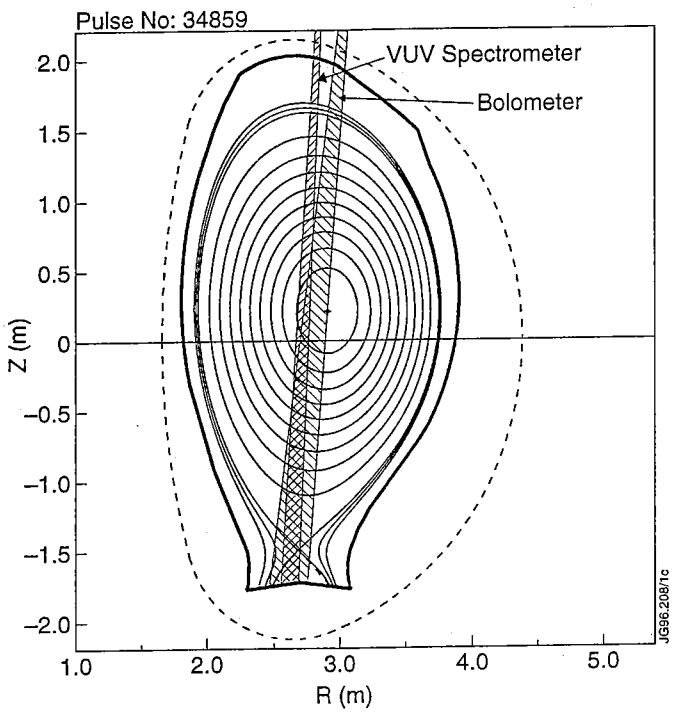

Figure 7.1: Bolometer channel and double SPRED spectrometer views overlayed on the magnetic equilibrium for pulse 34859.

with a view similar to that of the double SPRED (see Fig. 7.1). This view, which traverses the X-point region, also corresponds to that of maximum radiation at high density. Consequently, VUV spectroscopy can be exploited with some confidence for experimental identification and extensive measurements of the main contributors to the total radiated power from divertor plasmas.

7.2 Intrinsic Impurities: Spectroscopic Observations

7.2.1 Divertor Plasmas on CFC and Be Targets

In the absence of impurity injection, emission from DI and C II-IV dominates in the divertor in Ohmic, L-mode and H-mode discharges at moderate to high densities. This is exemplified in Fig. 7.2, which shows a spectrum from the 450-SPRED (a) and from the 2105-SPRED (b) during a high density L-mode discharge on the Be target. The deuterium radiated power is measured spectroscopically from the L_α and L_β line

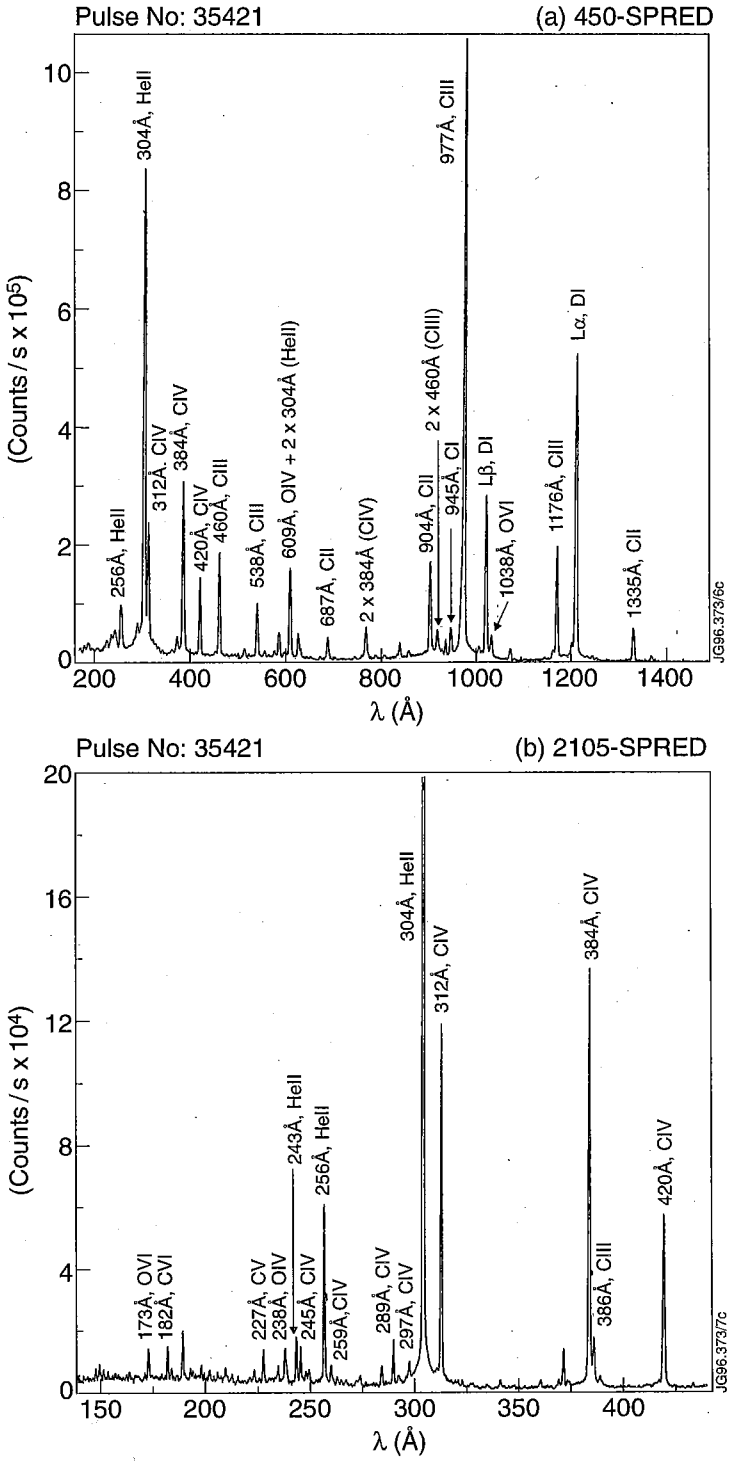

Figure 7.2: VUV spectrum of the divertor from the 450-SPRED (a) and the 2105-SPRED (b) during the high density phase of the L-mode discharge 35421 (t = 18.02 s). In fig. (b) the y axis scale is chosen so as to enhance the weaker lines.

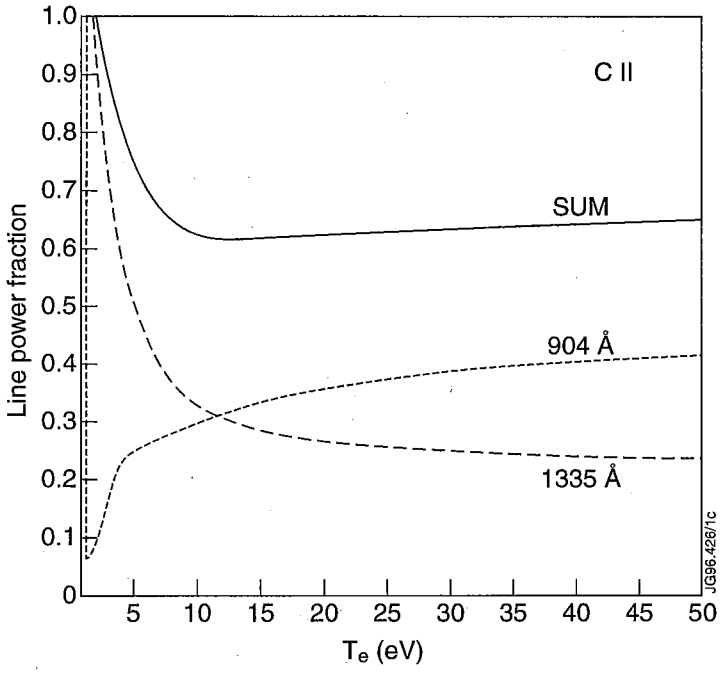

Figure 7.3: C II calculated line power fractions as a function of electron temperature for $n_e = 1 \times 10^{19} m^{-3}$ (from ADAS, 1993 calculations).

intensities. Therefore, within the uncertainty of the SPRED calibration, essentially all of the DI line power is accounted for. The C II radiated power is obtained from the 904 Å ($2s^2 2p\ ^2P - 2s2p^2\ ^2P$) and 1335.3 Å ($2s^2 2p\ ^2P - 2s2p^2\ ^2D$) line intensities. The 1036.8 Å ($2s^2 2p\ ^2P - 2s2p^2\ ^2S$) line was always rather weak and could not be resolved from the neighbouring O VI doublet. By comparing with the theoretical C II line power curves shown in Fig. 7.3 it can be seen that the measured C II lines account for about $\geq$70% of the total C II line power (assuming that emission due to electron excitation dominates, as will be shown in Chapter 8). In fact, recalling eq. 3.37 of Chapter 3, an estimate of the C II line power fraction obtained from the measured C II line intensities is given by:

$$P(C\ II) = \frac{\sum_{meas} q_{eff}^{exc}(\lambda)\ hc/\lambda}{PLT(C\ II)} \tag{7.1}$$

where the sum is taken over the measured C II transitions. The C III radiated power is measured from the singlet and triplet resonance transitions (977 Å, $2s^2\ ^1S - 2s2p\ ^1P$ and 1175.7 Å, $2s2p\ ^3P - 2p^2\ ^3P$) which carry most of the C III line power, and from the 538.2 Å ($2s2p\ ^3P - 2s3s\ ^3S$) and 459.6 Å ($2s2p\ ^3P - 2s3d\ ^3D$) line intensities. Thus the main radiators in C III are measured, as shown in Fig. 7.4. The C IV line power is emitted predominantly by the resonance line (1549.1 Å,

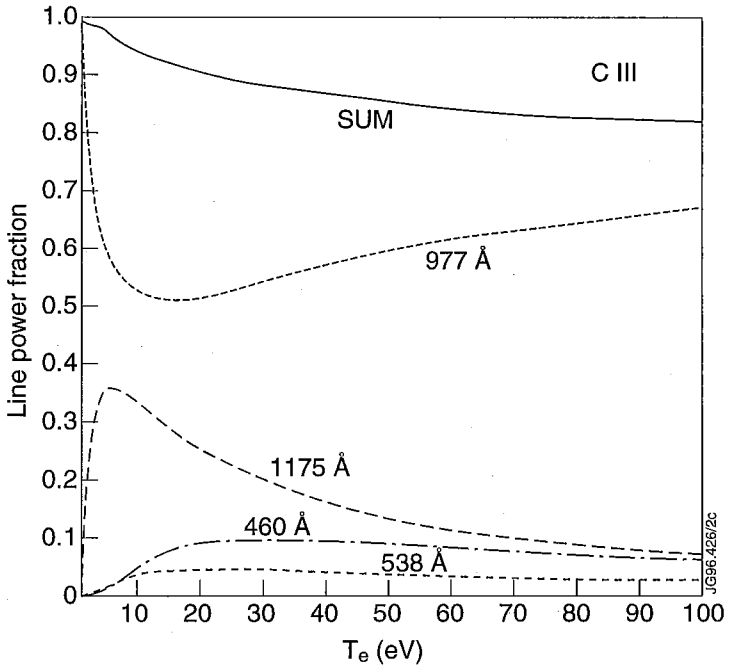

Figure 7.4: C III calculated line power fractions as a function of electron temperature for $n_e = 1 \times 10^{19} m^{-3}$ (from ADAS, 1996 calculations).

$2s\ ^2S - 2p\ ^2P$), but unfortunately this line cannot be measured with the 450-SPRED. Therefore the C IV line power has to be inferred from other line intensities. Two independent line ratios, using the $n = 3 - 2$ transitions (312.4 Å, 384.1 Å, 419.6 Å), provide an estimate of the electron temperature associated with the C IV emission layer along the SPRED LOS and subsequently the intensity of the resonance line is calculated from the ratio of 419.6 Å / 1549.1 Å. This line ratio depends strongly on T_e, unlike the ratios involving the $n = 3 - 2$ transitions, from which a temperature in the range T_e = 20-30 eV is inferred for all the discharges analyzed. Note that, as will be shown in the following sections, estimates of T_e from line ratios can have considerable errors. In part this is because different lines of the same ionization stage can emit at different values of T_e, when there are markedly different excitation energies of the upper levels of the transitions. In the divertor there can be very little spatial overlap of the emission since strong parallel T_e-gradients exist. In the case of C IV this could result in an underestimation of the emission from the resonance line and thus of the C IV radiation. Thus, if the C IV resonance line emits at 10 eV, rather than 20 eV, as shown by the line ratio measurements, the C IV line power is enhanced by a factor of 3. This, however, does not change the result that C III is measured to be the strongest radiator in these discharges. In addition, the line ratio

Ion	λ (Å)	Transition	Comment
C I	945.4	$2s^2 2p^2\ ^3P - 2s2p^3\ ^3S$	$\geq$20% of C I line power
C II	904.1	$2s^2 2p\ ^2P - 2s2p^2\ ^2P$	account for $\geq$70%
	1335.3	$2s^2 2p\ ^2P - 2s2p^2\ ^2D$	of C II line power
	1036.8	$2s^2 2p\ ^2P - 2s2p^2\ ^2S$	not used (blended with O VI doublet)
C III	977.0	$2s^2\ ^1S - 2s2p\ ^1P$	account for $\geq$90%
	1175.7	$2s2p\ ^3P - 2p^2\ ^3P$	of C III line power
	538.3	$2s2p\ ^3P - 2s3s\ ^3S$	
	459.6	$2s2p\ ^3P - 2s3d\ ^3D$	
C IV	1549.1	$2s\ ^2S - 2p\ ^2P$	not measured ($\geq$ 80% of line power)
	312.4	$2s\ ^2S - 3p\ ^2P$	used to estimate
	419.6	$2p\ ^2P - 3s\ ^2S$	total C IV
	384.1	$2p\ ^2P - 3d\ ^2D$	line power
C V	227.4	$2s\ ^3S - 3p\ ^3P$	account for ~2-3% of line power
	248.7	$2p\ ^3P - 3d\ ^3D$	
C VI	182.0	3-2	accounts for ~1% of line power

Table 7.1: Summary of spectral lines used for carbon radiated power measurements with the divertor double SPRED.

calculations assume electron impact excitation as the only mechanism populating the $2p$ and $n = 3$ levels. For these reasons the present estimate of the C IV line power cannot be accurate and the direct measurement of the C IV resonance line is strongly desired. This line can in principle be measured in JET by a VUV duochromator, which radially scans the divertor plasma, but unfortunately this diagnostic was not operational during the MkI campaign.

Radiation from C I was estimated from the only measured transition ($2s^2\ 2p^2\ ^3P - 2s\ 2p^3\ ^3S$ at 945 Å) to be negligible, consistent with simulations. The resonance transitions of C V- C VI were not measured. However, from the Balmer$_\alpha$ transition in C VI and $n = 3 - 2$ transitions in C V it was estimated, over a range of divertor-relevant electron densities and temperatures, that emission from these ionization stages did not contribute significantly to the power balance. This was confirmed by the simulations (see later). Visible spectroscopy observations of the divertor region also confirmed the lack of C VI emission from the divertor. Table 7.1 summarizes this discussion.

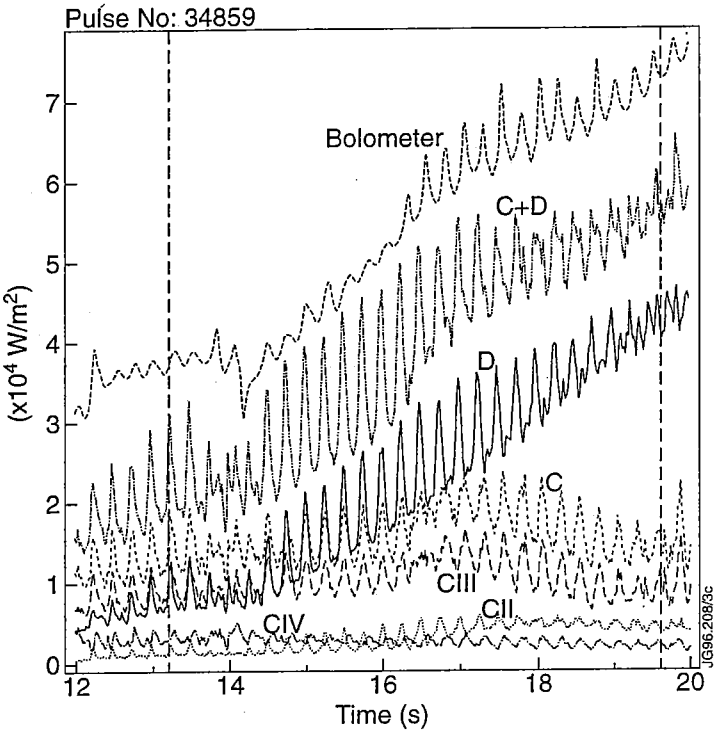

Figure 7.5: Radiated power measured by VUV spectroscopy for the Ohmic density limit pulse 34859.

Radiated power components measured by VUV spectroscopy are shown in Fig. 7.5 for an Ohmic discharge in which the density was ramped to the density limit by deuterium gas fuelling in the divertor. The main parameters of this discharge are shown in Fig. 7.6. The spectroscopic signals are more strongly influenced by the strike point sweeping across the target than the bolometer signal, due to the narrower acceptance cone of the VUV spectrometer. When comparing with spectroscopy, the core plasma contribution from inside the LCFS is subtracted from the bolometer measurement. This is done using a near-horizontal bolometer view and assuming uniform emission inside the LCFS. With this assumption, if $\epsilon(s)$ denotes the radiated power density on a given flux surface, one obtains:

$$\frac{\int_{VERC} \epsilon(s)\ dl_b}{\int_{HOR} \epsilon(s)\ dl_a} = \frac{b}{a} =: \kappa \tag{7.2}$$

where a and b are the plasma horizontal and vertical minor radius, κ is the elongation (~ 1.7 in JET) and the integrals in the numerator and denominator are the radiated power fluxes along a vertical (VERC) and a horizontal (HOR) line of sight through the plasma centre inside the LCFS respectively. Thus

$$\int_{Bolom} \epsilon(s)\ dl - \kappa \int_{HOR} \epsilon(s)\ dl_a \tag{7.3}$$

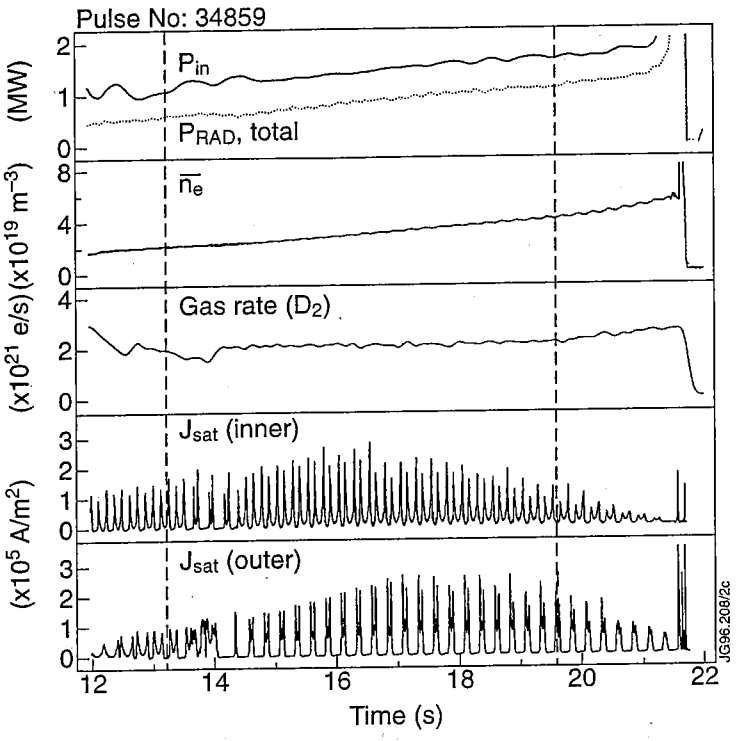

Figure 7.6: Ohmic density limit pulse 34859. The vertical dashed lines mark the time slices chosen for comparison with impurity simulations (see later).

gives an estimate of the radiated power flux [W/m^2] in the divertor plus X-point region along the line of sight of Fig. 7.1. In general, for the medium/high density divertor discharges analysed ($n_e \sim 10^{19} - 10^{20} m^{-3}$) the core plasma contribution is of order 10-20% of the total radiated power flux measured by the bolometer chord shown in Fig. 7.1.

From this analysis it emerges that of the carbon ionization stages C III is the strongest radiator. This result differs from the measurements reported from other divertor tokamaks, such as JT60-U [118] and DIII-D [119]. The main difference to notice is that JET operates at higher densities and lower divertor temperatures, especially in the inner (colder) divertor, where the measurements of this thesis were taken. Secondly, the DIII-D measurements, lacking many strong transitions (those with wavelength above DI, L_β) have to rely strongly on modelling and therefore are much less accurate. Thirdly, the more recent radiation measurements from JT60-U are derived from visible measurements and have to rely completely on modelling assumptions. I return to this issue later in this Chapter when the comparison with impurity transport modelling is addressed. However, it is clear that the lack of measurement of the C IV resonance line is a point of anxiety for the present analysis.

The results presented so far apply to discharges operated both on carbon and beryllium divertor targets. In fact the spectra of Fig. 7.2 were measured during a pulse run on the Be target. The results suggest that during beryllium operation the target surfaces were coated with a carbon layer, possibly originating from sputtering at the carbon walls of the tokamak. Also, in both cases the dominant impurity radiator is carbon, as measured by the double SPRED. These observations clarify why characteristics of plasmas on beryllium and carbon targets were very similar (see Section 2.13). Figs. 7.7 compare two steady state ELMy H-mode discharges, one on the CFC and one on the Be target, with very similar global plasma parameters. The measurements show that the carbon levels, as monitored by visible spectroscopy from C III line emission at 4650 Å at the inner and outer target, changed modestly with the two target materials. By contrast, the Be II influx, measured by line emission at 5270 Å, was considerably stronger (more than noise level) for plasmas diverted onto the Be target plates, especially from the outer divertor, to which the power flow is higher.

7.2.2 Be Melting Experiments

A series of experiments were carried out in the final period of the MkI campaign with controlled melting of the Be target tiles, in order to assess plasma performance on molten and damaged beryllium (see Section 2.13). These were the only experiments during which significant Be VUV emission was observed with the divertor double SPRED. Fig. 7.8 shows VUV emission measured during one such discharge, when about 15MW of additional heating was applied without sweeping of the strike points. During this phase beryllium is the strongest radiator, with Be II carrying most of the power towards the end of the heating phase (see Fig. 7.9), while the carbon line radiation is observed to decrease by an order of magnitude.

The double SPRED setup is however not optimized for the observation of Be spectral emission, so extensive atomic modelling is required in order to obtain an estimate of the total line power from Be ions. The Be II resonance line (3130.6 Å) lies in the near UV and could not be measured and of the observable $n = 3 - 2$ transitions, the 1036.7 Å ($2s - 3p$) line was severely blended with the O VI doublet and could not be used. Thus, the radiated power component for Be II is derived from the measured $n = 4 - 2$ line intensities (842 Å and 1143 Å). The sum total

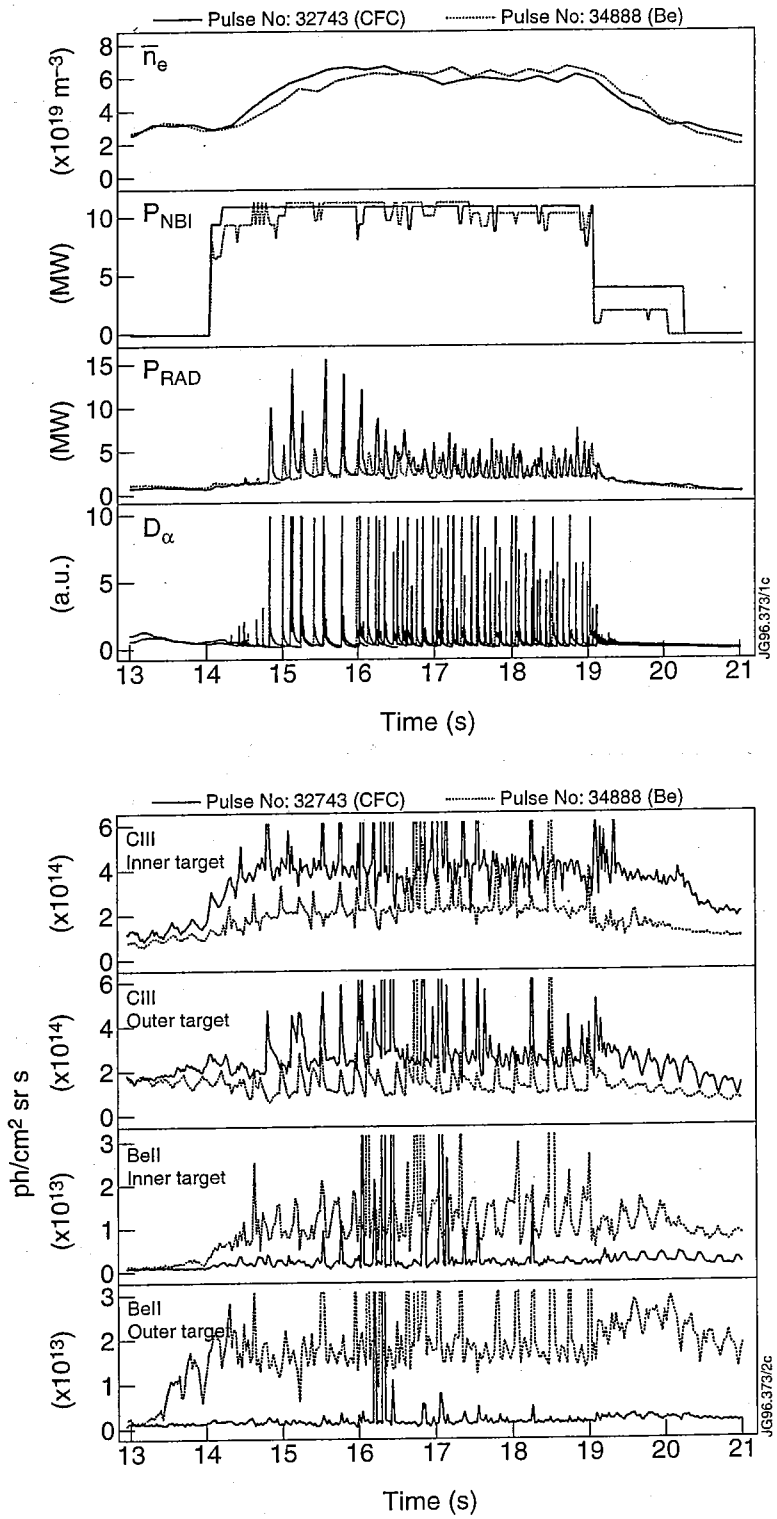

Figure 7.7: Comparison of ELMy H-mode discharges diverted on CFC and Be targets: (top) global plasma parameters of the two discharges; (bottom) C III (4650 Å) and Be II (5270 Å) visible emission from inner and outer divertor target plates.

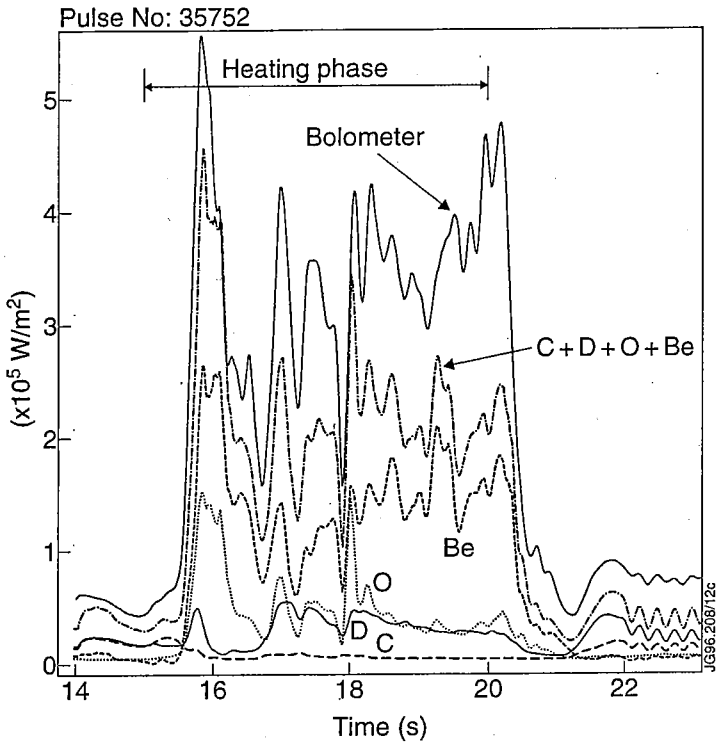

Figure 7.8: Radiated power components measured with the divertor double SPRED during a discharge with controlled Be target melting.

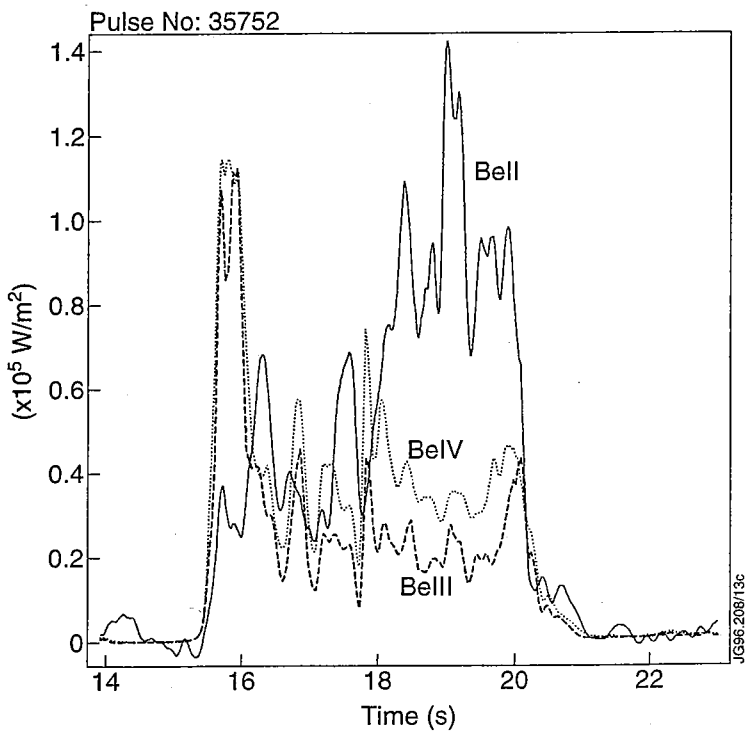

Figure 7.9: Be radiated power components for the discharge of Fig. 7.8.

Ion	λ (Å)	Transition	Comment
Be II	3130.6	$2s\ ^2S - 2p\ ^2P$	not measured
	1036.3	$2s\ ^2S - 3p\ ^2P$	not used (blended with O VI doublet)
	842.	$2s\ ^2S - 4p\ ^2P$	account for 1-1.5% of
	1143.	$2p\ ^2P - 4d\ ^2D$	Be II line power
Be III	100.3	$1s^2\ ^1S - 1s2p\ ^1P$	not measured
	675.7	$1s2p\ ^3P - 1s3d\ ^3D$	account for
	583.0	$1s2s\ ^3S - 1s3p\ ^3P$	~15% of
	725.6	$1s2p\ ^3P - 1s3s\ ^3S$	Be III line power
Be IV	410.0	3 – 2	1% of Be IV line power

Table 7.2: Summary of spectral lines used for beryllium radiated power measurements with the divertor double SPRED.

line power fraction from these two lines varies between 1-1.5% of the total Be II line power in the region of interest. The Be III resonance line (100 Å) lies just outside the 2105-SPRED wavelength range and the Be III radiated power component was thus obtained from $n = 3-2$ transitions (see Table 7.2). For Be IV the only line measured with the divertor SPRED is the Balmer$_\alpha$ (410 Å), which radiates about 1% of the total Be IV line power. It is evident that the lack of measurements of resonance line emission leads to large uncertainties (a factor of 2 or more) in the evaluated Be radiation. This example stresses the need of measurements of the resonance lines when undertaking this type of analysis and gives an idea of the large uncertainties that are inevitably associated with spectroscopic estimates of the radiated power from visible line emission!

Figs. 7.10 shows VUV spectra of the divertor measured with the double SPRED during the beryllium target melting discharge of Fig. 7.8.

As the power load to the target is increased and melting occurs, oxygen is released (see Fig. 7.8), most likely following molecular breakup of beryllium oxides. The oxygen radiation returns to negligible levels (which are characteristic of divertor plasma operation in the MkI) when the targets cool after the additional heating is switched off. The oxygen radiation is the sum of the radiated power components of O III-O VI and is obtained in the same way as described for carbon (see Table 7.3). In addition, the O VI resonance doublet can be measured and all of the resonance transitions in O IV contribute to the B-like oxygen radiated power. Of the oxygen

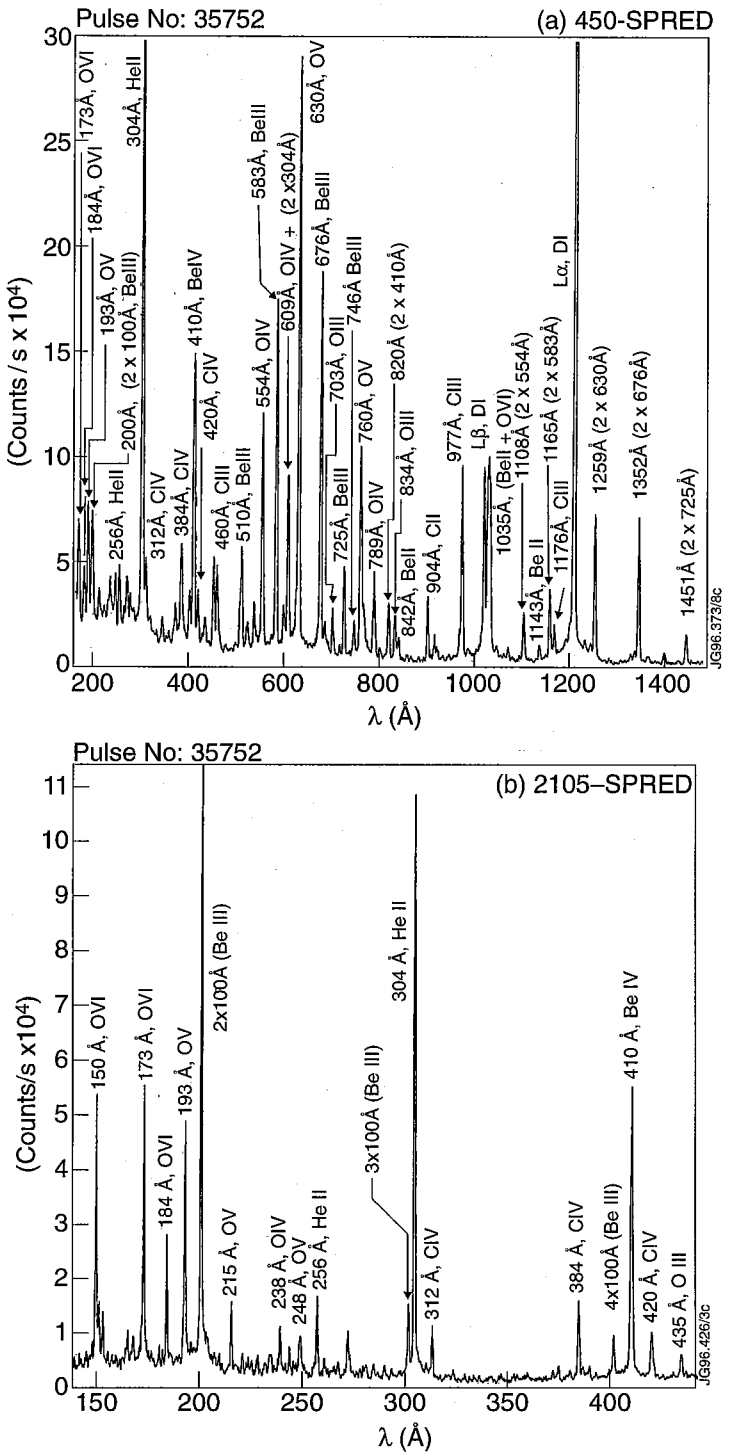

Figure 7.10: VUV spectra of the divertor measured with the double SPRED during the beryllium target melting discharge of Fig. 7.8: (a) 450-SPRED, (b) 2105-SPRED (t = 18 s). In Fig. (a) the y axis scale is reduced, to enhance the weaker lines.

Ion	λ (Å)	Transition	Comment
O III	834.5	$2s^2 2p^2\ ^3P - 2s2p^3\ ^3D$	
	703.4	$2s^2 2p^2\ ^3P - 2s2p^3\ ^3P$	
	599.	$2s^2 2p^2\ ^1D - 2s2p^3\ ^1D$	
		$2s^2 2p^2\ ^1S - 2s2p^3\ ^1P$	
O IV	554.4	$2s^2 2p\ ^2P - 2s2p^2\ ^2P$	
	609.4	$2s^2 2p\ ^2P - 2s2p^2\ ^2S$	
	789.4	$2s^2 2p\ ^2P - 2s2p^2\ ^2D$	
	238.5	$2p\ ^2D - 3d\ ^2D$	
O V	629.7	$2s^1\ ^1S - 2s2p\ ^1P$	
	760.4	$2s2p\ ^3P - 2p^2\ ^3P$	
	215.2	$2s2p\ ^3P - 2s3s\ ^3S$	
	192.9	$2s2p\ ^3P - 2s3d\ ^3D$	
O VI	1032+1038	$2s\ ^2S - 2p\ ^2P$	$\geq$90% of
	150.1	$2s\ ^2S - 3p\ ^2P$	O VI line power
	184.0	$2p\ ^2P - 3s\ ^2S$	
	173.0	$2p\ ^2P - 3d\ ^2D$	

Table 7.3: Summary of spectral lines used for oxygen radiated power measurements with the divertor double SPRED.

ionization stages, O VI is the strongest radiator.

As a test of the errors associated with line ratios to derive T_e , the intensity of the O VI resonance line is derived from line ratio measurements, in the same way as it was done for C IV, and then compared with the actual measurement. Using the 184/173 line ratio, one infers T_e ~100 eV, and then using the 184/1035 (doublet) ratio one deduces the O VI resonance line intensity, $I(1035) = 150 \times I(184)$. Instead the measurements show $I(1035) = (80 - 100) \times I(184)$, which corresponds to T_e ~50-60 eV, indicating that the resonance line radiates at lower temperature than the $n = 3 - 2$ transitions. However, in this case the error in the calculated resonance line emission is smaller (less than a factor of 2) than in the case of C IV, because O VI radiates at higher temperatures, where the $3s - 2p/2p - 2s$ line ratio changes less strongly with T_e than in the 10-20 eV range.

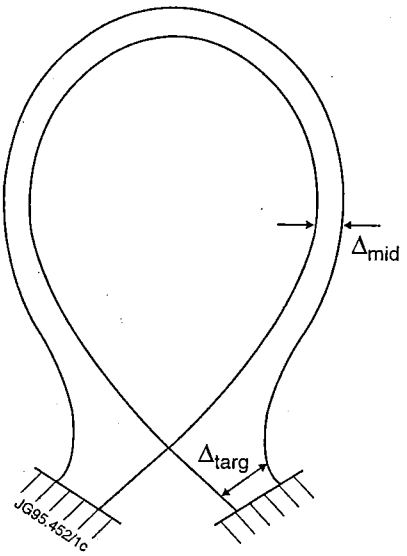

Figure 7.11: Schematic representation of a flux tube in the SOL, with midplane and target poloidal widths Δ_{mid} and Δ_{targ}.

7.2.3 Effect of Change in the Divertor Flux Expansion on C vs D Radiation

The effect of plasma-wall clearance on the relative importance of carbon and deuterium radiation is studied for a series of Ohmic density limit discharges with deuterium gas fuelling in the divertor. All these discharges were very similar (and one of these is the discharge shown in Fig. 7.6) but are separate into two sets according to the difference in the divertor flux expansion. The divertor flux expansion, F.E., is defined as the ratio of the poloidal width Δ of a flux tube, perpendicular to the poloidal field B_θ, at the target to the width upstream (see Fig. 7.11), e.g. at the midplane: F.E. $= \Delta_{targ}/\Delta_{mid}$.

At any given poloidal location, $\Delta = \Delta\psi/(\partial\psi/\partial n)$, where $\Delta\psi$ is the variation of the poloidal magnetic flux across the flux tube and $\partial\psi/\partial n = 2\pi R B_\theta$ is the normal derivative of the flux [120]. Thus, since the toroidal field does not vary too much from the midplane to the target ($R \sim$ constant) the cross sectional area of the flux tube projected perpendicular to the local field B is approximately constant poloidally, although it changes shape with varying magnetic field pitch, B_θ/B. For instance, near the X-point, where the pitch is small, Δ_{X-pt} is larger (see Fig. 7.11). Therefore, in order to increase the flux expansion in the divertor:

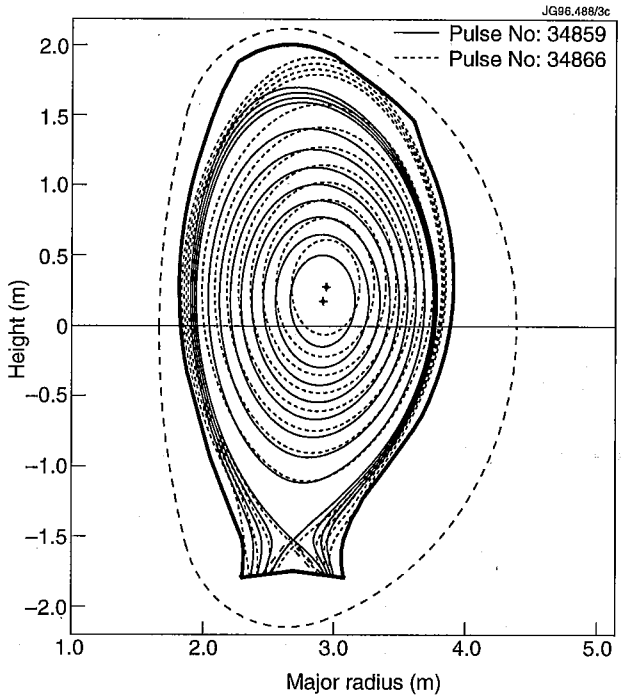

Figure 7.12: Magnetic equilibria for two discharges with different divertor flux expansion:pulse 34859, low flux expansion (well clear from walls), solid lines; pulse 34866, high flux expansion (low wall clearance), dashed lines.

$$F.E. = \frac{\Delta_{targ}}{\Delta_{mid}} = \frac{(B_\theta/B)_{mid}}{(B_\theta/B)_{targ}} \tag{7.4}$$

one has to work at shallow field angles. Increasing the flux expansion in the divertor increases the total target 'wetted' area, but also affects the plasma clearance from the walls, as shown in Fig. 7.12.

For all of the discharges analysed, the ratio of carbon to deuterium radiation, measured by VUV spectroscopy, progressively decreases with increasing plasma density and radiated power fraction, P_{RAD}/P_{IN}. However, in the case of high plasma clearance from the vertical walls (i.e. low flux expansion in the divertor), deuterium radiation strongly dominates at high density, whereas at low wall clearance (i.e. high flux expansion) the radiated power is equally distributed between deuterium and carbon, as shown in Fig. 7.13, presumably due to increased impurity influx from the walls.

These observations are correlated with the occurrence of the density limit (outside the time window of the double SPRED for these discharges) at higher densities for discharges with high wall clearance, though $P_{RAD}/P_{IN} \sim 80$ % for both high and low wall clearance cases at the density limit.

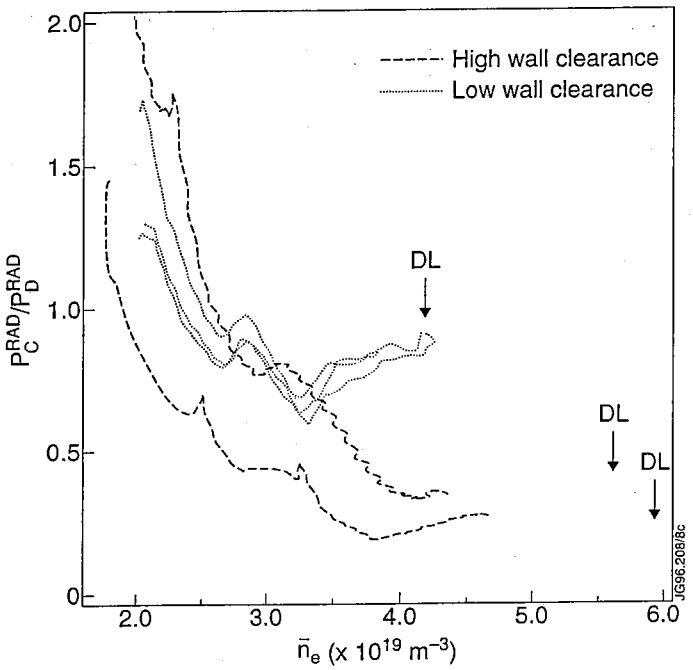

Figure 7.13: Ratio of carbon to deuterium radiated power versus volume averaged density for Ohmic low flux expansion (pulses 34859, 35430) and high flux expansion (pulses 34855, 34856, 34866) discharges. Also shown is the value of the density at the occurrence of the density limit (DL), outside the time window of the double SPRED for these pulses.

7.3 Comparison with Impurity Transport Simulations: Low Density

The Ohmic discharge shown in Fig. 7.6 was modelled in the low density and plasma detachment phases using 2D Monte Carlo simulations (DIVIMP/NIMBUS, see Chapter 6) of impurity and neutral hydrogen transport. These simulations are used to interpret the spectroscopic measurements in the divertor environment and, in turn, the physics assumptions in the models are challenged by the experimental findings.

The first step in modelling a discharge involves generating the spatial computational grid on which the calculations are performed. The grid is produced from the calculated magnetic equilibrium for the discharge, which uses as input measurements from pick-up coils. The grid also contains detailed information on the material structures inside the vacuum vessel, which affect the transport of the neutrals in the region between the plasma and the vessel walls. An example of computational grid is shown in Fig. 7.14 for pulse 34355.

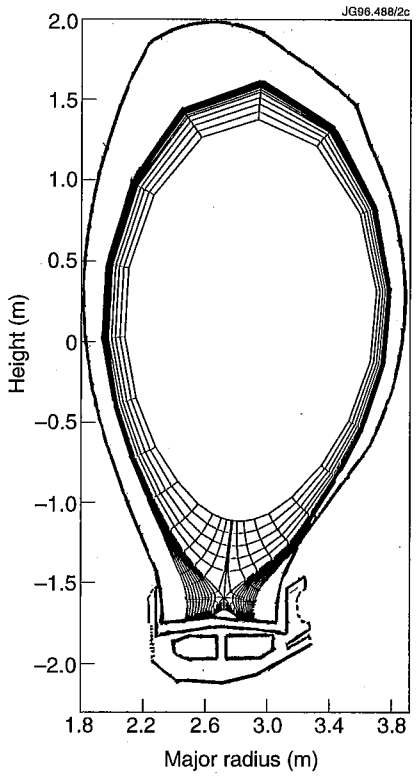

Figure 7.14: Computational grid for the discharge 34355.

7.3.1 The Hydrogenic Plasma

In the low density phase of the discharge, the hydrogenic background plasma is obtained by solving the steady state fluid equations for classical transport along the magnetic field, with boundary conditions from the Langmuir probe measurements of n_e and T_e at the divertor target ('onion skin' model within DIVIMP, as discussed in Chapter 6). The separatrix electron temperature is 5.7 eV at the inner and 17 eV at the outer target and the separatrix density is $3.7 \times 10^{19} m^{-3}$ and $1.0 \times 10^{19} m^{-3}$ at the inner and outer target, respectively. The ion temperature at the target is not measured but is assumed equal to the electron temperature. The lack of T_i measurements in the divertor region is a problem in most fusion experiments and knowledge of T_i remains one of the big serious deficiencies in divertor/edge plasma modelling at present.

A converged plasma solution is reached after few iterations with NIMBUS (two in this case), to yield the hydrogen ionization source distribution, as well as the neutral carbon ionization distribution. Spectral features may then be synthesized according to the specific viewing geometry of the various diagnostics. Fig. 7.15 (a) compares

the calculated and measured divertor D_α emission profiles (the measurement was obtained with the flux camera described in Chapter 5). It can be seen that although the overall shape of the profile is quite well reproduced, the deuterium density in the private plasma is severely underestimated in the model. This is even more evident when comparing L_α emission along the SPRED LOS (see Fig. 7.15 (a)), which is particularly sensitive to emission from the private plasma region. The inadequate modelling of neutral deuterium distribution in the private flux region in turn affects the modelling of the carbon source in this region, as will be shown in the following Section.

It remains unclear what is the cause of this relatively high neutral density in the private plasma, but it is thought that neutral recirculation in the sub-divertor region (through the gaps between pairs of tiles of the MkI target structure) plays a role. Increasing the electron density (and thus the neutral density) in the private plasma region does not produce any noticeable effect on the D_α emission profile. Increasing the values of the divertor targets 'transparency' in NIMBUS/EDGE2D simulations of a similar Ohmic pulse enhances the D_α emission in the private plasma region [121] although not to the extent observed experimentally. Note that, however, very high transparency values must be invoked (a factor of 3 to 4 higher than the nominal values, obtained from 3D Monte Carlo calculations of neutral random walk in the MkI divertor/subdivertor region) in order to enhance the D_α emission in the private plasma region. This is one of the areas where experiments in the MkII divertor, with its more closed target geometry, may provide some explanation.

7.3.2 Impurities

Since the Ohmic discharge 34859 was with Be target, but the spectroscopic observations show that carbon is the dominant impurity, two impurity simulations have been performed (using the same hydrogenic plasma). One assumes a carbon target and the other a beryllium target. Physical and chemical sputtering by deuterons and impurity self-sputtering determine the carbon source. Carbon production due to physical sputtering is obtained using the Bohdansky formula, with data as in [112]. The chemical yields are taken from the measured CD_4 yields as in [117]. Chemical sputtering is then modelled by releasing 0.1 eV carbon atoms from the target/wall surfaces. A constant $D_\perp = 1m^2/s$ for all impurity ionization stages is

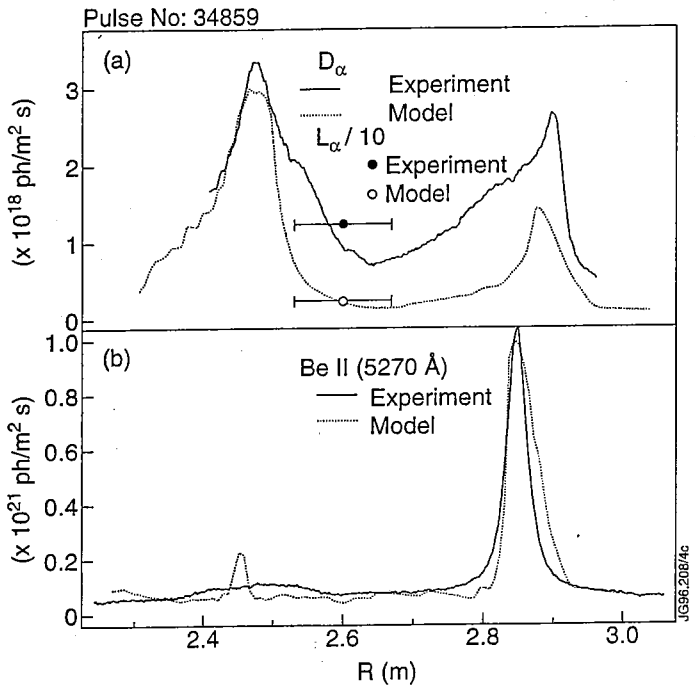

Figure 7.15: Comparison of measured and calculated D_α emission (a) and Be II emission (b) in the divertor for the Ohmic discharge 34859 at low density. Also shown in Fig. (a) is the comparison between calculated and measured L_α intensity along the divertor SPRED LOS.

assumed. Physical sputtering alone accounts for the beryllium source. However, BeO has to be assumed as target material in the model to reproduce the Be II emission, as measured by the flux camera viewing the divertor region from the top of the machine (see Fig. 7.15 (b)). BeO has the effect of both lowering the sputtering yield (by about a factor of 10 at 40 eV) and increasing the threshold energy for sputtering (E_{th} = 29 eV) with respect to the case of pure beryllium (E_{th} = 10 eV), [112]. The choice of BeO as a target is also justified by the spectroscopic observations during beryllium target melting experiments, reported earlier, which showed that under normal operation oxygen is gettered by beryllium. In practice, a more realistic picture would also have included the effect of carbon contamination of the beryllium target surfaces, but sputtering yields for beryllium carbides are not available. Similarly, the simulation with a pure carbon target does not take into account the presence of a Be substrate under the carbon layer. It is not known how this may affect the carbon sputtering yields.

The calculated beryllium radiation (see Fig. 7.16) is negligible ($< 1\ KW/m^2$) as expected from the spectroscopic observations. The total radiated power is a

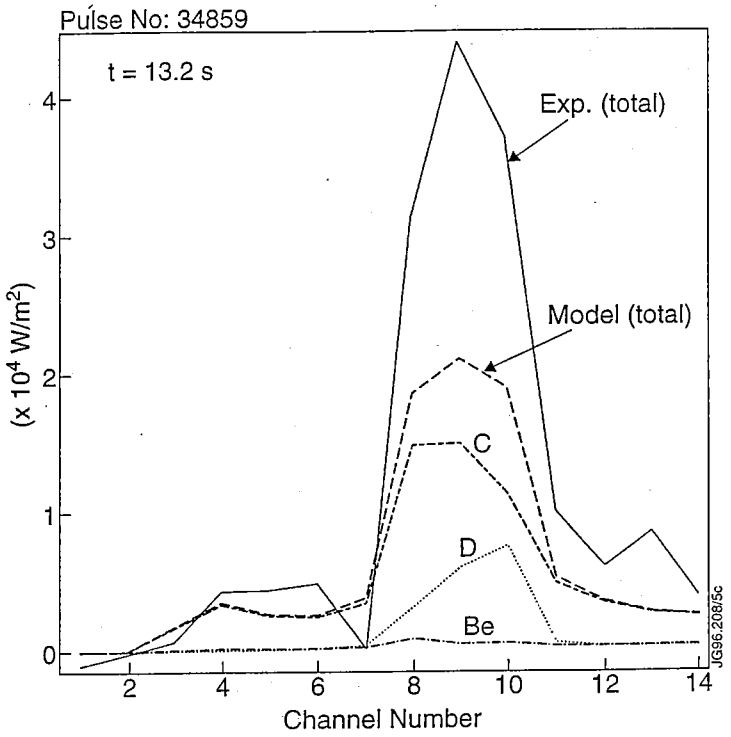

Figure 7.16: Comparison of measured (bolometer vertical lines of sight) and calculated radiated power components for pulse 34859 at low density.

factor of two lower than that measured with the bolometer. This discrepancy is due in part to underestimation of the deuterium radiation, especially in the private flux region (see Fig. 7.15), as discussed in the previous Section, and in part to underestimation of C III radiation. In fact, the ratio of C III to C IV radiation along the SPRED LOS is underestimated by a factor of five with respect to the experimental value. This is attributed to incorrect modelling of the carbon source from the private plasma target, due to the incorrect description of the deuterium density in this region. In fact, the VUV spectrometer LOS, which doesn't view the strike points, is particularly sensitive to carbon sputtering yields in the private plasma. Instead, C II-IV visible spectroscopy measurements integrated over the entire emission profiles are reasonably well reproduced. This is shown in Figs. 7.17-7.20, which summarizes the comparison of measured and calculated C II-C IV visible and VUV spectral emission at low density and detachment (see following Sections). The C II VUV line emission is reasonably well reproduced, but the C III resonance lines emission is grossly underestimated. On the other hand, the measured C IV $n = 3 - 2$ transitions and the derived resonance line emission are consistent with the simulation. Unfortunately, for this pulse carbon profiles from the flux camera

were not available, because the C II filter was substituted with the filter for Be II measurements. However, C II visible emission meaurements from three different spectral lines are available, at 5145 Å ($3s\ ^4P - 3d\ ^4P$), 6785 Å ($3s\ ^4P - 3p\ ^4D$) and at 7120 Å ($3p\ ^4D - 3d\ ^4F$).

7.4 Comparison with Impurity Transport Simulations: Plasma Detachment

The distinctive signature of divertor plasma detachment is the low peak ion flux to the divertor target, the high D_α emission from the divertor region (see Section 2.10), and the large radiative losses from the X-point region. As the main plasma density is increased from the low recycling to the high recycling regime, strong parallel gradients arise in the SOL, while the electron pressure is measured to remain constant. This means that high densities, and thus low temperatures, are achieved at the divertor target. In JET, usually n_e (inner divertor) > n_e(outer divertor), thus T_e(in) < T_e(out). When the divertor electron temperature decreases to values approaching 5 eV, the parallel electron pressure starts to decrease at the target, marking the onset of detachment. A mechanism to explain this pressure drop (momentum loss) in the divertor has been proposed, in which the plasma momentum flux is reduced by charge exchange collisons with the recycling neutrals in the divertor [122]. When $T_e \sim 5$ eV, $H - H^+$ charge exchange processes start to dominate over ionization (see Chapter 3). Thus, the residence time of the recycling neutrals in the divertor is increased and a significant fraction of the inflowing momentum is removed from the plasma ions through charge exchange collisions (and carried to the target by the neutrals), which reduces the ion flux to the divertor target. However, the charge exchange momentum losses cannot by themselves explain quantitatively the reduction of total ion flux to the divertor target observed experimentally at detachment. Borrass [123] concluded that plasma recombination must occur, providing a particle sink, to explain this drop in ion flux at the target and the enhancement of D_α emission in the divertor. There is experimental evidence in JET, from visible spectroscopy of deuterium emission, of the occurrence of plasma recombination at detachment. Evidence of this is obtaind from the behaviour of the peak ion flux measured by target Langmuir probes and by visible spectroscopy measurements of

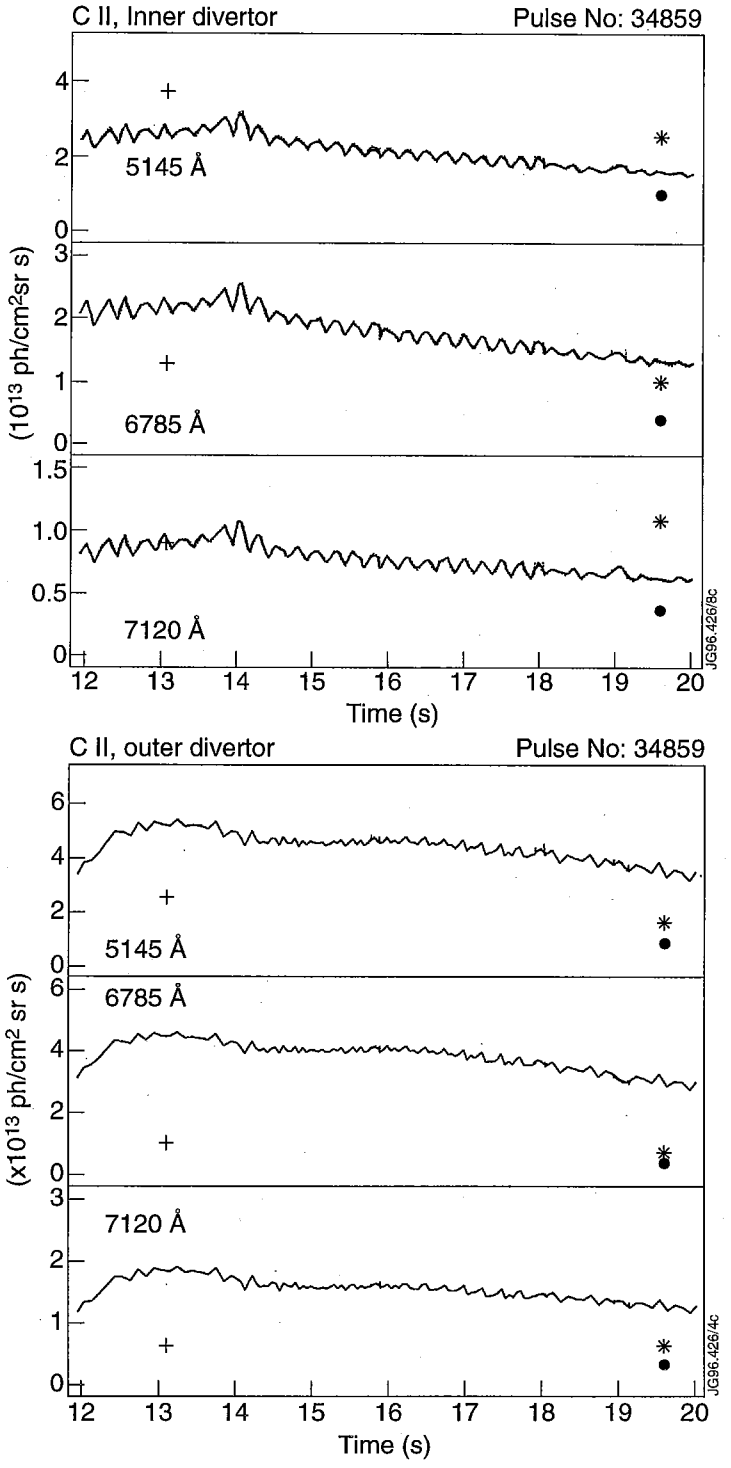

Figure 7.17: (a) C II visible emission, inner divertor, (b) outer divertor, for the Ohmic density limit discharge 34859: comparison with the simulations at low density (+) and plasma detachment (∗) first simulation, (•) 2nd simualtion, with modified T_e-gradient.

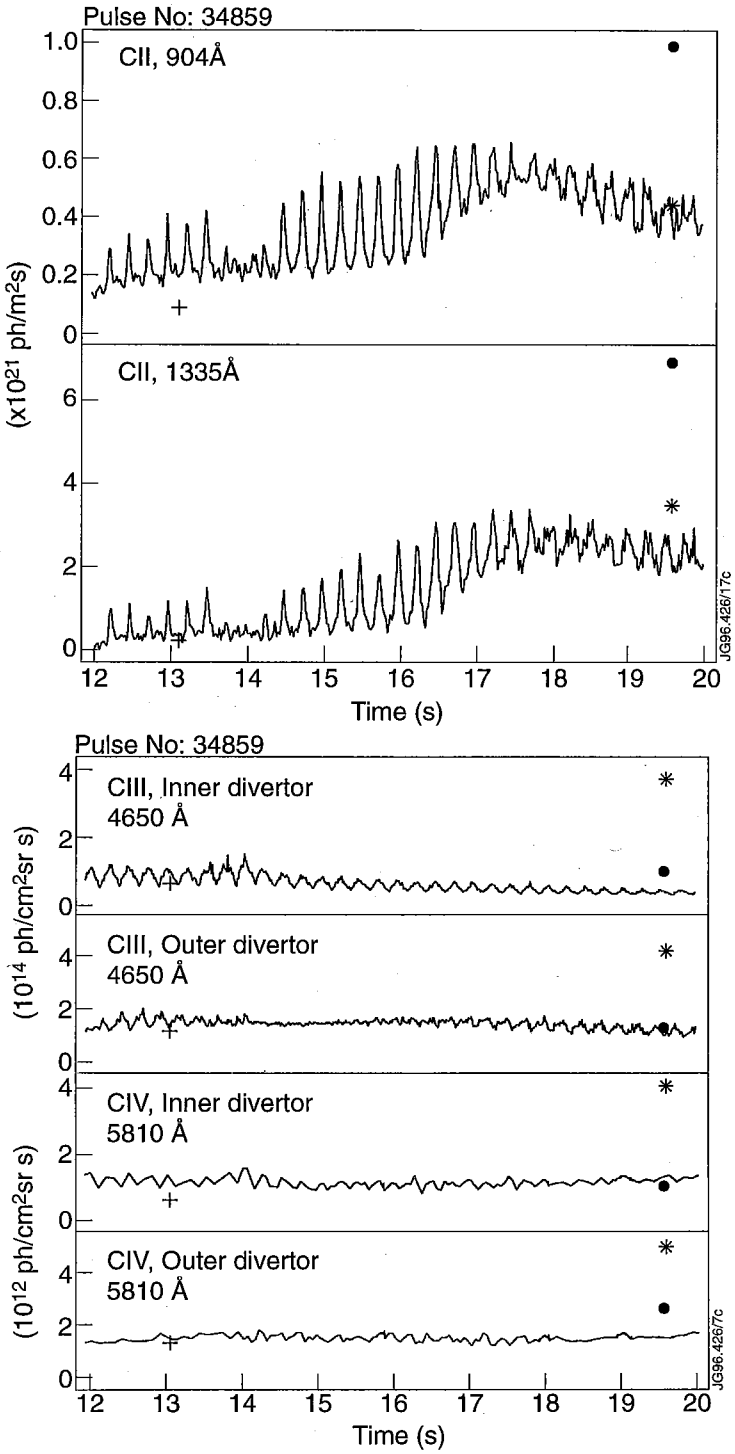

Figure 7.18: (c) C II VUV emission, double SPRED; (d) C III-C IV visible emission, inner/outer divertorfor the Ohmic density limit discharge 34859: comparison with the simulations at low density (+) and plasma detachment (∗) first simulation, (•) 2nd simualtion, with modified T_e-gradient.

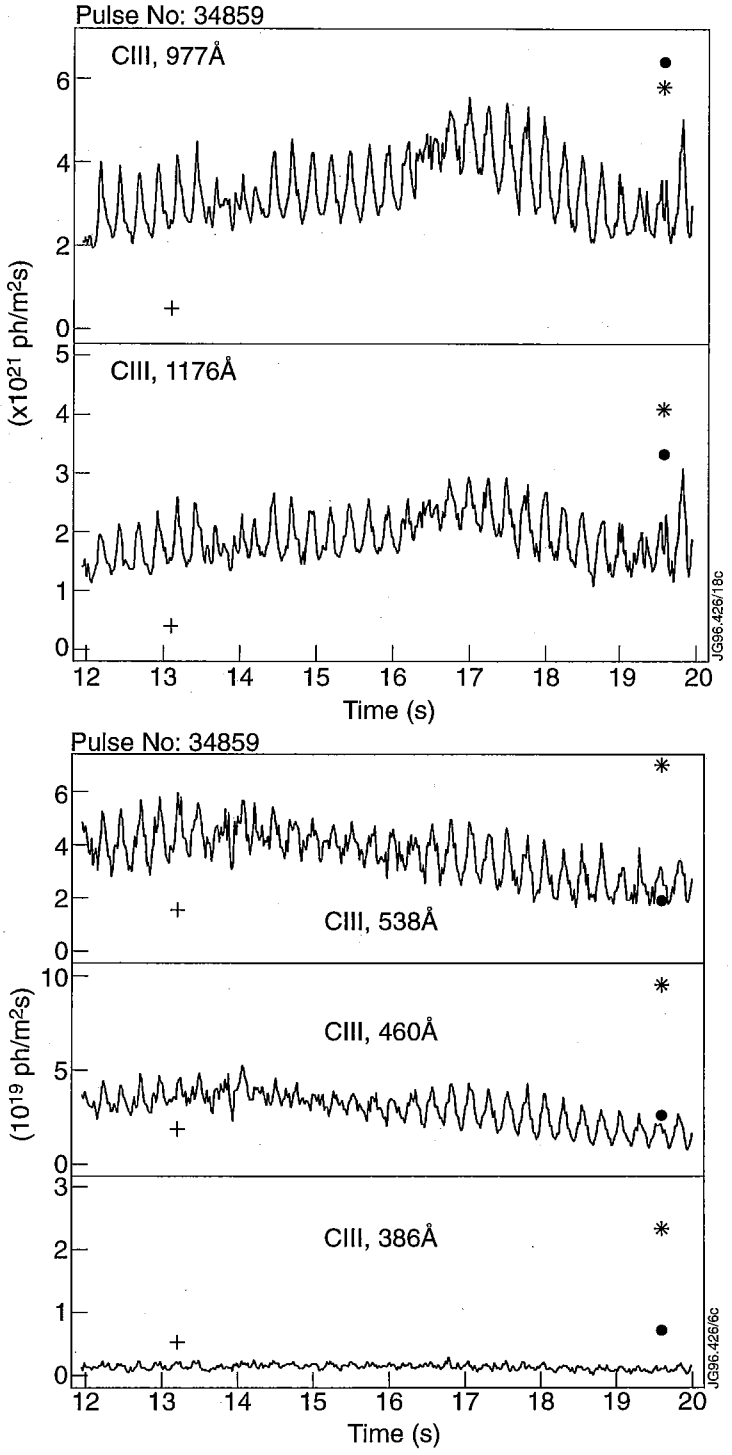

Figure 7.19: (e), (f) C III VUV emission, double SPRED, for the Ohmic density limit discharge 34859: comparison with the simulations at low density (+) and plasma detachment (∗) first simulation, (•) 2nd simualtion, with modified T_e-gradient.

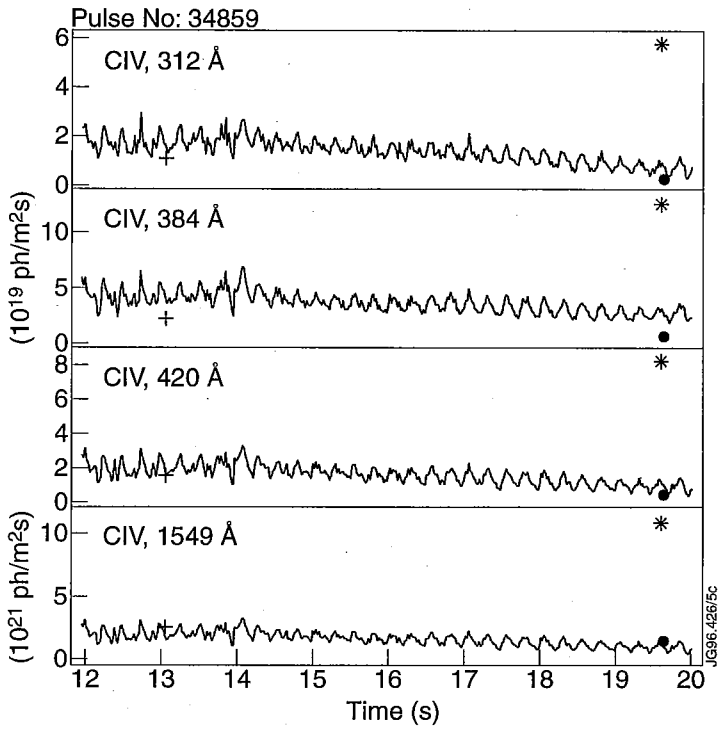

Figure 7.20: (g) C IV VUV emission, double SPRED, for the Ohmic density limit discharge 34859: comparison with the simulations at low density (+) and plasma detachment (∗) first simulation, (•) 2nd simualtion, with modified T_e-gradient.

DI emission.

In the low recycling regime, D_α emission from the divertor occurs in the vicinity of the target plates and, assuming a recycling coefficient of 1, is related to the ion flux to the target $\Gamma_{D+} = I_{D_\alpha} \cdot S/XB$, with S/XB the theoretical ionization/photon coefficient. At low recycling the ratio of the measured total ion flux to the target to D_α emission is typically 20-25 [32], consistent with S/XB values at $T_e(\sim 20$ eV) and $n_e(\sim 10^{19} m^{-3})$ characteristic of this regime. The measured ratio decreases drastically, as plasma detachment progresses, down to about 5 in the outer divertor and about 0.2 in the inner divertor, showing the difference in the degree of detachment between inner (colder) and outer (hotter) divertor [32]. Such low ratios in the inner divertor can only be reproduced in the calculations if recombination is included. Furthermore, evidence of recombination taking place at detachment is given by the increase of the measured ratio of D_γ to D_α intensity from the inner divertor as detachment proceeds. These ratios are a factor of 2-3 higher than those calculated when electron excitation is the driving populating mechanism of the DI excited states in the collisional radiaitve calculation, but are consistent with calculations

that include electron-ion recombination processes. These observations also indicate that the target electron temperature must be in the range of 1 eV for recombination to be dominant. This provides further evidence of the fact that in this regime the conventional interpretation of Langmuir probe I-V characteristics becomes questionable, resulting in a gross overestimate of T_e, especially at the inner divertor target, where temperatures below 5 eV cannot be measured even when the plasma is fully detached from the target.

Furthermore, in conditions of high densities and low temperatures, characteristic of detachment, the divertor plasma may become optically thick to Lyman radiation. This would modify the DI excited state populations and require a collisional radiative model coupled to the transport of radiation for the interpretation of deuterium emission. There is some experimental evidence of L_β reabsorption in the MkI divertor, obtained from the measurement of the L_β /D_α intensity ratio using the divertor double SPRED. This ratio is observed to decrease marginally [124] in Ohmic density limit discharges and more strongly in high density L-mode detached plasmas. In a uniform slab of plasma of neutral density $n_D \sim 10^{20} m^{-3}$, the absorption length for L_α is of 0.2cm, and of 2cm for L_β [35]. Thus, in low temperature, high neutral density plasmas the L_α absorption length could become comparable to the dimension of the neutral cloud. At present, however, a quantitative assessment of the experimental L_β /D_α ratios with realistic plasma modelling and radiation transport is not available, and this goes beyond the scope of this thesis.

Whereas it is certainly the case that recombination is needed as a particle sink in the codes to obtain the observed reduction in ion flux to the target, the details of the actual process are not yet clearly identified, given the large uncertainties associated with the measurement of T_e from Langmuir probes. Work is in progress to infer information on the value of T_e and parallel T_e-gradients in the divertor from spectroscopic measurements (e.g. D_α/D_γ line ratios, line ratios with a new divertor thermal helium beam diagnostic [125]).

7.4.1 The Hydrogenic Plasma

In its present form (with the inclusion of charge exchange momentum losses in the momentum balance equation, but without the recombination term in the continuity equation) the OSM is not suitable for modelling detached plasmas. In fact, at de-

tachment the basic assumption of the OSM, that the profiles at the target determine the plasma solution upstream is no longer valid. In this regime, enhanced parallel sources/losses and cross-field diffusion in the divertor determine the plasma solution upstream, which therefore becomes very insensitive on the boundary conditions at the target. Also, the plasma transport depends on the details of the radiated power profile along the flux tubes in the scrape-off layer, which are not known. For this reason, several attempts at modelling the detached phase of the Ohmic discharge 34859 (and of other discharges) with OSM have been unsuccessful. Therefore, an alternative approach was adopted, i.e. an empirical description of the hydrogenic plasma, based on the experimental observations and on the results from EDGE2D simulations of a similar discharge that are closer to the measured profiles. This is obtained by specifying a set of prescriptions for the plasma parameters of the SOL, divertor and private plasma and adjusting these values by comparing with the bremsstrahlung and D_α emission profiles from the divertor, measured by the flux camera, until a reasonable agreement with the measurements is obtained. The bremsstrahlung signal provides essential information at detachment, especially on the divertor density ($\epsilon_B \propto n_e^2/\sqrt{T_e}$), since D_α emission, unlike in the low recycling regime, is no longer representative of the ion flux to the target.

In the SOL the hydrogenic plasma is prescribed according to a 3-zone (collision, radiation+conduction, conduction) detachment model, which is an extension of the model proposed in [126]. In the collision zone (the 'cushion') the solution starts with specified profiles of n_e and T_e at the targets. The standard interpretation of Langmuir probe measurements at plasma detachment produces values of T_e that are too high ($\sim$ 6-7 eV) and inconsistent with the spectroscopic observations. Therefore the measured T_e profile is reduced by a factor of 4, consistent with spectroscopy. The electron density profile is then calculated from the ion saturation current assuming $M = 1$ at the target, where M is the Mach number. This gives an idea of the large uncertainties associated with the modelling of plasma detachment already at the first stage, when specifying the boundary conditions for the calculation of the background plasma.

In the collision region, where the model assumes no ionization sources, low values of T_e, T_i are specified, while n_e is increased linearly from the target value along the field lines. This is a crude approximation for the drop of parallel pressure at the target, since detailed information on the actual pressure profile is not available. In

the simulation for pulse 34859 the density is raised linearly by a factor of 8 along the field lines up to the X-point, where it takes the value of $\sim 2 \times 10^{20} m^{-3}$, while the temperature is kept constant at the target value of $T_e \sim$ 1-2 eV. These values are constrained by the measured D_α and bremsstrahlung profiles across the target (see Figs. 7.21, 7.22). This simulates a region of low temperature in which plasma recombination can take place. The background plasma velocity is set equal to the ion sound speed at the target. In this zone, since it is assumed that there is no ionization, $n(0)v(0) = n(s)v(s)$, from which $v(s)$ is deduced.

In the radiation+conduction zone the solution is obtained according to power balance, and specifying the fraction of power radiated in the SOL, as measured by the bolometers, with respect to the power flow to the target (estimated by Langmuir probe measurements). The density is obtained assuming constant pressure. The background plasma velocity $v(s)$ decreases linearly to zero at a specified distance upstream.

In the conduction zone the fluid equations are solved in the OSM at constant pressure. The measured bremsstrahlung profile shows the onset of an X-point marfe from the appearance of a third peak in the middle of the profile (see Fig. 7.21). This measurement, together with the assumption of pressure balance along the flux tubes, is used to constrain the value of the electron density in the viciniy of the X-point. The background flow velocity is also specified along the field lines, converging along inner and outer branches of the flux tubes at the X-point, where it is assumed close to the ion sound speed. The velocity is then linearly ramped down to zero by the midplane. This flow is necessary to retain the impurities at the X-point marfe, where the radiation peak is observed experimentally, although the forces acting on the impurities in the marfe region are not known at present.

The simulation, shown in Fig. 7.21 and 7.22, was obtained with $T_e = 5$ eV at the marfe, which corresponds to $n_e \sim 2 - 3 \times 10^{20} m^{-3}$ for this plasma.

The plasma in the private region must also be prescribed independently. The boundary conditions are given by the target n_e and T_e profiles. From these values n_e is increased up to halfway along the private plasma flux tubes, while T_e is kept constant, so as to produce a cold private plasma, without discontinuity from the rest of the SOL.

A comparison of measured and calculated D_α emission at detachment for this simulation is shown in Fig. 7.22. Note that in this solution 90% of the total D_α

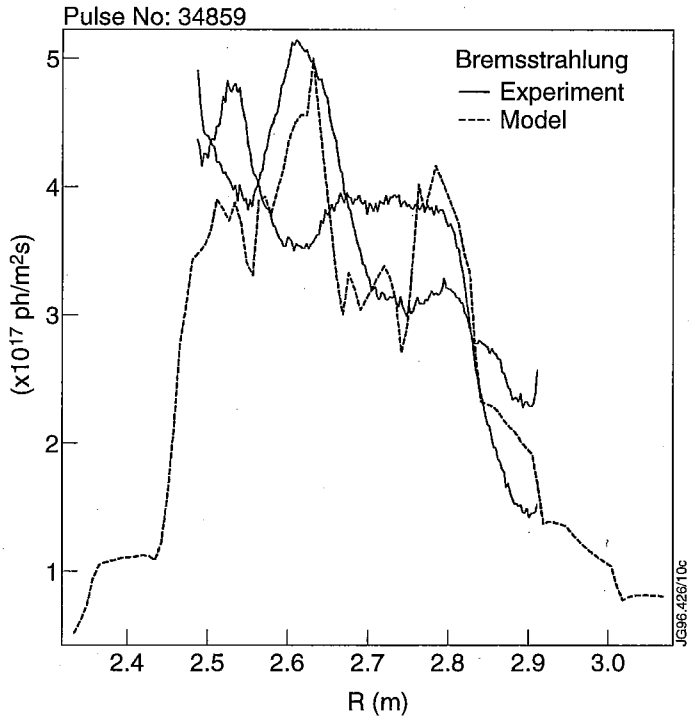

Figure 7.21: Comparison of measured and calculated bremsstrahlung emission at plasma detachment for the Ohmic pulse 34859. Two experimental profiles, within one cycle of the strike point sweeping, approximate the full profile measured by the flux camera.

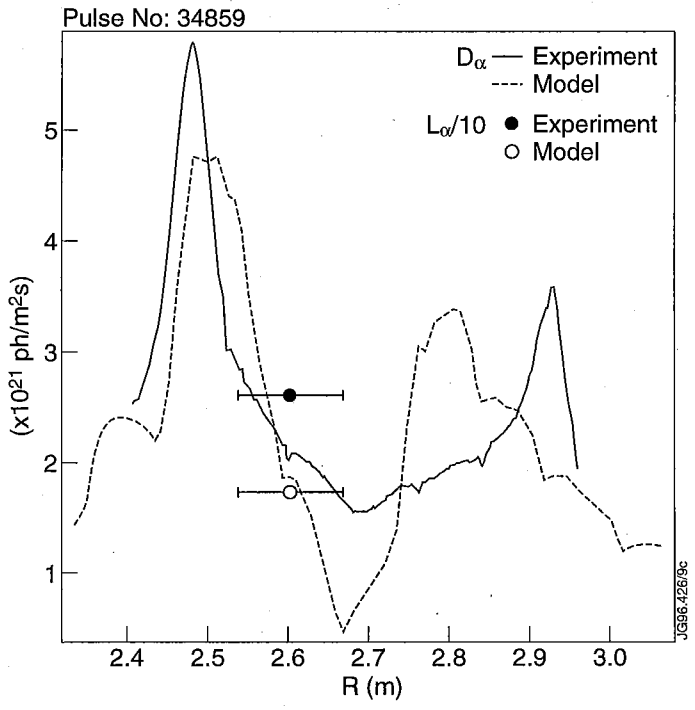

Figure 7.22: Comparison of measured and calculated D_α emission at detachment for the Ohmic pulse 34859. Also shown is the comparison between calculated and measured L_α intensity along the divertor SPRED LOS.

emission is due to recombination. The misplacement on the outer peak of the calculated D_α emission profile is linked to the asymmetry of plasma detachment observed in the MkI divertor. In fact, as already mentioned earlier, the level of detachment is different for inner and outer target, with a stronger decrease in ion flux measured at the inner target. This asymmetry cannot be obtained with the present prescription for the background plasma, which would require the flexibility to specify parallel T_e and n_e-gradients independently for the two divertor legs. It is noted that also at plasma detachment the D_α emission between the two peaks is underestimated, as in the low density case. Changing T_e $(= n_e)$ at the core marfe and/or increasing n_e in the private plasma region does not improve this result (it only produces a bremsstrahlung profile that diverges from the experiment). At present it is intended to include in the code the option to puff artificially D_2 into the private plasma to increase the local neutral deuterium concentration and bypass this problem. This should both increase the DI radiation and provide more realistic neutral distributions and sputtered carbon profiles.

7.4.2 D_α Emission from D_2 Molecular Dissociation

Hydrogen recycling at the walls and divertor target leads predominantly to the release of hydrogen molecules, which subsequently ionize or dissociate producing molecular ions, atoms or protons [40]. In view of the difficulty in reproducing the divertor D_α emission profile in the calculations, it is interesting to investigate if part of this emission may be due to dissociative excitation of hydrogen molecules:

$$H_2 + e^- \longrightarrow H(1s) + H^* + e^- \tag{7.5}$$

where H^* denotes an excited hydrogen atom (with $H^* = H(n = 3)$ for the purpose of this investigation).

In order to quantify the contribution to D_α emission from molecular dissociation the excitation rate coefficients for D_α for atomic and molecular hydrogen are first compared. The latter is obtained from the work of Sawada and Fujimoto [127], who calculate an effective ionization rate coefficient, S_{H_2}, and an S/XB coefficient for D_α for molecular dissociation. The effective excitation rate coefficient, $q^{exc}_{H_2}$, thus obtained represents a crude estimate because the S/XB ratios have to be extrapolated below 10 eV (to 1 eV) to obtain data relevant to the detached divertor plasma regime. In fact the authors only consider the case of an optically thin, ionizing,

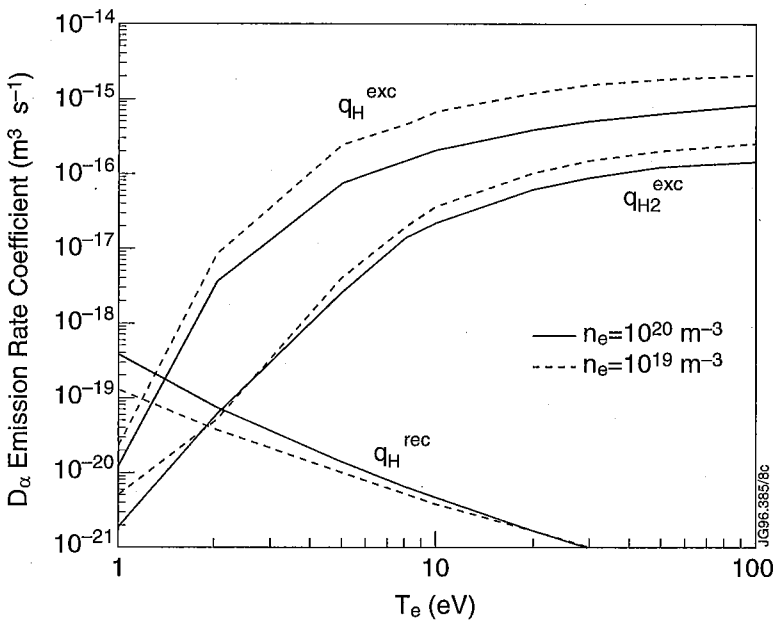

Figure 7.23: Atomic and molecular rate coefficients for D_α as a function of temperature. Also plotted for comparison is the D_α recombination rate coefficient.

high temperature edge plasma in their collisional radiative model. Moreover, processes starting from the molecular hydrogen ion H_2^+ are not treated in [127] and the authors note that "these processes can be even more important in divertor plasmas, but atomic data on various processes starting from H_2^+ are so scanty that it was impractical to evaluate the various rate coefficients". Therefore, the derived $q_{H_2}^{exc}(D_\alpha)$ represent an underestimate especially in high density, detached plasmas. Fig. 7.23 plots the atomic and molecular excitation rate coefficient together with the recombination rate coefficient for D_α as a function of temperature.

The rate coefficient for molecular hydrogen is a factor of 10 lower than the atomic rate, mainly due to the difference in magnitude of the cross sections for H_2 dissociative excitation and H excitation. Since in the detached plasma regime the excitation contribution to D_α emission is strongly suppressed (as discussed above) it is expected by the comparison of the rates shown in Fig. 7.23 that the contribution from D_2 dissociative excitation is negligible. On the other hand, the concentration of D_2 molecules in the vicinity of the target in this regime may be high enough to compensate the small value of $q_{H_2}^{exc}(D_\alpha)$. Indeed, for pulse 34859 the atomic and molecular emission measures, integrated along the flux camera viewlines, $\int n_e n_H \, dl$ and $\int n_e n_{H_2} \, dl$, obtained using the simulations of the previous Section, are comparable (see Fig. 7.24 (a)), but the 2D density contours show that n_{H_2} is concentrated

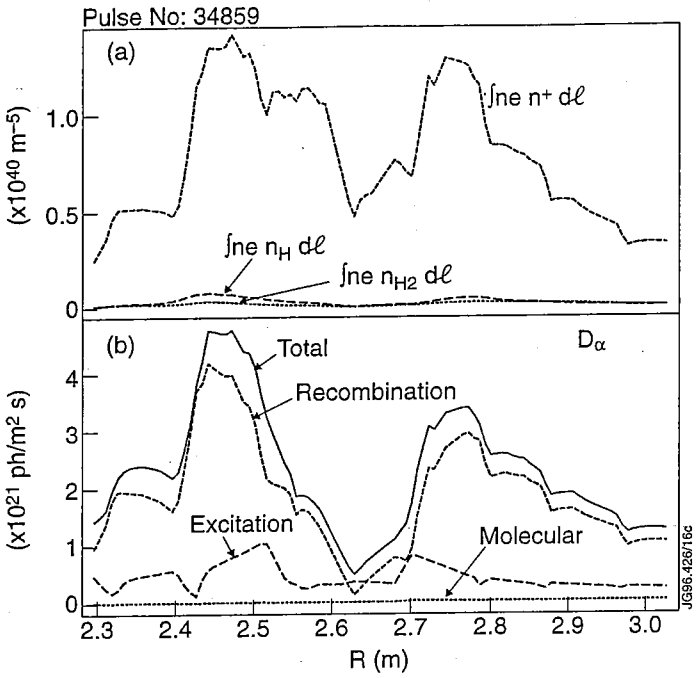

Figure 7.24: (a) Atomic and molecular hydrogen emission measures integrated along the flux camera viewlines for the Ohmic pulse 34859 at detachment. (b) Various components of the calculated D_α emission.

only in a thin layer close to the divertor plates, whereas the atomic deuterium cloud is more extended in space and further upstream.

Thus, with comparable emission measures at detachment there is very little contribution (a few %) to D_α emission from molecular dissociative excitation. This is shown in Fig. 7.24 (b).

In the low recycling regime, the integrated atomic and molecular hydrogen emission measures are of similar magnitude (see Fig. 7.25 (a)) and there is no contribution to D_α emission from e-p recombination. Due to the smaller rate coefficient, the D_α emission component due to H_2 dissociative excitation is only a negligible fraction of the total emission (see Fig. 7.25 (b)).

From this analysis it is concluded that the contribution to D_α emission due to molecular hydrogen dissociative excitation is negligible with respect to the total emission both at low density and plasma detachment. Therefore this process does not appear to be responsible for the discrepancies found between measured and calculated D_α emission in these simulations and can be neglected. However, the molecular rates used for this study are underestimated in conditions of divertor

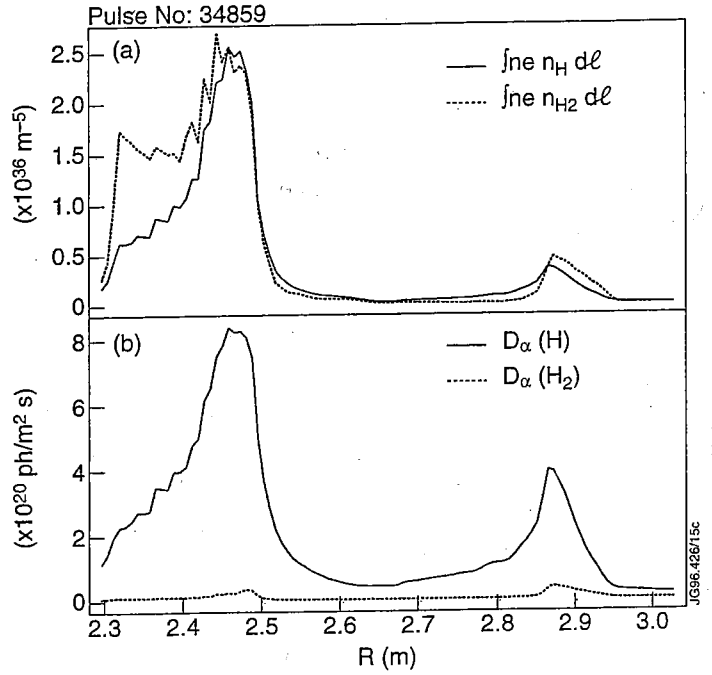

Figure 7.25: (a) Atomic and molecular D_α emission measures along the flux camera viewlines for the Ohmic pulse 34859 in the low recycling regime. (b) Contributions to D_α emission from atomic hydrogen excitation and H_2 dissociative excitation. In this regime there is no contribution to D_α emission from recombination.

plasma detachment, so that a more accurate quantitative investigation in this regime depends on improved data at low temperatures and on the inclusion of H_2^+ processes.

7.4.3 Impurities

With the hydrogenic plasma described in the previous Section, the transport of the carbon impurites is studied assuming a carbon target. The carbon source, which at these low temperatures is mainly due to chemical sputtering, is overestimated by the model by a factor of 10 and thus the chemical yield has to be reduced to 0.5% in order to obtain overall agreement with C II visible emission integrated over the inner and outer divertor target region. It is possible that this large discrepancy is due to considerably reduced CD_4 fuelling efficiencies at high deuterium fluxes to the divertor targets, as already reported in other machines, such as Asdex-U [128].

Good agreement is also obtained between model and experiment for C II VUV emission measured by the double SPRED (the (*) symbols in Figs. 7.17-7.20). However, the calculated C III and C IV emission, both in the visible and VUV, is overestimated with respect to the measurements. This leads to the radiated power profiles

Ion	λ (Å)	$< T_e >$ (eV) [$*$]	$< T_e >$ (eV) [$\bullet$]
C II	904	3.86	2.56
	1335	2.25	2.45
C III	977	6.2	3.42
	1176	6.0	3.7
	538	10.3	6.2
	460	11.4	7.1
	386	10.7	6.4
	4650	12.3	8.2
C IV	312	21.2	24.7
	384	21.1	23.4
	420	21.0	21.8
	1549	18.6	10.6

Table 7.4: $< T_e >$ calculated along the SPRED LOS as in eq. 7.6 for C II-C IV spectral lines at plasma detachment for the Ohmic discharge 34859. ($*$) indicates the simulation on the background plasma of section 7.4.1, ($\bullet$) the simulation with modified parallel T_e-gradient.

shown in Fig. 7.26, where it is evident that the total carbon radiation is too high, being comparable to the actual total radiated power measured by the bolometer. Instead, the deuterium radiated power component is consistent with the measurements (as shown in Fig. 7.22 by the comparison of measured and calculated L_α intensity).

Note that of the different C III lines, the resonance lines are overestimated by the model by about a factor of 2, while the lines emitted from the $3l$ shells are overestimated by a larger factor (3 to 10). By defining an average temperature $< T_e >$, associated with the emissivity $\epsilon(\lambda)$ of a given spectral line along the spectrometer LOS:

$$< T_e >= \frac{\int_{LOS} T_e \, \epsilon(\lambda) \, dl}{\int_{LOS} \epsilon(\lambda) \, dl} \tag{7.6}$$

it is found that the C III resonance lines emit at $< T_e > \sim$ 6 eV, whereas the lines originating from transitions from the $3l$ levels emit at higher $< T_e >$, as shown in Table 7.4. This is inconsistent with $T_e \sim 5$ eV obtained from the measured C III line ratios. 2D contours of C III emission show that the balance of thermal and friction forces in the divertor is such that the C III ions are pushed to emit above the X-point and further upstream along the SOL. This is even more pronounced for C IV. The

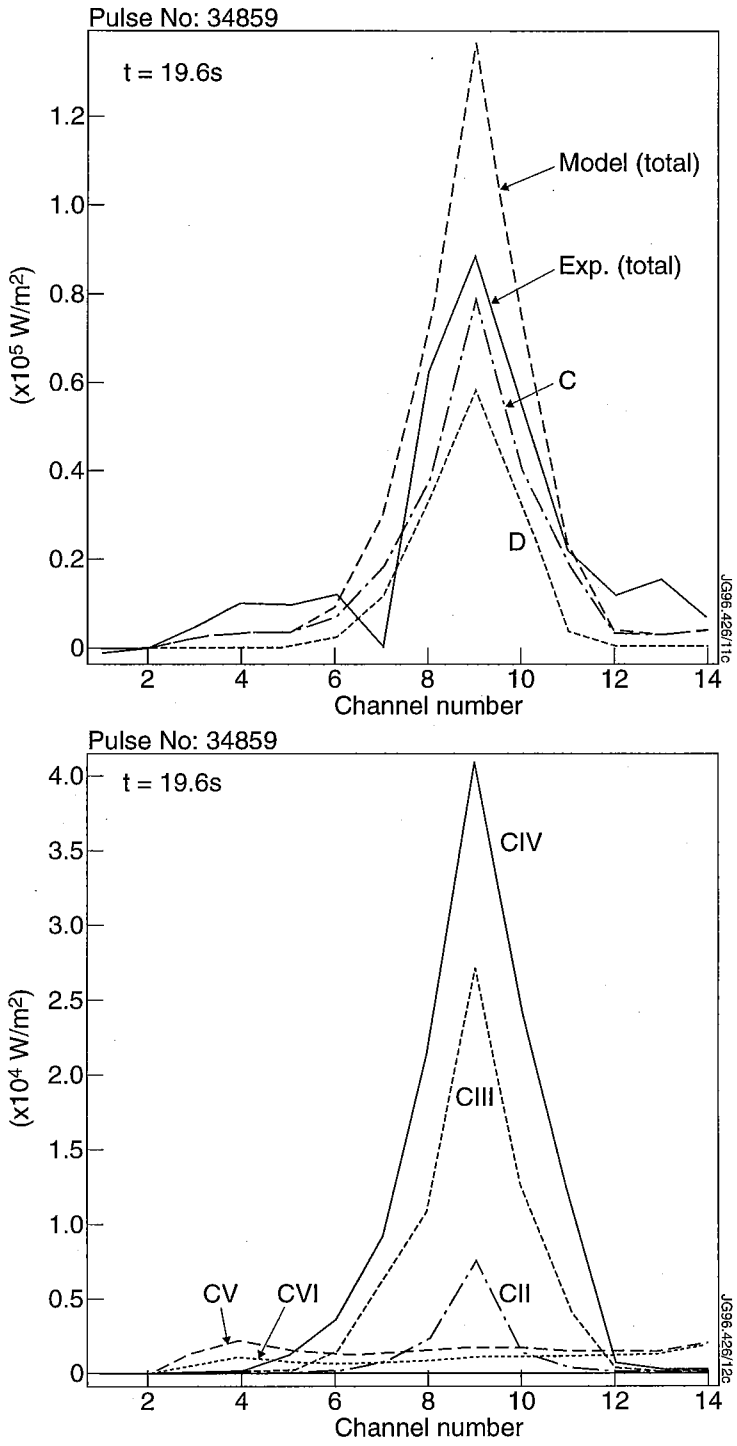

Figure 7.26: (top) Experimental and calculated bolometer radiated power at detachment for the Ohmic discharge 34859; (bottom) calculated bolometer radiated power components for carbon, whose sum is shown in the top figure. This simulation corresponds to the (∗) symbols in Figs. 7.17-7.20.

C IV visible emission is overestimated by a factor of 4 in the simulation (both in the inner and outer divertor) and by a factor of 6 to 10 in the VUV, which results in a much higher C IV radiated power component than measured experimentally.

In order to test the sensitivity of the impurity solutions on the transport parameters assumed, another background plasma simulation was performed, with modified parallel T_e-gradient. That is, in the collision region T_e is increased linearly by a factor of 2 from its target value and the remaining settings are kept equal to the previous simulation. This reduces the thermal force on the impurities and the result is that the C III ions emit in the X-point region and at lower $< T_e >$. However, while the C III and C IV emission is reduced to values which agree with the experiment, the C II emission is underestimated in the visible and overestimated in the VUV. That is, the C II emission layer has been pushed too close to the target (i.e. to too low temperatures). This is shown in Figs. 7.17-7.20, (•) symbols. The resulting radiated power profiles are shown in Fig. 7.27. The C IV emission layer has moved further away from the X-point on either side, therefore decreasing along the SPRED LOS, which is shown in the 'dip' of the C IV bolometer profile of fig. 7.27 (b). The C III resonance lines, and thus the C III radiated power, have remained essentially unchanged, whereas emission from the $3l$ shells (visible and VUV) agrees with the measurements, being emitted at lower $< T_e >$ than in the previous simulation. The C II radiated power component has increased significantly and this results in a decrease of only 25% of the carbon (and total) radiation. Also, the C IV profile has broadened, which disagrees with the experiment.

Thus, a small (linear) variation of the paralle T_e-gradient in the divertor can change significantly the force balance on the carbon impurities and thus the radiation profiles. There is no absolute basis for saying that the thermal forces should change linearly along the field lines. This cannot be tested with this model. More importantly, it is clear that in divertor impurity transport models the number of parameters (= unknowns) is too large for the available information from the measurements. Thus it is at present impossible to make a definitive statement regarding the behaviour of impurities in divertor plasmas. However, this study stresses the necessity of simultaneous observations in the VUV and visible spectral regions for impurity transport studies. In addition, it is evident that measurements of emission profiles across the divertor, which unfortunately were not available during the MkI campaign, are essential. They can provide vital information on impurity ion cross

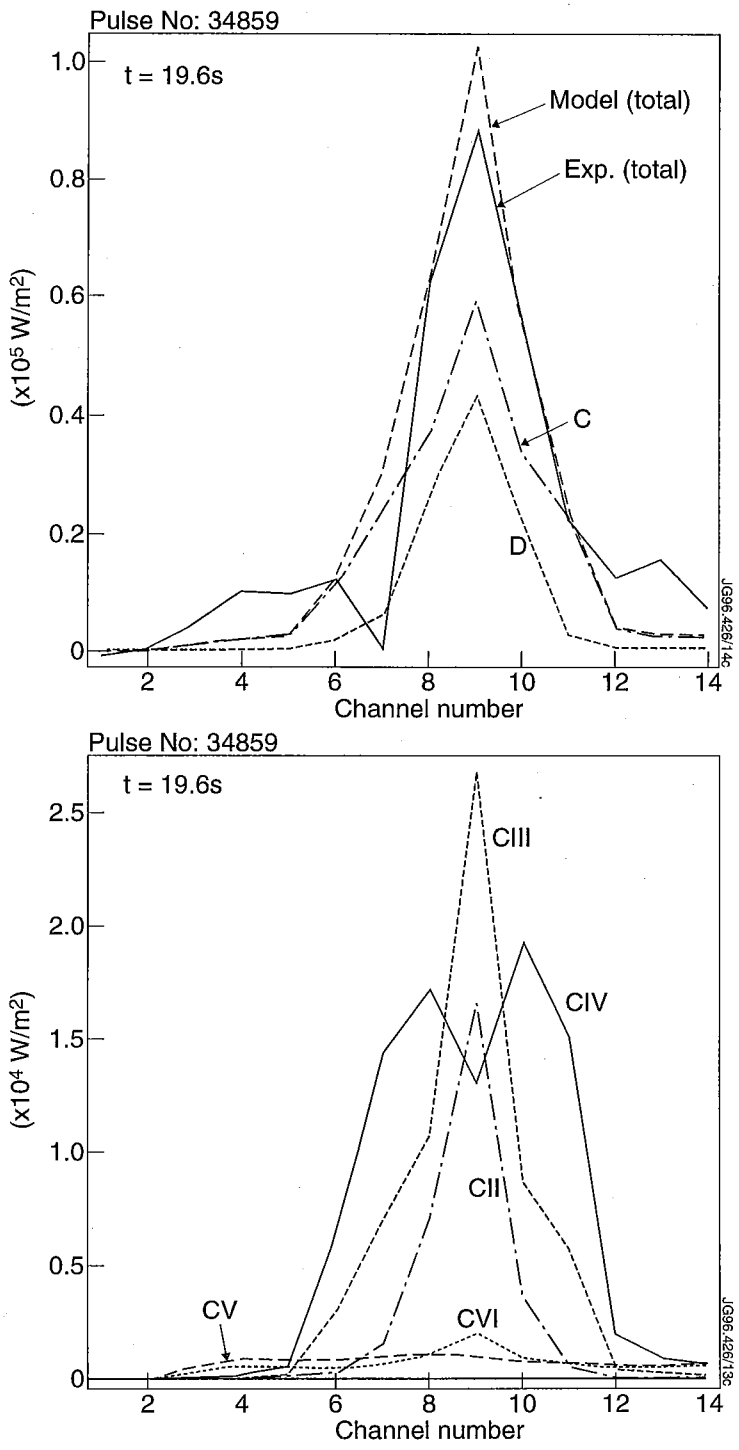

Figure 7.27: (top) Experimental and calculated bolometer radiated power at detachment for the Ohmic discharge 34859; (bottom) calculated bolometer radiated power components for carbon (whose sum is shown in the top Figure). This simulation corresponds to the (•) symbols in Figs. 7.17-7.20.

field transport and spatial distributions, that cannot be tested otherwise with the present spectroscopic arrangements.

7.5 Nitrogen Seeded Radiative Divertors: Spectroscopic Observations

Radiative divertor discharges have been established in JET during the MkI divertor phase by means of combined nitrogen seeding and deuterium fuelling in the divertor chamber (see Section 2.11). Nitrogen spectra for one such discharge are shown in Fig. 7.28 (a) and (b). The nitrogen radiation was measured with the divertor double SPRED from line emission of N II-N V. The various radiated power components were obtained following the scheme presented for carbon (and oxygen), but could not be compared with the theoretical line power fractions because these data are not yet available in ADAS. The spectral lines used for radiated power measurements are summarized in Table 7.5. Note that, unlike the case of carbon, the resonance transition of Li-like nitrogen is measured. Thus, the JET double SPRED is a powerful tool for measurements of nitrogen radiated power from the divertor without any need for collisional radiative modelling, that is independently of the atomic and transport processes leading to line emission from the various nitrogen ions.

The radiated power components measured by VUV spectroscopy for a nitrogen radiative divertor discharge (pulse 34361) are shown in Fig. 7.29 together with global plasma parameters of the discharge. The nitrogen radiation is about 80% of the total radiated power measured by the bolometer at detachment, while the remaining 20% is observed to be radiated by carbon and deuterium. Fig. 7.30 expands on the nitrogen radiated power components: it can be seen that Li-like nitrogen is the strongest radiator.

7.5.1 Comparison with Impurity Transport Simulations

As already mentioned, a full set of photon emissivity coefficients for nitrogen is not yet available in ADAS (however, work is starting in this area, motivated by the need for nitrogen atomic data for impurity transport studies). Thus simulations of nitrogen spectral emission could not be performed at this time. A study of transport based on the comparison of measured and calculated spectroscopic signals, similar

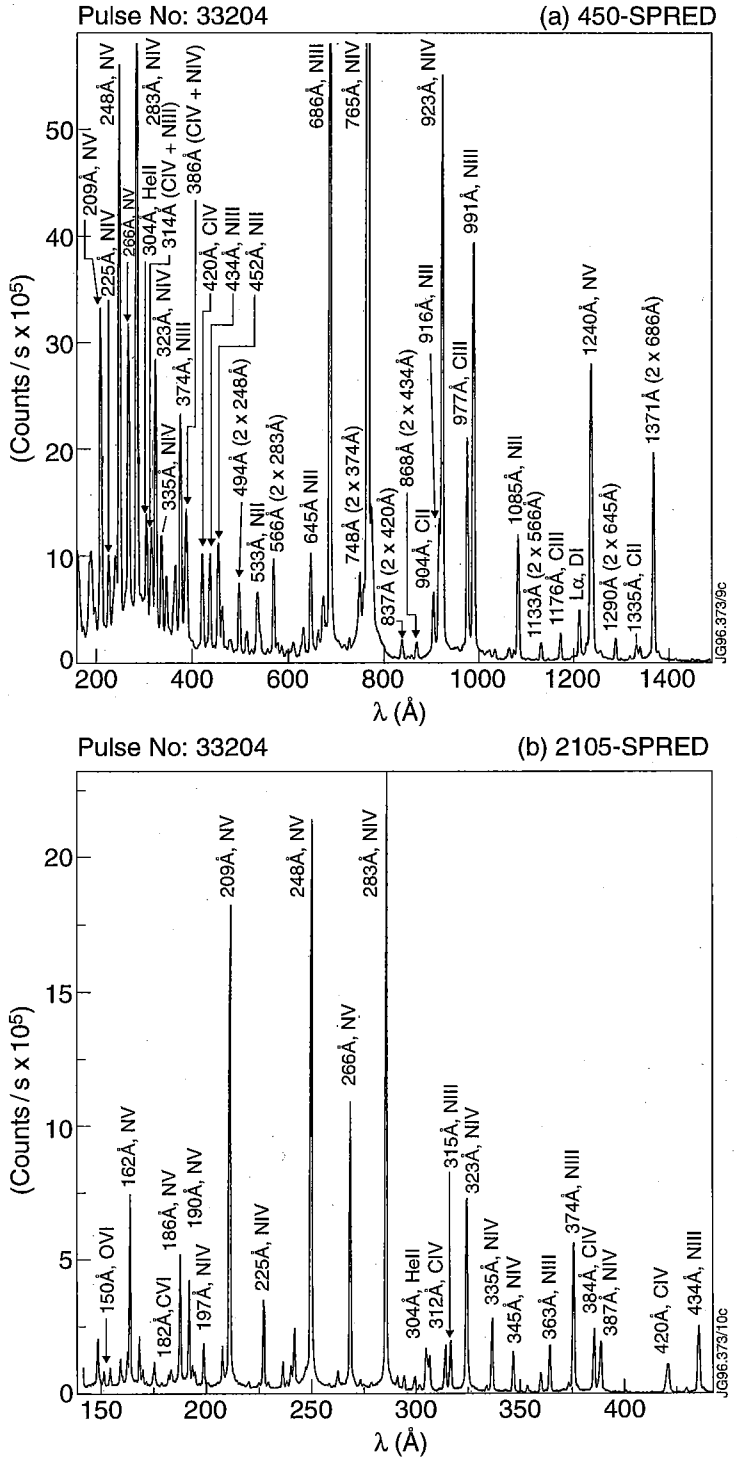

Figure 7.28: VUV spectra of the divertor from the 450-SPRED (a) and the 2105-SPRED (b) during a nitrogen seeded radiative divertor discharge (pulse 33204).

Ion	λ (Å)	Transition	Comment
N II	1085.1	$2s^2 2p^2\ ^3P - 2s2p^3\ ^3D$	
	645.0	$2s^2 2p^2\ ^3P - 2s2p^3\ ^3S$	
N III	991.0	$2s^2 2p\ ^2P - 2s2p^2\ ^2D$	
	685.7	$2s^2 2p\ ^2P - 2s2p^2\ ^2P$	
	764.0	$2s^2 2p\ ^2P - 2s2p^2\ ^2S$	not used, blend with N IV res. line
	374.4	$2p^2\ ^2P - 3d\ ^2D$	
	434.0	$2p^2\ ^4P - 3s\ ^4P$	
N IV	765.1	$2s^2\ ^1S - 2s2p\ ^1P$	most of N IV
	923.1	$2s2p\ ^3P - 2p^2\ ^3P$	line power
	335.0	$2s2p\ ^1P - 2s3d\ ^1D$	
	387.4	$2s2p\ ^1P - 2s3s\ ^1S$	
	283.5	$2s3p\ ^3P - 2s3d\ ^3D$	
	322.6	$2s2p\ ^3P - 2s3s\ ^3S$	
N V	1240.1	$2s\ ^2S - 2p\ ^2P$	most of N V line power
	266.3	$2p\ ^2P - 3s\ ^2S$	
	209.3	$2s\ ^2S - 3p\ ^2P$	
	247.7	$2p\ ^2P - 3d\ ^2D$	

Table 7.5: Summary of spectral lines used for nitrogen radiated power measurements with the divertor double SPRED.

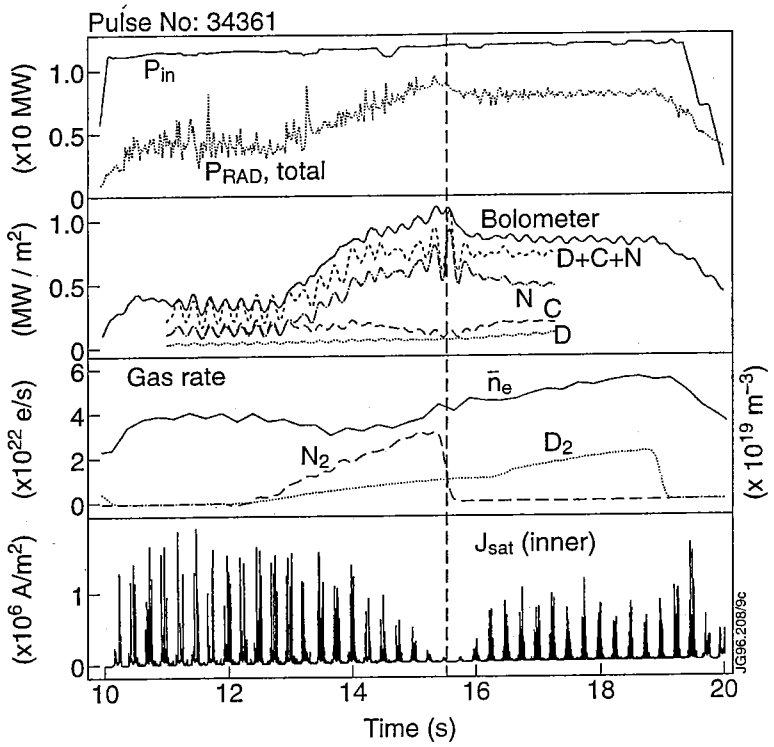

Figure 7.29: Radiative divertor discharge with deuterium fuelling and nitrogen seeding, pulse 34361.

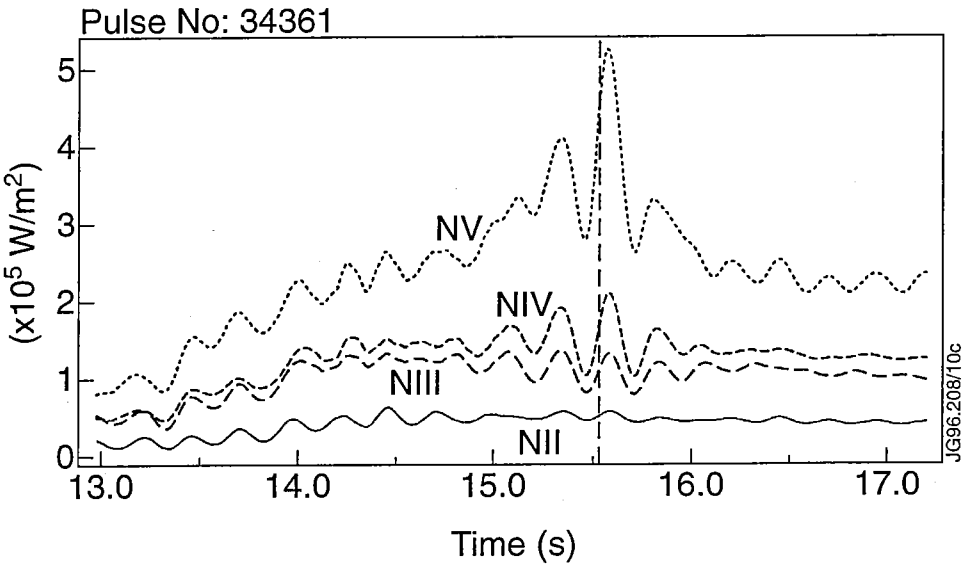

Figure 7.30: Nitrogen radiated power components for pulse 34361 (Fig. 7.29).

to that presented for carbon impurities, will be part of future work. However, some preliminary work on the study of nitrogen transport in radiative divertor discharges is presented. Most of the difficulties encountered point to the need for spectroscopic simulations.

The detached phase of the ELMy H-mode radiative divertor discharge of Fig. 7.29 was modelled following nitrogen particles (DIVIMP) on a self-consistent, 2D multi-fluid background plasma solution obtained with EDGE2D, as reported in [32]. At the time chosen for the simulation, this discharge was characterized by 11MW of total input power and the total radiated power was 8MW, with about 6MW radiated in the X-point/divertor region. The calculated D_α and bremsstrahlung emission profiles and ion flux to the target are in broad agreement with the measurements; the electron temperature in the divertor is extremely low, < 1 eV at the target and ~ 3 eV at the X-point, and this affects the impurity distributions, as shown later. Nonetheless, this represents the best current attempt at JET at modelling the hydrogenic plasma of such discharges. The effect of ELMs on the plasma and the impurities is not understood and the ELMs are included in the model only in an averaged way. This is one of the areas of divertor modelling where work needs to be done, since the ELMy H-mode radiative divertor is the preferred regime for ITER (see [32] for a review on the present status of modelling of ELMs and ELMy H-mode radiative plasmas).

In the impurity simulation nitrogen is injected in the private plasma region at thermal energies (1 eV) and the gas is treated as fully recycling (although the real case is probably something between a recycling gas such as neon and a non recycling impurity such as carbon, see Chapter 2). For this reason, the calculated nitrogen source has to be adjusted to match the experiment. This is obtained by normalizing the calculated radiated power to the power radiated in the X-point/divertor region as measured by the bolometer. The comparison between experimental and simulated bolometer radiated power at detachment is shown in Fig. 7.31. The calculated radiation profile is in good agreement with the experimental one, but the ratio of N V to N IV radiated power measured by VUV spectroscopy is not reproduced in the simulation, which weights the radiation distribution around N IV. This is thought to be due to underestimation of the electron temperature in the divertor region, which enhances the contribution from Be-like nitrogen radiation. A detailed analysis requires modelling of the spectroscopic signals, as discussed earlier, and will

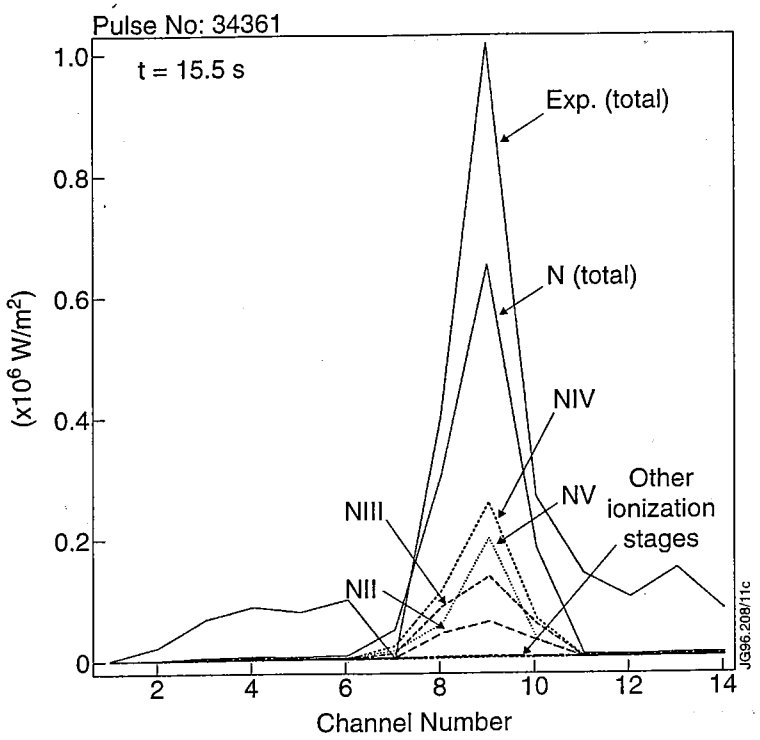

Figure 7.31: Experimental (total) and simulated (nitrogen) bolometer radiated power at detachment for the radiative divertor discharge of Fig. 7.29

be part of future work.

On the other hand, this simulation can be used to study the effect of transport on the global radiating characteristics of nitrogen compared to carbon in the divertor volume. In fact, if the same hydrogenic background plasma is used for another DIVIMP simulation in which the impurity is carbon, it turns out that a higher impurity concentration is needed in order to achieve the same radiated power as in the case of nitrogen. More specifically, for this hydrogenic plasma, with 6 MW of total impurity radiated power, the average nitrogen density is $\hat{n}(N) = 3.13 \times 10^{17}\ m^{-3}$ (average concentration $\hat{n}(N)/\hat{n}_e = 0.9\%$) while the average carbon density is $\hat{n}(C) = 5.32 \times 10^{17}\ m^{-3}$ ($\hat{n}(C)/\hat{n}_e = 1.5\%$). This difference in the radiating behaviour of carbon and nitrogen has been found in simulations of different discharges using both DIVIMP and the full 2D EDGE2D/NIMBUS multispecies calculations [129] and thus does not seem to depend on the characteristics of a specific background plasma. Therefore, in high density low temperature divertor plasmas nitrogen is a more efficient radiator than carbon, even though the difference in nuclear charge is only 1. Indeed, the radiated power curves of Fig. 3.17 show that for a uniform plasma in ionization equilibrium, with $n_e = 10^{20}\ m^{-3}$, the radiation efficiency of

nitrogen is a factor of 10 or more higher than that of carbon in the temperature range 10-50 eV. The impurity simulations for pulse 34361 are used to investigate the effect of a non uniform, non equilibrium divertor plasma on the power loss functions of carbon and nitrogen. It is expected that, in order to reconcile the carbon and nitrogen results, the divertor plasma conditions are such that, on average, the power loss function of nitrogen exceeds that of carbon in the divertor/SOL volume. For the comparison it is necessary to consider the whole divertor plasma, since 'local' comparisons (e.g. along a representative ring of the computational grid) can be misleading in Monte Carlo calculations. This is because they can introduce unreal features due to poor statistics in the region of the computational grid chosen for the comparison. Therefore, 2D contours of the nitrogen and carbon power loss functions, $p(A) = \sum_{z=0}^{Z_0} P_{RAD}(A^{+z}) / \sum_{z=0}^{Z_0} n_e n(A^{+z})$, with $A = C, N$, are calculated (see Chapter 3) and plotted in Figs. 7.32 and 7.33.

The charge exchange power contribution is neglected (see next Chapter) and since the contribution from recombination-bremsstrahlung is small, the radiated power is effectively the total impurity line power.

It can be seen that on average nitrogen is a more efficient radiator than carbon in high density, low temperature divertor conditions. In particular, the nitrogen power loss function has a greater overlap with the high density region in the vicinity of the X-point.

Note that in these simulations the effect of impurity radiation on the background plasma is included in the original EDGE2D self-consistent calculation, with nitrogen as the radiating impurity. However, the different spatial radiation distributions of carbon and nitrogen can lead to different background plasmas. On the other hand, the simulations of [129] were performed with identical terms in the equations, one with carbon and one with nitrogen, and the two background plasma solutions which resulted were very similar.

Calculations of photon emissivity coefficients for nitrogen ions are essential to validate the nitrogen atomic data used at present in the models against the spectroscopic measurements and so to strengthen the study presented in this Section.

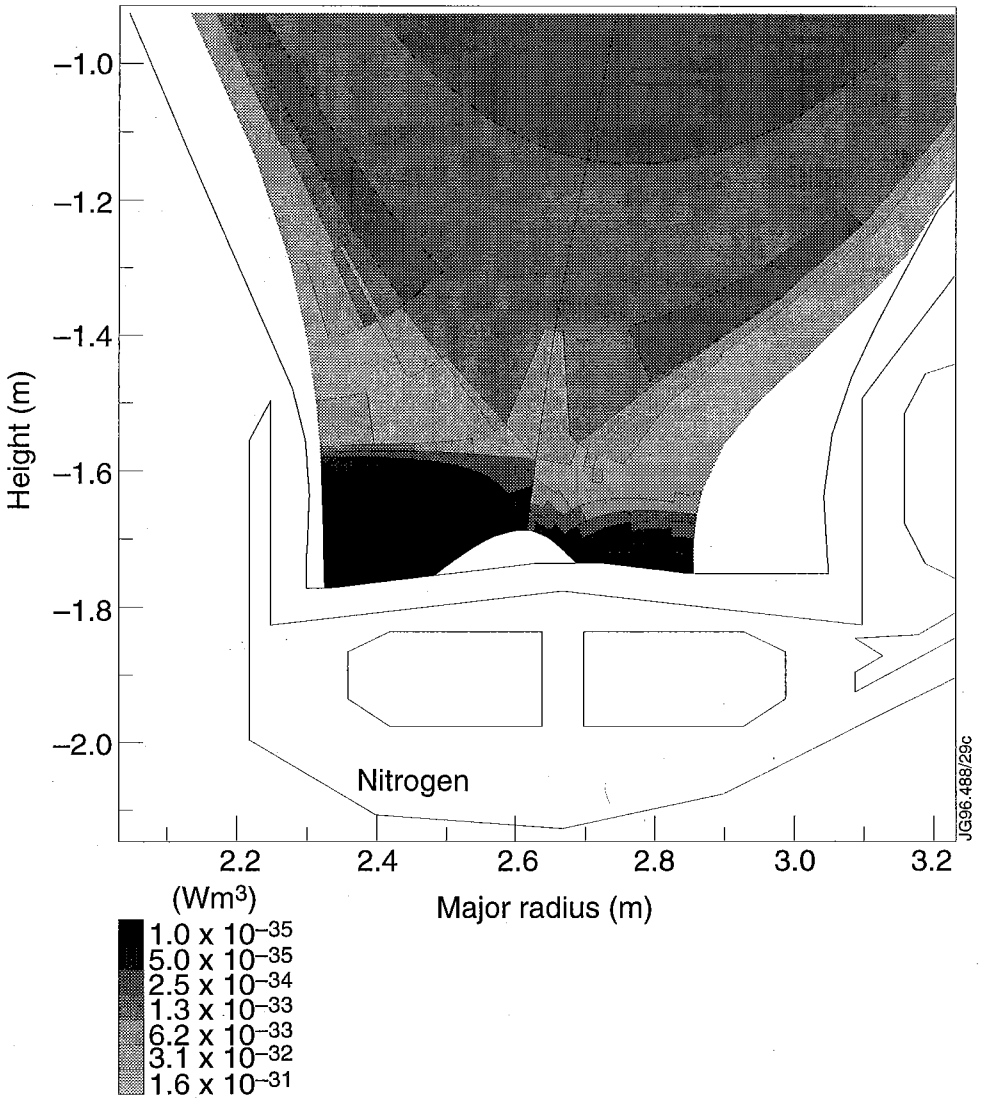

Figure 7.32: 2D contour of nitrogen power loss function in the divertor for the simulation of pulse 34361 with $P_{rad}(N) = 6$MW. On average nitrogen is a more efficient radiator than carbon (see Fig. 7.33) in high density, low temperature radiative divertor plasmas.

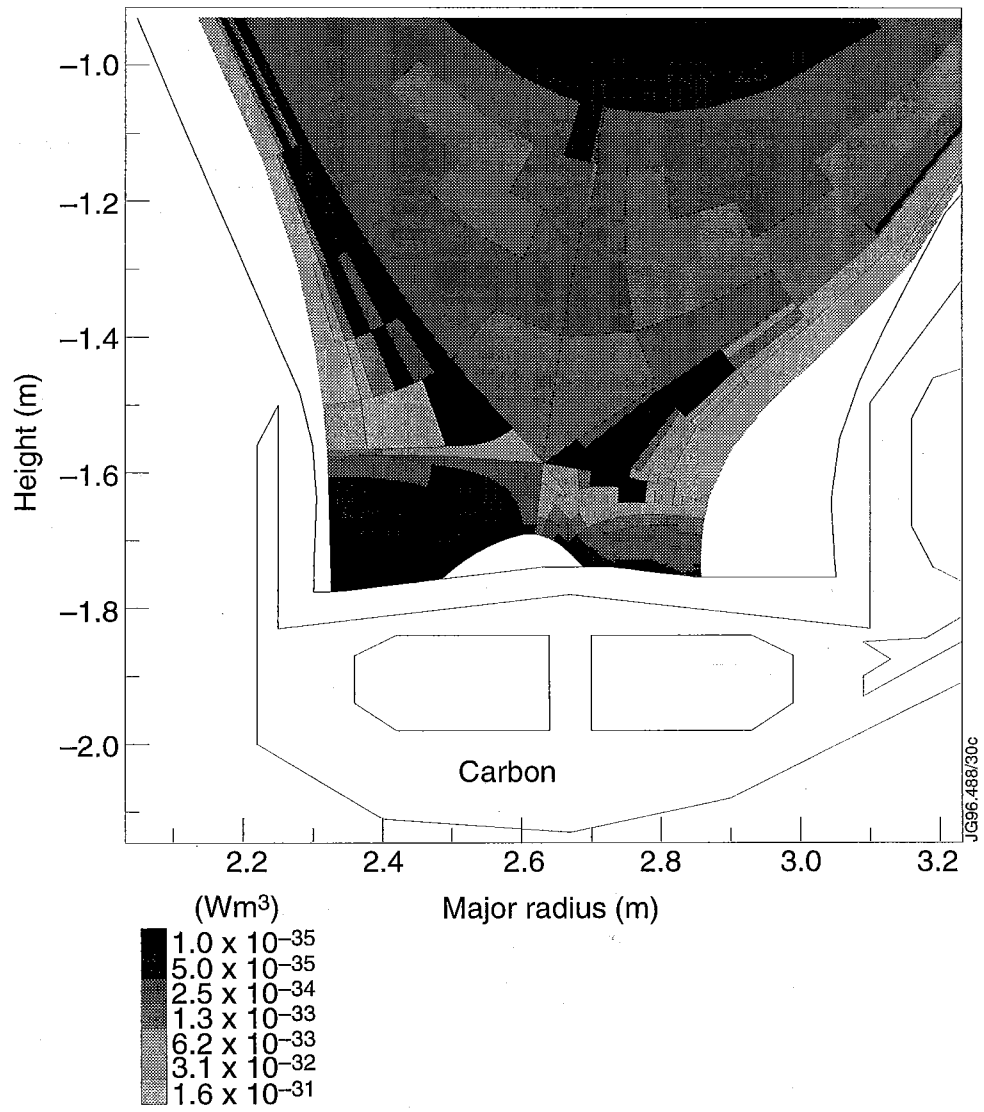

Figure 7.33: 2D contour of carbon power loss function in the divertor for the simulation of pulse 34361 with $P_{rad}(C) = 6$MW.

7.6 A Discussion on the Treatment of Metastables in Impurity Transport Simulations

It has already been noted in this thesis (see Chapter 3) that, for a given impurity ion, the lifetime of the metastable states is comparable to that of the ground state, which in turn is governed by collisions with the plasma ions and electrons and by transport. Therefore, in principle, a complete model for impurity transport should include the solution of a set of transport equations for each metastable state of a given ion. In present day impurity transport codes (e.g. DIVIMP, EDGE2D at JET) the implicit working assumption is that of equilibrium of the metastable states with the ground state of a given ion, which allows the solution of a smaller set of transport equations, one for each impurity charge state. Whereas it is clear that this assumption has its practical advantages - e.g. when solving the fluid equations simultaneously for all impurity charge states (5 for Be, 7 for C, 8 for N) - it is now being argued that this approach is not correct and may be the cause of some errors and that the transport codes should be modified to treat the metastable states properly. These modifications would imply a major restructuring of the existing codes and would also increase significantly the CPU time required for the calculations. Therefore two issues arise: is a large error made when modelling spectral emission from the divertor plasma if we assume the metastable ions in equilibrium with the ground state ions? and, can this assumption be responsible for some of the discrepancies found between experiment and models?

In this Section I will address these questions using spectroscopic measurements, and show that in JET medium/high density divertor plasmas a condition close to equilibrium between metastable and ground state levels is indeed established. For these investigations consider the C III ions ($2s^2\ ^2S$ ground state, $2s2p\ ^3P$ metastable state), which play a central role in impurity emission from the divertor, as shown by the studies in this Chapter.

At equilibrium a significant fraction of the C III population resides in the metastable state, e.g. for $n_e = 10^{20} m^{-3}$ and $T_e = 5$ eV the metastable to ground state population fraction is ~ 1. A measurement of the ratio of the singlet ($2s^2\ ^1S - 2s2p\ ^1P$, 977 Å) and triplet ($2s2p\ ^3P - 2p^2\ ^3P$, 1175.6 Å) resonance transitions can give an estimate of whether equilibrium between metastable and ground states holds or not. Fig. 7.34 a, b, c show respectively the calculated 977/1175.6 line ratio in

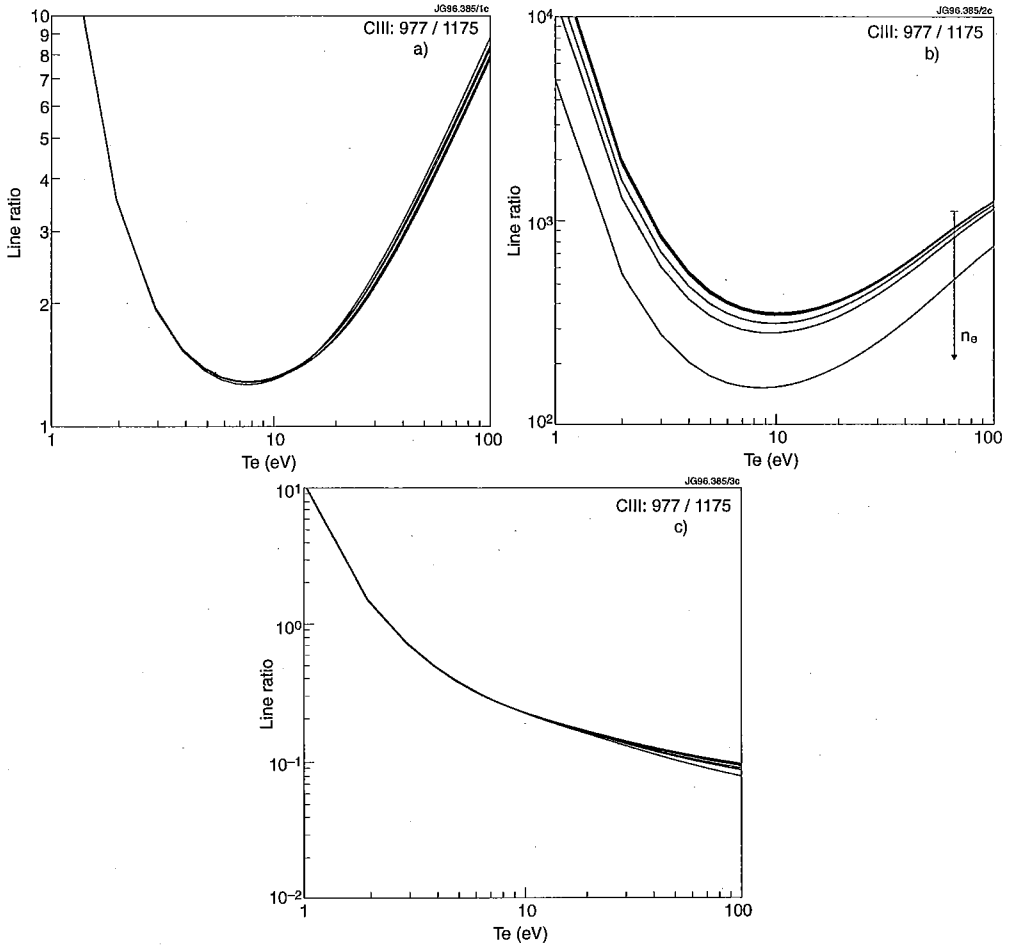

Figure 7.34: C III 977/1175.6 line ratio for $n_e = 10^{18}$ to $5 \times 10^{20} m^{-3}$ as a function of electron temperature : (a) equilibrium between ground and metastable states; (b) assuming population only from the ground state; (c) assuming population only from the metastable state.

the 'metastable unresolved' case (i.e. assuming equilibrium between metastable and ground states) and in the metastable resolved cases with respect to the ground and metastable state, which represent the two extreme cases. Since this line ratio varies mostly with T_e, it is necessary to have at least one line ratio of other C III lines that can be used to identify experimentally what is the average T_e at which the C III ion distribution is emitting. Two independent line ratios, measured with the double SPRED, are used, one involving singlet transitions (386/977 Å) and one triplet transitions (460/1175.6 Å). They are reasonably sensitive to temperature variations, as shown in Fig. 7.35. Figure 7.36 shows the measured 977/1175.6 line ratio for the Ohmic density limit pulse of Fig. 7.6. The first thing to note is that the measured ratio is well within the range of values predicted when the metastable unresolved calculation is used (see Fig. 7.34 (a)). Secondly, within the error bars of the SPRED

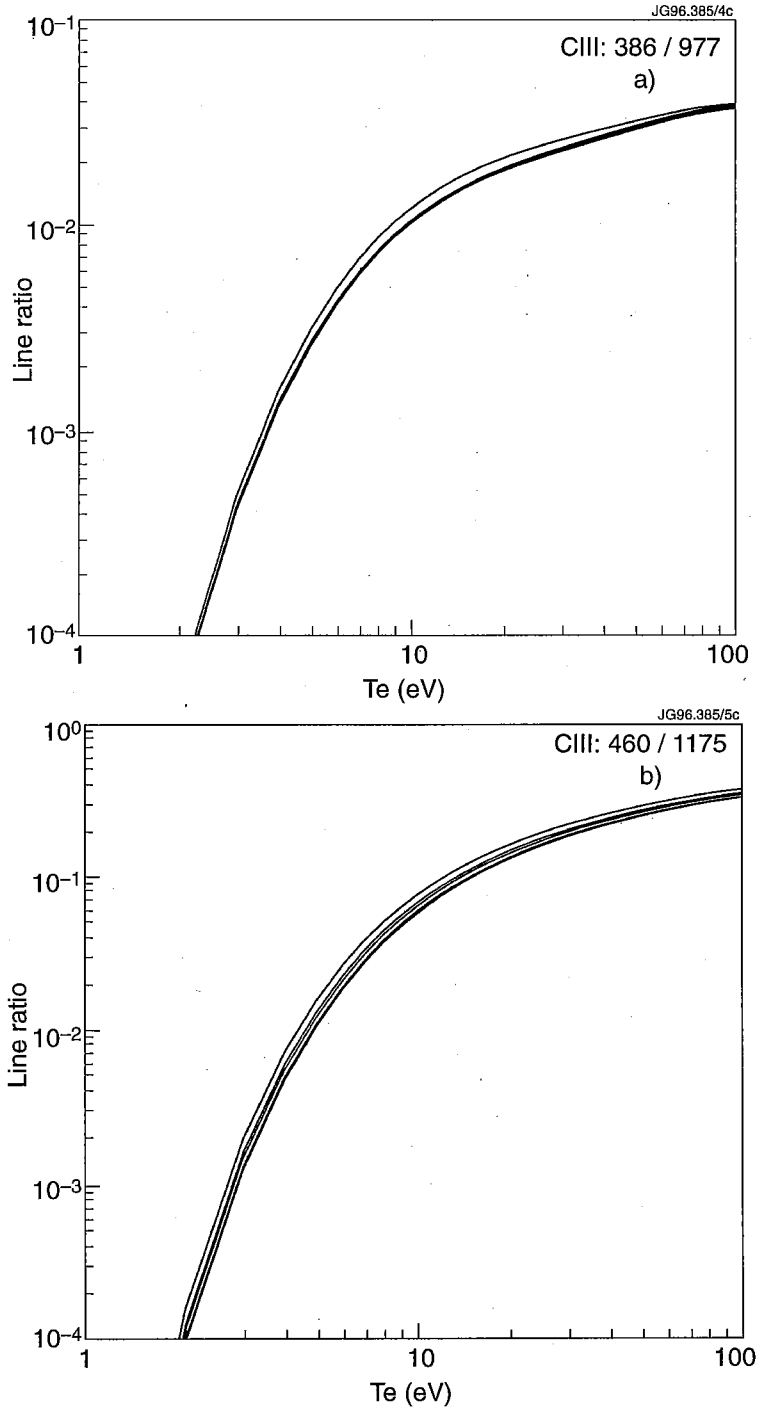

Figure 7.35: C III 386/977 (a) and 460/1175.6 (b) line ratios as a function of T_e for $n_e = 1 \times 10^{18}$ to 5×10^{20} m^{-3}.

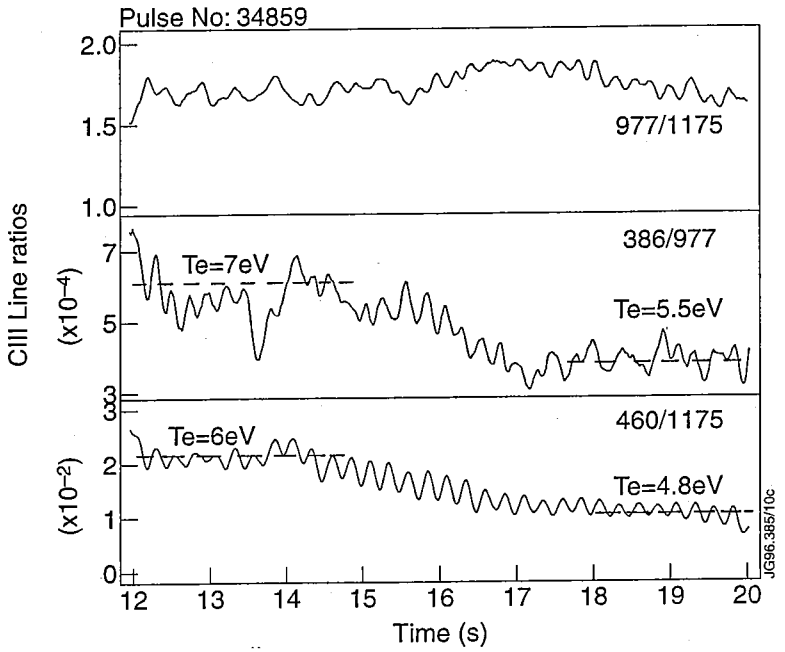

Figure 7.36: Measured 977/1175.6 line ratio for the Ohmic density limit pulse of Fig. 7.6 and T_e measurements from C III line ratios.

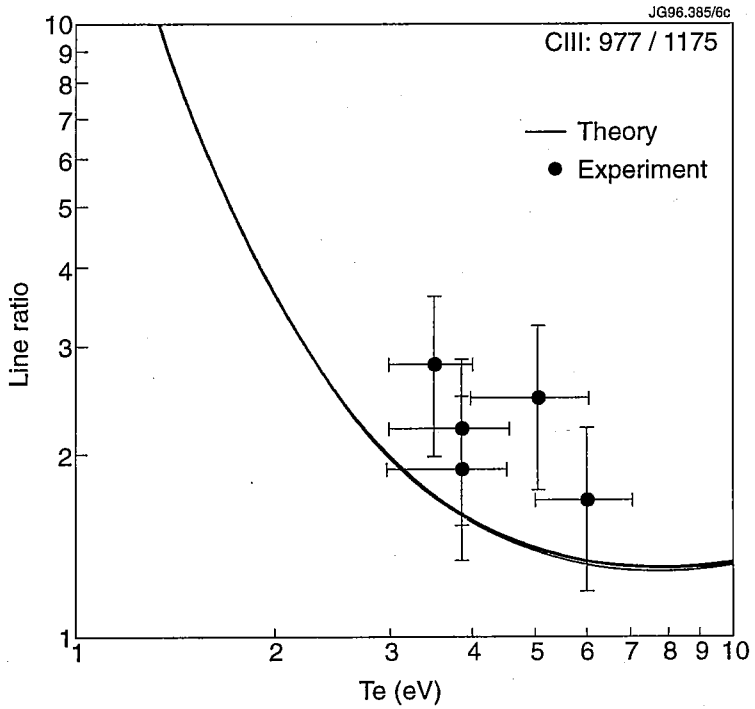

Figure 7.37: Comparison of theoretical (metastable unresolved) and measured 977/1175.6 line ratios for various high density Ohmic and L-mode divertor discharges. The data points span a range of electron densities from $n_e = 10^{19}$ to 10^{20} m^{-3}.

calibration, the two ratios of Fig. (b) and (c) are consistent in the estimate of T_e ($\sim$ 5-6 eV), which in turn is consistent with the ratio of 977/1175.6 $\sim$ 1.7. Fig. 7.37 summarizes similar results obtained for various Ohmic and L-mode discharges in which the density was ramped to divertor detachment (n_e range $10^{19} - 10^{20}$ m^{-3}).

This analysis suggests that in medium-high density divertor plasmas C III metastable ions are close to equilibrium with the ground state ions. This can be explained in terms of the relaxation time scales between the triplet and singlet spin systems (the so-called cross coupling time scales, as defined in [37]) compared to the ionization time scale for C III. For typical values of $T_e = 5$ eV, $n_e = 6 \times 10^{19} m^{-3}$, relevant to the measured C III emission, the calculated cross coupling time scale is $2\mu s$, while the average ionization time for C III in the divertor, as calculated with DIVIMP for the simulation of pulse 34859 at detachment, is much larger, $\tau_{iz} \sim$ 1ms. Note that, as the density increases, the cross coupling time scale becomes shorter. In such short time scales, the metastable population approaches equilibrium with the ground state well within τ_{iz}. Thus the metastable to ground population fraction is close to the equilibrium value. Therefore, the current treatment of metastable ions in divertor impurity transport simulations can be retained since it is not introducing any sizeable error in the models of impurity emission from the divertor plasma and is certainly a valid current working situation.

7.7 Conclusions

In this Chapter absolutely calibrated VUV measurements of deuterium and impurity line emission in the JET MkI divertor have been presented. They provide essential information towards improved understanding of hydrogenic and impurity transport and production mechanisms in the divertor region.

In the MkI divertor, without impurity injection, carbon and deuterium account for the total radiated power in discharges diverted on both carbon and beryllium target plates, consistent with simulations. This suggests that the beryllium targets were coated with carbon sputtered from the walls of the tokamak. Of the carbon ionization stages C III is the strongest radiator. However, large uncertainties are associated with the measurement of C IV line power due to the lack of measurement of the resonance transition. The measured beryllium emission is reproduced in the model if physical sputtering from BeO target surfaces is assumed. Beryllium radia-

tion dominates only during beryllium target melting experiments, when significant additional heating is applied without sweeping of the strike points. In Ohmic density limit discharges the ratio of carbon to deuterium radiation is observed to vary by a factor of two at high density, when varying the divertor flux expansion. This can be explained by the relative importance of sputtering from the divertor sidewalls and has a significant effect on the density limit.

Discrepancies in the detail of the radiation distributions between measurements and simulations are attributable to underestimation of the carbon source in the private plasma region. This is caused by inadequate modelling of the neutral deuterium density in the private plasma. These discrepancies are accentuated at detachment by the difficulty in describing the impurity forces which can produce the radiation profiles observed experimentally. However, in this regime spectroscopic measurements of deuterium and impurity emission provide essential information on the behaviour of the background hydrogenic plasma, e.g. when accurate measurements of T_e at the target cannot be obtained or concerning the balance of friction and thermal forces in the divertor plasma.

Further work is needed in the fusion community in order to understand the transport mechanisms connecting the impurity sources and the radiation distributions measured spectroscopically. In addition, measurements of emission profiles in the divertor are crucial for these studies.

Chapter 8

A Study of Carbon Impurity - Neutral Deuterium Charge Exchange in the Divertor Region

8.1 Introduction

Charge exchange recombination with neutral hydrogen modifies the equilibrium ionization balance of carbon:

$$\frac{n(C^{+z+1})}{n(C^{+z})} = \frac{S}{\alpha_{rec} + \frac{n_H}{n_e}\alpha_{CX}} \tag{8.1}$$

even for small fractions of n_H/n_e. This results in an increase of the fractional abundancies $n(C^{+z})/n(C_{tot})$ of the lower charge states, with consequent depopulation of the higher charge states. In other words, the lower ionization stages radiate at higher temperatures than when charge exchange recombination does not take place [130]. This effect becomes stronger with increasing n_H/n_e.

For this reason, it is expected that the high neutral deuterium densities characteristic of low temperature, high density divertor plasmas may be strongly influential on carbon impurity ionization balance and radiation through charge transfer reactions. However, this assumption has not yet been verified experimentally in divertor plasmas, nor has it been modelled in realistic conditions of divertor plasma discharges. A simple ionization equilibrium does not apply to divertor plasmas, since the characteristic time scales of transport and losses of impurity ions and hydrogen

neutrals are much shorter than the time scales needed to reach ionization equilibrium.

In an earlier study [130] it was shown how in conditions of transient ionization or recombination the charge exchange emission deviates from that in ionization equilibrium. The model considered there was that of a uniform plasma of constant electron temperature T_e and density n_e and constant neutral hydrogen temperature T_H and density n_H, in which impurity particle concentrations are followed in time from an initial state. For the case of transient ionization, an initial neutral carbon concentration is placed in the plasma and followed in time as it ionizes, until equilibrium is reached. In the case of transient recombination, an initial hydrogen-like carbon ion is followed until it reaches equilibrium, in this case by recombination to the lower charge states. For carbon impurities in transient recombination in a constant, uniform plasma, it was shown that the charge exchange emission is indeed enhanced with respect to that in ionization equilibrium for the same value of n_H/n_e. Instead, in transient ionization, the charge exchange emissivity is in deficit with respect to that in ionization equilibrium for the same plasma parameters.

However, the model of a constant, uniform plasma cannot be used to study the spectral emission from divertor plasmas, as shown in Chapter 7. An investigation of charge exchange processes in the divertor must be carried out together with a description of the transport mechanisms that determine the relative spatial distributions of the hydrogen neutrals and of the carbon ions.

This Chapter presents a study of the effect of deuterium-carbon impurity charge exchange in combination with divertor impurity transport in the model of JET MkI discharges. The main question to be answered is if charge transfer reactions can alter substantially the carbon impurity radiated power distributions in the divertor. This, of course, is of particular interest for detached and radiative divertor regimes, where the aim is to maximize radiative cooling of the plasma in the divertor volume, without increasing the impurity content of the core plasma.

8.2 Spectroscopic Observations

Intense spectral emission is induced by electron collisions in the edge/divertor regions, as shown in Chapter 7. Thus, experimental evidence of charge transfer reactions between neutral deuterium and carbon ions must be sought in spectral regions

where emission due to electron excitation is expected to be weak. Visible line emission from highly excited states of carbon ions is weak when electron impact excitation is the dominant collision process. However, it is strongly enhanced by electron capture from excited state hydrogen. For instance, in the case of $H(n=2)/C^{+6}$ charge transfer reactions, the cross section is maximum for capture into $C^{+5}(n=8)$ and C VI emission in the transition $n=8-7$ (5291 Å) is greatly enhanced. It is from the measurement of this line emission that the C^{+6} ion density and temperature in the core plasma are deduced by charge exchange recombination spectroscopy during high energy neutral beam injection into the plasma [131].

In a study of line emission from JET edge plasmas in single null configuration during the 1991/92 experimental campaign [132] it was shown that thermal charge transfer from excited state hydrogen ($H(n=2)$) into C^{+6} ions could account for the measured C VI ($n=8-7$) spectral line emission in the plasma edge upstream from the X-point region. The electron impact excitation contribution to the emission of this line was estimated to be more than a factor of 10 less than the charge exchange emission and thus the charge exchange origin of the line was assumed.

Additional spectroscopic observations relating to charge exchange reactions between deuterium neutrals and C^{+6} and C^{+5} ions can also be obtained in the XUV spectral region. For instance, measurement of the C VI Lyman series line emission from the plasma edge in old JET limiter configurations showed an enhancement of L_γ spectral emission, which was attributed to charge exchange with recycling hydrogen at the limiter and inner wall surfaces [133]. Similar measurements have also been obtained more recently in the plasma edge of JET during the initial, limiter phase of MkI plasmas, using a grazing incidence spectrometer as reported in [134]. Note, however, that no C VI charge exchange emission was observed during the X-point phase of the discharges.

In addition, XUV measurements in the plasma edge have been reported from Tore Supra with the ergodic divertor [135], [136] and from JET [134], showing modifications of the C V G-ratio (i.e. the ratio of C V intercombination to resonance line). This can be explained by charge transfer reactions between neutral deuterium and C^{+5} ions. In JET these measurements were obtained in the plasma edge during the limiter phase, at the beginning of the discharge and during the X-point phase in the SOL upstream from the X-point region. The measured G-ratio value of 0.7, compared to the equilibrium value of 0.45, was not observed to vary as the plasma

progressed towards detachment [134]. In these papers the charge exchange origin of the enhanced spectral emission is assumed and an estimate of the local neutral deuterium density necessary to explain the observed emission is given. However, none of these works includes comparisons with other spectroscopic observations related to deuterium emission in the region of interest (for instance D_α emission). Such observations are necessary to verify the level of neutral deuterium concentration needed to explain the charge exchange origin of the measured C VI and C V line emission.

Similar observations as those described above were envisaged for the divertor region in the MkI experimental campaign, as evidence of charge exchange occurring in divertor plasmas. However, no C VI $n = 8 - 7$ charge exchange emission was observed with visible spectroscopy in the divertor region. In addition, the lack of measurements in the XUV wavelength range along a LOS traversing the divertor region prevented the observation of the C VI Lyman series and of the C V resonance and intercombination lines. On the other hand, visible and VUV spectroscopic measurements, in agreement with the transport simulations, showed that C VI and C V emission from the MkI divertor region was negligible, as reported in Chapter 7.

The low concentration of the higher ionization stages of carbon in the divertor is thought to be due to the low electron temperatures characteristic of MkI divertor plasmas. Thus, it is believed that ionization into C^{+5} and C^{+6} ions takes place in the SOL upstream of the divertor region and inside the LCFS, and recombination of C^{+6} and C^{+5} ions into lower charge states occurs before the ions have entered the divertor volume. This is discussed in more detail later in this Chapter.

For these reasons, evidence of charge exchange had to be sought in spectral emission of lower ionization stages of carbon. As discussed in Chapter 3, electron capture from ground state hydrogen into C^{+3}, C^{+2} and C^{+1} ions selectively populates the low excited states $(3l, 2l)$ of these ions. Unfortunately these excited states are efficiently populated by electron excitation, leading to intense VUV and visible spectral lines. Therefore, spectroscopic observations in these spectral regions are not ideal. On the other hand, electron capture from excited state hydrogen, $H(n = 2)$, into C IV ions is expected to lead to the $n = 6 - 5$ charge exchange line emission at 4658 Å, but the spectrum is complicated by Be IV $n = 6 - 5$ charge exchange emission at the same wavelength. However, only a very weak spectral line was observed at this wavelength with divertor visible spectroscopy, and its intensity did not vary during a sequence of discharges that progressed towards higher electron

(and neutral) density and plasma detachment.

It is then concluded that no direct experimental evidence of charge exchange emission could be found in MkI divertor plasmas. Thus, the study of the effect of charge transfer reactions on carbon emission from divertor plasmas relies entirely on the interpretation of the measured C II-IV visible and VUV line emission originating from low excited states of these ions. As discussed in Chapter 7, this depends strongly on the model/prescriptions chosen for the hydrogenic plasma, on the assumptions of the impurity transport and is complicated by the uncertainties associated with the description of the carbon impurity source. On the other hand, the relative magnitude of the effect of charge transfer on divertor carbon emission can be studied, for a chosen simulation, by repeating the Monte Carlo impurity calculation including charge exchange collisions. This is the method adopted for the present investigation. The following Section describes how charge exchange recombination between neutral deuterium and impurity ions has been included in the DIVIMP impurity transport code.

8.3 Treatment of Charge Exchange in the Transport Model

As shown in Chapter 6, in the Monte Carlo calculations the change of charge state of the impurity ions is calculated from the characteristic times for ionization and recombination defined in eq. 6.37-6.39. For a given impurity ionization stage, calculation of the charge exchange recombination time, $\tau_{CX} = 1/n_D \alpha_{CX}$, requires the local neutral deuterium density, which is obtained from NIMBUS (see Chapter 6), and the rate coefficient for total charge transfer into that ionization stage. A full set of stage to stage charge exchange rate coefficients for carbon has been prepared, from the charge exchange cross section data set reviewed in Chapter 3 and they are plotted in Fig. 8.1. It is assumed that electron capture cross sections from a deuterium donor are equal to those from a hydrogen donor for the same collision speed. The rate coefficients were calculated for deuterium donors, which is the case relevant to JET MkI plasmas. Because of the low (thermal) collision energies in cold divertor plasmas and due to the similar masses of donor and receiver particles ($m_D = 2$ amu, $m_C = 12$ amu), the velocities of both reacting particles may

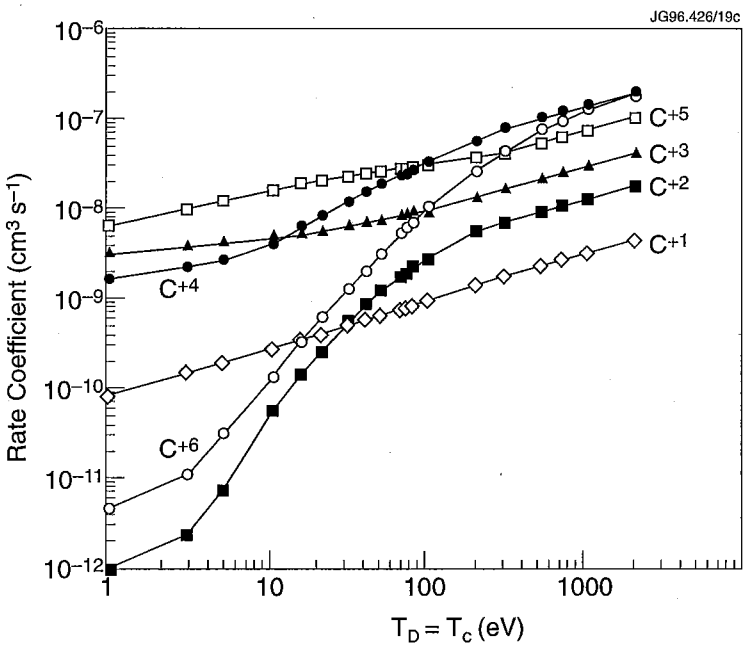

Figure 8.1: Total rate coefficients for charge exchange recombination between carbon ions and neutral deuterium, calculated from the cross section data set reviewed in Chapter 3. The rates were obtained assuming Maxwellian velocity distribution functions for the donor (deuterium) and receiver (carbon ion) particles and for equal temperatures $T_D = T_C$ (eV).

be comparable and the common simplification in elastic collisions of the impurity target being stationary is incorrect. The rate coefficients are correctly calculated by averaging over the velocity distribution functions of both particle species:

$$< \sigma v >_{CX} = \int \int f_D(\vec{v}_D)\ f_C(\vec{v}_C)\ |\vec{v}_D - \vec{v}_C|\ \sigma(|\vec{v}_D - \vec{v}_C|)\ d^3\vec{v}_D\ d^3\vec{v}_C \qquad (8.2)$$

where σ is the electron capture cross section, $|\vec{v}_D - \vec{v}_C|$ is the relative collision speed between the donor (neutral deuterium) and the receiver (C^{+z} ion) and $f_D(\vec{v}_D)$, $f_C(\vec{v}_C)$ are the velocity distribution functions of the donor and receiver species respectively (here the subscript C denotes a generic C^{+z} ion).

Two different distribution functions were allowed, Maxwellian and monoenergetic beam. Rate coefficients could be calculated for the various combinations of the two distribution functions, namely Maxwellian donor-Maxwellian receiver, Maxwellian donor/receiver-monoenergetic receiver/donor, monoenergetic donor- monoenergetic receiver. For the study presented here the rate coefficients were double Maxwellian averages, for equal donor and receiver temperatures ($kT_D = kT_C$). The general calculation allows for rate coefficients at different donor and receiver collision energies, but this is not compatible with the present structure of ADAS. In

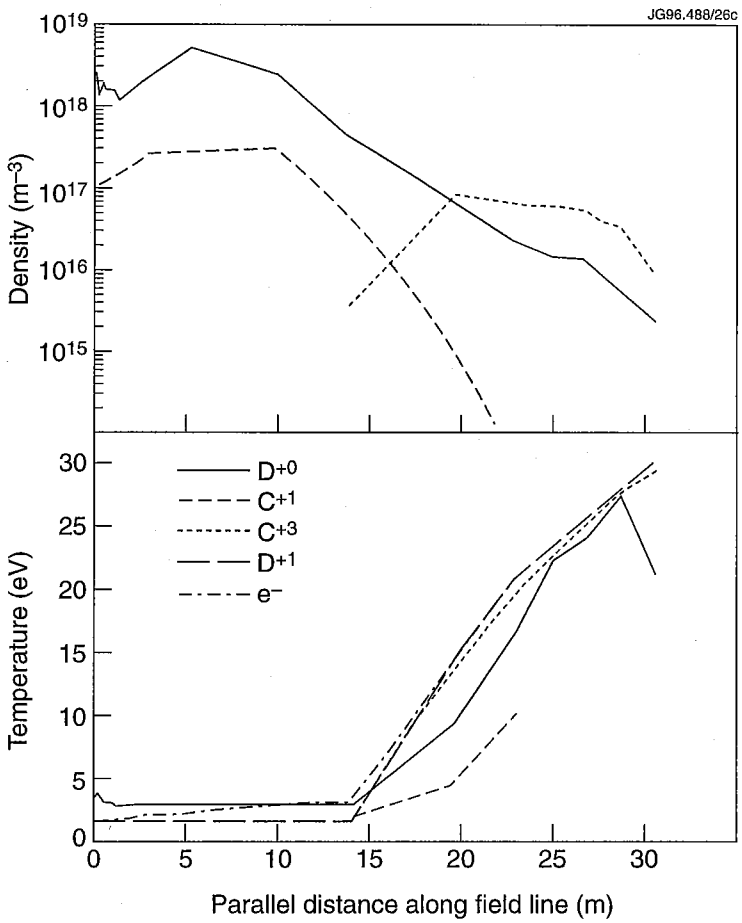

Figure 8.2: Neutral deuterium, C II, C IV, plasma ion and electron temperature versus parallel distance from the outer divertor target along the separatrix ring at plasma detachment for pulse 34859. In the top box the neutral deuterium, C II and C IV densities in the same region are shown.

conditions of low temperature, high density divertor plasmas, relevant to this study, this approximation appears to be acceptable. This is illustrated in Fig. 8.2 for the detached phase of the Ohmic density limit discharge (pulse 34859) studied in Chapter 7, where the neutral deuterium, C II, C IV and plasma ion and electron temperatures, plotted versus parallel distance along the separatrix for the first 30m from the outer target, are very similar. This can be understood in terms of the Spitzer energy transfer collison time, τ_T, introduced in Chapter 6. In the case of a C IV ion, in conditions of $T_i = 5$ eV and $n_i = 10^{20} m^{-3}$, typical of detached plasmas, $\tau_T = 5\mu s$.

The charge exchange rate coefficients are stored in ADAS for $T_D = T_C = T_e$, since α_{CX} also depends on electron temperature due to cascade in the collisional radiative calculation. This approximation does not introduce large errors in the

impurity transport calculations in high density divertor plasmas (see Fig. 8.2). Also, for situations in which T_e may be greater than T_D and T_C, this approximation would effectively overestimate the charge exchange rate coefficients, since these are an increasing function of temperature.

State selective charge exchange photon emissivity coefficients, q_{eff}^{cx}, have also been derived with collisional radiative calculations (see Chapter 3) for each carbon ionization stage. This excludes C^{+0}, due to the lack of C^{+1}/H state selective electron capture cross sections for this reaction in the literature. As a result, the population density of the C^{+z} excited levels directly affected by charge exchange is modified through electron collisions and radiative decay and an effective charge exchange contribution is provided to the population density of other terms of the ion.

8.4 Divertor Plasma Detachment

Since it is expected that the effect of charge exchange on carbon emission will be greater at high neutral deuterium densities, the case of divertor plasma detachment is considered first.

The Ohmic density limit discharge (pulse 34859) and the H-mode radiative discharge (pulse 34361), with carbon impurity transport, studied in Chapter 7 were considered. In terms of charge exchange analysis the results from these discharges are very similar. Therefore, without loss of generality and in order to avoid unnecessary repetitions, the Ohmic density limit discharge is considered for the discussion. Also, this allows direct comparison with the simulations of the spectroscopic signals already presented in Chapter 7.

For the same hydrogenic background plasmas presented in Chapter 7, two impurity simulations are carried out, the first as described in Chapter 7 and the other including charge exchange recombination in the model, as described in the previous Section. The comparison shows that the total carbon radiated power is very similar in the two cases. This is illustrated in Fig. 8.3 for the (•) simulation of Chapter 7. The carbon ion radiated power components are essentially unchanged when charge exchange recombination is included in the calculation.

The comparison of divertor spectral emission with and without charge exchange is shown in Figs. 8.4- 8.7. It can be seen that there is little change to C II-C IV visible and VUV line emission from these plasmas due to charge exchange collisions

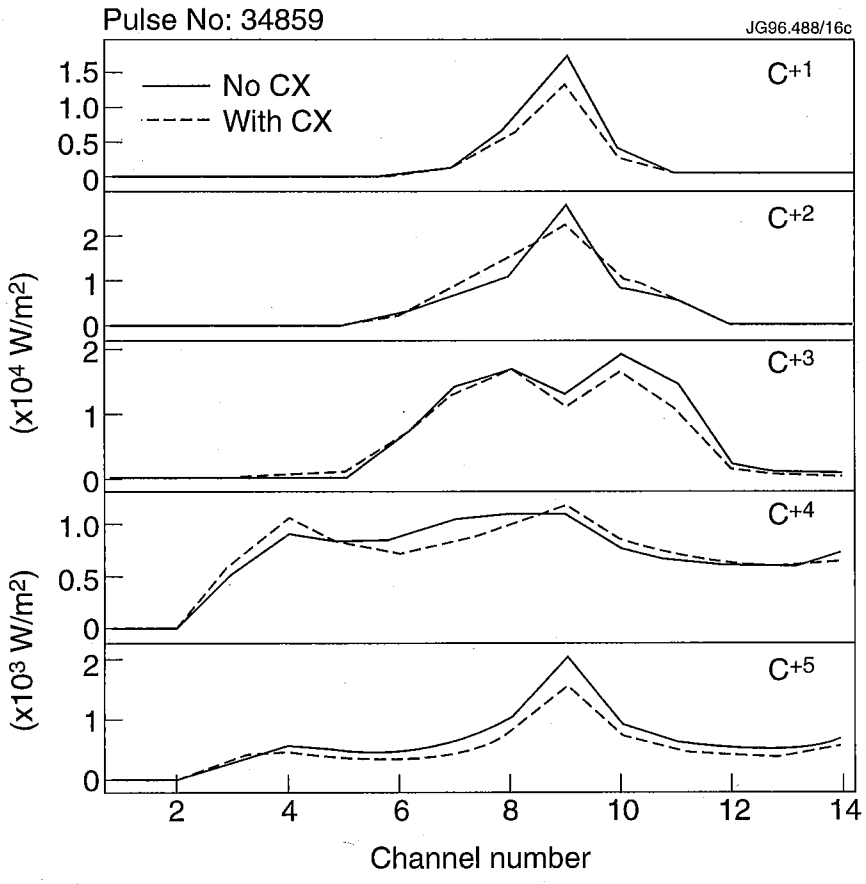

Figure 8.3: Comparison of carbon ion radiated power components with (dashed lines) and without (solid lines) charge exchange at plasma detachment for the (•) simulation of pulse 34859 presented in Chapter 7.

with neutral deuterium. Instead, as shown in Chapter 7, the largest difference is produced by modifications of the transport description of the background plasma. On average, the inclusion of charge exchange introduces a difference of 30-40% at most to the LOS integrated emission from the divertor, the exact value depending on the specific calculation for the background hydrogenic plasma. This variation is too small to be measured experimentally and, as shown in Fig. 8.4-8.7, falls within the uncertainty of the plasma and impurity transport model.

This weak sensitivity to charge exchange processes is due to the fact that, contrary to expectations, the carbon ion population fractions, $n(C^{+z})/n(C_{tot})$, are not appreciably modified by neutral deuterium through charge transfer reactions. The reason for this can be found in the comparison of the time scales for charge exchange recombination, ionization and electron recombination. These are obtained from the actual divertor plasma parameters (T_D, T_e, n_e, etc.), for a given simulation, and thus are a function of the plasma transport. For a given charge state the characteristic times for ionization to the stage above and recombination (free electron and charge exchange) from the stage above into that stage are compared. In particular, the variation of these characteristic times along the magnetic field lines for various rings of the computational grid is considered. The separatrix ring is chosen as representative.

Fig. 8.8 shows the characteristic times associated with C^{+0} ionization/C^{+1} recombination along the separatrix ring.

The source of C^{+1} ions, due to ionization of chemically sputtered carbon neutrals, is located on average some 15m along the field lines from the target plates (corresponding to about 10cm upstream of the target in the poloidal plane). A non negligible fraction of these ions are swept back to the target and lost to the walls or recombine into neutral atoms. Recombination of C^{+1} ions into C^{+0} neutrals is enhanced when charge exchange is included in the model, since $\tau_{CX} < \tau_{rec}$ in the divertor region. In fact, of the total number of recombination events, twice as many occur when charge exchange reactions are included in the impurity transport simulations. This shows that in detached plasma regimes, when the ionization front for carbon atoms is displaced from the sheath in front of the target to some distance upstream, C^{+1}/D charge exchange reactions can modify the carbon neutrals mean free path in the divertor region.

However, at present the Monte Carlo model for the impurities is such that

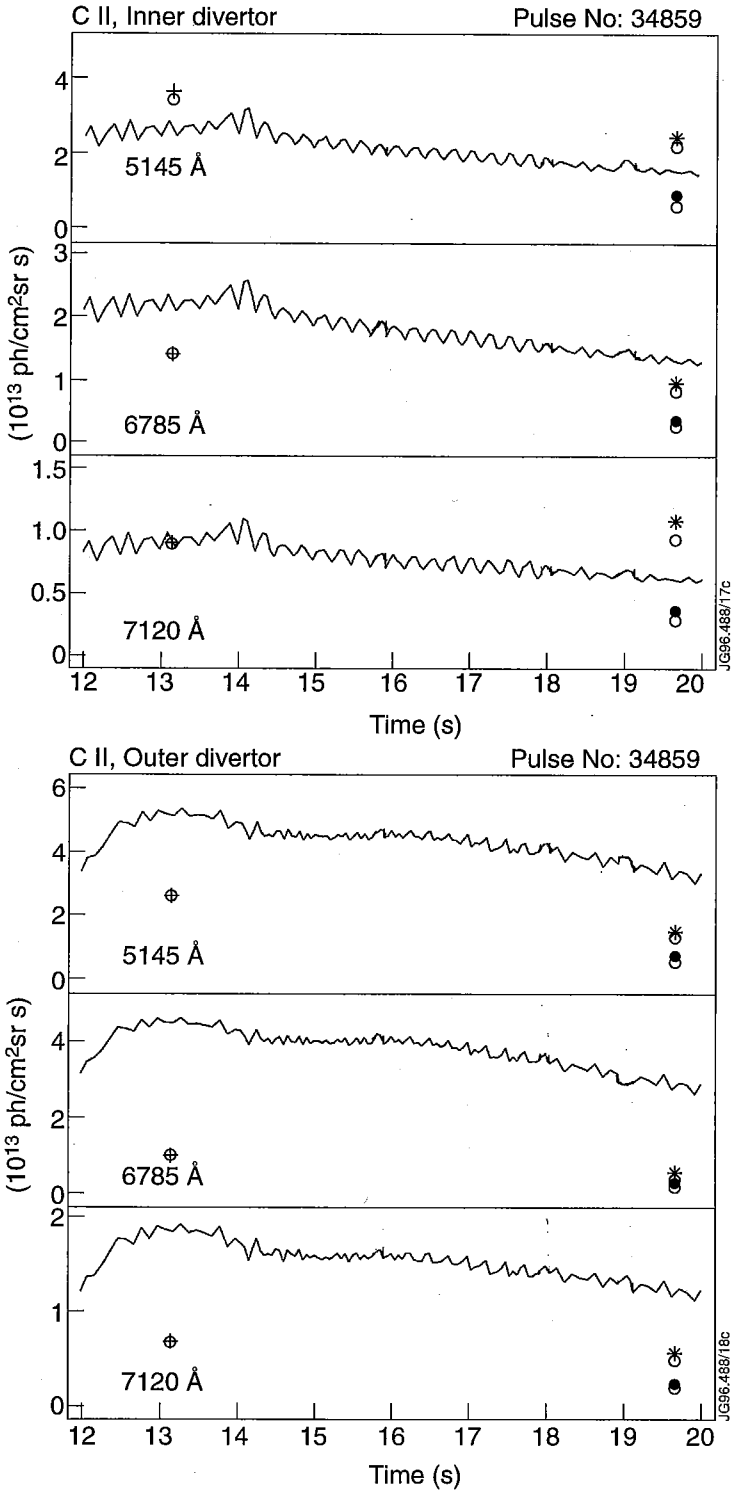

Figure 8.4: Comparison of C II visible spectral emission from the inner (top) and outer (bottom) divertor with and without charge exchange for the Ohmic density limit pulse 34859 of Chapter 7. The (+) symbols denote the low density simulation and the (∗), (•) symbols the simulations at plasma detachment, as in Chapter 7. The open circles denote the simulations with charge exchange recombination included in the model.

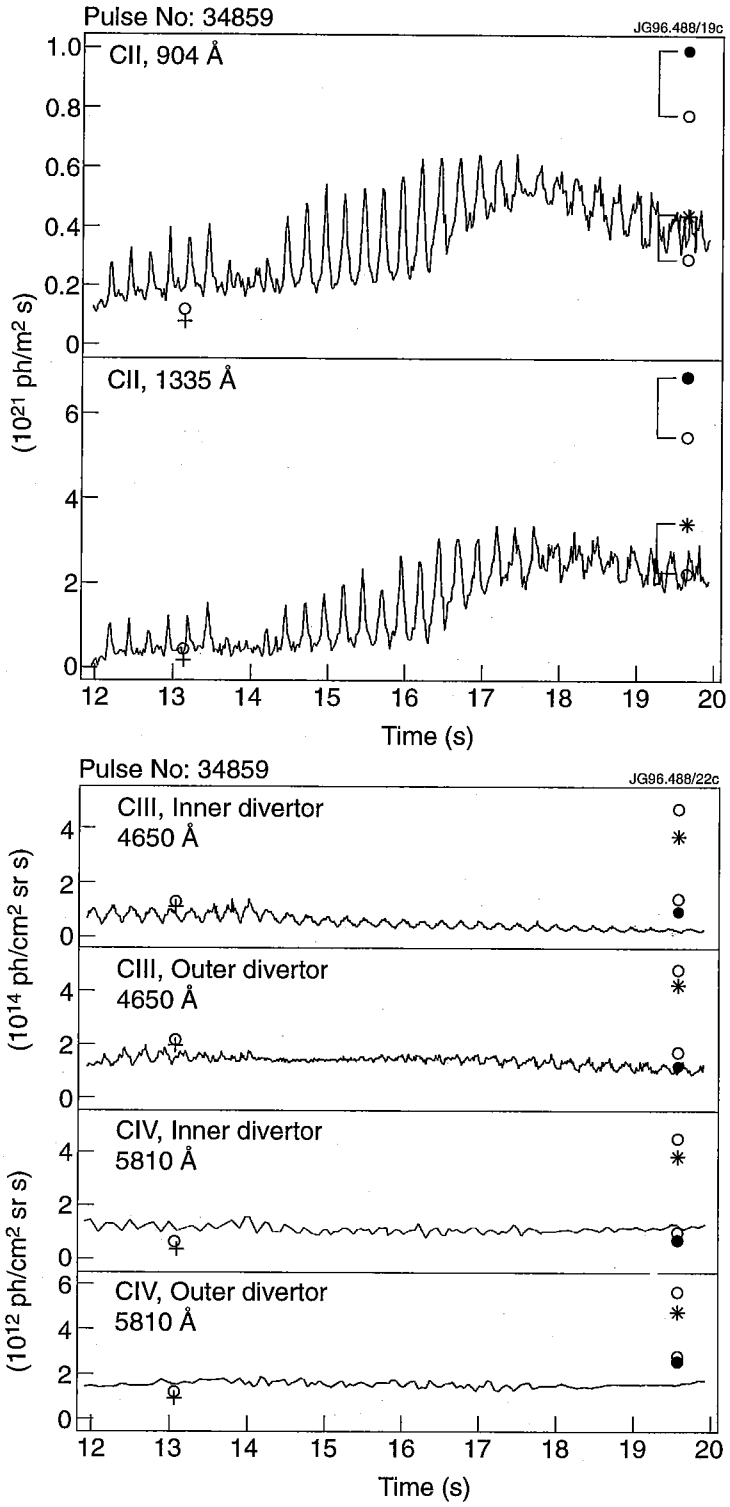

Figure 8.5: (top) Comparison of C II VUV emission, double SPRED, and C III-IV visible emission from inner/outer divertor (bottom) with and without charge exchange for the Ohmic density limit pulse 34859 of Chapter 7. The (+) symbols denote the low density simulation and the (∗), (•) symbols the simulations at plasma detachment, as in Chapter 7. The open circles denote the simulations with charge exchange recombination included in the model.

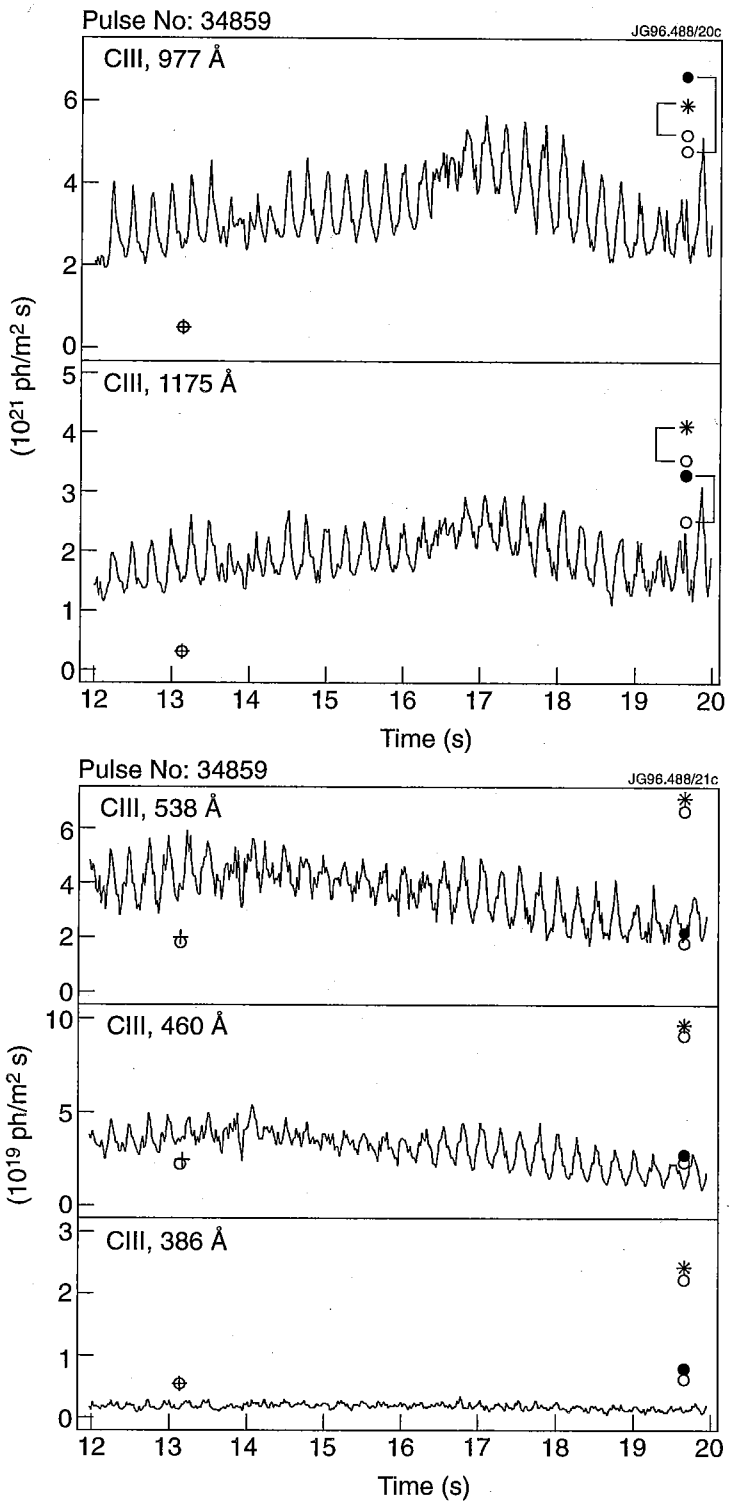

Figure 8.6: Comparison of C III VUV emission, double SPRED, from the divertor with and without charge exchange for the Ohmic density limit pulse 34859 of Chapter 7. The (+) symbols denote the low density simulation and the (∗), (•) symbols the simulations at plasma detachment, as in Chapter 7. The open circles denote the simulations with charge exchange recombination included in the model.

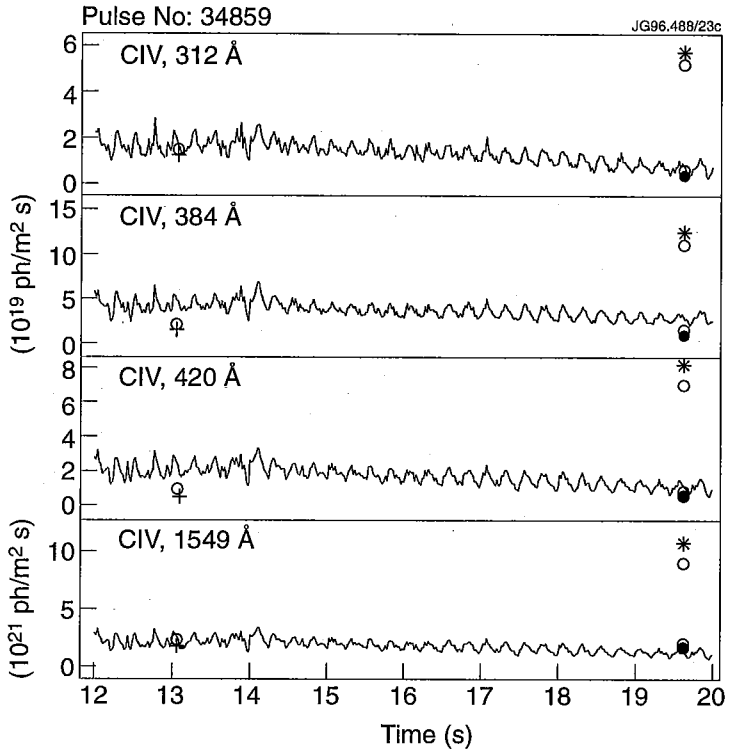

Figure 8.7: Comparison of C IV VUV emission , double SPRED, from the divertor with and without charge exchange for the Ohmic density limit pulse 34859 of Chapter 7. The (+) symbols denote the low density simulation and the (∗), (•) symbols the simulations at plasma detachment, as in Chapter 7. The open circles denote the simulations with charge exchange recombination included in the model.

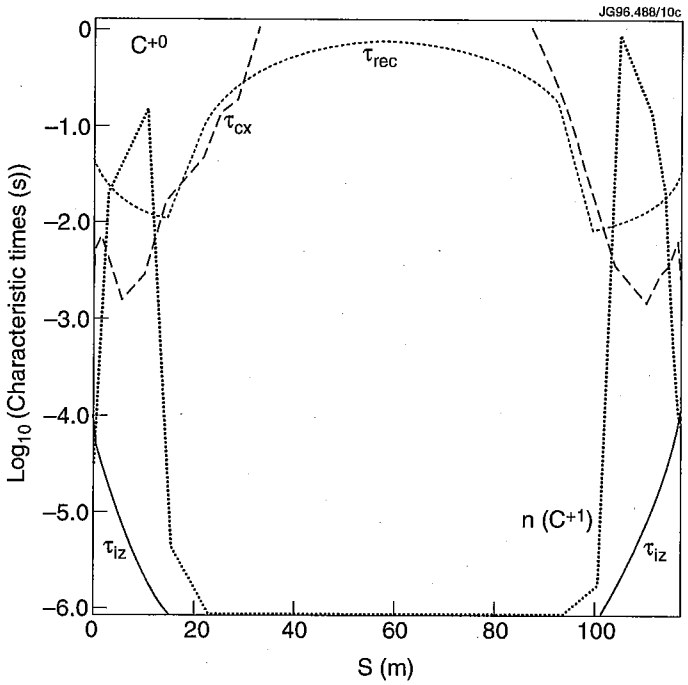

Figure 8.8: Characteristic times $\tau_{iz}, \tau_{rec}, \tau_{CX}$ for C^{+0} along the separatrix ring, from outer to inner target, for the simulation of pulse 34859 at detachment, (•) symbols. Overlayed is the normalized recombining C^{+1} ion density profile

when a C^{+1} ion recombines, the C^{+0} neutral atom is no longer followed in the calculation and another particle is launched. This approximation was so far assumed to be acceptable in conditions of 'attached', low density, high temperature divertor plasmas [137], where the neutral carbon atoms ionization length is very small, but it is clear, from what said above, that this is no longer valid when modelling detached plasmas. The analysis presented here has stimulated revision of the DIVIMP code, which is only starting at the time of writing this, to properly account for the motion of recombined neutral impurity particles until they are lost to the solid boundaries. Therefore, a quantitative assessment of the effect of charge exchange on the carbon neutrals mean free path in the divertor region will be part of future work.

In the case of C^{+1} ions, the impurity particle balance with and without charge exchange shows that a similar number of recombination events from C^{+2} occur in the two cases. This is illustrated in Fig. 8.9 with the variation of the characteristic times for C^{+1} ions along the separatrix ring.

Overlap between the C^{+2} ion density and τ_{CX}, τ_{rec} occurs in the region where the ionization time scale for C^{+1} is orders of magnitude smaller than the time scales for recombination. This, combined with the increased recombination of C^{+1} into C^{+0}

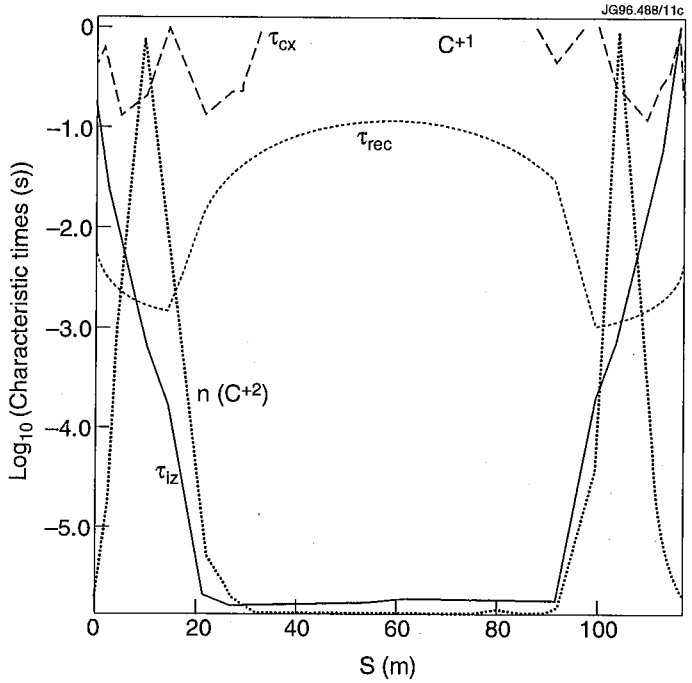

Figure 8.9: Characteristic times $\tau_{iz}, \tau_{rec}, \tau_{CX}$ for C^{+1} along the separatrix ring, from outer to inner target, for the simulation of pulse 34859 at detachment, (•) symbols. Overlayed is the normalized recombining C^{+2} ion density profile.

when charge exchange is included, produces the (slight) decrease of C II divertor radiation shown in Figs. 8.3 and 8.4-8.5.

C^{+3}/D charge exchange recombination increases by about 50% the number of recombination events into C^{+2} ions. Fig. 8.10 shows that for the separatrix ring $\tau_{CX} < \tau_{iz}$ in the first 20m along the field lines from the targets. However, the average C^{+2} ion source is situated at $s \sim 22$m for this detached plasma, where $\tau_{iz} < \tau_{CX}$ (see Fig. 8.10) and thus, on average, the C^{+2} charge state is ionizing.

The C^{+3} ionization stage represents the case where the ionization losses (into C^{+4}) approximately balance the recombination losses (into C^{+2}) in these detached plasma solutions. The C^{+3} source, due to ionization from C^{+2}, is located on average at $s \sim 28$m from the target plates. In this region charge exchange slightly enhances recombination into C^{+3} (see Fig. 8.11).

While the Li-like stage marks the case of almost balance between ionization and recombination losses, the C^{+4} and C^{+5} ions are recombining. In fact the ionization time scales for these ions are much longer than the corresponding recombination time scales in the divertor region. This is consistent with the lack of C VI spectral emission in the divertor, as observed with visible spectroscopy. Recombination from

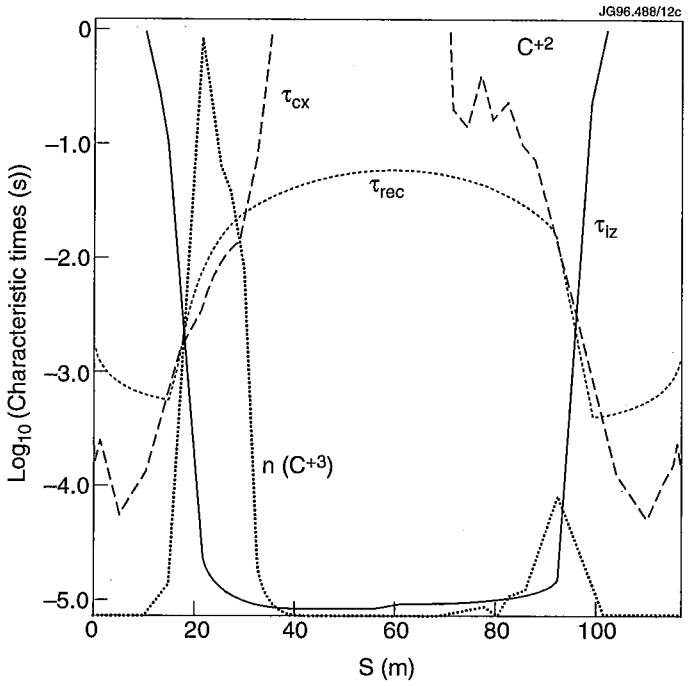

Figure 8.10: Characteristic times $\tau_{iz}, \tau_{rec}, \tau_{CX}$ for C^{+2} along the separatrix ring, from outer to inner target, for the simulation of pulse 34859 at detachment, (•) symbols. Overlayed is the normalized recombining C^{+3} ion density profile.

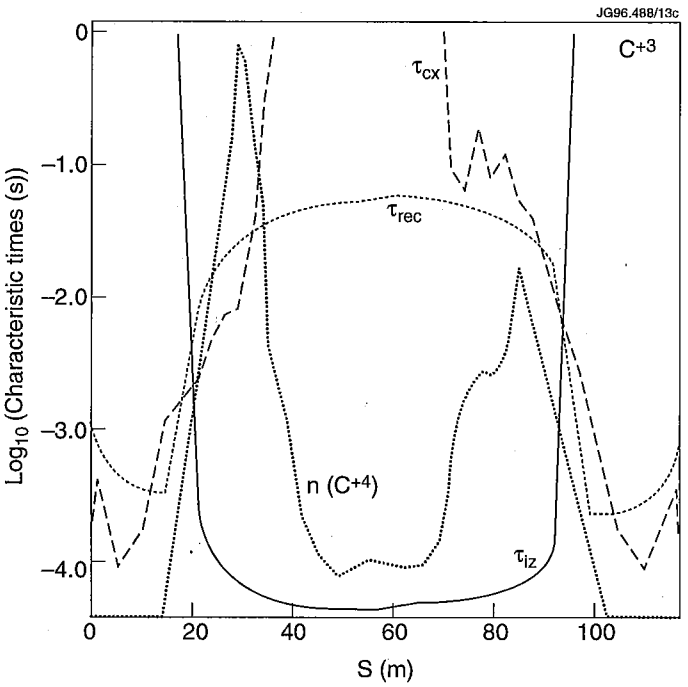

Figure 8.11: Characteristic times $\tau_{iz}, \tau_{rec}, \tau_{CX}$ for C^{+3} along the separatrix ring, from outer to inner target, for the simulation of pulse 34859 at detachment, (•) symbols. Overlayed is the normalized recombining C^{+4} ion density profile.

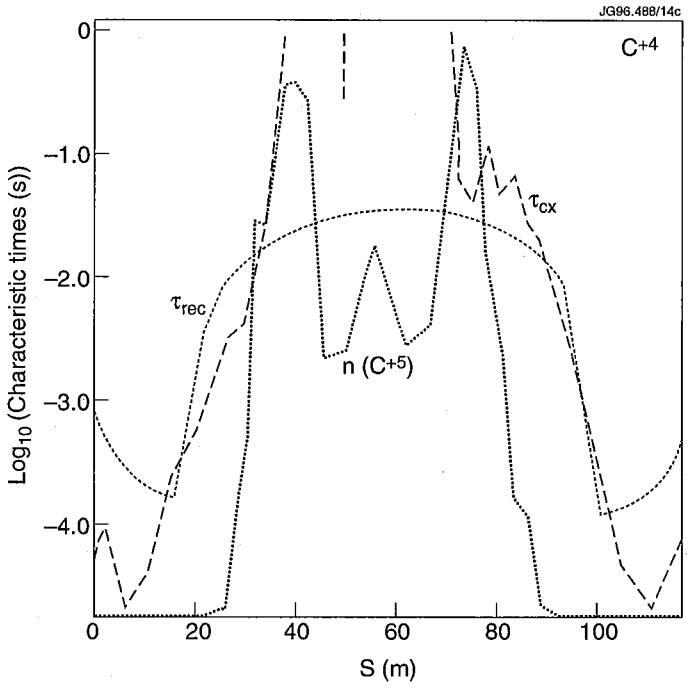

Figure 8.12: Characteristic times $\tau_{iz}, \tau_{rec}, \tau_{CX}$ for C^{+4} along the separatrix ring, from outer to inner target, for the simulation of pulse 34859 at detachment, (•) symbols. Overlayed is the normalized recombining C^{+5} ion density profile.

C^{+5} into C^{+4} is not modified when charge exchange is included in the model, as illustrated in Fig. 8.12, which shows that in the divertor region, where $\tau_{CX} \leq \tau_{rec}$, the spatial distributions of neutral deuterium and C^{+5} ion density do not overlap. Instead, recombination into C^{+5} is dominated by free electron recombination, as shown in Fig. 8.13.

8.5 Low Density Divertor Plasmas

In this Section the effect of charge exchange on divertor impurity emission in the low recycling regime is studied. The low density phase of the Ohmic density limit discharge of Chapter 7 is considered and the impurity transport simulation described there is compared with one on the same hydrogenic background plasma, in which charge exchange is included. All other modelling assumptions are unchanged.

As in the case of plasma detachment, charge exchange does not alter significantly the carbon impurity radiated power distribution. Figs. 8.4- 8.7 show the comparison of the two low density simulations, with and without charge exchange, for C II-IV VUV and visble emission, integrated along the double SPRED LOS and along the

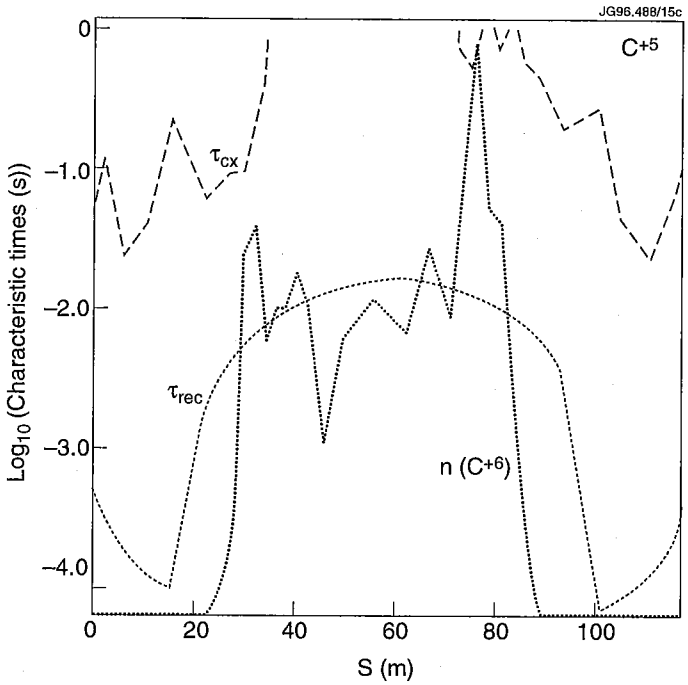

Figure 8.13: Characteristic times $\tau_{iz}, \tau_{rec}, \tau_{CX}$ for C^{+5} along the separatrix ring, from outer to inner target, for the simulation of pulse 34859 at detachment, (•) symbols. Overlayed is the normalized recombining C^{+6} ion density profile.

inner and outer divertor views of the visible spectrometer. It can be seen that also in this regime the inclusion of charge exchange in the model does not alter much the calculated spectral emissivities along vertical lines of sight directed at the inner and outer divertor targets.

Contrary to the case of plasma detachment, at low density all of the carbon charge states are ionizing, both with and without charge exchange in the model. The low charge state population fractions remain essentially unchanged when charge exchange is included in the calculation, since there is little recombination from C^{+1}, C^{+2} and C^{+3} due to charge exchange. This is exemplified in Figs. 8.14, 8.15 and 8.16, where the characterisic times for ionization from and recombination to C^{+0}, C^{+1} and C^{+2} are plotted along the separatrix. C^{+4}/D charge transfer enhances recombination into C^{+3} ions, but the effective volume of plasma where $\tau_{CX} \sim \tau_{iz}$ is too small (see Fig. 8.17) to produce any sizeable effect on the C IV spectral emissivities.

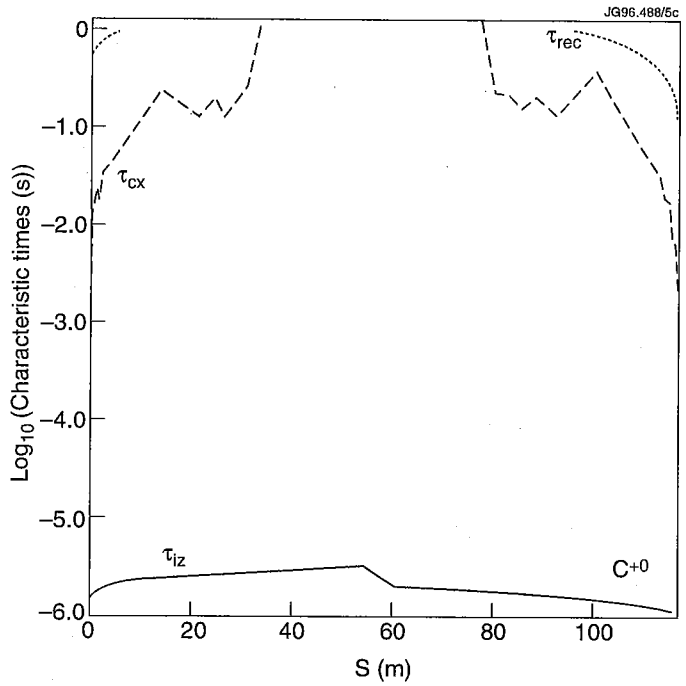

Figure 8.14: Characteristic times $\tau_{iz}, \tau_{rec}, \tau_{CX}$ for C^{+0} along the separatrix ring (from outer to inner target) for the simulation of the Ohmic density limit discharge 34859 at low density.

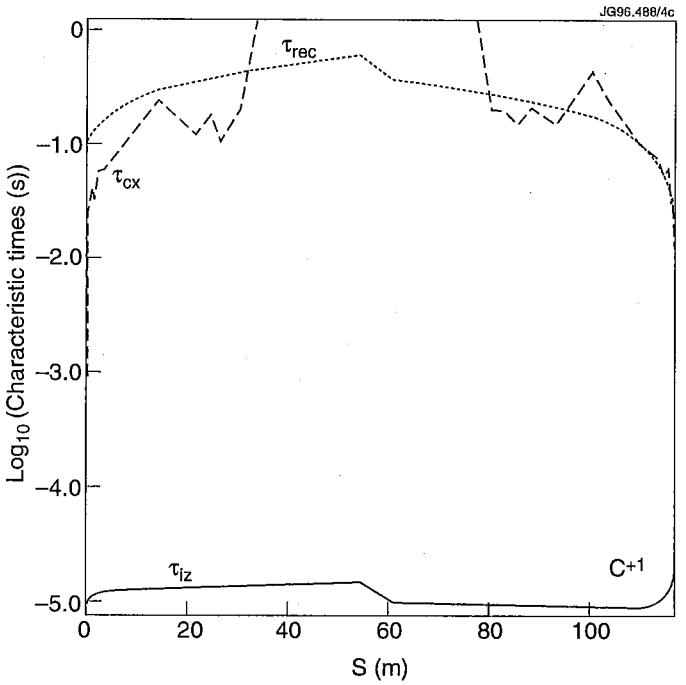

Figure 8.15: Characteristic times $\tau_{iz}, \tau_{rec}, \tau_{CX}$ for C^{+1} along the separatrix ring (from outer to inner target) for the simulation of the Ohmic density limit discharge 34859 at low density.

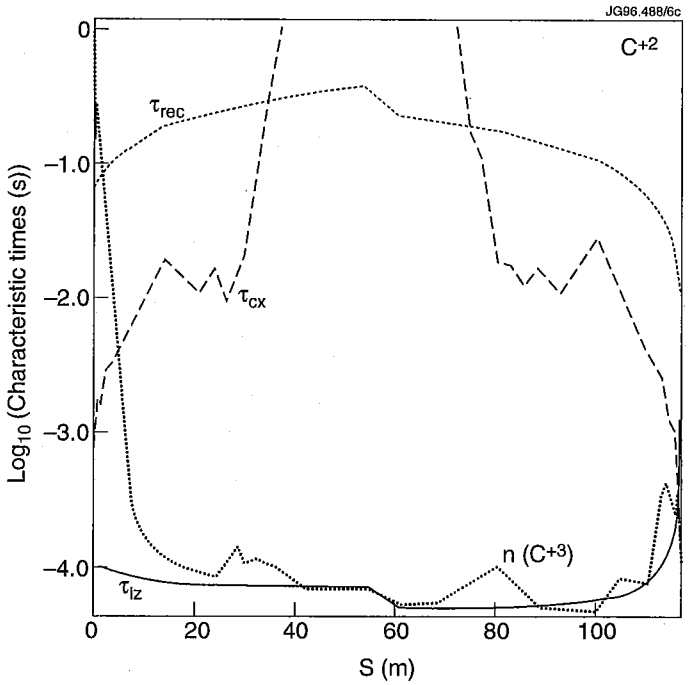

Figure 8.16: Characteristic times $\tau_{iz}, \tau_{rec}, \tau_{CX}$ for C^{+2} along the separatrix ring (from outer to inner target) for the simulation of the Ohmic density limit discharge 34859 at low density. Overlayed is the normalized C^{+2} density in arbitrary units.

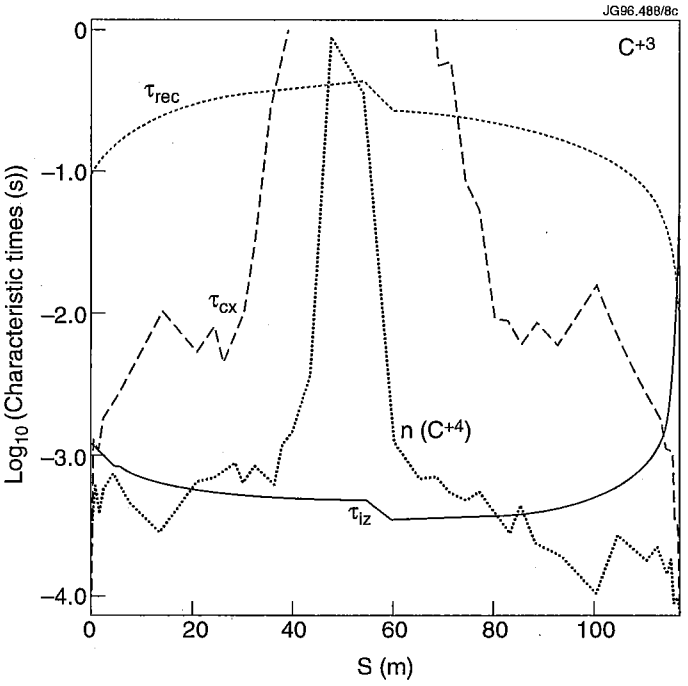

Figure 8.17: Characteristic times $\tau_{iz}, \tau_{rec}, \tau_{CX}$ for C^{+3} along the separatrix ring (from outer to inner target) for the simulation of the Ohmic density limit discharge 34859 at low density. Overlayed is the normalized C^{+4} density in arbitrary units.

8.6 Conclusions

In this Chapter the effect of charge exchange recombination with neutral deuterium on carbon impurity emission in the divertor region of JET has been studied. This investigation was stimulated by the result that charge exchange with neutral deuterium modifies the carbon impurity ionization balance in ionization equilibrium. It was expected that, especially in high density, detached plasma regimes, characterized by large neutral deuterium concentrations, charge transfer reactions would modify the radiation behaviour of carbon impurities in the divertor/SOL region. However, no direct spectroscopic evidence of charge exchange induced emission from the divertor region of JET MkI plasmas was obtained.

Low energy charge transfer was studied quantitatively in the model of MkI divertor Ohmic and H-mode radiative discharges in low density and plasma detachment regimes. To this end, the Monte Carlo impurity transport code DIVIMP was modified to include charge transfer collisions between neutral deuterium and impurity ions and a full set of charge exchange recombination rate coefficients for carbon were calculated for this analysis.

It is found that, contrary to expectations, charge exchange recombination does not alter much the carbon impurity radiated power distributions in the divertor region of JET, even at high neutral deuterium concentrations. Modifications to the LOS integrated spectral line emission from carbon ions are of the order of 30-40% at most, with respect to the case when charge exchange collisions are not included in the model. This is too small to be measured experimentally. This weak sensitivity on charge exchange recombination processes in divertor plasmas is explained by the comparison of the characteristic time scales for ionization, electron recombinaton and charge exchange for the different carbon impurity charge states. These time scales are calculated from the actual plasma parameters, for a given plasma simulation, and thus are a function of the plasma transport.

In the low recycling regime, the charge exchange time scales for the key radiating carbon ion states are generally comparable to or shorter than the electron recombination time scales in the divertor region. Thus, the total number of recombination events is enhanced. However $\tau_{iz} << \tau_{CX}$ or, in the case of C^{+3}, the effective volume where $\tau_{iz} \sim \tau_{CX}$ is very small and the effect of charge exchange recombination is therefore negligible. In this regime all the carbon charge states are ionizing.

In the plasma detachment regime, $\tau_{iz} < \tau_{CX}$ for the lower carbon charge states. There is, however, significant increase in recombination of C^{+1} into C^{+0} neutrals when charge exchange is included in the calculation, since $\tau_{CX} < \tau_{rec}$ in the divertor region. It is thought that C^{+1}/D charge transfer may affect the neutral carbon mean free path in detached divertor plasmas. The importance of this effect has stimulated revision of the DIVIMP code to properly account for the recombined neutral impurity particles, which at present are not followed in the Monte Carlo calculation. In the plasma detachment solutions C^{+3} marks the balance between ionization losses and recombination losses, while the higher charge states of carbon are fully recombining.

Both the low density and plasma detachment solutions show the lack of the high ionization stages of carbon (C V, C VI) in the divertor, consistent with visible spectroscopic observations.

Chapter 9

Conclusions

The measurement and interpretation of spectral emission from hydrogenic and impurity species in JET MkI pumped divertor plasmas has been presented. The study has been developed combining advanced atomic physics modelling of impurity and hydrogenic emission with the modelling of divertor plasma for the interpretation of line-of-sight integrated spectroscopic and bolometer signals.

VUV line emission, which forms the basis for analysis in the thesis, was measured with a new double SPRED spectrometer, installed in JET during the first phase of the MkI experimental campaign. The instrument was first characterized in the laboratory and then, after installation on the JET torus, commissioned and calibrated during plasma operation. The spectrometers were absolutely calibrated *in situ*, using branching ratio techniques and cross calibrating with other divertor diagnostics. The consistency of the SPRED intensity calibration with bolometer measurements was verified successfully. Consequently, the VUV spectroscopic measurements were exploited for experimental identification of the main contributors to the total radiated power from the MkI divertor in different plasma regimes and impurity scenarios. Moreover, the absolutely calibrated VUV measurements have allowed validation of the atomic physics data set for carbon ions. This has stimulated a revision of the entire data set and the production of a new complete set of internally consistent rate coefficients for carbon.

Radiative losses from intrinsic as well as injected impurities from the divertor region were investigated. Without impurity injection, carbon and deuterium account for the total radiated power in discharges diverted on both carbon and beryllium target plates, consistent with code simulations, while beryllium radiative losses are

negligible. These measurements clarify why plasmas operated on carbon and beryllium targets were found to be very similar and suggest that the beryllium target was coated with carbon sputtered from the walls of the tokamak. Beryllium radiation was measured to dominate only during beryllium target melting experiments.

The spatial distribution of the carbon source is closely linked with the magnetic configuration of the plasma discharges. The ratio of carbon to deuterium radiation is measured to vary by a factor of two in Ohmic density limit discharges when varying the divertor flux expansion (and thus the clearance of the plasma from the sidewalls). This can be explained by the relative importance of sputtering from the divertor sidewalls and has a significant effect on the density limit.

Of the carbon ionization stages, C III is measured to be the strongest radiator in medium to high density MkI divertor plasmas. However, uncertainties are associated with the measurement of the C IV line power and the direct measurement of the C IV resonance line is strongly desired. Extensive measurements of radiated power components were carried out during nitrogen seeded radiative divertor discharges, with nitrogen dominating the divertor radiation. Li-like nitrogen is measured to be the strongest radiator.

VUV and visible spectroscopy line emission and bolometer measurements have been compared with interpretative code modelling in the study of hydrogenic plasma and impurity transport in JET MkI divertor discharges. The analysis was carried out both in low recycling and plasma detachment regimes.

Discrepancies in the detail of the radiation distributions between measurements and simulations are in part due to the underestimation of the carbon source in the private plasma region and in part to the difficulty in describing the details of the forces acting on the impurity species. It is shown, however, that simultaneous measurements in the VUV and visible wavelength range can constrain the force balance on the impurities in the calculations.

The modelling of divertor spectral emission in detached plasma regimes has pushed the transport codes to conditions that had not been fully tested before. This has highlighted the main limitations of the Onion Skin Model for the background plasma in such extreme regimes.

The effect of charge exchange recombination with neutral deuterium on carbon impurity emission in the divertor region of JET has been studied. In high density divertor plasmas, characterized by large neutral deuterium concentrations, it was

expected that charge transfer reactions would influence the carbon ionization balance and thus modify the carbon radiative losses. However, no direct spectroscopic evidence of charge exchange induced emission from the divertor region of JET was obtained experimentally. Low energy charge transfer was thus studied quantitatively in the model of Ohmic and H-mode highly radiative divertor discharges in low density and plasma detachment regimes. To this end, the impurity transport code was modified to include charge transfer collisions between neutral deuterium and impurity ions. A review of low energy charge transfer cross sections for collisions between neutral hydrogen donors and carbon ions has been carried out. A complete set of stage to stage and state selective photon emissivity charge exchange recombination rate coefficients for carbon were calculated using a collisional radiative model.

It is found that, contrary to expectations, charge exchange recombination does not alter much the radiated power distribution of carbon in the divertor region of JET, even at high neutral deuterium concentrations. Larger modifications to the carbon radiation are instead induced by just slight variations of the hydrogenic background plasma transport parameters. This weak sensitivity on charge exchange recombination processes is explained by the comparison of the characteristic time scales for ionization, free electron recombination and charge exchange for the different ionization stages of carbon.

Further work is needed in order to understand the transport mechanisms connecting the impurity sources and the radiation distributions measured spectroscopically in the divertor. In addition, it is stressed that measurements of emission profiles across the diveror and along the scrape-off layer are crucial for these studies.

Appendix A

Acronyms

AO: Atomic Orbital
CCD: Charge Coupled Device
ELM: Edge Localised Mode
ETF: Electron Translational Factor
FE: Flux Expansion
FWHM: Full Width at Half Maximum
IR: Infra Red
ITER: International Thermonuclear Experimental Reactor
JET: Joint European Torus
LCFS: Last Closed Flux Surface
LOS: Line of Sight
MCP: Micro Channel Plate
MDS: Multichannel Detector System
MkI: MarkI
MO: Molecular Orbital
NBI: Neutral Beam Injection
OSM: Onion Skin Model
PDA: Photo Diode Array
PES: Photon Emission Spectroscopy
PSS: Perturbed Stationary State (Method)
RF: Radio Frequency
SOL: Scrape-off-Layer
SPRED: Survey Poor Resolution Extended Domain (Spectrometer)

TES: Translational Energy Spectroscopy

VUV: Vacuum Ultra Violet

Bibliography

[1] R. Pozzoli, *Fisica del Plasma Termonucleare e Astrofisico*, CLUED, Milano, 1984.

[2] *JET Joint Undertaking Progress Report*, 1995.

[3] P. C. Stangeby and G. M. McCracken, Nucl. Fusion 30 (1990) 1225.

[4] F. Wagner et al., Phys. Rev. Lett. 49 (1982) 1408.

[5] F. Wagner and K. Lackner, *Physics of Plasma Wall Interactions in Controlled Fusion*, volume 131 of *B: Physics*, page 931, Plenum Press, 1984, D. E Post and R. Behrish Eds., NATO ASI series.

[6] ITER-JCT and Home Teams (Presented by G. Janeschitz), Plasma Phys. Control. Fusion 37 (1995) A19.

[7] D. J. Campbell and L. D. Horton, JET-Scientific Council Meeting, 26 Sept., 1995.

[8] L. D. Horton, to be published in Plasma Phys. and Control. Fusion (23rd EPS Conf., Kiev, Ukraine), 1996.

[9] M. Ulrickson et al., J. Nucl. Mater. 176-177 (1990) 44.

[10] S. Clement et al., Controlled Fusion and Plasma Physics 19C-III (1995) 309, (Proc. 22nd EPS Conf., Bournemouth).

[11] H. Zohm, Plasma Phys. Control. Fusion 38 (1996) 105.

[12] P. N. Yushmanov et al., Nucl. Fusion 30 (1990) 1999.

[13] The JET Team (presented by D. Stork), Plasma Phys. and Control. Nucl. Fusion Res. I (1994) 51, (Proc. 15th Int. Conf., Seville, 1994).

[14] G. Saibene et al., Controlled Fusion and Plasma Physics 19C-III (1995) 309, (Proc. 22nd EPS Conf., Bournemouth).

[15] D. Reiter, G. H. Wolf, and H. Kever, Nucl. Fusion 30 (1990) 2141.

[16] M. R.Wade et al., J. Nucl. Mater. 220-222 (1995) 178.

[17] M. von Hellermann et al., in *3rd International Workshop on Helium Transport and Exhaust, Sept. 25-28 1995, Charleston, SC, USA*, 1995.

[18] K. Borrass and G. Janeschitz, Nucl. Fusion 34 (1994) 1203.

[19] L. D. Horton, Plasma Phys. and Control. Nucl. Fusion Res. I (1994) 541, (Proc. 15th Int. Conf., Seville, 1994).

[20] R. D. Monk et al., Controlled Fusion and Plasma Physics 19C-III (1995) 293, (Proc. 22nd EPS Conf., Bournemouth).

[21] R. D. Monk et al., Contrib. Plasma Phys. 36 (1996) S37.

[22] H. J. Jäckel et al., JET-P(95)72 (JET Posters presented to the 37th Annual Meeting, APS Division of Plasma Physics, Louisville, USA, 6-10 Nov.), 1995.

[23] J. Neuhauser et al., Plasma Phys. Control. Fusion 37 (1995) A37.

[24] S. Weber et al., Controlled Fusion and Plasma Physics 17C-II (1993) 767.

[25] R. Reichle et al., to be published in J. Nucl. Mater. (12th PSI Conf., St-Raphael, France, May 20-24 1996), 1996.

[26] U. Samm et al., Plasma Phys. Control. Fusion 35 (1993) B167.

[27] G. F. Matthews, Plasma Phys. Control. Fusion 37 (1995) A227.

[28] P. J. Harbour et al., Controlled Fusion and Plasma Physics 19C-IV (1995) 465, (Proc. 22nd EPS Conf., Bournemouth).

[29] R. Reichle et al., Controlled Fusion and Plasma Physics 19C-III (1995) 85, (Proc. 22nd EPS Conf., Bournemouth).

[30] The JET Team (presented by G.C. Vlases), Plasma Phys. and Control. Nucl. Fusion Res. 1 (1993) 287, (Proc. 14th Int. Conf., Wurzburg, 1992).

[31] A. Loarte et al., Controlled Fusion and Plasma Physics 19C-III (1995) 305, (Proc. 22nd EPS Conf., Bournemouth).

[32] A. Loarte, to be published in J. Nucl. Mater. (12th PSI Conf., St-Raphael, France, May 20-24 1996), 1996.

[33] D. J. Campbell and the JET Team, to be published in J. Nucl. Mater. (12th PSI Conf., St-Raphael, France, May 20-24 1996), 1996.

[34] B. Tubbing et al., Controlled Fusion and Plasma Physics 19C-III (1995) 453, (Proc. 22nd EPS Conf., Bournemouth).

[35] D. E. Post, J. Nucl. Mater. 220-222 (1995) 143.

[36] D. E. Post, Phys. Plasmas 2 (1995) 2328.

[37] W. J. Dickson, PhD thesis, University of Strathclyde, 1993.

[38] H. P. Summers, Adas, JET-IR(94)06, 1994.

[39] R. W. P. McWhirter and H. P. Summers, *Applied Atomic Collision Physics - Plasmas*, volume 2, page 51, Academy Press, 1984.

[40] M. Harrison, *Physics of Plasma-Wall Interactions in Controlled Fusion*, volume 131 of *B*, page 281, Plenum Press, New York, 1986, (D.E. Post, R.Behrisch Eds.) NATO ASI Series.

[41] R. K. Janev and H. Winter, Physics Reports (Review Section of Physics Letters) 117 (1985) 265.

[42] H. Bransden and C. J. Joachain, *Physics of Atoms and Molecules*, Longmann Scientific and Technical, 1983.

[43] R. K. Janev et al., At. Data and Nucl. Data Tables 40 (1988) 249.

[44] R. A. Phaneuf, Nucl. Fusion 2 (1992) 75, Atomic and Plasma-Material Interaction Data for Fusion Supplement.

[45] T. G. Heil et al., Phys. Rev. A 27 (1983) 2365.

[46] H. Tawara, IPPJ-AM-56 Report, Institute of Plasma Physics, Nagoya University, Nagoya, 1987.

[47] R. W. McCullough et al., J. Phys. B 17 (1984) 1373.

[48] R. J. Blint et al., Astrophys. J. 205 (1976) 634.

[49] W. D. Watson et al., Astrophys. J. 231 (1979) 627.

[50] T. G. Heil et al., Phys. Rev. A 23 (1982) 1100.

[51] S. Bienstock et al., Phys. Rev. A 25 (1982) 2850.

[52] L. Opradolce et al., J. Phys. B 21 (1988) 503.

[53] L. F. Errea et al., J. Phys. B 24 (1991) 4061.

[54] B. Herrero et al., J. Phys. B 28 (1995) 4607.

[55] C. C. Havener et al., Phys. Rev. A 51 (1995) 2982.

[56] R. A. Phaneuf et al., Phys. Rev. A 26 (1982) 1892.

[57] L. D. Gardner et al., Phys. Rev. A 21 (1980) 1397.

[58] R. A. Phaneuf et al., Phys. Rev. A 17 (1978) 534.

[59] D. H. Crandall et al., Phys. Rev. A 19 (1979) 504.

[60] D. Ciric et al., J. Phys. B 18 (1985) 3629.

[61] F. G. Wilkie et al., J. Phys. B 19 (1986) 239.

[62] D. Dijkkamp et al., J. Phys. B 18 (1985) 4763.

[63] W. Fritsch and C. D. Lin, J. Phys. B 17 (1984) 3271.

[64] R. Hoekstra, PhD thesis, University of Groningen, 1990.

[65] M. Gargaud et al., J. Phys. B 20 (1987) 1555.

[66] M. Gargaud and R. McCarroll, J. Phys. B 18 (1985) 463.

[67] R. E. Olson et al., J. Phys. B 11 (1978) 699.

[68] J. Hanssen et al., J. Phys. B 17 (1984) L323.

[69] H. Tawara et al., At. Data and Nucl. Data Tables 32 (1985) 235.

[70] N. Shimakura et al., Phys. Rev. A 45 (1992) 7876.

[71] E. J. Shipsey et al., J. Phys. B 14 (1981) 869.

[72] C. Bottcher and T. G. Heil, Chem. Phys. Lett. 86 (1982) 506.

[73] R. K. Janev and J. J. Smith, Nucl. Fusion 4 (1993) 167, Atomic and Plasma-Material Interaction Data Supplement.

[74] R. A. Phaneuf et al., Atomic data for fusion, ORNL-6090, 1987.

[75] T. A. Green et al., Phys. Rev. A 25 (1982) 1364.

[76] W. Fritsch and C. D. Lin, Phys. Rev. A 29 (1984) 3039.

[77] M. Kimura and C. D. Lin, Phys. Rev. A 32 (1985) 1357.

[78] H. P. Summers and M. B. Hooper, Plasma Physics 25 (1983) 1311.

[79] R. J. Fonck et al., Appl. Optics 21 (1982) 2115.

[80] J. Yvon, Diffraction gratings ruled and holographic.

[81] B. C. Stratton et al., Rev. Sci. Instrum. 57 (1986) 2043.

[82] K. D. Zastrow et al., Phys. Fluids B5 (1993) 4099.

[83] J. Yvon, private communication, 1996.

[84] E. M. Reeves and W. H. Parkinson, J. Opt. Soc. of America 53 (1963) 941.

[85] J. L. Wiza, Nucl. Instrum. Methods 162 (1979) 587.

[86] R. Wolf et al., JET-P(95)34, 1995.

[87] F. Paresce et al., Appl. Optics 10 (1971) 1904.

[88] N. Hawkes et al., in *UV and X-ray spectroscopy of Astrophysical and Laboratory Plasmas, Proc. 10th International Colloqium, Berkeley, California*, 1993.

[89] K. D. Lawson et al., Optics Communications 68 (1988) 121.

[90] R. D. B. Fraser and E. Suzuki, *Spectral Analysis: Methods and Techniques*, Marcel Dekker Inc., 1970.

[91] M. V. Klein and T. E. Furtak, *Optics*, John Wiley and Sons, New York, 1986.

[92] J. H. Brzozowski et al., Physica Scripta 43 (1991) 283.

[93] J. Z. Klose and W. L. Wiese, J. Quant. Spectrosc. Radiat. Transfer 42 (1989) 337.

[94] W. J. Karzas and R. Latter, Astrophys. J. Suppl. VI (1961) 167.

[95] N. Hawkes et al., JET-R(91)07, 1991.

[96] R. C. Isler and R. A. Langley, Appl. Opt. 24 (1985) 254.

[97] P. C. Stangeby and J. D. Elder, J. Nucl. Mater. 196-198 (1992) 258.

[98] E. Cupini, A. De Matteis, R. Simonini, NET Report EUR XII, 1984.

[99] S. I. Braginskii, Review of Plasma Physics 1 (1965) 205, Consultants Bureau, New York.

[100] P. C. Stangeby, *Physics of Plasma-Wall Interactions in Controlled Fusion*, volume 131 of *B*, page 41, Plenum Press, New York, 1986, (D.E. Post, R.Behrisch Eds.) NATO ASI Series.

[101] R. Chodura, *Physics of Plasma-Wall Interactions in Controlled Fusion*, volume 131 of *B*, page 99, Plenum Press, New York, 1986, (D.E. Post, R.Behrisch Eds.) NATO ASI Series.

[102] P. C. Stangeby, Phys. Fluids 27 (1984) 682.

[103] R. Simonini et al., Contrib. Plasma Phys. 34 (1994) 368.

[104] J. Neuhauser et al., Nucl. Fusion 24 (1984) 39.

[105] P. J. Harbour and J. Morgan, Control. Fusion and Plasma Phys. 7D-II (1983) 427, (Proc. 11th EPS, Aachen).

[106] P. C. Stangeby, Contrib. Plasma Phys. 28 (1988) 507.

[107] L. Spitzer, *Physics of Fully Ionized Gases*, Interscience Publishers, New York, 1962.

[108] J. Bohdansky, Nuclear Fusion Special Issue (1984) 61, Data Compendium for Plasma Surface Interactions.

[109] J. Roth, Nuclear Fusion Special Issue (1984) 72, Data Compendium for Plasma Surface Interactions.

[110] J. Roth, E. Vietzke, and A. Haasz, Supplement to Nucl. Fusion 1 (1991) 63.

[111] W. Eckstein, J. Bohdansky, and J. Roth, Supplement to Nucl. Fusion 1 (1991) 51.

[112] W. Eckstein et al., Sputtering data, IPP-9/82, 1993.

[113] J. Roth, *Physics of Plasma-Wall Interactions in Controlled Fusion*, volume 131 of *B*, page 389, Plenum Press, New York, 1986, (D.E. Post, R.Behrisch Eds.) NATO ASI Series.

[114] M. W. Thompson, Phil. Mag. 18 (1968) 377.

[115] C. Garcia-Rosales and J. Roth, Controlled Fusion and Plasma Physics 18B-II (1994) 770, (Proc. 21st EPS Conf., Montpellier).

[116] A. Haasz et al., J. Nucl. Mater. 231 (1996) 170.

[117] A. Pospieszczyk et al., Plasma Phys. Control. Fusion 19C-III (1995) 85, (Proc. 22nd EPS Conf., Bournemouth).

[118] H. Kubo et al., Plasma Phys. Control. Fusion 37 (1995) 1133.

[119] R. Wood et al., to be published in Control. Fusion and Plasma Phys., (Proc. 23rd EPS Conf., Kiev), 1996.

[120] J. Wesson, *Tokamaks*, Clarendon Press, Oxford, 1987.

[121] A. Loarte, private communication, 1996.

[122] P. C. Stangeby, Nucl. Fusion 33 (1993) 1695.

[123] K. Borrass et al., to be published in J. Nucl. Mater. (12th PSI Conf., St-Raphael, France, May 20-24 1996), 1996.

[124] T. Lovegrove et al., Plasma Phys. Control. Fusion 19C-III (1995) 301, (Proc. 22nd EPS Conf., Bournemouth).

[125] D. J. Campbell et al., to be published in J. Nucl. Mater. (12th PSI Conf., St-Raphael, France, May 20-24 1996), 1996.

[126] K. Borrass and P. C. Stangeby, Plasma Phys. Control. Fusion 17C-II (1993) 763, (Proc. 20th EPS Conf., Lisbon).

[127] K. Sawada and T. Fujimoto, J. Appl. Phys. 78 (1995) 2913.

[128] A. Kallenbach et al., Nucl. Fusion 37 (1994) 1557.

[129] R. Simonini, private communication, 1996.

[130] C. F. Maggi, Laurea Thesis, Universita' di Milano, (also as JET-IR(93)05), 1992.

[131] A. Boileau et al., Plasma Phys. Control. Fusion 31 (1989) 779.

[132] C. F. Maggi et al., Control. Fusion and Plasma Phys. 18B-II (1994) 826, (Proc. 21st EPS Conf., Montpellier).

[133] M. Mattioli et al., Phys. Rev. A 40 (1989) 3886.

[134] M. O'Mullane et al., to be published in Control. Fusion and Plasma Phys. (Proc. 23rd EPS Conf., Kiev), 1996.

[135] M. Mattioli et al., Nucl. Fusion 35 (1995) 807.

[136] C. D. Michelis et al., Controlled Fusion and Plasma Physics 19C-III (1995) 109.

[137] P. C. Stangeby, private communication, 1996.